INVESTIGATING THE ROLE OF ATM KINASE IN SYNAPSE DEVELOPMENT AND HOMEOSTASIS

by

MATTHEW JAMES TAYLOR

A thesis submitted to the University of Birmingham for the degree of

DOCTOR OF PHILOSOPHY

50,000 words

Institute of Cancer and Genomic Sciences
College of Medical and Dental Sciences
University of Birmingham
September 2023

Abstract

Mutations in Ataxia-telangiectasia mutated (ATM), a master regulator of the DNA damage response (DDR), result in early-onset cerebellar ataxia and neurodegeneration. There is increasing evidence of a neuronal-specific role for this ubiquitous kinase, and ATM both localises to synapses and is required for long-term potentiation. The mechanisms underlying its role in synaptic development and function are, however, unclear. Using the *Drosophila* third instar larval neuromuscular junction (NMJ), this thesis uncovers the requirement for presynaptic *Drosophila* ATM (dATM) in neurodevelopment, distinct from its function in the DDR. As with mammalian ATM, neuronal GFP-tagged dATM is predominantly cytosolic, forming foci within axons and synapses. Two processes which are held in delicate balance during the fine tuning of synapse development are oxidative stress and autophagy – each can promote synapse expansion, yet in excess are deleterious. Previous work has shown that cytosolic ATM interconnects these processes. Consistent with this, this thesis demonstrates that the function of presynaptic dATM involves its coordination of ROS signalling and autophagy through the conservation of the ATM-AMPK axis. *dATM* knockdown larvae exhibited sensitivity to excitotoxicity, while augmenting autophagy – both pharmacologically and genetically – alleviated the effects of dATM deficiency. Taken together, the evidence suggests a model in which dATM transduces presynaptic ROS levels, responding to increased ROS by activating the autophagic machinery to induce synaptic growth, while protecting the neuron from excitotoxicity.

Acknowledgements

Firstly, I thank my supervisor Dr Richard Tuxworth. I will always be grateful for your mentorship and the many opportunities you have given me. Your enthusiasm and passion for science have spurred me on during the times where I have found it most challenging. Thank you for all your support over the last 7 years!

To the other members of the Tuxworth lab, past and present, especially Kyle, Charlie, Niki, Alamin, Lauren, Laura, Megan, Ellena, Ruby, Alex, Lily, and Seham – plus all of those I have had the joy of sharing a lab with from the Smerdon and Coleman groups. It has been such a pleasure to have worked with you over the years – you all inspired and helped me in so many different ways and I would not have been able to do this PhD without you.

To my MIBTP friends, particularly Liam and Cat, with whom I have shared this journey warts and all! For those lunches where we could just vent and share our experimental woes, and for Liam's incredible life stories that never fail to entertain, I am so grateful.

To my friends and family, whom I love dearly and am so grateful for the many ways you have supported me throughout this whole process. I promise you I will finally stop being a student and get a real job…

And, finally, to my incredible wife, Sophie, who has supported me through the stresses and fears, and celebrated with me during the highs. You have the patience of a saint, and I dedicate this *Thesis* to you.

Contents

Chapter 1 – Introduction ***1***

1.1 - Ataxia-telangiectasia **2**

1.2 - Structure of ATM **6**

1.3 - Localisation of ATM **8**

1.3.1 - ATM in the nucleus – the DNA damage response (DDR) 10

1.3.2 - ATM in the cytosol – Oxidative stress and autophagy 18

1.3.3 - ATM in neurons 23

1.4 - The *Drosophila* Neuromuscular Junction (NMJ) – A model synapse **28**

1.4.1 – Larval NMJ development and structure 28

1.4.2 – Wingless and the anterograde signal 33

1.4.3 – The BMP retrograde signal 34

1.4.4 – The role of neuronal activity in NMJ development and homeostasis 36

1.4.5 – Oxidative stress, autophagy, and crosstalk 38

1.5 - Drosophila ATM - tefu **41**

1.6 - Structural comparison of hATM and dATM **46**

Chapter 2 – Materials and Methods ***55***

2.1 - *Drosophila* husbandry and experimental techniques **55**

2.1.1 - Food and incubation conditions 55

2.1.2 - Crossing schemes and generation of stocks 56

2.1.3 - 3rd instar larval dissections 57

2.1.4 - Electrophysiology 58

2.1.5 - Larval locomotion assay 59

2.1.6 – Induction of NMJ structural plasticity 60

2.1.7 - Immunohistochemistry 60

2.1.8 - Embryo microinjections and progeny screening 61

2.1.9 - Nucleic acid extraction 61

2.1.10 - Protein extraction 62

2.2 – Microscopy **62**

2.2.1 - Confocal imaging 62

2.2.2 - 2-photon microscopy 63

2.3 - Molecular Biology **64**

2.3.1 - Design of homology-directed repair construct for CRISPR knock-in of sfGFP into dATM locus 64

2.3.2 - Design and synthesis of UAS-dATM[msGFP2] construct 65

2.3.3 - Design of guide RNAs (gRNAs) 66

2.3.4 - PCR 66

2.3.5 - Gibson Assembly 67

2.3.6 - Restriction cloning and ligation of human ATM or dATM[msGFP2] cDNA into pUAST-attB 68

2.3.7 - Restriction cloning and ligation of gRNAs into pCFD3 69

2.3.8 - Plasmid DNA preparation and glycerol stock generation 70

2.3.9 - Cloning of blunt-ended PCR fragments into pCR-Blunt II-TOPO vector 70

2.3.10 – Sequencing 70

2.4 - Cell culture **71**

2.4.1 - Culture and maintenance of cell stocks 71

2.4.2 - Transfections 71

2.4.3 - Immunocytochemistry 72

2.5 - Western blotting **72**

2.6 - Analysis **73**

2.6.1 - Analysis of NMJ images in FIJI 73
2.6.2 – Analysis of caspase activation using GC3Ai 74
2.6.3 - Analysis of mitoGFP images 74
2.6.4 - Autophagy quantification 75
2.6.5 - Calculation of HRP-Dlg ratio 75
2.6.6 - Analysis and export of electrophysiology data 75
2.6.7 - Statistical analysis in Rstudio 77

Chapter 3 – Presynaptic ATM is required for neuromuscular junction development in Drosophila melanogaster ***86***

3.1 – Introduction **86**

3.2 – Results **91**

3.2.1 - Heterozygous dATM mutants have deficits in NMJ development 91
3.2.3 - Presynaptic ATM is required for normal NMJ development 93
3.2.4 – Knockdown of dATM with different drivers 99
3.2.5 – The role of presynaptic dATM in neurodevelopment is independent of the DNA damage response 101
3.2.6 – The functional requirement of presynaptic dATM – Electrophysiology 104
3.2.7 – The functional requirement of presynaptic dATM – Larval locomotion 109
3.2.8 – The effect of temperature on locomotion and NMJ structural phenotypes 111
3.2.9 – Neurodegeneration of posterior motor neurons at higher temperatures 113
3.2.10 – Detection of apoptosis using GC3Ai 117
3.2.11 – Exploring the role of dATM in short-term structural plasticity 121

3.3 – Discussion **129**

3.4 – Conclusion **142**

Chapter 4 – Localisation of endogenous and overexpressed GFP-tagged dATM ***144***

4.1 – Introduction **144**

4.2 – Results **149**

4.2.1 - Design and generation of CRISPR-mediated insertion into dATM locus 149
4.2.2 – Validation of initial CRISPR knock-in as a bona-fide dATM mutant 152
4.2.3 - Rescue of dATM function after piggyBac-mediated excision of DsRed and backcrossing 153
4.2.4 - Localization of dATM[sfGFP] 159
4.2.5 – Structural prediction of dATM[sfGFP] 168
4.2.6 – Attempting to rescue dATM with overexpression of hATM 170
4.2.7 – Overexpression of dATM[msGFP2] 173

4.3 – Discussion **180**

Chapter 5 – How does presynaptic dATM regulate neurodevelopment and homeostasis? ***186***

5.1 – Introduction **186**

5.2 – Results **190**

5.2.1 – Presynaptic dATM knockdown sensitises the NMJ to excitotoxicity 190
5.2.2 – Interaction of dATM with OS machinery 193
5.2.3 – Comparing ROS sensitivity at lower and higher rearing temperature 196
5.2.4 – Interaction of dATM and autophagy machinery 202
5.2.5 – Interaction of dATM with AMPK in NMJ development 204

5.2.6 – Quantification of autophagy 208
5.2.7 – Evidence of defective mitophagy 212
5.2.8 – Larval drug rescues 215
5.3 – Discussion 219
5.4 – Conclusion 234
Chapter 6 – Discussion 236
6.1 – Summary of findings 236
6.2 – The presynaptic requirement for dATM in larval NMJ development – undergrowth or degeneration? 237
6.3 – The balancing act of ROS and autophagy – mediated by ATM? 239
6.4 – The conservation of the dATM-AMPK-autophagy signalling axis in *Drosophila* neurodevelopment 241
6.5 – Localisation of dATM[msGFP2] 245
6.6 – Final thoughts on implications for Ataxia-Telangiectasia 247
6.7 – Conclusions 249
Bibliography 251

List of figures

Figure 1.1: A non-exhaustive summary of the main ATM kinase signalling pathways. 9

Figure 1.2: Neuronal ATM and its association with presynaptic vesicles. 23

Figure 1.3: The Drosophila 3rd instar larval neuromuscular junction. 31

Figure 1.4: Factors affecting synapse development and homeostasis, and associated mutations. 32

Figure 1.5: Sequence maps of ATM kinase with domains and regions annotated. 46

Figure 1.6: Using AlphaFold to predict the structure of dATM with reference to published structure of hATM. 51

Figure 1.7: Structural alignments of dATM AlphaFold prediction and hATM to predict homologous residues. 53

Figure 2.1 – Alignment of dATM with hATM focussing on the site of fluorescent protein insertion. 66

Figure 3.1: Overview of Drosophila NMJ imaging protocol and FIJI macro. 90

Figure 3.2: Drosophila larvae which are heterozygous for loss-of-function mutations in tefu (dATM) have smaller neuromuscular junctions (NMJs). 94

Figure 3.3: Pan-neuronal presynaptic knockdown of dATM 96

Figure 3.4: A screen of muscle, glial and neuronal dATM knockdown. 98

Figure 3.5: Overexpression of the 2 different dATM dsRNA constructs with different neuronal drivers at different temperatures. 99

Figure 3.6: Pan-neuronal knockdown of other components of the DNA damage response (DDR). 102

Figure 3.7: Example traces from electrophysiology experiments. 105

Figure 3.8: Quantification of electrophysiological properties of control vs pan-neuronal dATM knockdowns. 108

Figure 3.9: Presynaptic dATM knockdown negatively affects larval locomotor function. 109

Figure 3.10: Quantification of the effect of developmental temperature on the locomotion and structural phenotypes of control vs motor-neuronal dATM knockdown. 114

Figure 3.11: Posterior motor neurons of dATM knockdowns at higher temperature show “thinning out” and reduction of presynaptic structures. 115

Figure 3.12: Using GC3Ai to detect caspase activity. 120

Figure 3.13: Attempting to induce structural plasticity via high K+ pulses. 125

Figure 3.14: Attempting to induce structural plasticity via TrpA1 and temperature cycling. 128

Figure 4.1: Strategy for CRISPR-mediated knock-in of scarless-sfGFP::DsRed into dATM locus. 148

Figure 4.2: PCR screening of successful CRISPR/Cas9-mediated insertions and piggyBac transposase-mediated excision events. 151

Figure 4.3: Characterisation of CRISPR-generated DsRed dATM mutant and sfGFP “rescue”. 153

Figure 4.4: Complementation crosses. 156

Figure 4.5: Localisation of dATM[sfGFP] protein using endogenous fluorescence. 160

Figure 4.6: Attempt to localise dATM[sfGFP] using rabbit-GFP antibody. 162

Figure 4.7: Comparison of rabbit and chicken GFP antibodies. 165

Figure 4.8: Attempt to localise dATM[sfGFP] using alpaca-GFP nanobody. 167

Figure 4.9: Structural prediction of dATM[sfGFP]. 169

Figure 4.10: Expression of FLAG-tagged human ATM in S2 cells. 171

Figure 4.11: Expression of FLAG-tagged hATM in the larval nervous system. 172

Figure 4.12: Overexpression of hATM +/- dATM knockdown. 175

Figure 4.13: Overexpression of dATM[msGFP2] using OK371-GAL4 driver. 177

Figure 4.14: Punctate staining of dATM[msGFP2] in axons and the NMJ. 179

Figure 5.1: dATM knockdown sensitises larvae to excitotoxicity. 192

Figure 5.2: Knockdown of OS scavengers (catalase) at higher rearing temperatures (30°C) phenocopies dATM knockdown. 195

Figure 5.3: Overexpression of OS scavengers (catalase) at higher rearing temperatures (30°C) fails to rescue dATM knockdown. 197

Figure 5.4: Increasing ROS at lower rearing temperatures (19°C) rescues some aspects of NMJ development but is deleterious to others. 200

Figure 5.5: Increasing ROS at higher rearing temperatures (27°C) independently of neuronal activity has no effect on the dATM knockdown phenotype. 201

Figure 5.6: Assessing the interaction of dATM with autophagy regulators in NMJ development. 203

Figure 5.7: Knockdown of AMPK has no effect on NMJ development and qualitatively exacerbates the dATM knockdown phenotype. 206

Figure 5.8: Overexpression of AMPK rescues NMJ surface area and active zone number, but not bouton count. 207

Figure 5.9: Quantification of autophagic flux using mCherry-GFP-atg8a reporter. 209

Figure 5.10: Knockdown of dATM leads to an increased density of smaller mitochondria. 215

Figure 5.11: A screen of autophagy-enhancing drugs for rescue of larval locomotion. 218

Figure 6.1: A model for the function of synaptic ATM 243

List of abbreviations

Abbreviation	*Meaning*
ADP	Adenosine diphosphate
AMP	Adenosine monophosphate
AMPK	AMP-activated protein kinase
A-T	Ataxia-telangiectasia
ATM	Ataxia-telangiectasia mutated
ATP	Adenosine triphosphate
ATR	Ataxia-telangiectasia and Rad3 related
dATM	Drosophila ATM
BLAST	Basic local alignment search tool
BMP	Bone morphogenetic protein
BRP	Bruchpilot
BSA	Bovine serum albumin
Cat	Catalase
cDNA	Complementary DNA
CFP	Cyan fluorescent protein
CHK(1/2)	Checkpoint kinase (1/2)
CNS	Central nervous system
CRISPR	Clustered Regularly Interspaced Short Palindromic Repeats
DDR	DNA damage response
Dlg	Discs large
DNA	Deoxyribonucleic acid
dNTPs	Deoxynucleotide triphosphates
DSB	Double-strand break(s)
dsRNA	Double-stranded RNA
DuOx	Dual oxidase
(m)EJP	(Miniature) Excitatory junction potential
ELAV	Embryonic lethal abnormal vision
EMS	Ethyl methanesulfonate
(m)EPSC	(Miniature) Excitatory postsynaptic current
(m)EPSP	(Miniature) Excitatory postsynaptic potential
ETC	Electron transport chain
EtOH	Ethanol
FAT	FRAP, ATM and TRRAP

FBS	Foetal bovine serum
FIJI	(FIJI) Is Just ImageJ
FRET	Fluorescence resonance energy transfer
GABA	γ-Aminobutyric acid
gDNA	Genomic DNA
GFP	Green fluorescent protein
GOF	Gain-of-function
gRNA	Guide RNA
GTP	Guanosine-5'-triphosphate
hATM	Human ATM
HDR	Homology-directed repair
HR	Homologous recombination
HRP	Horseradish peroxidase
ICC	Immunocytochemistry
IF	Immunofluorescence
IHC	Immunohistochemistry
(m)IPSC	(Miniature) Inhibitory postsynaptic current
iPSC	Induced pluripotent stem cells
JNK	c-Jun N-terminal kinase
LKB1	Liver kinase B1
LOF	Loss-of-function
LTP	Long-term potentiation
LUT	Look-up table
MAPK	Mitogen-activated protein kinases
MEF	Mouse embryonic fibroblast
MN	Motor neuron
MRI	Magnetic resonance imaging
MRN	MRE11-Rad50-NBS1 complex
mRNA	Messenger RNA
msGFP2	Monomeric superfolder GFP 2
NAD(P)	Nicotinamide adenine dinucleotide (phosphate)
NES	Nuclear export sequence
NHEJ	Non-homologous end joining
NLS	Nuclear localisation sequence
NMJ	Neuromuscular junction
NMN	Nicotinamide mononucleotide
OS	Oxidative stress

PC	Purkinje cell
PCR	Polymerase chain reaction
PI3K	Phosphoinositide-3-kinases
pLDDT	Predicted local distance difference test
PPP	Pentose phosphate pathway
PPR	Paired-pulse ratio
Repo	Reversed polarity
RIPA	Radioimmunoprecipitation assay
RISC	RNA-induced silencing complex
RMSD	Root mean square deviation
RNA	Ribonucleic acid
RNAi	RNA interference
ROS	Reactive oxygen species
RRP	Readily-releasable pool
sfGFP	Superfolder GFP
SOD	Superoxide dismutase
SSB	Single-strand break(s)
tefu	Telomere fusion
TGFβ	Transforming growth factor beta
(m)TOR(C)	(mechanistic) Target of rapamycin (complex)
TRiP	Transgenic RNAi project
TrpA1	Transient receptor potential cation channel, subfamily A, member 1
TSC2	Tuberous sclerosis complex 2
UAS	Upstream activating sequence
ULK1	Unc-51-like autophagy-activating kinase 1
VAMP2	Vesicle-associated membrane protein 2
VGAT	Vesicular GABA transporter
VGLUT1	Vesicular glutamate transporter 1
VNC	Ventral nerve cord
WB	Western blot(ting)
Wnt/Wg	Wingless
YFP	Yellow fluorescent protein

Chapter 1 – Introduction

Although it has long been known that *Ataxia-telangiectasia mutated* (ATM) kinase deficiency leads to cerebellar ataxia and neurodegeneration, it is still not clear why cerebellar neurons are particularly vulnerable to the loss of this ubiquitous master regulator of the DNA damage response (DDR). In addition, it remains to be elucidated how ATM is involved in the normal development and maturation of synapses, and the development of the cerebellum. It is known that both oxidative stress and autophagy regulate synapse size in *Drosophila*, and ATM is both a ROS sensor and can upregulate autophagy through suppression of mTOR signalling. Yet the question of whether ATM links these two processes in the developing synapse has not been answered. Further, ATM has been shown to localise to synaptic vesicles and its deficiency leads to a reduction in synaptic plasticity. The purpose for the localisation of this DDR protein so far from home in synapses and the mechanism underlying its role in synaptic function is, however, unclear.

In this Introduction, I will review our current understanding of ATM kinase and its associated disease, Ataxia-Telangiectasia. I will highlight some of the controversy around ATM's subcellular localisation, present how the function of ATM depends on its mode of activation and discuss the increasing evidence for a neuronal-specific role. I will then introduce how the model organism Drosophila melanogaster *can be utilised as a model both for synapse biology and ATM function. The Introduction concludes with a comparison of the published crystal structure of human ATM with an AlphaFold-generated structure of* Drosophila *ATM and an evaluation of the utility of this process in predicting conserved functional residues. This paves*

the way for further **investigating the role of presynaptic ATM in synapse development and homeostasis.**

1.1 - Ataxia-telangiectasia

The disease Ataxia-Telangiectasia (A-T) is a complex, multi-system disorder which has been described as an early-onset neurodegenerative disease (Boder and Sedgwick, 1970; McKinnon, 2004), a neurodevelopmental disorder (Nissenkorn *et al.*, 2011; Nissenkorn and Ben-Zeev, 2015), and as a primary immunodeficiency disease (Amirifar *et al.*, 2019). The first clinical description of the disease and its naming came in 1957, with patients displaying progressive cerebellar ataxia, telangiectasia (dilated blood vessels appearing near the surface of mucus membranes), immunodeficiencies resulting in frequent sino-pulmonary infections, and erratic eye movements (Boder and Sedgwick, 1958). The estimated frequency of A-T heterozygotes is 2.8% (Swift *et al.*, 1986) and the median survival of A-T patients is 25 years (Crawford, 2005).

Evidence of progressive cerebellar neurodegeneration comes from MRI scans of A-T patients at different ages (Sahama *et al.*, 2014). In most patients, the first symptom is cerebellar ataxia, and young patients (~2 years) have no evidence of cerebellar atrophy (Tavani *et al.*, 2003). From roughly 3-7 years of age, evidence of atrophy of the lateral cerebellum and superior vermis begins to emerge; this then becomes more widespread across the cerebellum by the teenage years (Tavani *et al.*, 2003). In this regard, A-T is similar to other cerebellar ataxias, including ataxia with oculomotor apraxia type 1/2 (AOA1/2) and infantile-onset spinocerebellar ataxia (Al-Maawali, Blaser and Yoon, 2012).

In addition to progressive cerebellar neurodegeneration, there is some evidence of defective neurological development in A-T (Vinters, Gatti and Rakic, 1985). Post-mortem samples from A-T patients displayed abnormal dendritic arborisation in the Purkinje cell layer of the cerebellum, and displacement of the Purkinje cells. Because of how the cerebellum develops *in utero*, the authors argue that these phenomena must have occurred prior to the formation of the macrostructure of the parallel fibres and before the Purkinje cells have formed their dendritic tree. This means that A-T disease must affect Purkinje cell differentiation or the interaction of their dendritic tree with parallel fibres during development, which identifies A-T as a neurodevelopmental disorder (Vinters, Gatti and Rakic, 1985). However, the study also reports that the position of the Purkinje cells has no impact on their rate of degeneration, when compared to normally positioned cells in the same samples (Vinters, Gatti and Rakic, 1985), which begs the question of what the actual consequence of Purkinje cell displacement is.

The neurological deficiencies in A-T patients are profound, present from childhood and non-progressive (Shaikh *et al.*, 2013). Postural and kinetic tremors are common, while resting tremor is less intense. Non-rhythmic movements are also present including athetosis (writhing fingers), and myoclonus and dystonic jerks (Shaikh *et al.*, 2013). Further to these peripheral symptoms, there is also evidence of disrupted cerebellar control of vestibular reflexes, with an increase in the gain of the vestibulo-ocular reflex and abnormal eye movements orthogonal to the axis of head rotation (Shaikh *et al.*, 2011).

Because of the diversity of symptoms in A-T, it was initially suspected the disease was polygenic – an early genetic linkage study mapped localised the defect to the human chromosomal region 11q22-23 (Gatti, Berke and Boder, 1988). In this paper, it was speculated

that THY1/CD90 may be involved in the disease, since it localises to this region and was the first discovered marker of T-cells (Reif and Allen, 1964), which would potentially explain the immunological phenotype of A-T. In addition, other genes in this region include those encoding apolipoproteins, N-CAM and CD3-T-cell receptor molecules. CD3 antibodies, despite being generated to identify T-cells, exclusively label Purkinje cells in the human cerebellum (Garson *et al.*, 1982). It seemed that this locus identified genes whose loss-of-function could explain both the neurological and immunological aspects of A-T.

However, it was later discovered that the disease is monogenic, resulting from mutations in a single gene at that locus which was given the name Ataxia-Telangiectasia Mutated (ATM) (Savitsky *et al.*, 1995). ATM shares homology with phosphoinositide-3-kinases (PI3K) (see *structure of ATM*) , a number of which are involved in the DNA damage response (DDR) (Lovejoy and Cortez, 2009) (see *ATM in the nucleus*). This involvement explains the sensitivity to ionising radiation and radiomimetic agents in A-T patients, patient-derived cell lines and mammalian models of the disease (Barlow *et al.*, 1996; Toyoshima *et al.*, 1998). Further, ATM is essential to the process of V(D)J recombination within lymphocytes (Ito *et al.*, 2007) which may be the reason for immunodeficiency in A-T patients (Boder and Sedgwick, 1970; Savitsky *et al.*, 1995; Bott *et al.*, 2007).

Commonly, A-T arises from complete ATM loss-of-function, with diagnosis occurring early in childhood. However, a substantial number of patients present with a milder phenotype. These “A-T variants” may have a subset of symptoms of “classical A-T" and diagnosis may occur later in adolescence or into adulthood (Taylor *et al.*, 2015). This can be the result of mutations which reduce the expression level of ATM, or where the kinase retains a low level of activity

(Verhagen *et al.*, 2012). Various clinically relevant mutations in the *ATM* locus have been reported, and intriguingly some of these dissociate the different aspects of classical A-T disease, and the different cellular functions of ATM. These will be the focus here as they give some insight into the mechanism of ATM function, rather than mutations which affect overall expression levels or result in a severely truncated protein product.

Missense mutations of 1514T>C and 1547T>C cause a disease that reduces ATM levels without abolishing them (unlike classical A-T), produces a mild neurological phenotype and cerebellar degeneration without telangiectasia, but still causes T-cell acute lymphoblastic leukaemia (Bielorai *et al.*, 2013). 1514T>C is predicted to lead to a protein change of F505S while 1547T>C is predicted to result in L516S. Lymphoblastoid cell lines derived from these patients show slowed kinetics of KRAB-associated protein 1 (KAP1) phosphorylation in response to ionising radiation (Bielorai *et al.*, 2013).

Other variants of the ATM gene include a truncating mutation 9139C>T (R3047X) which shortens the protein by 10 amino acids but does not affect overall levels of ATM detectable by western blotting (Gilad *et al.*, 1998; Toyoshima *et al.*, 1998). On its own, this mutation does not cause significant radiosensitivity (Gilad *et al.*, 1998), likely because the R3047X mutant is still responsive to DNA damage (Guo *et al.*, 2010). However, when combined with a L2656P substitution, the R3047X truncation results in classical A-T but without immunodeficiency (Toyoshima *et al.*, 1998). These early studies also suggested that in-frame deletions within the N-terminal portion of the protein resulted in a milder disease, with reduced immunodeficiency, varying levels of protein, but all exhibiting chromosomal instability (Gilad *et al.*, 1998). By contrast, truncations within the C-terminus produced the classical A-T phenotype, which gave a hint as to the location of the functional domains in ATM.

Some of these mutations target the regions and residues responsible for different aspects of ATM signalling in the DNA damage response (DDR, see *ATM in the nucleus – the DNA damage response*). With classical A-T, western blotting reveals severely reduced ATM levels and failure to phosphorylate downstream DDR effectors after irradiation, such as SMC1, KAP1 and NBN (Taylor *et al.*, 2015). The V2424G mutation does not significantly reduce ATM protein levels and leads to reduced (but not abolished) DDR kinase activity and both a later disease onset with slower progression (Stewart *et al.*, 2001). Intriguingly, there are other mutations such as F2827C and W412R which lead to reduced ATM levels but with some residual DDR kinase activity, and yet an absence of the standard ATM activation marker - autophosphorylation on S1981 (Taylor *et al.*, 2015). This suggests flexibility in the requirement for S1981 phosphorylation in ATM activation. In general, these patients expressing ATM variants that retain some level of kinase activity do not present with cerebellar ataxia (Taylor *et al.*, 2015).

These disease-causing mutations and the differentiation of resultant A-T symptoms indicated that ATM has a diverse range of functions which are affected independently by mutations in the different domains of the protein.

1.2 - Structure of ATM

The human *ATM* gene codes for a protein of 3056 amino acids, belonging to the phosphatidylinositol-3-kinase-like kinase (PI3K) family (Savitsky *et al.*, 1995). This family also contains other DNA repair coordinators ATR and DNA-PKcs, in addition to mTOR, SMG-1 and TRAAP (Lovejoy and Cortez, 2009). Although ATM is a key component of the DDR across the majority cell types, there is still a lack of mechanistic and structural understanding of this

kinase, likely due to its large size (Williams, Yates and Zhang, 2020). However, a number of groups have recently independently published crystal structures of both monomeric (Xiao *et al.*, 2019) and dimeric human ATM (Lau *et al.*, 2016; Baretić *et al.*, 2017), in addition to individual domains (Abd Rahim *et al.*, 2019).

Like other PIKKs, ATM contains a C-terminal kinase domain (251 residues) with a FAT (*FRAPP, ATM, TRAPP*) domain preceding it. ATM also contains an FATC (*FAT-C-terminus*) domain of around 33 residues. The FAT domain contains HEAT-repeats (Xiao *et al.*, 2019) which have been shown to be required for binding to the C-terminus of NBS1 (You *et al.*, 2005). This binding is then proposed to lead to conformational change within the distal kinase domain resulting in activation, in a similar way to how the binding of RHEB to the FAT domain of another PIKK family member, mTORC1, leads to conformational changes of its kinase domain (Yang *et al.*, 2017; Williams, Yates and Zhang, 2020). In addition, the N-terminal portion of the protein consists of multiple HEAT repeats forming an α-solenoid, a common feature of cytoplasmic proteins such as PP2A and mTOR (Yoshimura and Hirano, 2016).

Under physiological conditions, ATM is held inactive in cells as a dimer (Bakkenist and Kastan, 2003). Intermolecular autophosphorylation of S1981 within the FAT domain (Bakkenist and Kastan, 2003) and acetylation of K3016 (Sun *et al.*, 2007) leads to dissociation of dimeric ATM into active, monomeric ATM. Comparison of the cryo-EM structures of dimeric and monomeric ATM reveals the monomeric form has a more open conformation of its catalytic pocket, allowing for substrate entry – this requires a conformational change in its PIKK regulatory domain, which is normally prevented by the autoinhibitory structure of the dimer (Xiao *et al.*, 2019).

However, the dimeric form of ATM can also be active upon direct oxidation by reactive oxygen species (ROS), which is mediated by intermolecular disulphide bond formation at C2991 (Guo *et al.*, 2010). This activation was shown to be independent of the DNA damage response since the C2991L mutant form of ATM could be activated by MRN+DNA but not by H_2O_2. Replacing endogenous ATM with the R3047X variant discussed earlier displayed similar behaviour to the C2991L mutant (Guo *et al.*, 2010). More recently, it has been reported that dimeric ATM exists in a dynamic equilibrium between closed and open conformations (Baretić *et al.*, 2017). In the closed form, the PIKK regulatory domain acts as a pseudo-substrate and blocks the active site, whereas this is accessible in the open form (Baretić *et al.*, 2017). The authors do stress however that because C2991 lies within the disordered centre of the PIKK regulatory domain, how intermolecular disulphide bonds dependent on this residue link to activation of the dimer is not completely clear.

Thus, ATM can function in different ways depending on its conformation and its mode of activation.

1.3 - Localisation of ATM

There seems to be controversy in the literature surrounding the localisation of ATM kinase, particularly in neurons. Conclusions seem to depend on the methodology used and the cell type studied and, potentially, the developmental stage of the cell type under study. Early work using immunohistochemistry to localise ATM protein in human cerebellar neurons at different developmental stages demonstrated that Purkinje cells express ATM from late prenatal stages, and that the protein is distributed within the cytoplasm but not the nuclei (Oka and Takashima, 1998). Around the same time, work in lymphoblastoid cell lines showed that ATM

is both nuclear and cytoplasmic and this distribution is not affected by irradiation (Watters *et al.*, 1997). More recent studies have suggested that neurons are unique in having a cytoplasmic pool of ATM in addition to nuclear ATM (Li *et al.*, 2009) which is involved in synaptic function and long-term potentiation (Vail *et al.*, 2016). One study attempted to

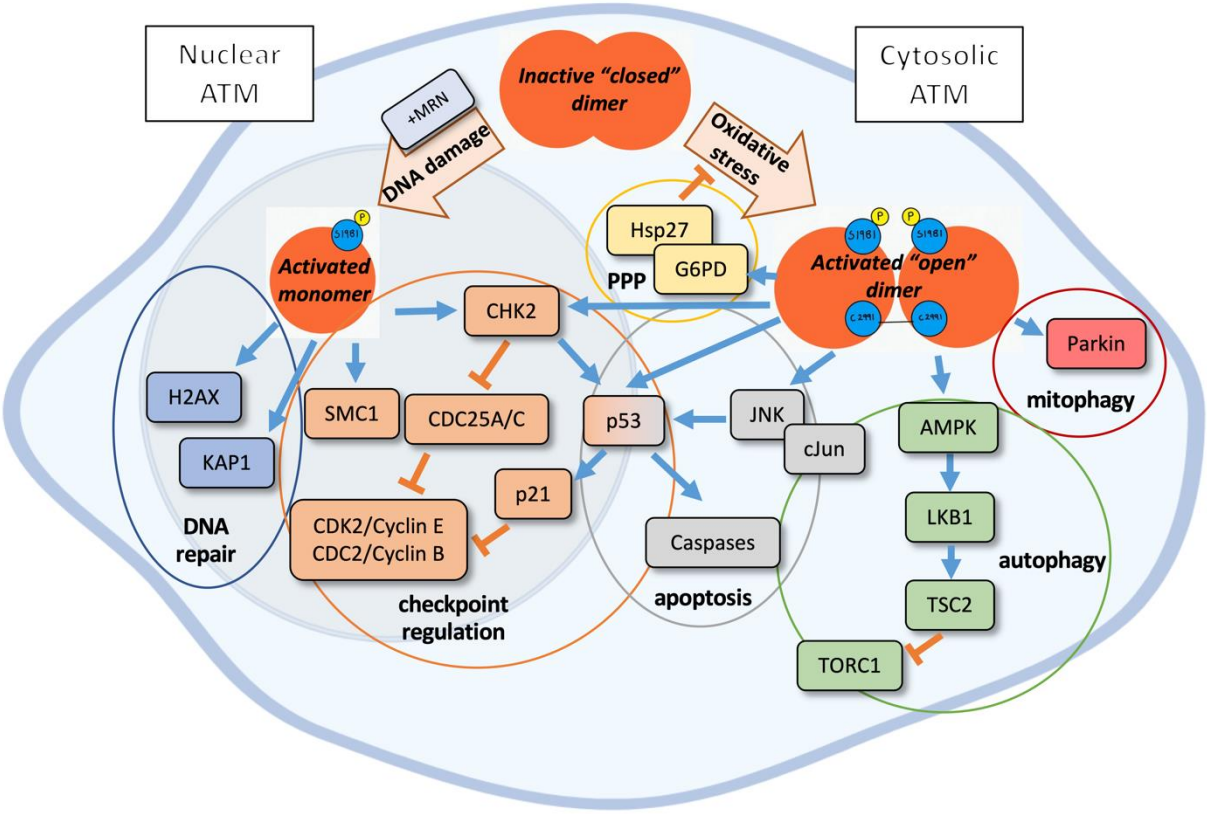

Figure 1.1: A non-exhaustive summary of the main ATM kinase signalling pathways. Under normal conditions, ATM is held as an inactive dimer. DNA damage can induce its autophosphorylation on S1981, leading to monomerization and formation of nuclear foci on double-strand breaks, characterised by phosphorylation of H2AX. In response to DNA damage, ATM coordinates DNA repair, checkpoint regulation, and if DNA damage is excessive, apoptosis. Dimeric ATM can also be directly oxidised in the cytosol by ROS, leading to distinct downstream targets, such as the autophagy and mitophagy machinery and the pentose phosphate pathway, which in turn regulates redox homeostasis. Significant crosstalk exists between the modalities of activation.

generate a mathematical model of ATM nucleo-cytoplasmic shuttling in which the major form of ATM is cytosolic dimers that monomerise upon radiation-induced DNA damage and enter the nucleus (Bodgi and Foray, 2016). In support of this model, the authors provide

immunofluorescence imaging purporting to demonstrate relocalisation of cytoplasmic ATM to the nucleus upon IR, but these could alternatively be interpreted as nuclear ATM forming foci and the overall independent pools of ATM staying unchanged (Watters *et al.*, 1997).

Taking the data as a whole, it appears that the function of ATM differs depending on its mode of activation and cellular compartmentalisation. The following section will focus on the different roles of ATM in each compartment, the conditions in which its activation occurs, and downstream phosphorylation events that result from its activation.

1.3.1 - ATM in the nucleus – the DNA damage response (DDR)

When a cell suffers DNA damage in the form of double strand breaks (DSBs), there are two major repair mechanisms at its disposal: non homologous end joining (NHEJ) or homologous recombination (HR). In the former, the broken DNA ends are recognised by the Ku70-Ku80 heterodimer which assembles around the lesion and acts as a scaffold for other repair components, including XRCC4 and the DNA-dependent protein kinase catalytic subunit (DNA-PKcs) (Mari *et al.*, 2006; Chang *et al.*, 2017). The process proceeds through stabilisation and bridging of the broken ends, before the lesion is ligated and the complex dissembles (Davis and Chen, 2013). NHEJ can occur throughout the cell cycle since it does not require a homologous template. By contrast, HR is restricted to S-phase or G2-phase when a sister chromatid will be present (Zhao *et al.*, 2017). NHEJ is also the pathway that predominates, with one estimate being that cells show a ratio of NHEJ to HR of 9:1 (Mao *et al.*, 2008). The same authors estimate that NHEJ is around 14X faster than HR. Because of this speed, in order for HR to predominate during S and G2, it was determined that NHEJ must be negatively

regulated during these phases: this occurs via the cell-cycle dependent NHEJ inhibitor CYREN, which binds to and inhibits the Ku heterodimer (Arnoult *et al.*, 2017).

ATM kinase is regarded as a master regulator of the DNA damage response (Paull, 2015), and has a role in regulating both HR and NHEJ, but specifically responds to DSBs (Lee and Paull, 2005, 2007). ATM can negatively regulate NHEJ and promote HR: ATM phosphorylates DNA-PKcs accumulated on DNA ends which is required for its removal (Britton *et al.*, 2020), and indirectly mediates the detachment of the Ku complex by phosphorylating CtIP (Chanut *et al.*, 2016); Deletion of ATM in a mouse model of Aicardi-Goutières Syndrome results in aberrant activation of toxic NHEJ, which can be rescued by inhibition of Lig4 (Aditi *et al.*, 2021). But ATM is also able to promote NHEJ through recruitment of SHIELDIN to DSBs (Gupta *et al.*, 2018) and phosphorylation of 53BP1, which protects DNA ends from resection favouring NHEJ and inhibiting HR (Bothmer *et al.*, 2011). DNA-PKcs has a reciprocal role in the regulation of ATM activity. If the catalytic subunit of DNA-PK is chemically inhibited, ATM becomes hyperactive, and it was discovered this is due to loss of an inhibitory phosphorylation of ATM by DNA-PKcs at a number of target sites (Zhou *et al.*, 2017).

However, despite its clear role in the regulation of the DDR, other groups have found that ATM is dispensable for the repair of at least 75% of DSBs (Goodarzi *et al.*, 2008). Inhibition of ATM (unlike that of DNA-PKcs) does not seem to affect the repair kinetics of DSBs within euchromatin, but does reduce its accuracy (Caron *et al.*, 2015). ATM seems to be specifically responsible for the repair of DSBs that are associated with heterochromatin, where it phosphorylates KAP1, which causes dispersal of the chromatin re-modeller CHD3 from breaks and enables repair (Ziv *et al.*, 2006; Goodarzi *et al.*, 2008; Goodarzi, Kurka and Jeggo, 2011). Further, ATM-deficient mouse embryonic fibroblasts (MEFs) that are confluence-arrested in

G0/G1 show an accumulation of DSBs specifically in heterochromatin regions, where the protein Artemis also functions downstream of ATM in their repair (Woodbine *et al.*, 2011).

Mechanistically, monomeric ATM is recruited to sites of DNA DSBs (Bakkenist and Kastan, 2003; Berkovich, Monnat and Kastan, 2007; You *et al.*, 2007). This interaction is dependent upon the DSB-sensing MRN complex, which consists of MRE11, NBS1 and Rad50, and the addition of MRN plus purified fragmented DNA is sufficient to activate ATM (Lee and Paull, 2005). Cells that are deficient in the MRN complex consequently show defective ATM activation (Uziel *et al.*, 2003). The interaction between MRN and ATM is mediated by a 20 residue C-terminus motif in NBS1, conserved between NBS1, ATRIP and Ku80 and responsible for their interaction with ATM, ATR and DNA-PKcs respectively (Falck, Coates and Jackson, 2005). In addition, the 2RA allele of ATM which has the mutations R2579A-R2580A has reduced MRN affinity and defective DDR activation (J.-H. Lee *et al.*, 2018), suggesting that this is a key motif for MRN recognition. The MRN complex binds to exposed DNA ends, unwinds 15-20bp and holds open the structure in an ATP-dependent manner (Cannon *et al.*, 2013). ATP binding by the Rad50 component of the complex is essential for subsequent stimulation of ATM (Lee *et al.*, 2013). Activation of ATM in response to DNA damage involves autophosphorylation on S1981 which leads to dissociation of the inactive dimeric form of the protein (Bakkenist and Kastan, 2003), although the presence of residual kinase activity in A-T cell lines in which S1981 phosphorylation is absent challenges the notion of its requirement (Taylor *et al.*, 2015). In addition to this phosphorylation, other phosphorylation and autophosphorylation sites that correlate with ATM activation such as S367, S1893, T1885 and S2996 have been found (Kozlov *et al.*, 2006, 2011). Further, acetylation mutants of ATM at K3016 or knockdown of the acetyltransferase Tip60 prevents upregulation of ATM in response

to DNA damage (Sun *et al.*, 2007), suggesting that this is another site crucial for ATM DDR activity.

Many other proteins interact with MRN and ATM on the broken DNA strand to coordinate and modulate the activity of ATM. The BRCT domains of 53BP1 interact with the MRN complex through Rad50, which leads to phosphorylation of NBS1 and promotion of ATM activity (Lee *et al.*, 2010). There is evidence of crosstalk between the transforming growth factor-β (TGFβ) and ATM pathways, since Smad7 interacts with NBS1, forms nuclear foci after ionising radiation and enhances interaction between NBS1 and ATM (M. Wang *et al.*, 2013); overexpression of Smad7 enhances the ATM-mediated DDR while knockdown reduces ATM phosphorylation on S1981 (Park *et al.*, 2015). Amplification of DNA damage signals occurs through a positive feedback loop between MDC1, H2AX and ATM; MDC1 binds to γH2AX in an ATM-dependent fashion (absence of MDC1 does not affect ATM phosphorylation but prevents its recruitment into γH2AX-associated foci), which promotes accumulation and retention of DNA repair factors (Stucki *et al.*, 2005; Lou *et al.*, 2006). More recently, evidence has accumulated of the role of ubiquitylation and UFMylation in the activation of ATM and upregulation of the DDR: Pellino1, a ubiquitin ligase, is activated by ATM-mediated phosphorylation and recruited into γH2AX foci, where it ubiquitylates NBS1, stabilises the MRN complex and results in positive feedback activation of ATM (Ha *et al.*, 2019); Ubiquitin-fold modifier 1 (UFM1) UFMylates MRE11 on K282, which is required for MRN complex formation and optimal ATM activation (Wang *et al.*, 2019).

Negative feedback of this pathway occurs both directly through interaction with ATM and its subsequent deacetylation/dephosphorylation, and indirectly through returning open chromatin to a more repressive state. The former involves the activity of SIRT7 deacetylase,

which interacts with the FATC domain of ATM to deacetylate ATM on K3016 (Tang *et al.*, 2019). This is a prerequisite to the dephosphorylation of ATM on S1981 by Wip1 phosphatase, which downregulates ATM activity (Fiscella *et al.*, 1997; Shreeram *et al.*, 2006; Jaiswal *et al.*, 2017). In addition, NOTCH1 interacts with the FATC domain of ATM, and constitutively-active forms of NOTCH1 lead to a reduction of DDR foci containing pATM, 53BP1 and γH2AX (Vermezovic *et al.*, 2015). ATM is also essential for the early phase of BLM helicase recruitment (Tripathi *et al.*, 2018). While the helicase activity of BLM is required for assembly of both HR and NHEJ complexes onto chromatin initially, its activity is repressive during repair, where it inhibits HR in S-phase and NHEJ in G1 (Tripathi *et al.*, 2018). At the level of the chromatin structure, there is a negative feedback loop involving histone methylase Suv39H1 at DSBs: H3K9 methylation increases Tip60 activation; this leads to increased activity of ATM, which phosphorylates KAP1; subsequently, KAP1 acts to release Suv39H1 from DSBs, reducing methylation, returning chromatin to a more repressive state and dampening down ATM activity (Ayrapetov *et al.*, 2014). These direct and indirect feedback processes likely explain the oscillatory behaviour of ATM and its downstream targets that have been reported following DNA damage (Batchelor *et al.*, 2008).

While DSBs are the principal source of ATM activation, there is recent evidence for other forms of DNA damage as potential ATM activators. Single-stranded breaks (SSBs) can be converted into DSBs at S-phase in a replication-dependent fashion – despite this, there is evidence that ATM can be activated by excessive SSB formation independently of DSBs, where it promotes a delay in S-phase and prevention of these SSBs from converting into DSBs (Khoronenkova and Dianov, 2015). It should be noted that authors of that study do not seem to account for potential cross-talk of ATM and ATR signalling pathways which could be

confounding (Fedak *et al.*, 2021). Other DNA lesions which are known to activate ATM and result in the formation of DSBs include topoisomerase cleavage complexes (TOPcc) and R-loops (Lin *et al.*, 2009; Sordet *et al.*, 2009).

Multiple key pathways are downstream of ATM in the context of DNA damage signalling (fig 1.1), and the pathway favoured is dependent on factors ranging from the level and type of damage, the cell cycle phase, and the mechanism of ATM activation. In addition to the feedback targets described above, all three members of the MRN complex are phosphorylated by ATM in response to DNA damage: MRE11 is phosphorylated by ATM which reduces both its affinity for DNA in addition to ATM loading onto chromatin, demonstrating negative feedback of DNA repair (Di Virgilio, Ying and Gautier, 2009); ATM-dependent Rad50 phosphorylation on S635 is required for downstream phosphorylation of SMC1, and subsequent DNA repair and cell-cycle arrest (Gatei *et al.*, 2011); NBS1 is phosphorylated by ATM on S278 and S343, and this is thought to control the gain of DNA repair, with mutants at these sites only showing significant deficit of phosphorylation of downstream ATM targets at higher levels of irradiation (Li and Wang, 2011).

The HR repair process requires short- and long-range DNA end resection to enable RAD51-mediated strand invasion (Krejci *et al.*, 2012), and ATM coordinates this process. The resection is promoted by CtIP; ATM both aids in the recruitment of CtIP to DSBs and phosphorylates it on Thr589 to facilitate resection (You *et al.*, 2009; H. Wang *et al.*, 2013). Additionally, BLM helicase accumulation and activity is dependent on ATM phosphorylation which is necessary for long-range resection during HR (Ababou *et al.*, 2000). Likewise, BRCA1, which forms a complex with RAD51, is another phosphorylation target of ATM. While

phospho-mutant BRCA1 constructs displayed normal subnuclear localisation upon DNA damage, S-phase arrest was significantly abrogated, suggesting that this is the key downstream pathway for the ATM-mediated S-phase checkpoint in DSB repair (Cortez *et al.*, 1999; Xu *et al.*, 2002)

Another key downstream target of ATM is checkpoint kinase 2 (CHK2), which is phosphorylated by ATM on Thr-68 following double-strand breaks and negatively regulates Cdc25C in order to block mitotic entry (Matsuoka, Huang and Elledge, 1998; Lee and Paull, 2005). This is dependent on recruitment to DSBs by the MRN complex (Uziel *et al.*, 2003) and interaction with NBS1 in particular, which appears to be dependent on phosphorylation of its S343 by ATM (Buscemi *et al.*, 2001); however, this does not appear to be the case in mouse developing cortical neurons, in which NBS1-deficiency impairs the ATR-CHK1 pathway, while the ATM-CHK2 pathway is still active (although the subsequent activation of p53 in this case leads to non-canonical defective neuro-proliferation rather than apoptosis) (Li *et al.*, 2012). The requirement of NBS1 on CHK2 phosphorylation may only become explicit at higher levels of DNA damage (Li and Wang, 2011). In addition, there is evidence to suggest that NBS1 is tightly located to DNA lesions while pCHK2 is pan-nuclear, so may coordinate a more global response (Lukas *et al.*, 2003). Acetylation mutants of ATM, e.g., K3016R, result in abolished ATM-dependent phosphorylation of CHK2 (Sun *et al.*, 2007), suggesting that this is a key motif in the regulation of downstream ATM signalling in addition to its role in ATM DSB recruitment.

The tumour-suppressor protein, p53, is a downstream target of pCHK2 (Hirao *et al.*, 2000) where it is phosphorylated on serine-20 (Shieh *et al.*, 2000). p53 can also be phosphorylated on serine-15 by ATM directly (Banin *et al.*, 1998; Canman *et al.*, 1998). Activation of p53 seems to be dependent, however, on interactions between ATM and the

p53 regulators MDM2 and MDMX, both of which are also downstream targets of ATM (Cheng and Chen, 2010). Unlike phosphorylation of CHK2 which occurs at DSBs, p53 phosphorylation occurs throughout the nucleus (Falck, Coates and Jackson, 2005). At p53, the already expansive signalling pathway further diverges since p53 coordinates the decision between repair or apoptosis of DNA damaged cells (Williams and Schumacher, 2016; Kastenhuber and Lowe, 2017). Phosphorylated p53 upregulates $p21^{Cip1}$, which negatively regulates the cell-cycle by inhibiting cyclin-dependent kinases (Morgan and Kastan, 1997). This inhibition of the cell-cycle is strengthened by another ATM target, $p27^{Kip1}$, which is phosphorylated on serine-140 and leads to G1 arrest (Cassimere, Mauvais and Denicourt, 2016). Finally, feedback of this axis is achieved through WIP1, a phosphatase that can dephosphorylate ATM-activated p53 and $p27^{Kip1}$ and allow cell-cycle re-progression following DNA repair (Choi *et al.*, 2020).

This homeostatic feedback also likely contributes to the oscillatory nature of the p53 response to DNA damage highlighted earlier (Batchelor *et al.*, 2008), where troughs in the activity give time for the cell to assess the extent of the damage and progress of DNA repair. Persistent DNA damage then causes reactivation of ATM kinase, until a threshold is reached and the cell enters apoptosis (Batchelor *et al.*, 2008; Kracikova *et al.*, 2013). A 'threshold' response such as this opens the door to the possibility of ATM in regulating distinct cellular processes depending upon its mode of activation, the amount of ATM activation, and the wider cellular context in which it is active – a theme which will be returned to throughout this thesis.

An additional role of nuclear ATM is in the response to hypoxia. ATM is autophosphorylated under hypoxic conditions independent of DNA damage, HIF1α activity and MRN recruitment. This occurs in the nucleus, and although foci formation is not observed,

a number of DDR proteins are phosphorylated by ATM in these conditions including 53BP1 and KAP1 (Bencokova *et al.*, 2009). Others have found that HIF1α can be activated by DNA-damage independent phosphorylation of γH2AX by ATM; in this context, ATM is recruited to mUb-γH2AX after mono-ubiqutination of γH2AX by TRAF6 (Rezaeian *et al.*, 2017). This indicates that ATM and γH2AX have DDR-independent roles in hypoxia signalling. Heat shock causes similar behaviour, since it is sufficient to induce S1981 phosphorylation on ATM, which leads to phosphorylation of H2AX in the absence of DNA damage (Hunt *et al.*, 2007).

1.3.2 - ATM in the cytosol – Oxidative stress and autophagy

There have been various lines of evidence to suggest that ATM is involved in extra-nuclear redox signalling (fig 1.1). In the earliest studies of ATM kinase, it was argued that ATM is primarily a sensor of oxidative stress and that loss of neurons in A-T is a result from being in a continuous state of oxidative stress, leading to progressive unresolved oxidative damage to organelles and DNA (Rotman and Shiloh, 1997). The $ATM^{-/-}$ mouse cerebellum, but not cortex, shows increased reactive oxygen species (ROS) levels and mitochondrial superoxide dismutase 2 (SOD2) activity (Kamsler *et al.*, 2001; Quick and Dugan, 2001), which indicates the vulnerability of cerebellar neurons specifically to ATM loss. SOD2 catalyses the breakdown of superoxide radicals into hydrogen peroxide (Sheng *et al.*, 2014), itself an oxidative agent – albeit less potent – so its upregulation indicates an increase in mitochondrial ROS production. N-acetyl cysteine (NAC), a ROS scavenger, reduces levels of H_2O_2 in $ATM^{-/-}$ MEFs and improves survival of $ATM^{-/-}$ mice (Ito *et al.*, 2007). ATM-deficient cells show increased sensitivity to oxidative stress induced by *tert*-butyl-hydroperoxide (TBH) and fail to induce p53 (Shackelford

et al., 2001). Taken together, the evidence suggests a clear role for ATM kinase in ROS-sensing and coordinating the response to oxidative stress.

This begs the question of how ATM can act as a sensor of ROS, and whether it is a direct interaction or mediated through other ROS sensors, or downstream of the response to oxidative damage. Pertaining to the former, cytosolic, dimeric ATM can be activated directly by oxidative stress in the absence of DNA damage (Guo *et al.*, 2010). Application of H_2O_2 to primary human fibroblasts induces phosphorylation of the downstream targets of ATM, p53 and CHK2, in addition to ATM on S1981, but not DNA repair components H2AX or KAP1; this activity is independent of MRN and does not depend on monomerization (Guo *et al.*, 2010). Activation of ATM in this manner requires intermolecular disulphide bond formation at C2991 and the disease-associated mutation R3047X (*see above*) has similar behaviour to the C2991L mutant which is defective in disulphide bond formation (Guo *et al.*, 2010). Further, when testing to determine which residues are required for the inhibitory phosphorylation of ATM by DNA-PKcs, it was found mutants unresponsive to DNA-PKcs phosphorylation (e.g., S85D/T86E) were still normally-responsive to H_2O_2 treatment (Zhou *et al.*, 2017), which suggests differences in the regulatory mechanisms of the different forms of activation.

There is, therefore, a dissociation between the role of monomeric ATM in the nucleus and dimeric ATM in the cytosol and in the downstream pathways upregulated following the different types of ATM activation. However, despite this dissociation, it is clear that there is scope for cross-talk between these different pathways, especially given that oxidative stress can induce DNA damage (Cooke *et al.*, 2003; Cadet and Wagner, 2013) and *vice versa* (Rowe, Degtyareva and Doetsch, 2008).

If ATM can be activated independently of DNA damage signalling, the next question is whether it subsequently has different downstream targets. Under conditions of oxidative stress, cytosolic ATM is a regulator of autophagy. Extranuclear ATM has been localised to peroxisomes, small organelles which contain catalase, the enzyme responsible for reducing H_2O_2 into its constituent H_2O and O_2 (Watters *et al.*, 1999; Zhang *et al.*, 2015). This localisation is dependent on PEX5, and addition of H_2O_2 to peroxisome fractions induces phosphorylation of S1981 on ATM (Zhang *et al.*, 2015). The result of this activation is repression of mTORC1, as indicated by reduction in pS6K, p4EBP1 and pULK1 S757 (the mTORC1 phospho-site). This results in upregulation of pAMPK and pACC and induction of autophagy, measured by ULK1 S317 phosphorylation (the AMPK phospho-site), p62 depletion and LC3-II accumulation. (Zhang *et al.*, 2015). Repression of mTORC1 by ATM in response to elevated ROS occurs through activation of TSC2 via the LKB1/AMPK pathway (Alexander *et al.*, 2010). Other groups have similarly reported a link between oxidative activation of ATM and upregulation of autophagy, since the C2991L variant described earlier displays elevated ROS levels, a significant reduction of macroautophagy, and widespread protein aggregation in a U2OS cell model (J.-H. Lee *et al.*, 2018). In *C. elegans*, ATM has been proposed to signal through a non-canonical, p53-independent but autophagy-dependent mechanism to drive apoptosis in response to increased oxidative stress (Moriwaki, Yamasaki and Zhang-Akiyama, 2018). Therefore, there is increasing evidence that ATM links together oxidative stress signalling with the autophagy machinery, a link which may have important implications for the development and homeostasis of synapses, which will be explored later in this thesis.

There are also links between the ROS-sensing role of ATM and cytoskeletal rearrangements, although some of the data here are contradictory. It has recently been

identified that pharmacological inhibition of ATM in HeLa cells can increase ROS levels leading to non-canonical direct activation of the cytoskeletal re-modeller Rac1 (Tolbert *et al.*, 2019). This hyperactivation of Rac1 results in cellular migration through increased spreading, which is mediated by cytoskeletal rearrangements. However, other groups have found that loss of ATM can reduce breast cancer cell migration, while oxidised ATM can phosphorylate cortactin and promote association with the Arp2/3 complex and thus increase actin branching (Lang *et al.*, 2018). This may have consequences in neuronal development, as oxidative stress is a positive regulator of synapse size and neuronal growth requires remodelling of the actin cytoskeleton (see *ATM in neurons*).

Intriguingly, ATM protein also localises to mitochondria (Valentin-Vega *et al.*, 2012). A-T models have a basal upregulation of Parkin, and $ATM^{-/-}$ thymocytes show increased mitochondrial ROS levels and disrupted mitophagy (Valentin-Vega *et al.*, 2012). Gallic acid-induced mitochondrial dysfunction and endoplasmic reticulum Ca^{++} release activates cytosolic ATM, which leads to pJNK activation and apoptosis (Lu *et al.*, 2016). Low-dose irradiation in wild-type cells leads to increased mitochondrial mass, accumulation of mitochondrial ROS and damage which is recognised by Parkin, leading to mitophagy – a process which is disrupted in ATM-deficient fibroblasts (Shimura *et al.*, 2016). Interestingly, there is also evidence that mitochondrial oxidative stress leads to activated nuclear ATM dimers, although it is not known if there is shuttling of these dimers between the nucleus and cytosol (Zhang *et al.*, 2018). However, thioredoxin-1 negatively regulates ATM redox dimerisation, and itself is localised in both the cytosol and nucleus (Zhang *et al.*, 2018). Redox-activated ATM is also critical for inducing S-nitrosoglutathione reductase (GSNOR) in order to remove damaged mitochondria through mitophagy, and thus reduce the oxidative stress burden of cells (Cirotti *et al.*, 2021).

Further evidence for ATM as key to the regulation of mitochondrial function comes from studies attempting to understand the pathology of A-T (Chow *et al.*, 2019). ATP depletion generates ROS which activates ATM, and this activation outside of the DDR leads to NRF1 phosphorylation by ATM; this upregulates mitochondrial transcription and enhances the capacity of the electron transport chain to cope with the ATP demand. It is proposed that in A-T, the reduction of ATM in Purkinje cells overwhelms their capabilities to cope with ATP depletion as a result of neuronal activity (Chow *et al.*, 2019) and thus A-T is largely a mitochondrial disorder. However, this would not explain why these neurons are particularly vulnerable compared to other large, highly-active neurons such as Betz cells or the Calyces of Held, given that ATM is expressed in all cells, or that other long-lived, highly energetically active cells, for instance cardiomyocytes, are not vulnerable to loss of ATM.

In ATM-deficient human lymphoblasts, lower efficiency of the pentose phosphate pathway (PPP) is observed. This is due to the reduction in glucose-6-phosphate dehydrogenase (G6PD) activity caused by a failure of ATM to phosphorylate the key intermediate, Hsp27 (Cosentino, Grieco and Costanzo, 2011). Further work demonstrated that this pathway was downstream of redox-activated ATM as the redox-insensitive C2991L form fails to upregulate the PPP (Zhang *et al.*, 2018). This results in a decrease in NADPH levels, reducing antioxidant capacity and leading to an accumulation of mitochondrial ROS (Zhang *et al.*, 2018). Together, this evidence suggests that cytosolic ATM is an essential ROS sensor, signal transducer and guardian against excessive oxidative stress.

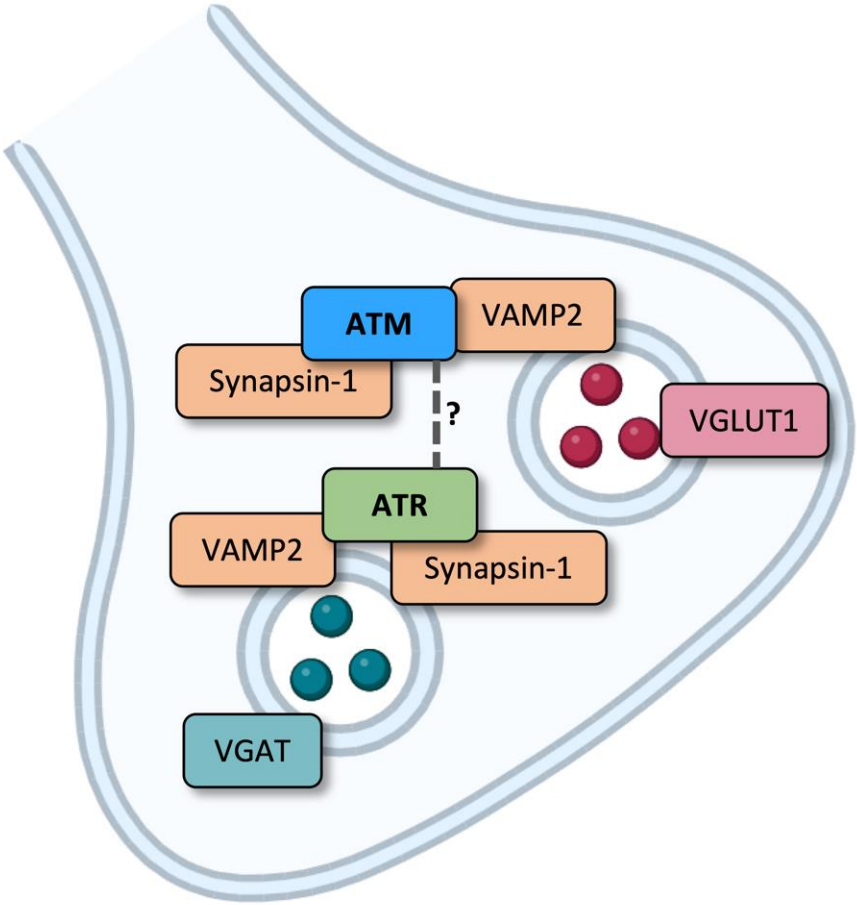

Figure 1.2: Neuronal ATM and its association with presynaptic vesicles. Recent evidence has accumulated for the synaptic localisation of ATM and its role in synaptic plasticity. ATM colocalises with markers of excitatory presynaptic vesicles, while ATR is associated with inhibitory vesicles. There is some evidence that the sister kinases are in complex with each other in synapses, forming a bridge between synapsin-1 and VAMP2 and regulating the balance between excitatory and inhibitory neurotransmission.

1.3.3 - ATM in neurons

Although ATM is a key regulator of the DDR in most cell types, there is increasing evidence to suggest that it has neuronal-specific functions (fig 1.2). As discussed above (*ATM in the nucleus*), there is evidence that the ATM-CHK2-p53 pathway has a non-canonical role in the regulation of neural progenitor proliferation versus apoptosis (Li *et al.*, 2012), potentially alluding to a unique role for ATM in the developing nervous system. Cerebellar slices from ATM-/- mice show that, while the overall structure of the Purkinje cell layer is similar to wild-

type and there is no difference in the basal electrical properties of the neurons (resting membrane potential, input resistance and rectification), there is a progressive deficit in the duration of calcium spike bursts and calcium currents (Chiesa *et al.*, 2000). Since there is a wealth of evidence on the involvement of calcium signalling in synaptic plasticity (Kapur *et al.*, 1998; Nanou, Scheuer and Catterall, 2016; Nanou and Catterall, 2018), these experiments suggest that ATM may be involved in the induction of long-term potentiation (LTP). However, given the multiplicity of ATM functions, there is a question of whether the changes in neuroplasticity of A-T Purkinje cells are a direct or indirect consequence of ATM deficiency.

Nevertheless, studies focussing on the neuronal functions of ATM have shown that ATM plays a more direct role in synaptic plasticity than originally considered. Neurons appear to have a significantly greater distribution of cytosolic ATM than other cell types (Barlow *et al.*, 2000), with Purkinje cells having a uniquely high concentration of the kinase (Oka and Takashima, 1998). Again, the evidence surrounding the cytosolic localisation of ATM is contested – for example, in 2007, two groups independently published papers containing evidence on the localisation of ATM in neuronal cells: one found that in both embryonic stem cell-derived and neural stem cell-derived neurons, ATM was almost exclusively nuclear (Biton *et al.*, 2007); the other found that differentiating neuron-like SH-SY5Y cells resulted in a translocation of ATM from primarily nuclear to primarily cytoplasmic localisation (Boehrs *et al.*, 2007). In some studies, the pool of cytosolic ATM in neurons has been shown to be unresponsive to DNA damage, i.e., this pool is not phosphorylated on S1981 after irradiation, while the nuclear pool is (Li *et al.*, 2009). What is less controversial is that ATM is required for normal neurophysiology: recordings from Schaeffer collaterals in ATM-deficient mouse hippocampal slices have a significant deficit in LTP without any change in their input-output

relationship (Li *et al.*, 2009; Vail *et al.*, 2016). Furthermore, in ATM-deficient mice, paired-pulse facilitation is significantly impaired (Vail *et al.*, 2016).

There is also growing evidence to support a synaptic localisation for neuronal ATM. High-resolution optical microscopy of cultured mouse cortical neurons has demonstrated co-localisation between ATM and presynaptic markers such as VAMP2 and piccolo, as opposed to postsynaptic markers such as homer (Vail *et al.*, 2016; Cheng *et al.*, 2018). Intriguingly, co-immunoprecipitation experiments show a physical interaction between ATM, VAMP2 and synapsin-1, suggesting that ATM physically associates with synaptic vesicles (Li *et al.*, 2009). The same group showed that synapsin-1 but not VAMP2 is an enzymatic target of ATM, while the reverse is true for ATR, and ATR is also in a complex with these two synaptic vesicle proteins. In the absence of ATM, VAMP2 and synapsin-1 failed to immunoprecipitate with each other, suggesting a role for ATM in structurally linking the two. Finally, they also demonstrated that tagged forms of ATM and ATR could be immunoprecipitated together, but only from cytosolic fractions and not nuclear, which suggests that neuronal ATM and ATR form a complex and bridge synaptic vesicles (Li *et al.*, 2009). However, the picture is complicated by the fact that a more recent study has shown ATM exclusively interacting with excitatory synaptic vesicles (marked by VGLUT1 expression) while ATR exclusively interacts with inhibitory synaptic vesicles (marked by VGAT expression) (Cheng *et al.*, 2018). It is difficult to interpret how ATM and ATR could bridge vesicles of different neurotransmitters while exclusively interacting with vesicles of a specific variety, unless there further dynamic changes occurring that are yet to be elucidated. However, the complementary homeostatic interactions between ATM and ATR at the synapse could explain why increased inhibitory

neurotransmission is observed in ATM-deficient hippocampal neuronal cultures (Pizzamiglio *et al.*, 2016).

ATM is clearly involved at the presynaptic site in modulating synaptic output, but it is not clear if this role is separate from its role as a sensor of oxidative stress or whether it acts as the link between ROS signalling and synaptic plasticity. Application of H_2O_2 to *in vitro* frog sartorius or mouse diaphragm muscles produces a marked pre-synaptic depression at the neuromuscular junction (NMJ) as measured by a reduction in excitatory postsynaptic current (EPSC) amplitude, and the frequency of miniature excitatory postsynaptic potentials (mEPSPs) (Giniatullin *et al.*, 2006). This is reported to be due to inhibition of SNARE complex formation with SNAP25 showing particular sensitivity to oxidative stress (Giniatullin *et al.*, 2006). ROS can also affect the morphology of the NMJ: for example, the *spinster* mutant in *Drosophila* have increased levels of ROS at the NMJ which is accompanied by overgrowth of the NMJ – this can be rescued by inhibition of JNK (Milton *et al.*, 2011). Further, autophagy is also a positive regulator of synapse size in *Drosophila* (Shen and Ganetzky, 2009). Since ATM is located at the synapse (in mammals – the possibility of *Drosophila* ATM localising to synapses is explored later in this thesis) and is involved in both the oxidative stress and autophagy signalling pathways, it is possible that ATM responds to ROS locally at the NMJ and signals through the autophagic machinery to modulate presynaptic plasticity. However, this link is yet to be directly shown.

There is also a putative role for ATM in the development of neurons. Cultured $ATM^{+/-}$ neurons from mouse embryos show increased frequency of mIPSCs, increased inhibitory/excitatory ratio, increased numbers of inhibitory synapse vesicles, increased density of vGAT (vesicular GABA transporter), and reduction in proportion of neurons excited

by GABA (Pizzamiglio *et al.*, 2016). These phenomena can be replicated in wild type mice through acute knockdown of ATM using siRNA (Pizzamiglio *et al.*, 2016). Both ATM and ATR have a preference for phosphorylating sites that contain serines/threonines followed by glutamine (S/TQ), and their target sites often contain at least 3 of these motifs within a short stretch, defined as an SCD domain (Traven and Heierhorst, 2005). Not only are these SCD motifs found in a variety of proteins involved in the DDR, they are also over-represented among proteins involved in the development in the nervous system: for example the neuron-specific transcription factors PAX6 and DLX1 among others, axon guidance proteins DCC and ROBO2/3, and cytoskeleton organisation components NES and NF1 (Cara *et al.*, 2016). Cytoplasmic ATM can be activated by insulin signalling and proceed to activate Akt (Halaby *et al.*, 2008). Akt signalling is developing neurons is known to lead to growth cone expansion through Rac1 and branching of axons via mTOR (Grider *et al.*, 2009), so it is possible that ATM signalling may be involved in the coordination of this process.

Additionally, Methyl-nucleotide IP sequencing (MeDIP-seq) of ATM mutant mice Purkinje cells identifies genes that are predicted to be dysregulated by loss of ATM function, which included those involved in neuron fate commitment, spinal cord development, forebrain regionalisation and neuronal differentiation (Jiang *et al.*, 2015). The same authors identified TET1, the enzyme that converts 5-methylcytosone (5mC) to 5-hydroxymethlycytosine (5hmC), as a target of ATM; ATM deficiency thus leads to TET1 disruption, reducing levels of 5mC, leading to epigenetic disruption of genes involved in neuronal development, which may help explain the pathology of A-T (Jiang *et al.*, 2015). Thus, there is a significant body of evidence which suggests significant neuronal-specific roles of

ATM and given A-T is characterised by the progressive loss of neurons, it is important that further research is done into how ATM is involved in their development and maintenance.

1.4 - The *Drosophila* Neuromuscular Junction (NMJ) – A model synapse

The *Drosphila* larval NMJ is an established model for synapse development, given its genetic tractability, conservation of key molecular pathways, straightforward dissection, and the ability to deploy high-resolution imaging techniques (Keshishian *et al.*, 1996; Ruiz-Cañada and Budnik, 2006; Brent, Werner and McCabe, 2009; Ehmann *et al.*, 2014). In addition, while its use of glutamate as a neurotransmitter contrasts with mammalian NMJs (which are cholinergic), this increases its utility as a model of mammalian glutamatergic cortical synapses. Various conserved protein pathways involved in synapse formation and plasticity have been discovered from studies utilising the *Drosophila* NMJ (Keshishian *et al.*, 1996; Marqués, 2005; Collins and DiAntonio, 2007). Further, the GAL4-UAS system in *Drosophila* (Fischer *et al.*, 1988; Brand and Perrimon, 1993) enables cell-type specific expression of transgenic constructs, e.g., RNA interference (RNAi) dsRNAs, or UAS-cDNAs, which enable the knocking-down or overexpression of genes of interest in a cell-type specific manner.

1.4.1 – Larval NMJ development and structure

Motor axons emerge from the ventral nerve cord (VNC) through one of 3 major nerves. The transverse nerve (TN) is bilaterally symmetrical, while the remaining pathways arise from a pair of lateral nerves which exit each side of the VNC, their grouping determined by whether they are segmental (SN) or intersegmental (ISN) (Hoang and Chiba, 2001). These motor

neurons (MNs) project onto the 30 different body wall muscles per hemisegment (Bate and Rushton, 1993; Landgraf *et al.*, 1997). The ISN branch innervates the dorsal muscles, SNa motor neurons innervate the lateral region, SNb/d innervate the ventral musculature while SNc and TN innervate the ventral muscles in the superficial layer (Hoang and Chiba, 2001; Ruiz-Cañada and Budnik, 2006). MNs are also classified by their "boutons," which are swellings along the terminal which contain the majority of the active zones – these fall into 4 categories based upon both morphology and electrophysiological properties (Hoang and Chiba, 2001). Their size ranges from the largest (type Ib, around 3-6 μm), medium-sized type III (2-3 μm) and type Is (2-4 μm), and finally the smallest (type II, 1-2 μm).

Type I boutons are glutamatergic, while types II and III are neuro-modulatory (Menon, Carrillo and Zinn, 2013). The type I MNs are further distinguished by the number of target muscles which they project to, with Ib MNs innervating single muscles while Is neurons project to groups of muscles (Hoang and Chiba, 2001). This suggests differential functions for these neurons, with Ib required for lower-threshold, more precise movements and Is required for higher-threshold recruitment of functional units, which is also reflected in their electrical properties – Is MNs have lower resting membrane potential, higher voltage threshold and longer delay-to-spike than Ib MNs (Schaefer, Worrell and Levine, 2010). The exclusivity of MN axonal branches targeting specific muscles is controlled through trans-synaptic interactions between Dprs and DIPs from the IgSF cell surface protein family (Ashley *et al.*, 2019). An interesting recent finding is that individual active zones show significant heterogeneity in release probability ranging from those which are completely silent or those which only participate in spontaneous neurotransmitter release, to those which are highly active (Akbergenova *et al.*, 2018). While the exact mechanism of how individual active zones are

specialised into different release probabilities is currently under investigation – although there is some evidence that it correlates with the heterogenous distribution of Ca^{++} channels (Gratz *et al.*, 2019) – there are hints as to how this is achieved on a more global level. Type Ib boutons contain the SNARE regulator protein Tomosyn, which acts to suppress release probability of the active zones within, thereby reducing the depletion of the readily-releasable pool of vesicles and contributing to the tonic properties of these MNs (Sauvola *et al.*, 2021). By contrast, type Is MNs lack Tomosyn, resulting in an intrinsically high probability of neurotransmitter release from their active zones which depletes the readily-releasable pool of vesicles and contributes to their phasic firing properties (Sauvola *et al.*, 2021).

In addition, these different neuron types show significant homeostatic plasticity when system is perturbed. For example, genetically controlled ablation of Is MNs results in an expansion of neighbouring Ib MNs through increased bouton budding and formation alongside increased spontaneous and evoked neurotransmission from these Ib MNs, suggesting an intrinsic structural and functional plasticity induced by loss of Is (Wang *et al.*, 2021). Intriguingly, this plasticity is not seen if the Is MNs are absent during development and do not initially co-innervate the muscles, is not related to changes in active zone density or glutamate receptor clustering and may instead be due to a shift in active zone neurotransmitter release probability to a more highly active state, as discussed above (Wang *et al.*, 2021).

For the purposes of this thesis, the focus will be on muscle 4 (fig 1.3) – following the *Crossley et al., (1978)* naming convention – unless otherwise specified. This muscle obeys the general principle of synaptic exclusion whereby no more than one axon from each bouton

type is present – hence, it is innervated by 3 motor neurons from the ISN branch, which are characterised by their bouton type: MN4-Ib, MNISN-Is, and MNISN-II (Hoang and Chiba, 2001).

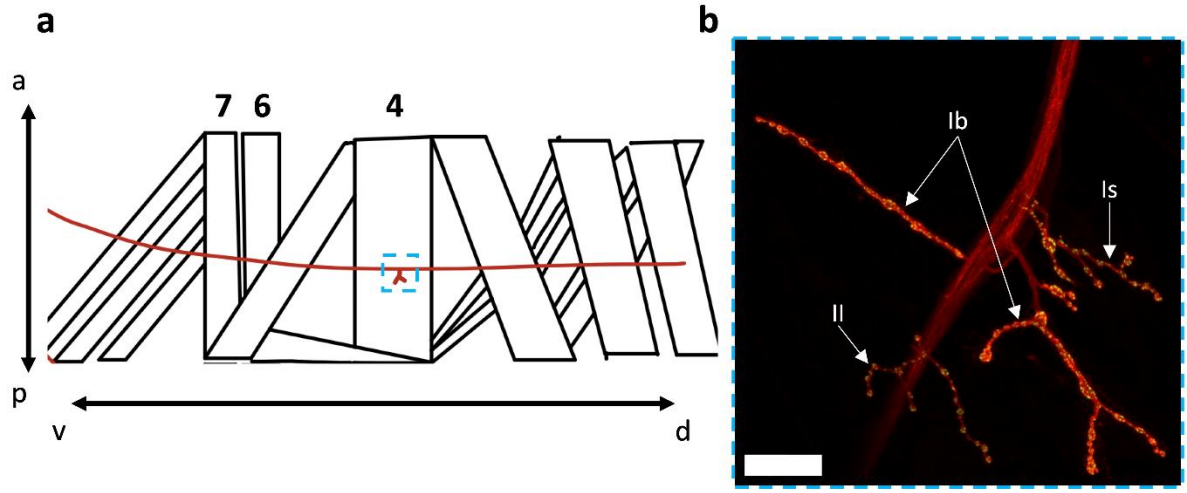

Figure 1.3: The *Drosophila* 3rd instar larval neuromuscular junction. a) Simplified diagram of the body wall musculature from a larval hemisegment. Muscles 4, 6 and 7 highlighted. Neuron shown in red. Not all muscles shown. *Axis labels: a = anterior, p = posterior, v = ventral, d = dorsal.* **b)** Dashed-blue inset – muscle 4 neuromuscular junction with the different bouton types indicated. HRP staining in red (neuronal membranes), BRP staining in green (active zones). Scale bar = 20 µm. Anterior = up.

The development and maturation of the larval NMJ involve a sophisticated interplay of intrinsic and extrinsic signals. By the conclusion of embryogenesis, the overall patterning of the neuromuscular system is complete; yet, since the larva undergoes remarkable growth during its successive moults, the NMJ must expand in parallel. A careful balance exists between growth, retraction and degeneration, and numerous mutations and genetic manipulations have been described which upset this balance (see fig 1.4 for a summary). Two

key mechanisms guide the developmental expansion of the larval NMJ: anterograde and retrograde trans-synaptic signalling.

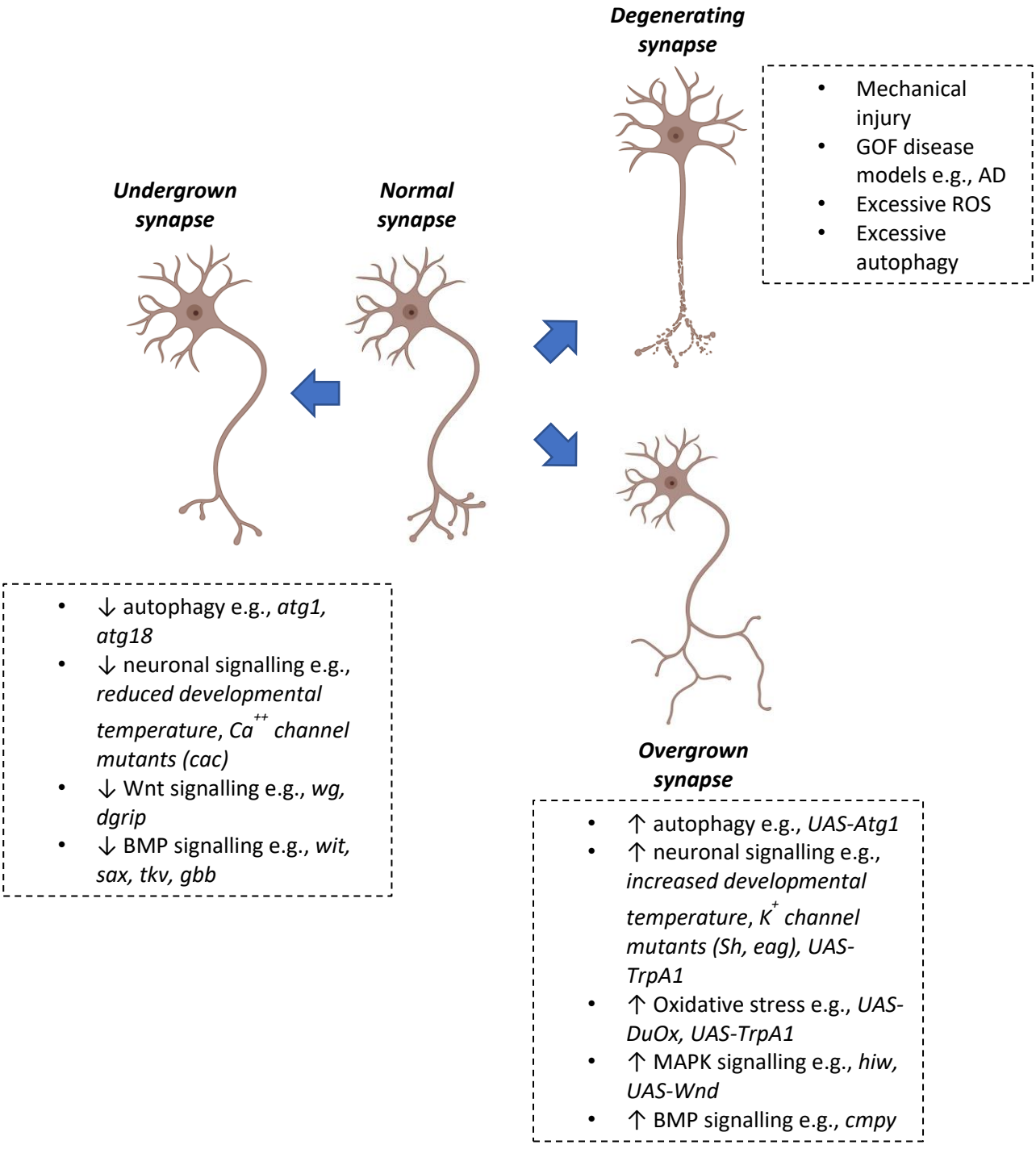

Figure 1.4: Factors affecting synapse development and homeostasis, and associated mutations.

1.4.2 – Wingless and the anterograde signal

The Wnt/Wg pathway is the principal driver of anterograde signalling at the NMJ (Koles and Budnik, 2012). Wg is secreted from type Ib boutons and binds to its receptor, DFz2, on the postsynaptic muscle, leading to DFz2 C-terminus nuclear translocation (Packard *et al.*, 2002; Mathew *et al.*, 2005). Temperature-sensitive *Wg* mutant NMJs have fewer, irregularly shaped boutons with cytoskeletal defects, and transient reduction of Wg secretion is sufficient to prevent NMJ expansion in response to muscle growth (Packard *et al.*, 2002). This anterograde Wg signalling occurs through the Frizzled nuclear import (FNI) pathway: the C-terminal component of the Frizzled receptor is cleaved and translocates to the muscle nucleus in a dGRIP-dependent fashion, leading to changes in gene expression (Mathew *et al.*, 2005; Ataman *et al.*, 2006). Furthermore, Wg has a unique autocrine signalling role at the NMJ. Locally secreted Wg can bind to presynaptic Frizzled receptors, activating an offshoot of the canonical Wg pathway. This cascade involves Dishevelled's activation, which then blocks the GSK3β Shaggy, ultimately releasing its inhibitory hold on the microtubule organizer, Futsch. These events pave the way for the formation of new boutons and the NMJ's synaptic growth (Miech *et al.*, 2008).

While it was clear that DFz2 promotes synaptic maturation since mutants have an increased frequency of “ghost boutons,” the mechanisms were unclear. Recently, Timothy Mosca’s group have shown that inhibiting cleavage of DFz2 blocks synaptic maturation because it impairs DFz2 C-terminus nuclear translocation, and further identified postsynaptic ɣ-secretase as the enzyme responsible for DFz2 cleavage (Restrepo *et al.*, 2022). Intriguingly, pharmacological inhibition of ɣ-secretase in cultured rat cortical neurons modestly reduced spine density and significantly impaired spine maturation (Restrepo *et al.*, 2022), highlighting

a conservation of this pathway between invertebrates and vertebrates and again demonstrating the utility of the *Drosophila* NMJ in enabling novel discoveries for synaptic biology.

1.4.3 – The BMP retrograde signal

The primary retrograde transsynaptic signal is provided from the bone morphogenetic protein (BMP) pathway. BMPs are part of the TGF-β superfamily, known for their roles in cell differentiation, proliferation, and apoptosis (Bayat, Jaiswal and Bellen, 2011). At the *Drosophila* NMJ, the BMP ligand, Glass bottom boat (Gbb), is secreted by the muscle cell and binds to presynaptic BMP receptors (McCabe *et al.*, 2003): Type I, composed of Thickveins (Tkv) and Saxophone (Sax), and type II receptor Wishful Thinking (Wit) (Aberle *et al.*, 2002; Rawson *et al.*, 2003). Once activated, these receptors trigger the phosphorylation of the Smad, Mothers against decapentaplegic (Mad). Phosphorylated Mad, in combination with co-Smad Medea, translocates to the neuronal nucleus and modulates the transcription of genes essential for NMJ growth and function (McCabe *et al.*, 2004). Mutations in the BMP pathway components, including in *gbb*, *tkv*, *sax*, or *Mad*, result in undergrowth of the NMJ, characterized by fewer synaptic boutons and reduced synaptic branching (Rawson *et al.*, 2003; McCabe *et al.*, 2004). By contrast, mutations in *crimpy*, which antagonises Gbb signalling to restrict inappropriate NMJ growth, lead to NMJ expansion (James and Broihier, 2011). Canonical BMP signalling is additionally believed to influence actin through controlling the transcription levels of the presynaptic Rho-GEF Trio, thereby limiting synaptic growth (Ball *et al.*, 2010). Parallel to canonical Mad signalling, DLIMK1 functions downstream of Wit where it promotes synaptic stability, and overexpression of DLIMK1 can rescue the electrophysiological

deficits of *wit* mutants (Eaton and Davis, 2005). This demonstrates that retrograde BMP signalling regulates NMJ development through both canonical and non-canonical pathways.

As with Wg signalling, BMP also has an autocrine role at the larval NMJ which results in a separation of synapse homeostasis from NMJ structural changes (Goold and Davis, 2007). Alongside the structural deficits described above, mutations in *wit* lead to a failure to induce a homeostatic increase in presynaptic neurotransmission in response to expression of a dominant negative glutamate receptor subunit in the postsynaptic muscle (Haghighi *et al.*, 2003). Induction of homeostatic plasticity in the larval NMJ can occur even when the connection to the cell body is severed (Frank *et al.*, 2006) which suggests canonical BMP signalling (through nuclear translocation of pMad) cannot be solely responsible. Recently, it has been shown that activity-dependent release of Gbb from the motor neuron can trigger a local BMP response. The calcium channel subunit $\alpha_2\delta$-3 can interact with BMP released from the neuron, retaining it in proximity such that Wit receptors are activated, triggering this local response (Hoover *et al.*, 2019). This activity-dependent release is dependent on Crimpy, which is involved in trafficking Gbb to vesicles prior to release from the neuron (James *et al.*, 2014). There may be a temporal separation between the requirements of the local *versus* transsynaptic BMP signalling pathways, with the muscle-derived signal required earlier in L1 and the sustained neuronal signal required later (Hoover *et al.*, 2019). This requires the NMJ to distinguish neuronally-derived BMP from muscle-derived BMP, and a secondary role for Crimpy may aid this – the C-terminal ectodomain is also released alongside Gbb upon synaptic activity, which may define the neuronal pool of BMP (James *et al.*, 2014). The mechanism behind the NMJ expansion in *crimpy* mutants is thus reasoned to be a failure to distinguish the muscle-derived pro-growth Gbb signal from the neuronally-derived signal. Further,

neuronal Tao, a regulator of Hippo signalling, has a Hippo-independent role in providing presynaptic negative feedback on BMP signals (Politano *et al.*, 2019). In this way, the developing NMJ integrates pro- and anti-growth anterograde, retrograde, and autocrine transsynaptic signalling to appropriately expand during the growth of the larva.

1.4.4 – The role of neuronal activity in NMJ development and homeostasis

The regulation of the development and homeostasis of NMJ structure is also neuronal activity-dependent on both short- and long-term timeframes. Increasing larval rearing temperature increases bouton and active zone number and potentiates neurotransmission (Sigrist *et al.*, 2003; Oswald *et al.*, 2018). After only 2 hours of increased locomotor activity, enhancement of evoked excitatory junction potentials can be observed (Sigrist *et al.*, 2003), while a 90-minute temperature increase of intact larvae is sufficient to induce nascent bouton formation (Maldonado-Díaz, Vazquez and Marie, 2021). Mutants with combined LOF of two voltage-gated K+ channels, Ether-a-go-go (Eag) and Shaker (Sh), contain neurons with heightened excitability and increased bouton count (Zhong, Budnik and Wu, 1992; Mosca *et al.*, 2005). This evidence indicates that both structural and functional NMJ properties are under the influence of acute and chronic changes in developmental temperature and neuronal activity.

Calcium influx and cAMP play a significant role in these activity-dependent phenotypes: mutations that affect cAMP levels such as *dunce* or *rutabaga* can enhance or suppress a *eag;Sh* double mutant phenotype, respectively (Zhong, Budnik and Wu, 1992), while *Dmca1A* (*cacophony*) mutants have reduced calcium influx into the NMJ upon neurotransmission and subsequent synapse growth defects (Rieckhof *et al.*, 2003). It is interesting that these calcium channel mutants show signs of synaptic undergrowth without

evidence of synaptic retraction, a phenotype more commonly observed with Wg or BMP-pathway mutations. This may suggest neuronal activity is the primary signal for the NMJ to regulate its overall expansion, and subsequent or parallel anterograde and retrograde transsynaptic signalling balances and stabilises the structural changes.

Indeed, as discussed above, BMP release is also activity-dependent, and it was found that *wit* or *gbb* mutants abrogated the overgrowth phenotype associated with *eag;Sh* double mutants, indicating that the canonical BMP pathway is required for this activity-dependent NMJ expansion (Berke *et al.*, 2013). In addition, while dispensable for overall NMJ growth, non-canonical BMP signalling is critical for activity-dependent synaptic maturation. A local pool of pMad accumulates presynaptically, dependent on BMP signalling through BMP receptors Wit and Sax, and in response to active postsynaptic GluRIIA receptors (Sulkowski *et al.*, 2016). Synapse homeostasis at the larval NMJ is highly dependent on the subunit composition of postsynaptic glutamate receptors, since mEJP amplitude is reduced in NMJs expressing only type B receptors, and the ratio of GluRIIA to GluRIIB subunits determines the postsynaptic response to the release of neurotransmitter from a single presynaptic vesicle fusion event (quantal size) (DiAntonio *et al.*, 1999). Loss of this presynaptic pMad pool results in reduction of postsynaptic GluRIIA and a decrease in the IIA/IIB glutamate subunit composition ratio (Sulkowski *et al.*, 2016), demonstrating how this pathway monitors synaptic activity and enables the synapse to mature and stabilise accordingly.

A further key regulator of activity-induced synaptic homeostasis through regulation of glutamate receptor composition is the auxiliary subunit Neto, which is well conserved from insects to mammals. *Drosophila* Neto exhibits two isoforms, Neto-α and Neto-β. The latter is the predominant isoform expressed at the NMJ and regulates the accumulation and

stabilisation of postsynaptic Type A receptors, but cannot alone refine the size of the postsynaptic density (PSD) (Ramos *et al.*, 2015). By contrast, Neto-α has pre and postsynaptic functions: presynaptically, it regulates basal neurotransmission and modulates presynaptic homeostatic plasticity (PHP); postsynaptically, it sets the limit on the size of the PSD (Han *et al.*, 2020). These two Neto isoforms therefore operate in tandem to regulate GluR composition and synaptic homeostasis, although at the time of writing it is unclear how they interact with other modulators of activity-induced synapse homeostasis, such as the BMP pathways discussed above.

1.4.5 – Oxidative stress, autophagy, and crosstalk

An additional layer of complexity is the role that oxidative stress and autophagy play in shaping the developing synapse and in its homeostasis. Both oxidative stress and autophagy can cause the NMJ to expand (Shen and Ganetzky, 2009; Milton *et al.*, 2011), but there exists a careful balance since either in excess can lead to neurodegeneration (Liu and Levine, 2015; Fracassi *et al.*, 2021). Mutations in ATG proteins, such as *atg1, atg2* and *atg18*, lead to significant undergrowth of the NMJ, while neuronal overexpression of ATG1 leads to overgrowth (Shen and Ganetzky, 2009). Raising larvae on the TORC1 inhibitor rapamycin replicates this overgrowth, which is abrogated in the *atg18* mutant background due to ATG18 lying downstream of TORC1 (Shen and Ganetzky, 2009). The mechanism behind autophagic regulation of synapse size is thought to involve the degradation of the E3 ubiquitin ligase, Highwire. *hiw* mutants were known to have dramatically enlarged synapses (Wan *et al.*, 2000). Highwire normally regulates the degradation of the MAPKKK Wallenda, which signals through JNK and the transcription factor Fos to induce synapse growth. *wnd* mutants suppress the *hiw*

phenotype, while overexpression of Wallenda leads to an increase of smaller boutons – this is suppressed by dominant negative Fos or JNK (Collins *et al.*, 2006). Highwire protein levels accumulate in autophagy mutant larvae, and overexpression of Highwire can rescue the overgrowth of ATG1 overexpression NMJs (Shen and Ganetzky, 2009). Further, there is a role for Highwire in the negative regulation of BMP signalling, since it can bind to the co-Smad Medea, presumably promoting its degradation, while the *hiw* overgrowth phenotype is dependent on BMP signalling (McCabe *et al.*, 2004).

Oxidative stress induction of synaptic overgrowth is also known to involve these signalling pathways. *spin* mutants have elevated levels of ROS and expanded NMJs, which show electrophysiological deficits (Sweeney and Davis, 2002). Increasing ROS scavenging, reduction of autophagy through *atg* mutants or expression of dominant-negative versions of JNK or Fos rescue the overgrowth phenotype (Milton *et al.*, 2011), which links ROS and autophagy signalling in NMJ development through regulation of the MAPK pathway. Further crosstalk can be observed with the BMP pathway, since BMP receptor mutants (e.g., *tkv*) also suppress the *spin* phenotype (Sweeney and Davis, 2002).

Other groups have shown that directly increasing ROS burden can influence NMJ morphology and function. For example, ectopic overexpression of the NADPH oxidase Dual Oxidase (DuOx), the temperature-gated cation channel TrpA1, or knockdown of the ROS-scavenging Catalase leads to a significant increase in bouton number (Oswald *et al.*, 2018). Further, they established that increased oxidative signalling mediates activity-induced synapse growth since knockdown of the NADPH oxidases DuOx or Nox abrogated TrpA1-induced NMJ overgrowth (Sobrido-Cameán *et al.*, 2023). The same group identified DJ-1β as a key redox-sensitive ROS sensor in neurons - *DJ-1β* mutants rescued DuOx-induced

overgrowth, and the oxidation-deficient C104A mutant was unable to respond to ROS-mediated growth signalling (Oswald *et al.*, 2018). Oxidised DJ-1β was found to inhibit the phosphatase PTEN, leading to an increase in PIP_3, increased PI3K signalling, which leads to NMJ growth (Oswald *et al.*, 2018; Sobrido-Cameán *et al.*, 2023). This evidence demonstrates the interplay of neuronal activity with oxidative stress in the regulation of NMJ structure and function.

Baines et al., (2015) have identified a critical period (CP) in *Drosophila* NMJ development; artificially increasing neuronal activity during this window in embryogenesis can cause seizures to emerge at later stages of larval development (Giachello and Baines, 2015). More recently, it been shown that ROS have an active role in signalling during the CP. Low temperature (18°C) rearing during the CP results in enriched DGluRIIB expression, which can be abolished with elevated embryonic ROS levels achieved by feeding gravid females di-ethyl maleate (DEM) (Oswald et al., Neurofly 2020 poster *NEUROFLY2100149*). Exogenous increases in ROS scavenging during the CP, through Trolox feeding or UAS-Catalase expression, increases GluRIIB expression, and this effect is downstream of temperature experience (Oswald et al., Neurofly 2020 poster *NEUROFLY2100149*). It has also been shown that confining ROS overproduction to this critical window is sufficient to induce the structural overgrowth seen when ROS is over-produced throughout the larval stage (private communication of unpublished material). Thus, oxidative stress helps to shape the developing nervous system from as early as embryogenesis.

It is not fully clear how neuronal activity levels could alter autophagic flux; however, as a sensor of the ADP:ATP ratio, AMPK activity is upregulated in response to neuronal firing, where it induces mitochondrial respiration (Marinangeli *et al.*, 2018), further linking neuronal

activity to ROS generation and signalling. Hyperactivated AMPK is observed in Alzheimer's disease, promoting excessive autophagy upregulation which causes loss of synapses (Domise *et al.*, 2019), which suggests that in the normal state it may play a role in autophagy induction in response to neuronal activity. Thus, a clearer picture of the coordination between neuronal activity, oxidative stress signalling and autophagy in shaping the development and homeostasis of synapses is beginning to emerge.

1.5 - Drosophila ATM - tefu

The *Drosophila* homolog of ATM is *telomere fusion (tefu)* – hereon referred to as *dATM* for clarity – encoding a protein of 2767 amino acids in length (Oikemus *et al.*, 2004; Song *et al.*, 2004). Mutations in *dATM* lead to radiation sensitivity and the phenotype from which the gene's name is derived: frequent fusions of chromosomes at their telomeres throughout mitosis and meiosis (Queiroz-Machado *et al.*, 2001), which is also observed in lymphocytes derived from A-T patients (Metcalfe *et al.*, 1996). To date, there are no crystal structures of this protein available. However, protein-protein BLAST comparisons of the FAT and kinase domains between *Drosophila* and human ATM indicates protein sequence similarity of 42.8% and 76.2%% respectively. There is also a region at the N-terminus that shares 37.4% similarity between dATM and hATM. However, the small, 33 amino acid FATC domain at the C-terminus of dATM does not show similarity with human or other mammalian homologues of ATM; this domain seems to have diverged much earlier, as it does show similarity with ATM homologues found in other insects, arachnids, nematodes, and crustaceans. One study demonstrated that the point mutations in EMS-generated *dATM* mutants all either encode a premature stop codon within the N-terminal region leading to a severely truncated protein, or target these

conserved functional domains in the C-terminal portion (Pedersen, Tiong and Campbell, 2010). Intriguingly, one of the mutant alleles is a temperature-sensitive hypomorph, *dATM*$^{-8}$. This contains a mutation in the final residue at the C-terminus and is sufficient to confer a phenotype, potentially orthologous to the R3047X mutation in hATM discussed above. The potential structural conservation of dATM will be evaluated towards the end of this introduction (*Structural comparison of hATM and dATM*).

As in mammalian cells, dATM is required for the initial phase of cell-cycle arrest in response to DNA damage via activation of CHK2 and mediates apoptosis through p53 signalling; however, unlike in mammals, homozygous ATM null mutants are inviable in *Drosophila*, suggesting a more crucial role in development and potentially less functional redundancy (Song *et al.*, 2004). Interestingly, reducing p53 levels can rescue the lethality of *dATM* mutants, suggesting that p53 activity mediates the viability defect in *dATM* mutant flies (Pedersen, Tiong and Campbell, 2010). Moreover, dATM appears to be more focused on promoting DNA repair than its mammalian counterpart, while Drosophila ATR (dATR) primarily maintains cell-cycle arrest during DNA repair processes (Joyce *et al.*, 2011). This is supported by the fact that inhibition of dATM but not dATR leads to a large increase in the number of DSBs as measured by ɣH2Av foci (the fly equivalent of ɣH2AX), with evidence of functional redundancy between the two kinases in H2Av phosphorylation (Joyce *et al.*, 2011). This is in contrast to mammalian cells where H2AX is predominantly phosphorylated by ATM and not ATR upon DSB formation, where the residual levels of H2AX phosphorylation upon ATM inhibition is established as originating from DNA-PK (Burma *et al.*, 2001). However, the above study was focussed on meiotic DNA damage within oocytes, where induction of DSBs is required for crossing over and genetic recombination, as opposed to DSBs induced through

irradiation (Joyce *et al.*, 2011). Another reason for this difference could be the absence of a *Drosophila* homologue for DNA-PK (Doré *et al.*, 2004) which results in dATM having a broader role than hATM in coordinating different mechanisms of DNA repair.

The DNA damage response (DDR) in *Drosophila* to double strand breaks (DSBs) is well conserved with the mammalian DDR. The ATM-CHK2-p53 and ATR-CHK1 axes are conserved (Brodsky *et al.*, 2004; Song, 2005), and unrepaired excessive DSBs lead to apoptotic cell death through p53-mediated activation of the proapoptotic machinery, including *hid, reaper,* and *grim* (Goyal *et al.*, 2000; Moon *et al.*, 2008; Xu *et al.*, 2009). Complementation studies have identified the ability of *rpr* to induce apoptosis in mammalian cell lines, such as HeLa cells (Tait *et al.*, 2004). However, unlike in mammals, dCHK2 is the primary regulator of p53 activation in *Drosophila,* as inhibition of dCHK2 but not dCHK1 can suppress the rough-eye phenotype induced by overexpression of p53 (Peters *et al.*, 2002). Furthermore, mutations in *dCHK2* or *p53* do not cause lethality or other defects in external morphology in *Drosophila,* which contrasts with studies in mice (Song, 2005).

As in mammals, dATM is mainly involved in heterochromatic DNA repair, where it promotes expansion of heterochromatin and relocalisation of repair foci (Chiolo *et al.*, 2011; Caridi *et al.*, 2017), although in *Drosophila*, dATR also plays a more prominent role in this. One recent study performed an RNAi screen for genes which sensitise larvae to I-CreI -induction – this restriction enzyme targets sequences in the pericentric region of the X chromosome and leads to acentric chromosomes following DNA repair. In this screen, ubiquitous *dATM* RNAi sensitised larvae to I-CreI induction (reduction in survival to adulthood compared to expression of the RNAi alone), while *dATR* RNAi was consistently lethal before adulthood regardless of I-CreI induction (Vicars *et al.*, 2021).

There is also evidence that suggests a differentiation between the role of dATM in proliferating *versus* non-proliferating cells, similar to mammalian ATM. In proliferating haematopoietic progenitor cells of the third instar larval lymph gland, mutations in *dATM, dCHK2, p53* or *rpr* result in a suppression of activated caspase activity following irradiation, while cell death in the differentiated mature haemocytes is dCHK2- and p53-independent (Nguyen, Shim and Song, 2021). In these differentiated cells, it was found that IR-induced apoptosis is mediated by a direct interaction between dATM and the sole JNK orthologue in *Drosophila, bsk,* which is an intriguing parallel with the known ROS-induced activation of JNK by ATM in mammals (Lu *et al.*, 2016). In addition, knockdown of dATM in the germline significantly compromises stem cell renewal, leading to a reduction in their number, which can be rescued by dCHK2 knockdown (Ma *et al.*, 2016). This relationship has also been observed in the nervous system, where knockdown of dATM in glial cells has been shown to lead to neurodegeneration (Petersen, Rimkus and Wassarman, 2012), while confining dATM RNAi to adult neurons is neuroprotective and extends lifespan in a *Drosophila* model of Alzheimer's disease (Taylor *et al.*, 2022).

The neuronal role of dATM is poorly established compared to the putative neuronal functions of mammalian ATM. It is not known whether dATM localises to the synapse, although expression data suggests moderate levels of enrichment in the larval central nervous system (*FlyAtlas2, https://motif.mvls.gla.ac.uk/FlyAtlas2*). Whole-organism *dATM* mutants show evidence of neurodegeneration such as a rough-eye phenotype and "holes" throughout the adult brain (Pedersen, Tiong and Campbell, 2010). Pan-neuronal knockdown of dATM using RNAi throughout larval development has had mixed results, with some studies demonstrating that this leads to adult-onset progressive neurodegeneration (Rimkus *et al.*,

2008), while others have found no such effect (Petersen, Rimkus and Wassarman, 2012). Further, while dATM overexpression in haemocytes is sufficient to induce apoptosis in the absence of irradiation (Nguyen, Shim and Song, 2021), overexpression in photoreceptors has no effect on eye phenotype and is moderately protective in a neurodegeneration model (Gregory *et al.*, 2007).

As discussed above, both autophagy and oxidative stress regulate synapse development and homeostasis in *Drosophila,* and these two processes have been shown to converge on the JNK signalling pathway (Shen and Ganetzky, 2009; Milton *et al.*, 2011). Given that redox activated ATM can induce both autophagy - through phosphorylation of AMPK (Alexander *et al.*, 2010) - and JNK signalling (Lu *et al.*, 2016), it begs the question of whether ATM coordinates these processes at the synapse during development. In addition, there must exist a balance between autophagy/ROS-induced overgrowth and autophagy/ROS-induced degeneration. ATM's involvement as a ROS sensor and DDR master regulator, and its intriguing co-localisation with presynaptic vesicles, makes it a potential candidate as the local synaptic mediator of this balance. This question will be explored in detail throughout this thesis.

1.6 - Structural comparison of hATM and dATM

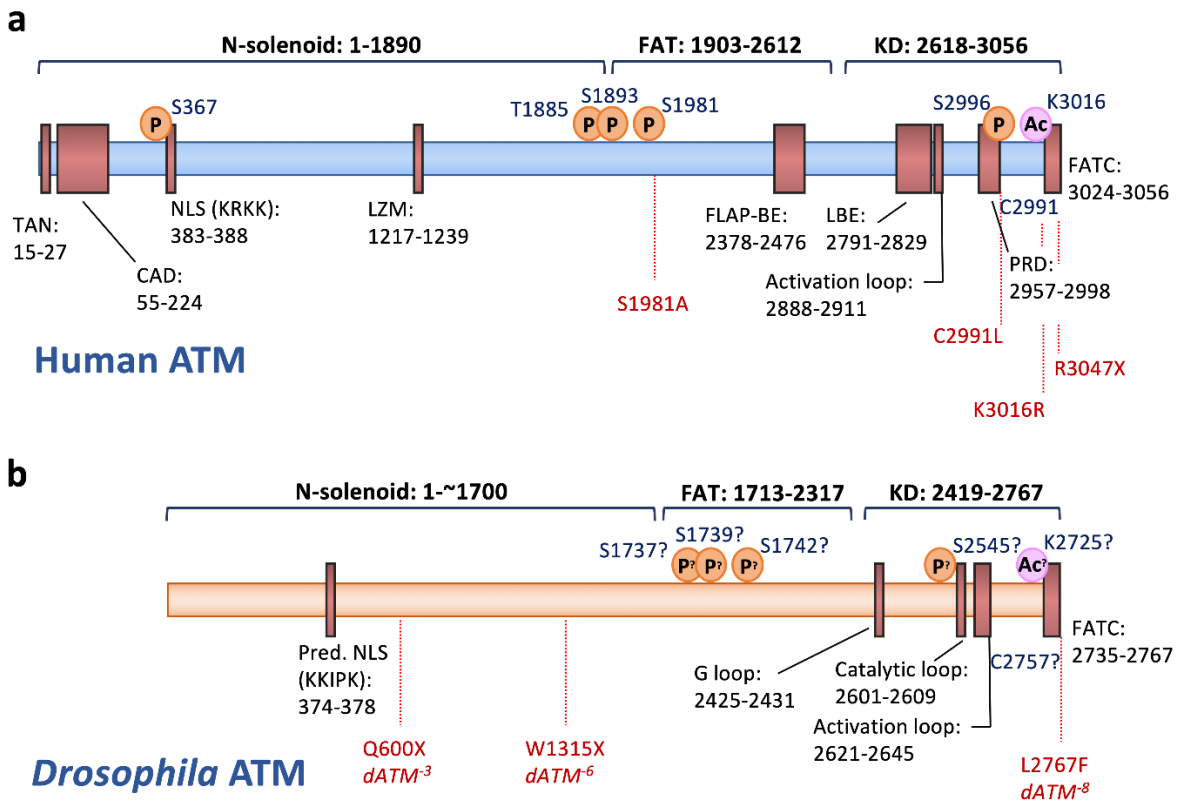

Figure 1.5: Sequence maps of ATM kinase with domains and regions annotated. a) Human ATM. Autophosphorylation sites on S367, T1885, S1893, S1981 and S2996, in addition to acetylation site on K3016, are associated with hATM activation. C2991 required for disulphide bridge formation and redox activation of dimeric hATM. Shown in red are key studied mutations which affect the different functions of hATM. **b)** *Drosophila* ATM (tefu). The predicted homologous residues for autophosphorylation, acetylation, redox activation and nuclear localisation based on structural alignments are annotated (see below). In red are the characterised mutations in the *dATM* mutant lines used in this thesis.
Abbreviations: TAN = Tel1/ATM N-terminal motif; CAD = chromatin association domain; NLS = nuclear localisation sequence; LZM = leucine zipper motif; FLAP-BE = FLAP-binding element; LBE = Lst8 binding element; PRD = PIKK regulatory domain; FAT = FRAP ATM TRRAP domain; FATC = FAT C-terminal domain; KD = kinase domain.
Figure adapted from *Ueno et al., (2022).*

As shown in fig 1.5a, the functional domains of hATM and key residues required for its activation under different signalling contexts has been well-studied. dATM is predicted to form a similar structure based on its sequence, with a conserved N-solenoid, FAT and PI3K domains, and a C-terminal FATC domain (fig 1.5b). In hATM, the FATC domain is known to be important for the redox activation of the dimer since the R3047X mutation abrogates activation by H_2O_2 while preserving activation by MRN and DNA (Guo *et al.*, 2010). However, a protein-protein BLAST suggests no sequence homology between the dATM and hATM FATC domains. A similar result is found when comparing the N-solenoid regions, while the FAT and PI3K domains have 42.8% and 76.2% similarity, respectively. However, the idea that protein structure is better conserved than protein sequence is well established. Plotting the root mean square deviation (RMSD) of structural alignments with sequence identity reveals an exponential relationship such that relatively low conservation is compatible with comparatively low RMSD (Chothia and Lesk, 1986). In addition, there are far fewer distinct possible protein structures and possible folds than distinct protein sequences (Holm and Sander, 1996). This relationship has in fact been quantified, as one study estimated that protein structural cores evolve at 1/3 to 1/10 the speed of protein sequences (Illergård, Ardell and Elofsson, 2009).

At the time of writing, there is no published structure for dATM. To generate a structural prediction for dATM, the amino acid sequence was broken into 3 overlapping fragments and input into the AlphaFold2-based Google *ColabFold* notebook (Mirdita *et al.*, 2022). This is a Jupyter Notebook within Google's Colaboratory which takes a raw protein sequence as input, utilises MMSeqs2 to search for sequence homology (Steinegger and Söding, 2017) and build

templates, and then runs this through the *AlphaFold2* neural network to generate structural predictions (Jumper *et al.*, 2021). The size of dATM (2767 aa) necessitated its breakup into 3 smaller fragments, such that the overlap between the fragments would allow these "identical" sections to be aligned onto each other when constructing the entire protein in *PyMol*. Each segment was input separately into *ColabFold*, and 5 iterations of structural prediction were generated. The prediction with the highest "rank" was then imported into *PyMol* as a *.pdb* file for further analysis.

Fig 1.6a shows the 3 sections built by *ColabFold* which have been subsequently aligned in *PyMol* to generate the entire monomeric form of dATM, with the N-terminus towards the top of the image. This prediction has a strikingly similar overall appearance to the hATM monomeric structure. As suggested by the sequence alignments, the C-terminal portion of the prediction has closer structural homology to hATM than the N-terminal portion. Using the *US-align* software from the Zhang Lab (Zhang *et al.*, 2022), alignment of the N-terminal portion to hATM (PDB = 7SIC) produced a TM-score of 0.78637; for the middle portion, this was 0.79749; for the C-terminal portion, this was 0.83847. (A score of >0.5 is usually considered to indicate significant structural similarity). The N-terminal portion of dATM is predicted to encode structural motifs known as HEAT repeats (Perry and Kleckner, 2003; Pedersen, Tiong and Campbell, 2010) which typically form domains of α-solenoids crucial for protein-protein interactions (Fournier *et al.*, 2013). Previous characterisation of these domains has demonstrated that they can retain high levels of structural homology even when the sequence of the HEAT repeats shows great variability (Andrade and Bork, 1995). The *ColabFold*-generated dATM structure presented here supports this observation, since it predicts that the

N-solenoid of dATM shows significant structural homology to hATM despite the lack of sequence homology (Pedersen, Tiong and Campbell, 2010).

Through duplication then alignment of the C-terminal portions to each chain of the hATM dimer, then using this to anchor the rest of the dATM structure alignment, a prediction of the putative dimeric form of dATM was generated (fig 1.6e). This is clearly no guarantee that dATM dimerises at all, let alone in the same way as hATM, and would need to be validated through biochemical approaches. However, the predicted structural similarities are at least indicative of the possibility for dATM dimerisation.

More is known about the function of mammalian ATM than dATM. Upstream and downstream pathways have been elucidated, alongside key residues for activation, inactivation and dimerisation. Therefore, one of the aims of generating this structural prediction was to use it to enable estimation of the equivalent residues in dATM (if they exist at all) through topological alignment and nearest-neighbour approaches. As a proof-of-concept, an attempt was made to predict the nuclear localisation sequence (NLS) of dATM using the online tool *NLStradamus*, (Nguyen Ba *et al.*, 2009). The NLS of hATM has previously been characterised, consisting of a KRKK motif between amino acid positions 385 and 388 (Young *et al.*, 2005). According to the published crystal structures of hATM, this motif lies within a disordered loop between two alpha helices (fig 1.7a). *NLStradamus* predicted that the most likely NLS sequence in dATM is the KKIPK motif between positions 374 and 378. Strikingly, when the *ColabFold* dATM structure is aligned to hATM, this motif is topologically proximal to the disordered loop containing the hATM NLS (fig 1.7a). This result suggested that a topology-based approach could complement approaches for identifying conserved residues based on sequence alone.

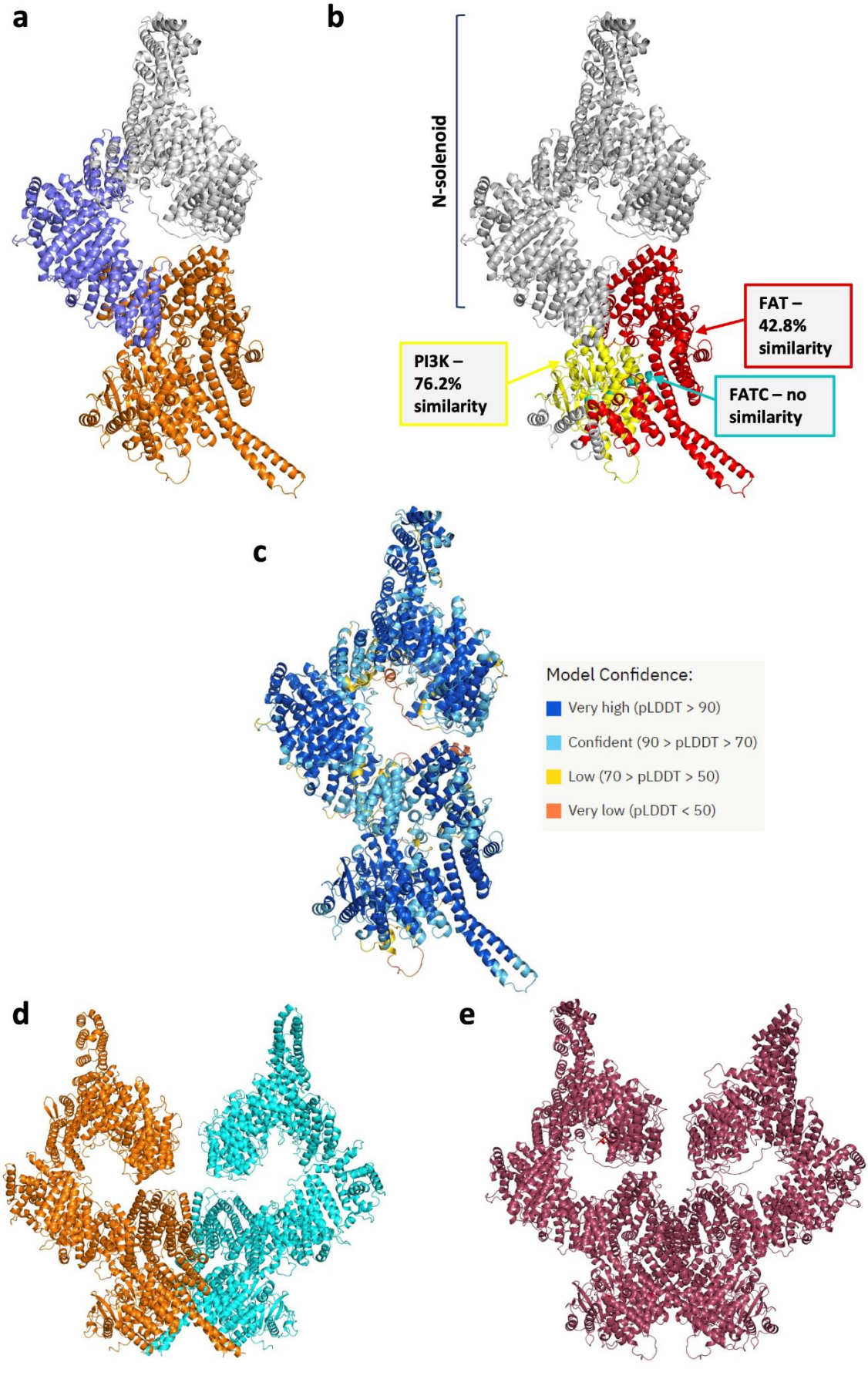
a
b
N-solenoid
FAT – 42.8% similarity
PI3K – 76.2% similarity
FATC – no similarity
c
Model Confidence:
Very high (pLDDT > 90)
Confident (90 > pLDDT > 70)
Low (70 > pLDDT > 50)
Very low (pLDDT < 50)
d
e

Figure 1.6: Using *AlphaFold* to predict the structure of dATM with reference to published structure of hATM. a) Monomeric dATM coloured by *AlphaFold* generated sections. Grey is N-terminal 1000 amino acids. Blue is 755 amino acids in the centre. Orange is C-terminus (about 1100 amino acids). Each has about 100aa overlap to neighbour. Assembled in PyMol using *align*. **b)** Monomeric dATM coloured by functional domains, with associated sequence similarity to hATM. Red = FAT; yellow = PI3K; cyan = FATC. **c)** dATM monomer coloured by pLDDT (confidence of *AlphaFold* model). **d)** Human ATM dimer (PDB = 7SIC). Orange = chain A; cyan = chain B. **e)** Putative dATM dimer based on aligning C-terminal *AlphaFold* prediction to 7SIC and subsequently aligning the rest of dATM onto this.

This approach was extended to other residues known to be important for hATM function, such as the autophosphorylation sites on S2996 and S1981 (figs 1.7b and c, respectively), the acetylation site on K3016 (fig 1.7d) and the cysteine known to be crucial for dimeric hATM redox activation, C2991 (fig 1.7e). With the K3016 acetylation site, it was intriguing to find a nearby lysine residue in the dATM structure in a strikingly similar orientation, 23.5Å away in the aligned molecule. This lysine was not predicted as a conserved residue by a standard sequence alignment. This discovery makes it a good future candidate for site-directed mutagenesis to determine whether this is a true functionally-equivalent residue to hATM K3016, where mutation to K3016R prevents acetylation by Tip60 and activation of hATM by the DNA damage response (Sun *et al.*, 2007).

For S2996, S1981 and C2991, topological alignment was challenging as these functional residues are contained within disordered regions of the protein structure, which were thus unsolvable during crystallography. *ColabFold* is unable to handle disorder and will instead force these regions into a specific conformation during the prediction. This is also clearly seen with the loop containing the predicted NLS in dATM (fig 1.7a) – where with hATM there is just a gap between N358 and I389, the equivalent loop in dATM is forced into a particular conformation connecting the neighbouring alpha helices. Intriguingly, this region is predicted

to be disordered using the *PredictProtein* online resource (Bernhofer *et al.*, 2021), and consequently has a low pLDDT score in the *ColabFold* prediction. The region in dATM containing the putative equivalents of S1981 is also predicted to be disordered using the same software yet is given a static structure in the *ColabFold* prediction. Again, these residues were not predicted to be conserved residues by a standard sequence alignment, so the topological approach may prove useful if these can be confirmed through future site-directed mutagenesis experiments. Further, it is interesting to observe that the "closest" cysteine in dATM to the disordered region containing hATM C2991 is within dATM's FATC domain, unlike the hATM FATC domain which contains no cysteine residues. It is possible, therefore, that any potential dATM dimerisation or redox activation is mediated through its FATC domain, which explains why mutation of a single amino acid within this domain is sufficient to confer a temperature-sensitive deleterious phenotype, as is the case with the *dATM*$^{-8}$ allele.

Figure 1.7: Structural alignments of dATM *ColabFold* prediction and hATM to predict homologous residues. a) Using *NLStradamus* to predict dATM NLS predicts residues in a loop topologically close to the known hATM NLS when structures are aligned.
Region surrounding disordered loop containing **b)** S2996 and **c)** S1981 in hATM shown in yellow. In red are the closest serines in dATM topologically. **d)** K3016, acetylated prior to hATM activation, shown in yellow. Closest topological dATM lysine is K2725, 23.5 angstrom away, in similar orientation. **e)** C2991, required for redox activation of hATM, resides in a disordered loop. Closest topological cysteine in dATM is C2757 within the FATC domain.
In all images: maroon = dATM backbone; red = dATM highlighted residues; orange = hATM backbone; yellow = hATM highlighted residues; dashed lines = disordered region.

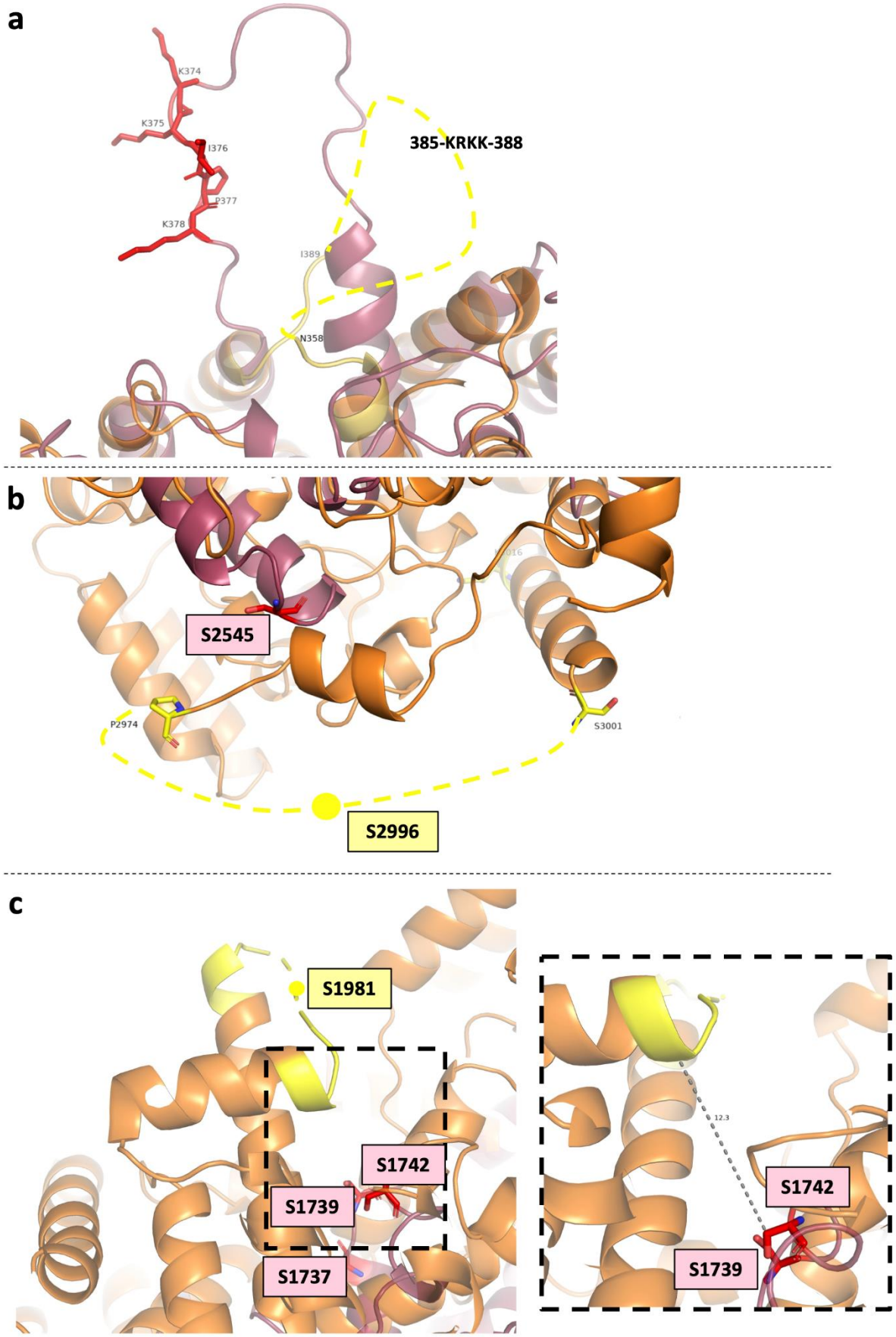
a
K374
K375
I376
P377
K378
385-KRKK-388
I389
N358
b
S2545
P2974
S3001
S2996
c
S1981
S1742
S1739
S1737
12.3
S1742
S1739

d

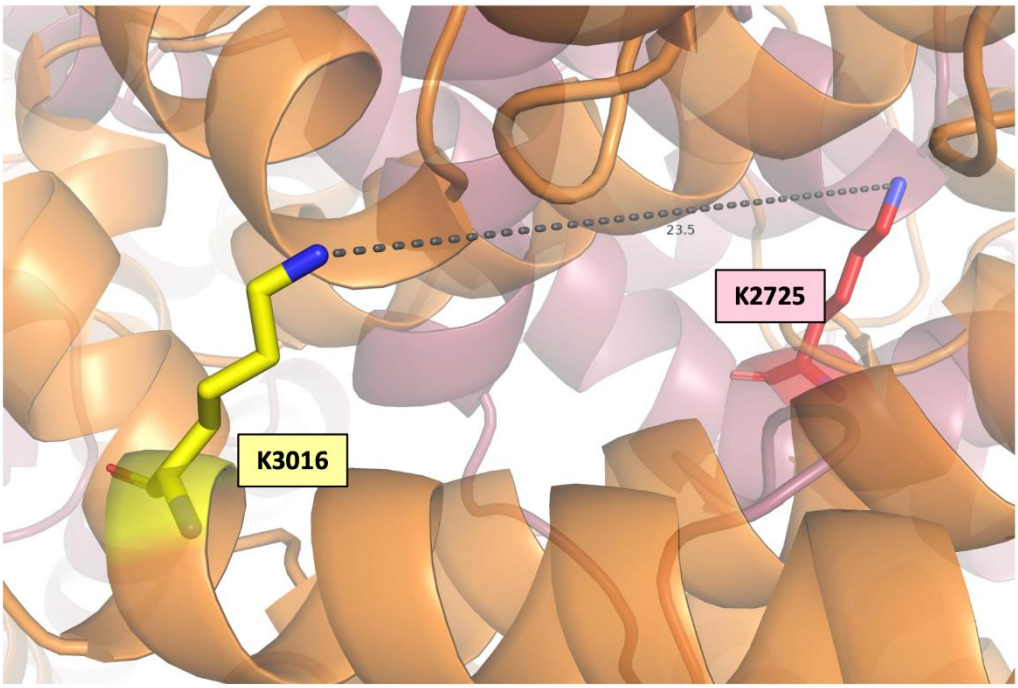

e

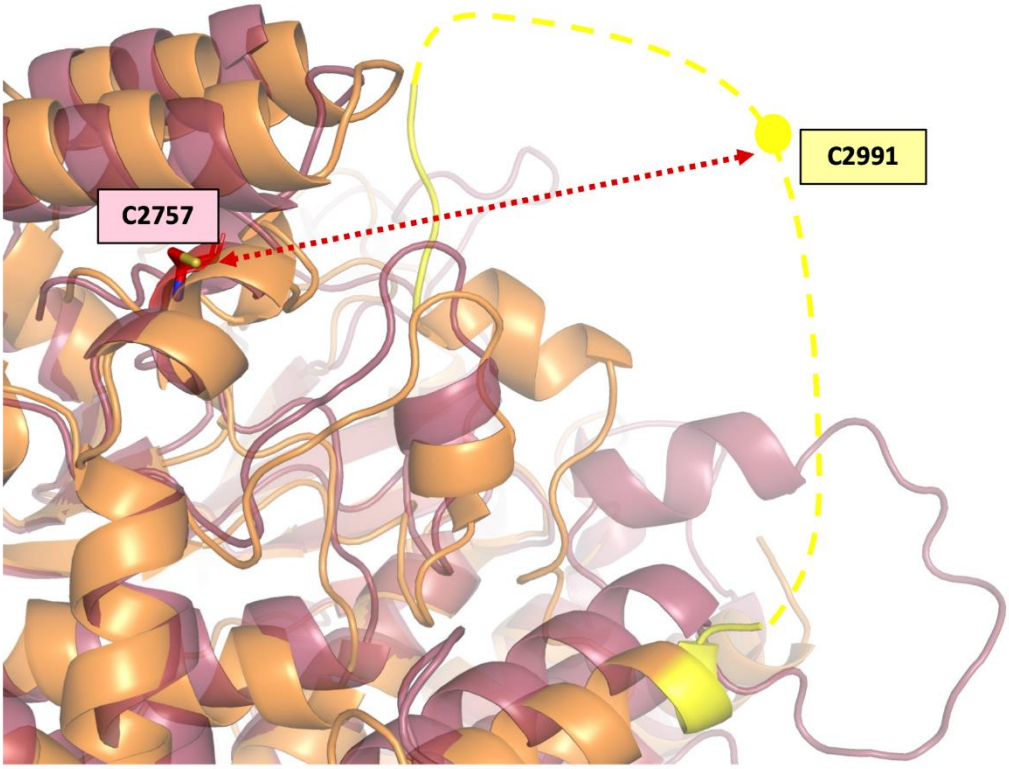

Chapter 2 – Materials and Methods

2.1 - *Drosophila* husbandry and experimental techniques

2.1.1 - Food and incubation conditions

Fly stocks were maintained at 18˚C in an automated 12-hour/12-hour light/dark incubator and transferred onto fresh food every ~21 days. Crosses were performed at 25˚C, and experimental lines for NMJ dissections were raised at 25˚C prior to dissection unless otherwise stated. Stocks and crosses were maintained on standard yeast-sugar-agar food, containing:

- 5% w/v brewers' yeast
- 5% w/v glucose
- 1% w/v soy flour
- 0.8% w/v agar

This food was prepared using the standard "Media" program on a Systec Mediaprep series 10, or manually using a hot plate and standard pressure cooker.

Experimental crosses were maintained upon "German" food, which was essentially standard food fortified with extra supplements, containing:

- 8% w/v brewers' yeast
- 2% w/v yeast extract
- 6% w/v glucose
- 3% w/v sucrose
- 2% w/v peptone
- 0.05% w/v magnesium sulphate
- 0.05% w/v calcium chloride

- 0.8%w/v agar

This food was prepared manually using a magnetic stirrer/hotplate and a conical flask. All food contained the following anti-fungal reagents:

- 1% v/v of 10% methyl-4-hydroxybenzoate in EtOH
- 0.3% v/v propionic acid

Where developmental timing synchronicity was important, crosses were maintained in Kisker egg-laying chambers on plates containing grape juice suspension in agar, with a small amount of yeast paste on top. After 24 hours, L1 larvae were selected and transferred to the experimental food.

2.1.2 - Crossing schemes and generation of stocks

Stocks are listed in *Table 2.5*. Virgin females were exclusively used for crosses and were collected twice daily following rearing at 18°C overnight (16 hr) and 25°C during the day (8 hr). Almost exclusively, experimental crosses were set up with the females as the driver line (particularly with *elav-GAL4;UAS-Dcr2* as the GAL4 is on the X chromosome). For balancing of genetic constructs, the *CyO, Dfd::YFP* balancer and *TM6B, Tb, Hu* balancer were used preferentially for balancing on the 2nd and 3rd chromosome, respectively, as these contained dominant markers which were visible at the larval stage. Occasionally, stocks obtained from BDSC were therefore rebalanced to ensure correct larval stage selection when used in experimental crosses.

For backcrossing the CRISPR knock-in after piggyBAC excision of 3xP3::DsRed, *dATM[sfGFP]* virgin females were sequentially crossed to w^{1118} males. From the F1, 10-15 virgin females were selected and individually crossed to w^{1118} males. After egg-laying, genomic

DNA was extracted from the females, and the presence or absence of the *dATM[sfGFP]* construct determined via diagnostic PCR. Positive crosses were kept, and the process repeated 6 times. Finally, the males from the final generation were crossed to a 3rd chromosome balancer, again checked by diagnostic PCR for the presence of *dATM[sfGFP]*, and ~20 stocks were generated and followed to determine whether they became homozygous.

2.1.3 - 3rd instar larval dissections

NMJs - Drosophila wandering 3rd instar larval NMJ "fillet" dissections were performed as described elsewhere (Brent, Werner and McCabe, 2009). Briefly, wandering 3rd instar larvae were selected, pinned at the mouthparts and posterior spiracle, and stretched out dorsal-up. An incision along the dorsal cuticle was made and the internal organs removed. The corners of the cuticle flaps were pinned, and the body was stretched. The CNS was left intact, except for electrophysiology experiments where it was removed to prevent spontaneous muscle contractions. After pinning, the larvae were washed and fixed in 4% paraformaldehyde/PBS solution for 10-20 minutes at room temperature. This was followed by washing in PBS and storage in ice cold *PBS* prior to immunostaining.

CNS and salivary glands - the CNS was exposed from wandering 3rd instar larvae by gentle application of tension to the mouth-hooks. The salivary glands, eye discs and any excess tissue was then separated from the CNS. The isolated CNS and salivary glands were stored in *PBS* prior to immunostaining.

For irradiation experiments, larvae were irradiated with 8 Gy (CellRad X-ray irradiator) followed by 30 minutes of recovery prior to dissection.

All dissections were performed in *HL3.1 (low Ca^{++})*, an isotonic buffer that mimics the larval haemolymph (Feng et al., 2004) – see *Table 2.1*.

2.1.4 - Electrophysiology

3rd instar larval electrophysiology was performed as described elsewhere (Zhang and Stewart, 2010a). Larvae were dissected as for the larval NMJ preps described above, in *HL3.1 (low Ca^{++})* to minimise muscle contraction during dissection. The motor neuron axons were severed at the base of the CNS, and the CNS was removed to prevent spontaneous muscle contraction during recordings. The preps were washed in *HL3.1 (low Ca^{++})* and recordings were performed in *HL3.1 (electrophysiology)* containing 1.5 mM Ca^{++}. Recordings were taken from muscle 6/7 in segments A2-A5 unless otherwise specified. Single-electrode current clamp recordings were performed using the bridge mode of an AxoClamp-2B amplifier with a HS-2A headstage (Axon Instruments), with stimulation provided by a DS2A Isolated Voltage stimulator (Digitimer Ltd).

To manufacture the recording electrode, borosilicate glass capillaries (GC150F-10, Harvard Apparatus) were pulled using a Narishige PC-100 puller to a resistance of 15-25 MΩ and filled with 3 M KCl. The stimulation electrode holder was constructed following a standard protocol (Zhang and Stewart, 2010b). Stimulation (suction) electrodes were pulled to a resistance of 5 MΩ, the tip gently broken against a microscope lens tissue, and backfilled with HL3.1 using negative suction.

The motor neuron innervating the respective segment was identified and gentle application of negative suction brought the severed axon end into the stimulation electrode. Prior to insertion of the recording electrode into the muscle, pipette resistance was offset by

injecting a -1 nA current and using the bridge control to bring the voltage drop to 0. In addition, the input offset was adjusted to 0 mV.

After insertion of the recording electrode, various exclusion criteria were looked for:

- A voltage drop to a V_m of at least -55 mV
- A muscle R_{in} of at least 4 MΩ as measured by the voltage drop following a -1 nA current injection.
- Correctly identified segmental motor neuron – validated by manually stimulating to check that an excitatory junction potential (EJP) was evoked.
- Recruitment of both Ib and Is motor neuron inputs (see below).

EJPs were evoked initially by 200 µs stimulation at increasing voltages (ranging from 1-8 V) to find the minimum voltage required to recruit both Ib and Is motor neuron consistently, which could be seen by first a small EJP response at one threshold and then a distinct, discrete increase with addition of extra voltage. Mean EJP amplitude was calculated from 10 evoked EJPs at 0.5 Hz. Mini excitatory junction potentials (mEJPs) were observed by recording fluctuations in V_m for at least 2 minutes post-stimulation.

Data were recorded in *Spike2 v9.14-16*.

2.1.5 - Larval locomotion assay

Individual wandering third instar larvae were transferred into a custom-made 3D printed arena with wells containing 2% agarose coloured with a small amount of Orange-G dye. Larval locomotion while freely crawling was tracked for 5 minutes using *EthovisionXT* software, and the resulting metrics for mean speed and percentage time moving were output into *Excel* files. 8-12 larvae were recorded simultaneously. The agarose was replaced at the beginning of each

day's recording and upon occasions where larvae would start to burrow. Only larvae with a mean speed and percentage time moving > 0 were used for subsequent analysis.

2.1.6 – Induction of NMJ structural plasticity

Two different methods for inducing NMJ structural plasticity were attempted (Maldonado-Díaz, Vazquez and Marie, 2021). For K^+-induced depolarisations, larvae were fillet-dissected in *HL3.1 (low Ca^{++})* and subject to consecutive incubations and washout in *HL3.1 (high Ca^{++} and K^+)* and *HL3.1 (low Ca^{++} and K^+)* – see *Table 2.1.* Three rounds of 2 min high K^+ "stimulation" with 15 min "rest" periods were followed by a 4 min and a 6 min high K^+ "stimulation," again with 15 min "rest" in between. For temperature/TrpA1-induced depolarisations, intact larvae were transferred to PCR tubes containing a small piece of Kimwipe soaked in water to prevent drying out and transferred to a PCR machine with the same timing cycles as above, except the "stimulation" and "rest" conditions were 29°C and 21°C, respectively. After the final stimulation, larvae were allowed to recover for 45 min at room temperature before dissection, fixation, and immunohistochemistry.

2.1.7 - Immunohistochemistry

Dissected larval tissues were permeabilised for 15 mins in *PBT* and blocked in *Blocking solution (IF)* for 1 hour (Table 2.1). The primary antibody step was performed at 4°C for 1-3 days in *Blocking solution (IF)*, before washing in *PBS*. Samples were generally incubated in secondary antibodies in *PBS* 4hrs-overnight at 4°C. For primary and secondary antibodies used, see *Table 2.6* and *Table 2.7.* Finally, the preparations were washed in *PBS* and mounted on glass slides in either Fluoromount (with DAPI) or Prolong Gold (without DAPI).

2.1.8 - Embryo microinjections and progeny screening

Drosophila embryo microinjections were carried out by the FlyORF Injection Service at the University of Zurich, Switzerland, or by BestGene Inc, Chino Hills CA. To generate the CRISPR knock-in, a mix of the gRNA-containing plasmids (25 ng/µL) and the HDR plasmid (400 ng/µL) were injected into ~640 embryos of vas-Cas9.RFP flies. From the ~280 surviving larvae, G0 crosses were set up to a yw stock and the progeny of these crosses were screened for DsRed expression. DsRed-positive males were then out-crossed to yw virgin females (F1) and the larvae of these crosses shipped to the UK.

From the F2, DsRed-positive males were selected and crossed to virgin females of a third-chromosome balancer stock (w-; +; MKRS,Sb/TM6B,Tb,Hu) to establish a balanced stock of the CRISPR construct.

To generate UAS-hATM or UAS-dATM[msGFP2], transgenes were subcloned into *pUAST-attB* (see *3.3 – Restriction cloning*) and sent to FlyORF or BestGene for microinjection and *phiC31*-mediated transgenesis. For these transgenic stocks, the presence of w^+ was followed by crossing to balancers from a w^- background.

2.1.9 - Nucleic acid extraction

Genomic DNA was extracted from individual larvae or adult *Drosophila* by homogenising the animal in 50 µL *squishing buffer* (Table 2.1), incubating at 37°C for 30 minutes, inactivation of proteinase K through a 5-minute 95°C incubation, before centrifugation to remove cellular debris. To increase purity of the resulting DNA, 0.1 volumes of 3M NaOAc and 2.5-3 volumes

of 95% EtOH were added to the DNA mix, before incubation at -20°C for at least 4 hours to precipitate the DNA. Subsequently, the mixture was centrifuged at 12,000 x g for 30 minutes, followed by two pellet washing steps using 70% ethanol and further 10-minute 12,000 x g centrifugations. The DNA pellet was then rehydrated in RNAse-free ddH_2O and used for downstream applications.

2.1.10 - Protein extraction

Larvae or adult *Drosophila* were homogenised manually using Konte pestles in 1.5 mL microtubes containing *protein extraction buffer* (Table 2.1). Samples were briefly sonicated before a 15-minute incubation on ice. Extracts were centrifuged at 12,000 x g for 5 min at 4°C. Supernatant was transferred to a fresh microtube, and protein concentration quantified either using a Pierce 660nm assay (Thermo) or via nanodrop. 6X SDS loading buffer was added to the supernatant to a final concentration of 1X, while 1X SDS loading buffer was added to the pellet. Both were heated to 95°C for 5 min prior to SDS-PAGE or storage at -20°C.

2.2 – Microscopy

2.2.1 - Confocal imaging

All images were taken using either a Zeiss LSM 780 or LSM 880 confocal microscope unless otherwise stated. Whole NMJ prep images were obtained using a 10X water immersion lens, using a single scan capturing at both 488 nm and 594 nm. For NMJ quantification, the NMJ on muscle 4 was imaged using a 63X water immersion lens; the images consisted of Z-stacks through the entire NMJ with 0.25 µm step sizes. For dATM[sfGFP] and dATM[msGFP2]

localisation, NMJ images were captured using the 100X oil immersion N.A. 1.46 lens. For NMJ analysis, the resultant Zeiss raw (.czi) file format was converted into .tiff format using a *FIJI* macro, and these .tiff images were imported into *FIJI* for further analysis (see *Analysis of NMJ images in FIJI*).

For live imaging of the *GFP-mCherry-Atg8a* reporter, dissected tissues were maintained on ice in *HL3.1 (low Ca^{++})* solution and transferred to 35 mm glass-bottom dishes. CNS and salivary gland preparations were allowed to sink to the bottom these dishes prior to live imaging, which was performed on the inverted LSM 880 microscope. CNS and salivary glands were imaged using the 20X oil immersion lens, with a single track using both the 488 nm and 594 nm laser lines, with a z-step size of 2 µm.

2.2.2 - 2-photon microscopy

Live-imaging of the *mito-roGFP2-orp1* ratiometric H_2O_2 sensor was performed with the help of Dr Dean Kavanaugh. Larvae were dissected in the same way as for electrophysiology and maintained on ice in Sylgard-coated dishes in *HL3.1 (low Ca^{++})*. Z stack images were taken using a 2-photon microscope (Olympus FVMPE-RS). As the sensor required conventional excitation at 405 and 488 nm with emission detection at 500-570 nm (Albrecht *et al.*, 2011), this had to be altered for 2-photon microscopy (where by rule-of-thumb excitation wavelengths are generally doubled). It was determined that the optimum excitation wavelengths were 770 and 900 nm, respectively, with the 515-560 nm collection filter used for emission. Z-stacks had to be generated sequentially for each excitation wavelength. The CNS and a defined muscle 4 NMJ were imaged for each sample, before and after 15-minute incubation in 10 µM H_2O_2 to

promote oxidation of the sensor as a positive control. The resulting *.oir* files were imported into *FIJI* using the *Bioformats* plugin for further analysis.

2.3 - Molecular Biology

2.3.1 - Design of homology-directed repair construct for CRISPR knock-in of sfGFP into dATM locus

The design of the *dATM* homology-directed repair (HDR) construct was mapped out in *Microsoft Word* before being imported into *SnapGene* for *in silico* cloning and primer design. The HDR construct consisted of the following:

- DsRed under control of 3xP3 promoter for selection.
- STOP codon after sfGFP in the piggyBac right inverted repeat to generate mutant.
- piggyBAC repeat sequence for excision of DsRed.
- Superfolder GFP (with flexible linker sequence).
- 100nt homology arms to exon 1 of *dATM* to allow targeting – from (Kanca *et al.*, 2019).
- Unique PAM sites so that the construct can be excised from the TOPO vector in the fly germline using unique gRNA. These synthetic gRNA sequences do not exist in the *Drosophila* genome. Again from (Kanca *et al.*, 2019).

The source of the superfolder GFP (sfGFP) was the plasmid *pScarlessHD-sfGFP-DsRed* (Addgene #80811). Primers were designed to amplify, from genomic DNA, 100-nucleotide homology arms to the 5' and 3' ends of the insertion site in *dATM*. These primers also included the gRNA sequence that was unique to the HDR vector.

In addition, primers for amplification of the entire insertion construct from the *pScarlessHD-sfGFP-DsRed* plasmid, including the Gibson assembly-required 30 bp overlap with the amplicons from the fly genomic DNA, were generated. The pCFD3-dU6:3gRNA plasmid (Addgene #49410), hereafter referred to as pCFD3, was used to clone the guide RNAs used for excision of the targeting construct and generation of a double strand break in the *dATM* locus for HDR.

2.3.2 - Design and synthesis of UAS-dATM[msGFP2] construct

The design of a fluorescently-tagged dATM overexpression construct was performed in conjunction with a separate project attempting to create a CFP/YFP-tagged hATM for FRET analysis. The desire was to find the equivalent fluorescent protein insertion site in dATM as had been used in hATM, and this was achieved by aligning the *AlphaFold* predicted dATM structure with the published hATM structure and locating the dATM residues in closest physical proximity to the site of hATM CFP/YFP insertion (fig 2.1). Subsequently, insertion of msGFP2, chosen because of its ability to resist dimerization which could affect the function of dATM (Valbuena *et al.*, 2020), was located prior to T486 in dATM. The nucleotide sequence of msGFP2 was thus inserted into this location in the cDNA of dATM using *SnapGene*, and the entire construct synthesised by GenScript and cloned into the pUC57 vector.

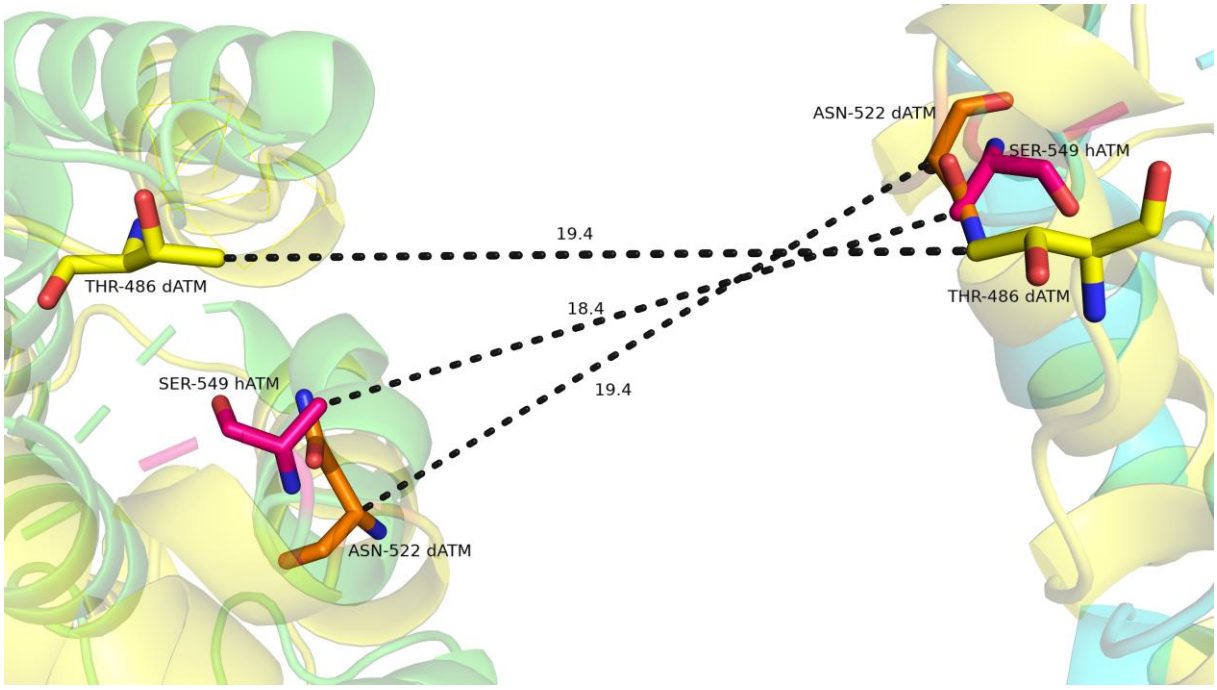

Figure 2.1 – Alignment of dATM with hATM focussing on the site of fluorescent protein insertion. The *AlphaFold* predicted structure of dATM (yellow) was aligned onto the published dimeric structure of hATM (green and cyan) using PyMol. The closest physical residues to hATM S549 (chosen in a separate project for CFP/YFP insertion as the residue of closest approach to the N-terminal domains of the two chains) are shown, and their distances in Å between the corresponding residue in the other chain.

2.3.3 - Design of guide RNAs (gRNAs)

gRNA design was aided by free online tools, including *e-CRISP* and *FlyCRISPR*. The gRNA targeting the *tefu* locus was selected based on a trade-off of proximity to the site of editing versus an optimal Specificity Annotation Efficacy (SAE) score (*e-CRISP*). The gRNA targeting, and unique to, the HDR vector was referenced from (Kanca *et al.*, 2019).

2.3.4 - PCR

All PCRs (except diagnostic/colony PCRs) were performed using proofreading Phusion polymerase (NEB) with all concentrations of DNA (primers, template, dNTPs) in the reaction mix as recommended by the supplier. All reactions took place in a Techne 3Prime thermocycler, with 28-32 cycles being standard, extension times of 30 s per kb, and annealing

temperatures according to the ThermoFisher Tm calculator – this accounts for the fact that Phusion is part of the new generation of polymerases and uses higher annealing temperatures than Taq. All PCRs also contained an initial denaturation of 30 s to 1 min and a final extension time of at least 5 minutes.

Diagnostic/colony PCRs were performed using DreamTaq polymerase (Thermo) following the manufacturer-recommended protocol.

After reaction completion, 6X gel loading dye was added (if not in the reaction mix), and the samples were loaded onto a 1% agarose/TBE gel containing 1:20,000 Midori Green (Nippon Genetics) for agarose gel electrophoresis; 100 V for 45 minutes was typical.

Gels were imaged using either a Vilber Lourmat Fusion using the UV gel setting, or a BioRad GelDoc system.

2.3.5 - Gibson Assembly

The Gibson Assembly of purified DNA fragments was performed according to the protocol for the Gibson Assembly Cloning Kit (NEB, E5510S). Fragments were diluted in the reaction mixture to a final amount of 0.02 pmol of each fragment per reaction. This was followed by incubation at 50°C for 30 minutes.

1 µL of this mixture was then used as template DNA for PCR amplification; products of the correct size were excised from the agarose gel and purified using a Promega gel purification kit according to the manufacturer protocol.

2.3.6 - Restriction cloning and ligation of human ATM or dATM[msGFP2] cDNA into pUAST-attB

The source of human ATM kinase cDNA was the plasmid *pcDNA3.1(+)Flag-His-ATM wt* (Addgene #31985) - hereafter referred to as pCMV-ATM. The pUAST-attB plasmid (Addgene #5556) was a kind gift from Dr Johannes Bischof (University of Zurich, Switzerland).

pCMV-ATM was digested using NotI-HF and XhoI using the manufacturer's recommended conditions (CutSmart buffer, 1 µg of DNA plasmid, 37°C for 15 min). The cut DNA was separated using agarose gel electrophoresis and the larger band (9645 bp) excised and purified.

pUAST-attB was digested using the same conditions, with the following exceptions: the reaction was allowed to proceed overnight to aid full digestion; the digested product was purified directly without running on a gel (since the unwanted fragment was small enough to pass unimpeded through the purification column).

For dATM[msGFP2], the pUC57-dATM[msGFP2] vector and pUAST-attB were sequentially digested using NotI overnight and KpnI for 3 hours due to buffer incompatibility. Digests were subject to agarose gel electrophoresis, and the bands of the correct size were excised and purified (Promega Wizard SV Gel Purification kit).

The ligation reactions were performed using either using Quick Ligation Kit (NEB) or T4 ligase (Thermo), with a 1:3 vector:insert ratio, following the respective manufacturer's recommended protocol. The product was transformed into NEB Stable Cells using the manufacturer's high efficiency transformation protocol, spread onto ampicillin selection plates, and grown at 30°C for 2 days. Colonies were then screened for successful insertion by PCR, mini/midi-prepped (Sigma GenElute kit) and sent for sequencing.

2.3.7 - Restriction cloning and ligation of gRNAs into pCFD3

gRNA primers were designed in according to the protocol found at crisprflydesign.org. Briefly, the sequences generated in *Design of guide RNAs (gRNAs)* were converted into primers compatible with BbsI-mediated cloning into pCFD3 through the addition of GTCG/AAAC at the 5' ends of the sense/antisense oligo respectively (with the antisense oligo being the reverse complement of the gRNA sequence). These primers were sourced from Eurofins Genomics, with 5' phosphorylation added.

The complementary oligos were annealed in a Techne 3Prime thermocycler, with the following conditions: 10 µM sense/antisense oligo suspended in *oligo ligation buffer*; incubated at 95°C for 5 mins; cooled to 25°C at rate of 5°C/min.

pCFD3 was digested using BbsI-HF according to the manufacturer's protocol except using a 4 h incubation at 37°C followed by a 20 min incubation at 65°C to inactivate the enzyme. The digested plasmid was purified using the same method as the pUAST-attB above.

Ligation of the annealed gRNA oligos into the digested pCFD3 was performed using the Quick Ligase Kit (NEB) following the *crisprflydesign.org* protocol, followed by transformation into competent bacteria and spreading onto ampicillin plates. Successful transformants were screened by colony PCR. Colonies positive for the insertion were midi-prepped and sent for sequencing.

2.3.8 - Plasmid DNA preparation and glycerol stock generation

Depending on the amount of DNA required, positive colonies were amplified in selective LB broth in an appropriate volume for the kit being used. Colonies were incubated overnight at 37°C or for 36 hours at 30°C depending on the stability of the plasmid, before mini, midi, or maxi preparations according to the standard manufacturer's protocol (Sigma, GenElute plasmid mini/midi/maxiprep kits). Glycerol stocks were prepared from cultures by transferring 500 µL of the culture to a cryovial and adding 500 µL of 30% (v/v) glycerol. Purified plasmid stocks eluted in ddH_2O, and glycerol stocks, were stored at -20 °C and -80 °C, respectively.

2.3.9 - Cloning of blunt-ended PCR fragments into pCR-Blunt II-TOPO vector

Purified Gibson-assembled linear DNA fragments were cloned into the pCR-Blunt II-TOPO vector using the manufacturer recommended protocol. Reactions were incubated for at least 5 minutes at 25°C before transformation into competent bacteria and incubation at 37°C on kanamycin growth plates. Resistant individual colonies were screened for successful insertion of the construct, and plasmid preps from these colonies sequenced with primers designed to cover the entire construct.

2.3.10 – Sequencing

All sanger sequencing of cloned constructs was performed by Source Bioscience (Nottingham, UK). Comparison of the sanger sequencing results with the expected sequence was performed using the sequence alignment tool within *A plasmid Editor* (*ApE*, M. Wayne Davis, https://jorgensen.biology.utah.edu/wayned/ape/).

2.4 - Cell culture

2.4.1 - Culture and maintenance of cell stocks

Drosophila S2 cells were maintained in Schneider's Insect Medium supplemented with L-glutamine, supplemented with 10% fetal bovine solution (FBS, Thermo) and 5 mL/L Penicillin-Streptomycin solution. Media was replaced 2x per week and cells were incubated at 25°C. Passaging the cells occurred roughly 1-2x per week when the cells reached 90-95% confluence (as determined manually using an upright light microscope).

To cryopreserve aliquots of cells for future use, counting was performed following the standard Trypan Blue staining protocol for the Countess II Automated Cell Counter (Thermo). This was followed by pelleting the cells at 1000 rpm for 5 mins, removing the old media, and resuspending at a density of $2x10^6$ cells/mL. Finally, an equal volume of growth media supplemented with 20% v/v DMSO was added (to a final concentration of 10% DMSO), and 1 mL aliquots of this suspension were stored at -80°C.

2.4.2 - Transfections

All transfections were performed using Lipofectamine 3000 reagent and the manufacturer recommended protocol. Cells were seeded onto sterile, 15 mm concanavalin-A (Sigma) coated coverslips in 6-well plates such that their confluence would be 80-90% at the time of transfection. Each well was transfected with either 1 or 2.5 µg of plasmid DNA, complexed in a 1 µg:1 µL ratio with P3000 enhancer reagent and 1 µg:3 µL ratio of Lipofectamine 3000 transfection reagent in Schneider's medium without FBS supplementation. Cells were

incubated in the presence of the DNA transfection mix for 6-24 hours and transfection efficiency assessed by the proportion of GFP-positive cells (depending on the experiment).

2.4.3 - Immunocytochemistry

After transfection, media was removed and the cells washed in *PBS*, followed by fixation in 3.7% formaldehyde for 20 minutes. Cells were permeabilised for 15 mins in *PBT* and blocked in *Blocking solution (IF)* for 1 hour. Primary antibody incubation was performed in blocking solution overnight at 4°C, followed by PBS wash steps, and secondary antibody incubation for 1 hr at 4°C. For primary and secondary antibodies used, see *Table 2.6* and *Table 2.7.* Finally, the cover slips were washed in *PBS*, with a final rinse in dH_2O to remove salt crystals. Cover slips were mounted on glass using a drop of Fluoroshield (with DAPI, Sigma).

2.5 - Western blotting

Protein samples were heated to 95 °C for 3-5 min and then separated using SDS-PAGE. Loading volumes were adjusted to achieve a consistent protein concentration. A 15-min stack at 75 V was followed by separation for 60-90 min at 150 V in GelRad tanks containing *SDS-PAGE running buffer*. Blotting paper (3 mm, Whatman) and PVDF membranes (0.45 µm, Invitrogen) of the appropriate size were equilibrated in 1X *Tris-Glycine transfer buffer*; the PVDF was activated in methanol for 30 s beforehand. Gels were equilibrated in the buffer for 10 min. Wet transfers were conducted for 60-90 min at 400 mA, 4°C. Membranes were blocked for 40 min at room temperature in *Blocking solution (WB)*, then incubated with the primary antibody overnight at 4 °C. After being washed in P/TBST three times for 5 min, they were exposed to secondary antibodies for 1 h at room temperature, followed by another series of P/TBST

washes. Membranes were exposed to SuperSignal West Femto ECL (Thermo) for 1 min and then a Vilber Lourmat Fusion imager was used to image the chemiluminescent signal. Where required, the subsequent images were processed in *FIJI* to determine the relative density of the bands compared to a) the background and b) a housekeeping protein, e.g., actin.

2.6 - Analysis

2.6.1 - Analysis of NMJ images in FIJI

Batch processing of larval NMJ images was performed using the *Drosophila NMJ morphometrics* plugin in *FIJI* (Nijhof *et al.*, 2016). This plugin takes 2-channel Z-stacks containing HRP and BRP signal in the *.tif* format as input and produces a text file containing various metrics (such as NMJ area, perimeter, length, number of boutons, number of active zones) as output. Briefly, the workflow was as follows:

- Convert the LSM 880 output *.czi* files to *.tif* format using a simple *FIJI* macro.
- Run the *Drosophila NMJ morphometrics* sub-macros 'Convert to Stack' and 'Define ROI,' which is run iteratively on each file and allows the definition of the NMJ borders through the standard *FIJI* ROI selector functions.
- Run the 'Analyze' macro to quantify the NMJ morphometrics.

The .txt results files were then imported into *Rstudio* for statistical analysis.

The surface area of muscle 4 was measured for each larva using the polygon selection tool and inbuilt *measure* function in *FIJI*. The mean muscle surface area (MSA) was then calculated for each genotype and the ratio of this MSA to the control MSA for each experiment

generated. All datapoints were then scaled using this ratio to account for differences in muscle size between the genotypes.

2.6.2 – Analysis of caspase activation using GC3Ai

Maximum intensity projection images were split into separate channels using *FIJI*. The image containing the endogenous GFP fluorescence (from caspase activation) was used for automated cell counting analysis. A ROI corresponding to the VNC was manually selected using the freeform selection tool. To remove background fluorescence, the minima and maxima were adjusted in the brightness/contrast manager to leave only clearly lit-up cells and minimise false positives. Subsequently, a "max entropy" *auto threshold* algorithm was applied, and the *analyze particles* plugin was used for cell counting, with a minimum pixel size of 40 to exclude noise. The resulting cell count was exported into *Excel*.

2.6.3 - Analysis of mitoGFP images

Quantification of mitochondrial number per NMJ and density was performed essentially the same as above, using the *Drosophila NMJ morphometrics* plugin, with mitoGFP replacing the BRP channel. To quantify mitochondrial size and circularity, higher magnification images were taken of the NMJs, and a custom *FIJI* script applied to the images. This script allowed selection of the NMJ as a ROI, *thresholding* to find NMJ outline, then applied this to the mitoGFP channel. The background was subtracted, and an *auto threshold* was applied to isolate the mitoGFP signal from background, and finally the size and circularity of the particles detected was measured.

2.6.4 - Autophagy quantification

For quantification of autophagic flux using the *GFP-mCherry-Atg8a* reporter (Nezis *et al.*, 2010), z-stack maximum intensity projections were imported into *FIJI* and analysed using a custom-made *FIJI* script. Essentially, the script would: iterate through each file in a directory; prompt the user to draw a freehand selection around the salivary glands; clear outside the selection; split the channels; process the GFP channel by thresholding (using the *auto threshold mean* function) and selecting the salivary gland border as the region of interest (ROI); apply this ROI to the mCherry channel; automatically adjust contrast to a fixed saturation value (to ensure consistency between samples); *auto threshold* (using *otsu*); and finally *analyse particles* again to select and quantify the mCherry foci. The results were exported as an *Excel* file and imported into *Rstudio* for statistical testing.

2.6.5 - Calculation of HRP-Dlg ratio

A custom *FIJI* script was written which would iterate through max intensity projections in a directory, select the HRP channel and ask the user to roughly draw a ROI around the NMJ. *Auto threshold* was used to detect the NMJ outline, which was then used to automatically select the entire NMJ as a ROI. This ROI was re-applied to both the HRP and DLG channels, and the mean intensity of the signal measured, and the ratio of the two calculated.

2.6.6 - Analysis and export of electrophysiology data

Raw electrophysiology data from *Spike2 v9* were analysed using custom active cursors within *Spike2*. For detection and quantification of EJPs, three cursors were used: the first would iterate through the *events* i.e., the points automatically marked where each stimulus was

delivered; the second would then find the maximum value within one second of this event, while a third would find a minimum. The max V_m, min V_m and difference was then output.

For mEJP detection and quantification, events were not specifically marked since they were spontaneous, so an automatic detection pipeline was set up. Firstly, the data channel was duplicated, and a low pass filter applied. To this, a DC removal filter was applied with a time constant of 50 ms to generate a memory channel. Finally, a smoothing filter with a time constant of 0.65 ms was applied to the duplicated data channel to smooth out high frequency noise. Active cursors were then applied in a similar way as above, except the first cursor was set up to find peaks of at least 0.3mV in amplitude in the DC removed memory channel. The next cursor looked for the maximum V_m value within +/- 5 ms seconds of the original while the final cursor found the minimum V_m value within 20 ms prior to the former.

All these processes were encapsulated in custom scripts to automate the pipeline and data were exported into an *Excel* spreadsheet. Frequency of mEJPs was calculated by taking the number of automatically detected mEJPs and dividing by the time difference between the first and last observed mEJP. Amplitudes were corrected for differences in baseline V_m (i.e., corrections for non-linear summation) using:

$$v' = E(\ln[E/(E-v)])$$

where:

- v' = corrected amplitude
- E = driving force (assumed to be equal to V_m in this case given a reversal potential of 0mV)
- v = recorded amplitude (Stevens, 1976; McLachlan and Martin, 1981; Feeney *et al.*, 1998)

Quantal content was calculated by dividing corrected EJP amplitude by corrected mEJP amplitude. Data were then read into an *Rstudio* environment for statistical analysis.

2.6.7 - Statistical analysis in Rstudio

All statistical analysis and graph production was performed in *Rstudio v3.6.0*, using the following libraries*: readxl, ggplot2, dplyr, ggthemes, ggpubr, ggsignif, ggthemr, tidyverse, ISLR, Rfast, rstatix, ggtext. RolorBrewer, ggsci* and *MASS*.

An R script was made for each experiment type e.g., NMJ structural analysis, electrophysiology, autophagy quantification *etc*. In *Excel*, if more than one datapoint was generated from one larva (i.e., the right-side NMJ vs the left-side NMJ), the data for that larva was averaged to avoid inflating the n number with non-independent datapoints. These .xlsx files were then read into the *Rstudio* environment using *readxl*.

Boxplots were generated using *ggplot2* and statistical tests performed using embedded functions within the *rstatix* and *multcomp* packages. Data were checked for normality using the 'shapiro.test()' function. T-tests were used for pairwise comparisons of normally distributed data (Wilcoxon tests if not normally distributed), while multiple comparisons with the control genotype as the reference group were performed using Dunnett's tests. If no group was selected as control (i.e., testing every condition against every other condition) then Tukey's Honest Significant Differences tests were performed.

For the complementation experiments in *Chapter 4*, stacked bar plots were generated using the *dplyr* and *tidyr* libraries. Chi-squared tests were performed using a custom function, comparing the *expected* and *observed* proportions of heterozygous vs *trans*heterozygous

larvae and eclosed pupae for each genetic combination, and the resulting p-values were manually overlayed onto the graphs post-export.

Table 2.1 – Buffers

Buffer	Recipe
Phosphate-buffered saline (PBS)	137 mM NaCl, 2.7 mM KCl, 10 mM Na_2HPO_4, 1.8 mM KH_2PO_4, pH 7.4
PBST	PBS, 0.1% (v/v) Tween-20
PBT	PBS, 0.3% (v/v) TX-100
Tris-buffered saline (TBS)	50 mM Tris-HCl, 150 mM NaCl, pH 7.6
TBST	TBS, 0.1% (v/v) Tween-20
Squishing buffer[a]	10 mM Tris, 25 mM NaCl, 0.05% (v/v) Triton X-100, 1 mM EDTA, 4 mg/ml Proteinase K, pH 8.0
Protein extraction buffer	1X RIPA buffer, protease/phosphatase inhibitors (Sigma)
Blocking solution (WB)	PBST/TBST, 5% (w/v) milk, 0.02% (w/v) NaN_3
Blocking solution (IF)	PBS, 1% (w/v) BSA, 0.02% (w/v) NaN_3
Oligo ligation buffer	10 mM Tris-HCl, 50 mM NaCl, 1 mM EDTA
HL3.1 (low Ca^{++})[b]	70 mM NaCl, 5 mM KCl, 0.1 mM $CaCl_2$, 4 mM $MgCl_2$, 10 mM $NaHCO_3$, 5 mM trehalose, 115 mM sucrose, 5 mM HEPES.
HL3.1 (electrophysiology)[b]	70 mM NaCl, 5 mM KCl, 1.5 mM $CaCl_2$, 4 mM $MgCl_2$, 10 mM $NaHCO_3$, 5 mM trehalose, 115 mM sucrose, 5 mM HEPES.
HL3.1 (low Ca^{++} and K^+)[c]	70 mM NaCl, 5 mM KCl, 0.1 mM $CaCl_2$, 10 mM $MgCl_2$, 10 mM $NaHCO_3$, 5 mM trehalose, 115 mM sucrose, 5 mM HEPES.
HL3.1 (high Ca^{++} and K^+)[d]	40 mM NaCl, 90 mM KCl, 1.5 mM $CaCl_2$, 20 mM $MgCl_2$, 10 mM $NaHCO_3$, 5 mM trehalose, 115 mM sucrose, 5 mM HEPES.
SDS-PAGE running buffer	25 mM Tris-HCl, 192 mM glycine, 0.1 (w/v) SDS, pH 8.3
Tris-Glycine transfer buffer	25 mM Tris-HCl, 192 mM glycine, pH 8.3
Tris-Borate-EDTA (TBE)	100 mM Tris-HCl, 100 mM boric acid, 20 mM EDTA

[a] *Georg Dietzl in Barry Dickson's Lab, IMP Vienna 12/2002 – retrieved from here*
[b] *Feng, Ueda and Wu, (2004)*
[c] *Maldonado-Díaz, Vazquez and Marie, (2021)*
[d] *Vasin* et al., *(2019)*

Table 2.2 - Oligonucleotides for generation and validation of CRISPR dATM[sfGFP] construct

Primer name	Sequence (5'-3')
genomic_3'tefu_homology_to_sfGFP	GTAGTACGATCATAACAACGAGGCTTAAAGAGAGCCTCCTTCGACG
genomic_5'tefu_homology_to_sfGFP	GTAGTACGATCATAACAACGAGGCAGAGGTCACTCTAAGTACATTTTG
genomic_sfGFP_to_3'_tefu_homology	CTGGTGGTTCAGGAGGTTCCAGTGCACTTCTAAACGAAATCCAGCG
genomic_sfGFP_to_5'tefu_homology	GGAACCTCCAGATCCACCCATCCTGGCTGCCCGGCATAAC
3'tefu_homology_linker_sfGFP	ATTTCGTTTAGAAGTGCACTGGAACCTCCTGAACCACCAG
5'tefu_homology_linker_sfGFP	TTATGCCGGGCAGCCAGGATGGGTGGATCTGGAGGTTCCG
gRNA1_insert_plasmid_pCFD3	GTCGTAGTACGATCATAACAACG
gRNA1_insert_plasmid_pCDF3_revcom	AAACCGTTGTTATGATCGTACTA
gRNAtarget_tefu_pCFD3	GTCGTTTAGAAGTGCACTCATCC
gRNAtarget_tefu_pCFD3_revcomp	AAACGGATGAGTGCACTTCTAAA
5'tefu_genomic_to_CRISPR	CTAGTTCTCCATCGGCACTT
3'tefu_genomic_to_CRISPR	CTTATCCAGATCCTCTCGGC
piggybac_right_fwd	CCCGATAACCACTACCTGAG
piggybac_right_rev	TTGAATTGTCGCTCCGTAGA
piggybac_right_rev2	AACCTCGATATACAGACCGA
5'tefu_insert_to_pTOPO	TGCTCAGGTAGTGGTTATCG
3'tefu_insert_to_pTOPO	ACTACACCATCGTGGAGCAG

Homology shown by colour: RED = gRNA1; BLUE = tefu homology arms; GREY = short polypeptide linker.

Table 2.3 - Oligonucleotides for sequencing pUAST-attB plasmid and insertions

Primer name	Sequence (5'-3')
5'UAST_to_insert	ATACAAGAAGAGAACTCTGAATAG
3'UAST_to_insert	AGTAAGGTTCCTTCACAAAG
attB_seq_fwd	GCCATACCACATTTGTAGAGG
attB_seq_rev	AGAACTAGTGTCGACATGCC
mini-white_seq_fwd	ACATTTGCTCAAGAACGGTG
mini-white_seq_rev	CGTTAGGGAGCCGATAAAGA

Table 2.4 – Plasmids

Plasmid name	Purpose	Source
pcDNA3.1(+)Flag-His-ATM wt	Source of human ATM cDNA	Addgene #31985
pScarlessHD-dsRed	Vector for CRISPR HDR template	Addgene #64703
pCR-Blunt II-TOPO	Blunt cloning Gibson-assembled fragments for amplification	Thermo (Zero Blunt TOPO PCR cloning kit)
pUAST-attB	UAS vector for phiC31-mediated integration into *Drosophila* genome	Dr Johannes Bischof, University of Zurich, Switzerland
pMT-GAL4	Cu-inducible GAL4 promoter for S2 cell line gene expression	DGRC Stock 1042
pUC57-tefu-msGFP2-thr485	Source of msGFP2-tagged dATM cDNA	GenScript

Table 2.5 – Fly stocks

Stock (abbr)	Description/Purpose	Source
w^{1118}	Wild-type line	BDSC #5905
w^{-};+;dATM^{-3}/TM6B	dATM mutant	BDSC #8625
w^{-};+;dATM^{-6}/TM6B	dATM mutant	BDSC #8626
w^{-};+;dATM^{-8}/TM6B	dATM mutant	BDSC #8624
w^{-};If/CyO,Dfd::YFP	2nd chromosome balancer	
w^{-};;MKRS/TM6B	3rd chromosome balancer	
w^{-};If/CyO,DfD::YFP; Dr/TM6B	Double balancer	Derived from BDSC #59967
Elav-GAL4;UAS-Dcr2	GAL4 driver line (pan-neuronal)	BDSC #25750
Nsyb-GAL4 on III	GAL4 driver line (pan-neuronal)	BDSC #51635
yw;;Actin-GAL4/TM6B	GAL4 driver line (ubiquitous)	BDSC #3954
yw;;Mef2-GAL4	GAL4 driver line (muscle)	BDSC #27390
w^{1118};;Repo-Gal4/TM6B	GAL4 driver line (glia)	Derived from BDSC #7415
w^{1118};OK371-GAL4/CyO,Dfd::YFP	GAL4 driver line (motor neurons)	BDSC #26160
yv;dATM$^{[HMS02790]}$	TRiP dsRNA to dATM	BDSC #44073
yv;;dATM$^{[JF01422]}$	TRiP dsRNA to dATM	BDSC #31635
yv;;dMRE11$^{[HMC02995]}$	TRiP dsRNA to dMRE11	BDSC #50628
yv;dATR$^{[HMS02331]}$	TRiP dsRNA to dATR	BDSC #41934
yv;dCHK2 $^{[HMC05499]}$	TRiP dsRNA to dCHK2	BDSC #64482
yv;;Cat $^{[JF02173]}$	TRiP dsRNA to Catalase	BDSC #31894
yv;;Atg18a$^{[HMS01193]}$	TRiP dsRNA to Atg18a	BDSC #34714
yv;;AMPK$^{[JF01951]}$	TRiP dsRNA to AMPK	BDSC #25931

w;UAS-Cat	Overexpression of Catalase	BDSC #24621
yw;L/CyO;UAS-hDuOxII	Overexpression of hDuOxII	BDSC #78412
yw;UAS-Atg1	Overexpression of Atg1	BDSC #51654
yw;;UAS-Atg1	As above, on 3rd chromosome	BDSC #51655
w^{1118};UAS-AMPK	Overexpression of AMPK	BDSC #32108
w^{*};UAS-GC3Ai	Overexpression of marker of activated caspases, GC3Ai	Derived from BDSC #84313
w^{*};;UAS-GC3Ai	As above, on 3rd chromosome	Derived from BDSC #84301
w^{*};UAS-TrpA1	Overexpression of TrpA1	BDSC #26263
w^{*};;UAS-TrpA1	As above, on 3rd chromosome	BDSC #26264
w^{*};;dATM[sfGFP::DsRed]*	CRISPR insertion stock containing sfGFP, 3xP3::DsRed and piggybac sequences	This study
w^{*};;dATM[sfGFP]	CRISPR insertion stock after piggybac excision of 3xP3::DsRed	This study
w^{*};UAS-hATM	Overexpression of hATM cDNA	This study
w^{*};;UAS-hATM	As above, on 3rd chromosome	This study
UAS-GFP-mCherry::Atg8a	Overexpression of dual colour reporter of autophagic flux	Professor Ioannis Nezis, University of Warwick, UK
w^{1118};;UAS-mitoGFP	Overexpression of mitochondria localised GFP	BDSC #8443
w^{1118};UAS-mito-roGFP2-Orp1	Overexpression of mitochondria localised ratiometric H_2O_2 sensor	BDSC #67667

BDSC = Bloomington Drosophila *Stock Centre; TRiP = Transgenic RNAi Project*

Table 2.6 – Primary antibodies and conjugates

Description	Host	Use	Concentration	Source
α-Brp	Mouse	IHC	1:100	DSHB (nc82)
α-γH2Av	Mouse	IHC, WB	IHC: 1:100-1000 WB: 1:1000	DSHB (UNC93-5.2.1)
α-actin	Mouse	WB	1:3000	DSHB (JLA20)
α-GFP	Rabbit	IHC, WB	IHC: 1:1-2000 WB: 1:1000	Abcam (ab290)
α-GFP	Chicken	IHC	1:400	Invitrogen (A10262)
α-GFP VHH	Alpaca	IHC	1:1000	ChromoTek (gt)
α-elav	Rat	IHC	1:100	DSHB (7E8A10)
α-dlg	Mouse	IHC	1:200	DSHB (4F3)
α-repo	Mouse	IHC	1:1000	DSHB (8D12)
α-FLAG	Mouse	IHC, ICC	IHC: 1:200 ICC: 1:400	DSHB (12C6c)
Alexa Fluor 594 α-HRP	Goat	IHC	1:400	Jackson (123-585-021)

IHC = immunohistochemistry; ICC = immunocytochemistry; WB = western blotting; DSHB = Developmental Studies Hybridoma Bank.

Table 2.7 – Secondary antibodies and DNA stains

Description	Host	Use	Concentration	Source
HRP α-mouse	Horse	WB	1:5-10,000	CST (#7076S)
HRP α-rabbit	Goat	WB	1:5000	CST (#7074S)
Alexa Fluor 488 α-mouse	Donkey	IHC, ICC	1:1000	Jackson (715-545-150)
Alexa Fluor 488 α-mouse	Goat	IHC, ICC	1:1000	Jackson (115-545-003)
Alexa Fluor 594 α-rat	Goat	IHC	1:1000	Jackson (112-585-167)
Alexa Fluor 488 α-chicken	Goat	IHC	1:400	Thermo (A32931)
Alexa Fluor 488 α-alpaca	Goat	IHC	1:1000	Jackson (128-545-230)
TOPRO3	-	IHC	1:2000	Invitrogen (T3605)
Hoescht 33342	-	IHC, ICC	1:10,000	Thermo (62249)

IHC = immunohistochemistry; ICC = immunocytochemistry; WB = western blotting; CST = Cell Signalling Technologies.

Chapter 3 – Presynaptic ATM is required for neuromuscular junction development in *Drosophila melanogaster*

3.1 – Introduction

The evidence for the neuronal function of *Drosophila* ATM (dATM) is so far limited and, at times, contradictory. Null alleles generated by P-element mediated excision are predominantly homozygous lethal, but some "escapers" make it to adulthood. These flies display a rough-eye phenotype, a hallmark of neurodegeneration in *Drosophila* (Song *et al.*, 2004). However, this cannot be separated from the general gross reduction in viability and contains no information about a specific role for dATM in neurons, other than the fact that neurons are vulnerable in whole-organism *dATM* mutants. The vulnerable cells in this and related studies were proliferating cells rather than mature neurons (Silva *et al.*, 2004). Nevertheless, other work explicitly reducing dATM levels in neurons, or subgroups of neurons, demonstrated an adult phenotype; specifically, expressing RNAi constructs to dATM in the eye using *GMR-gal4* or pan-neuronally using *elav-GAL4* throughout development also led to the rough-eye phenotype in adulthood, followed by progressive neurodegeneration (Rimkus *et al.*, 2008). Further, *elav*-driven knockdown at 25°C (but not 18°C) resulted in lethality, suggesting a temperature-dependence of the phenotype (Rimkus *et al.*, 2008). Yet this study stands in contrast to another which showed that dATM knockdown in glial cells resulted in neurodegeneration and reduced survival, whereas *elav*-mediated knockdown did not, and in fact showed an extension of survival (Petersen, Rimkus and Wassarman, 2012). Overexpression of dATM has not been widely studied, although in an enhancer/suppressor screen for modifiers of the rough-eye phenotype induced by knockdown of *pebble*, a Rho-GTP exchange factor, overexpression of dATM was found to be moderately protective, while

overexpression in a wild-type background had no effect on the eye phenotype (Gregory *et al.*, 2007).

On the other hand, previous work in the Tuxworth lab showed that confining dATM knockdown specifically to *Drosophila* adulthood and only after a critical period of young adult neurodevelopment conferred neuroprotection in different models of adult-onset neurodegenerative disorders (Taylor *et al.*, 2022). Thus, there appears a disconnect between the role of dATM in developing *vs.* mature neurons; a phenomenon which is as yet under-studied. Despite all of this, and the fact that the human disorder associated with ATM-deficiency (Ataxia telangiectasia) is a childhood-onset neurodegenerative disorder, the consequences of dATM-deficiency on the development and plasticity of the larval nervous system has not been characterised.

Therefore, to study the role of ATM kinase in synapse development, the *Drosophila melanogaster* wandering third instar larval neuromuscular junction (NMJ) was used as a model. The larval NMJs are the synapses formed between segmental and transverse motor neurons onto their postsynaptic targets – the body wall muscles – to control larval locomotion. As discussed previously, this system has numerous advantages, such as its genetic tractability, ease of access through dissection, the variety of techniques and tools available for its study, and the conservation of key pathways involved in synapse development and plasticity. Further, these synapses are not static but are rather shaped throughout the growth of the larva, altering their size, strength, and structure in response to endogenous and exogenous stressors. Studying the larval NMJ also avoids any issues that may arise because of metamorphosis during the pupal stage, where the nervous system undergoes dramatic

pruning and rewiring in a way truly distinct from the mammalian nervous system. Any adult fly phenotypes following this could therefore be confounded by potential dATM involvement in metamorphosis processes, which may not be directly relevant to the study of the human disorder. As such, the larval nervous system offers the potential to dissect out the specific function of dATM in neurons during development at both short- and long-term timeframes, and in both cell autonomous and non-autonomous contexts.

Several metrics can be measured from the NMJ, including the number of active zones (the sites of neurotransmitter release), the overall size of the NMJ scaled to muscle surface area, and the number of presynaptic "boutons" – these are small swellings containing a high density of active zones. Recently, an ImageJ-FIJI plugin was developed that automatically quantifies these (and other) metrics (Nijhof *et al.*, 2016; Castells-Nobau *et al.*, 2017). The process is summarised in fig 3.1. As an input, the plugin requires 2-channel z-stack images, with one channel containing the neuronal membrane (fig 3.1b, *left*, HRP) and the other containing the active zones (fig 3.1b, *right*, nc82/BRP).

The plugin uses selected thresholding algorithms to determine the extremities of the NMJ and from this calculates area, perimeter, and the branch lengths etc. Where the plugin detects an invagination of the membrane, it will designate this region a bouton, provided the enclosed space is above the selected minimum bouton size – this process uses a watershed algorithm (Beucher and Lantuejoul, 1979; Ramesh and Tasdizen, 2021). Preliminary testing suggested that there was no significant difference between what the plugin designated as boutons and what a manual experimenter did (not shown). The plugin also counts the number of nc82-positive foci within the green channel to determine the number of active zones. The

settings that were settled on to use consistently in these experiments are shown in fig 1c. These settings were arrived at following the recommended steps in Castells-Nobau *et al.,* (2017). Fig 1d shows the graphical output of the plugin, consisting of the NMJ outline, skeleton, boutons, and the marked active zones. The plugin also outputs a text file containing the results. All the subsequent NMJ data was generated using this plugin, with a predominant focus on the area of the NMJ, number of boutons, and number of active zones, all scaled to the surface area of the postsynaptic muscle.

Using this system, this chapter characterises the phenotypic consequences of loss of dATM function on the development of the larval NMJ. Using cell-type specific knockdowns, the requirement of presynaptic dATM is established, independent of its role in the DNA damage response. Presynaptic dATM knockdown is shown to lead to structural and functional changes. By using an established method for increasing neuronal activity and inducing growth of the NMJ, presynaptic dATM is shown to be required for activity-induced structural and functional plasticity. The question of whether the loss of dATM leads to a neurodevelopmental or neurodegenerative condition is also addressed, with evidence of increase caspase activity and withdrawal of the presynaptic membrane from the end-plate observed at higher larval rearing temperatures. This data forms the basis of a model in which dATM is a necessary sensor of neuronal activity levels, translating this into a growth signal, while potentially also guarding against the toxic effects of increased neuronal activity.

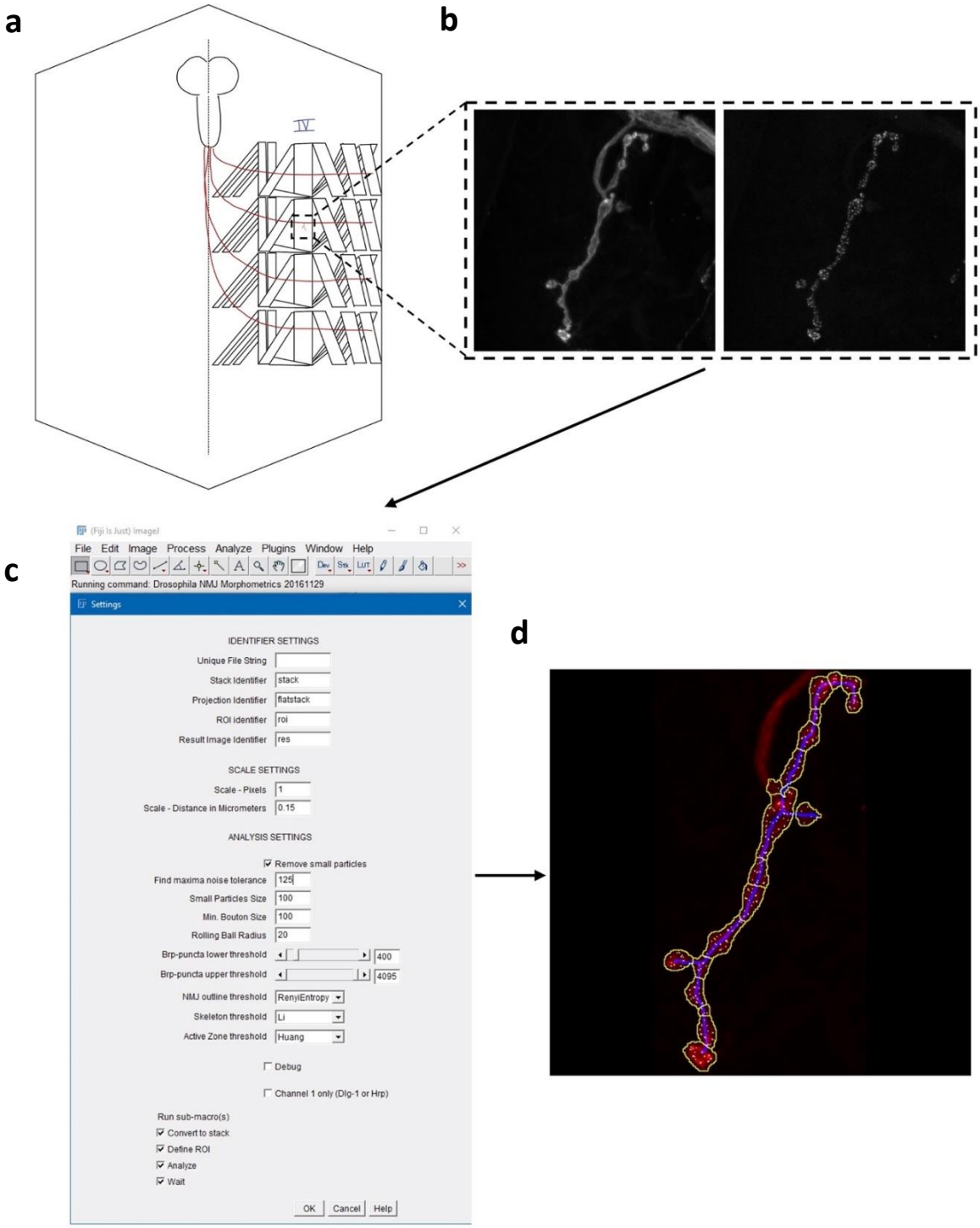

Figure 3.1: Overview of *Drosophila* NMJ imaging protocol and FIJI macro. a) Diagram of wandering 3rd instar larval neuromuscular junction (NMJ). Muscle 4 is indicated. b) Confocal images of the muscle 4 NMJ. *Left* is stained for horseradish peroxidase (HRP, labels neuronal membranes); *right* is stained for nc82/Brp, an active zone marker. c) Image of the FIJI plugin *Drosophila NMJ morphometrics* with the standard settings used in this report. d) Output of the plugin, with the NMJ outline selected, boutons delineated, and active zones marked.

3.2 – Results

3.2.1 - Heterozygous dATM mutants have deficits in NMJ development

The first experiment was to assess the effects of carrying heterozygous mutations in the *tefu* locus (which encodes the *Drosophila* ATM protein, herein referred to as dATM). The three *dATM* mutants in this study originated from an ethyl methane-sulphate (EMS) screen (Silva *et al.*, 2004); $dATM^{-3}$ and $dATM^{-6}$ are both non-conditional, pharate lethal mutants, while $dATM^{-8}$ is a temperature-sensitive hypomorph (Silva *et al.*, 2004). Under this study's laboratory conditions on the standard food recipe, both $dATM^{-3}$ and $dATM^{-6}$ were only ever viable as heterozygous larvae. For $dATM^{-8}$, at lower temperatures (<23°C), homozygous larvae were infrequently present, while the temperature at which the flies are raised for these NMJ experiments (25°C) was non-permissive for this allele. When transheterozygous, these mutants were viable until the pupal stage, where they would then fail to eclose, indicative of pharate lethality.

Allele	**Codon change (position)**	**AA change**	**Domain affected**	**Consequence**
tefu/dATM^{-3}	CAA->TAA (2007)	Q600term	N-terminal	Premature stop, truncated dATM, homozygous lethal
tefu/dATM^{-6}	TGG->TAG (4724)	W1315term	N-terminal	Premature stop, truncated dATM, homozygous lethal
tefu/dATM^{-8}	CTT->TTT (9850)	L2767F	FATC	Very last AA, temperature sensitivity.

Previous studies using the temperature sensitive *dATM*$^{-8}$ allele either as homozygotes (Petersen, Rimkus and Wassarman, 2012) or trans-heterozygotes (Pedersen, Tiong and Campbell, 2010) have demonstrated signs of neurodegeneration in adult flies, such as a rough-eye phenotype or 'holes' in brain sections. However, the neurodevelopmental phenotype of carrying *dATM* mutations has not been studied. Given that A-T is a neurodevelopmental/early-onset neurodegenerative disorder, it therefore made sense to look at the effects of dATM deficiency on the developing larval nervous system.

To test this, males of the *dATM* mutants were crossed to females of the *w*^{1118} "wild-type" control line, the progeny dissected at wandering 3rd instar, and the type Ib NMJ of muscle 4 imaged. In every relevant metric measured by the *Drosophila NMJ morphometrics* FIJI plugin (see *Methods*), i.e., the size of the NMJ, number of active zones, and number of boutons, the *dATM* heterozygous mutant larvae demonstrated a statistically significant reduction compared to the wild-type control line (fig 3.2a-c). Note that all the data is scaled to the mean surface area (MSA) of muscle 4 per genotype. This indicates haploinsufficiency of ATM in the development of the NMJ.

For the "genomic rescue", a 20 kb BAC (the CH322-15C8 clone) containing wild-type *dATM* locus plus approximately 5 kb of upstream sequence and 5 kb of downstream sequence (fig 3.2e) was cloned into the second chromosome into the attP-3B site (VK00037 at 22A3) and crossed into the *dATM*$^{-8}$ mutant background. When trans-heterozygous with the *dATM*$^{-8}$ allele (abbreviated to 15C8; dATM^{-8}/+ on the graph), it produced somewhat of a mixed rescue. NMJ surface area was not significantly different from controls by a Tukey Honest Significant Differences test and was only significantly increased from the *dATM*$^{-3}$*/+* condition but not the

other alleles (fig 3.2a). Bouton count was significantly rescued across all conditions (fig 3.2b), while active zone number was not significantly rescued across any (fig 3.2c).

However, because the above involves a) mutations generated by EMS, which means the flies could carry mutations in other relevant genes, and b) heterozygous mutants, meaning all cell types expressing dATM will likely have reduced protein levels, this result does not necessarily point to a role for dATM in NMJ development; the reduction in NMJ size, whilst not due to reduction in muscle volume, could be due to the consequences of dATM heterozygosity in multiple cell types, and gives no information about the specific role of dATM in the developing larval nervous system.

3.2.3 - Presynaptic ATM is required for normal NMJ development

The NMJ is composed of three distinct compartments: the presynaptic motor-neuron; the postsynaptic muscle cell; and the perisynaptic ensheathing glia. The GAL4-UAS system enables the expression of UAS-promoter-driven constructs in each of these compartments separately using cell-type-specific GAL4 "drivers." GAL4 spatiotemporal specificity is achieved through enhancer trapping using a P-element containing the GAL4 expression construct (Brand and Perrimon, 1993); as an example, the *elav-GAL4* line expresses GAL4 in the same pattern as *elav* expression, i.e., pan-neuronally. These GAL4 lines can then be combined with other lines containing constructs under the control of the UAS-promoter, to which GAL4 binds and activates transcription. This can be used for overexpression e.g., of a cDNA or fluorescent protein, or alternatively to knockdown mRNA levels through RNA interference (RNAi) via expression of a dsRNA complementary to an mRNA of interest.

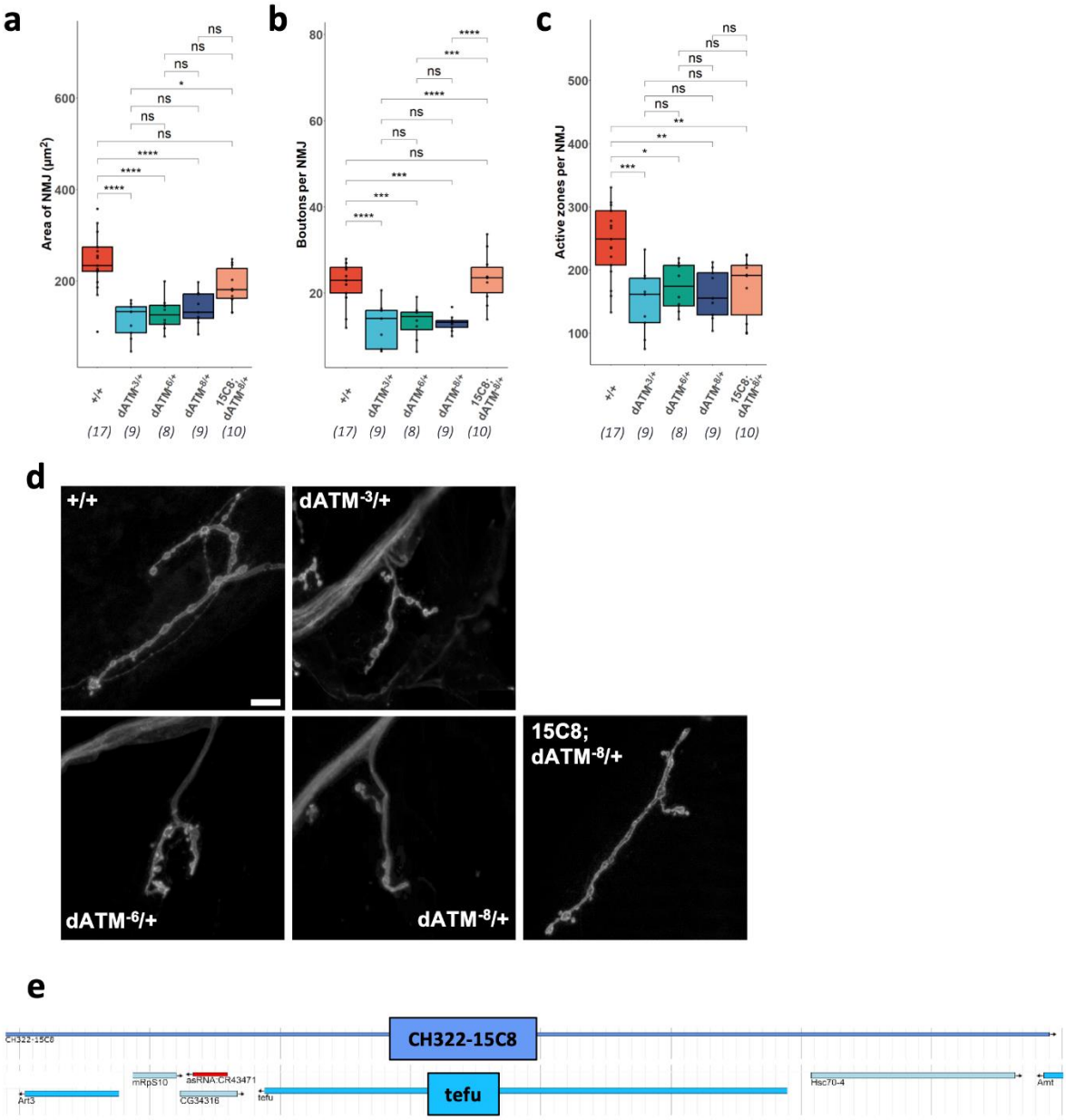

Figure 3.2: *Drosophila* larvae which are heterozygous for loss-of-function mutations in *tefu* (dATM) have smaller neuromuscular junctions (NMJs). Larvae transheterozygous for *dATM* null and wild-type alleles have a reduction in **a**) mean surface area of NMJs, **b**) the number of presynaptic boutons per NMJ, and **c**) the number of active zones per NMJ. All data is scaled to mean muscle surface area for muscle 4. The control group is always to the left of each plot; "genomic rescue" is shown in pink. Shown are adjusted p-values from a one-way ANOVA with Tukey's Honest Significant Differences test for multiple comparisons. p≤0.05 *, p≤0.01 **, p≤0.001 ***, p≤0.0001 ****. N = 9-17 larvae per genotype, each datapoint a mean of the values from the NMJ of the left and right flank of each larva (indicated below genotype labels). **d**) Representative images of muscle 4 NMJs of the indicated genotypes. Anterior = up. Expression of genomic rescue construct rescues gross NMJ anatomy but not active zone count. Scale bar = 10 µm, all images the same scale. **e)** Diagram of 'genomic rescue' BAC with reference to the *tefu* locus (from JBrowse).

To understand further the cell-type specific role of dATM, a screen of knockdowns of dATM in these different compartments during larval NMJ development was performed. Females of different "driver" GAL4 lines were crossed to males of two different *dATM* UAS-dsRNA lines from the *Drosophila Transgenic RNAi Project (TRiP).* The two dATM-targeting RNAi lines used here were TRiP[HMS02790] which contains a short-hairpin dsRNA on the 2nd chromosome, and TRiP[JF01422] which contains a long-hairpin dsRNA located on chromosome 3. The pan-neuronal driver line was *elav-GAL4;UAS-Dcr2*, the glial driver was *repo-GAL4*, and the muscle driver was *mef2-GAL4.* As a control, the drivers were crossed to wild-type w^{1118} males. *UAS-Dcr2* is built into the *elav-GAL4* driver line to improve RNAi efficiency, since *Dicer-2* is required for RNA-induced silencing complex (RISC) formation in the processing of dsRNAs (Lee *et al.*, 2004).

A note on genotype labelling convention in this thesis*: On the x-axis of the graphs in this report, I will use the convention of signifying the GAL4 driver line used (e.g.,* elav *for neurons), then a ">" followed by the genetic construct to indicate what the GAL4 is driving the expression of. For example, "elav > dATM$^{[HMS]}$" indicates that the UAS-dsRNA on the second chromosome targeting tefu (dATM) is being expressed in neurons. The full genotype here would be: elav-gal4/+; UAS-Dcr2/UAS-dATM$^{[HMS02790]}$; +/+. The control is "elav > w^{1118}".*

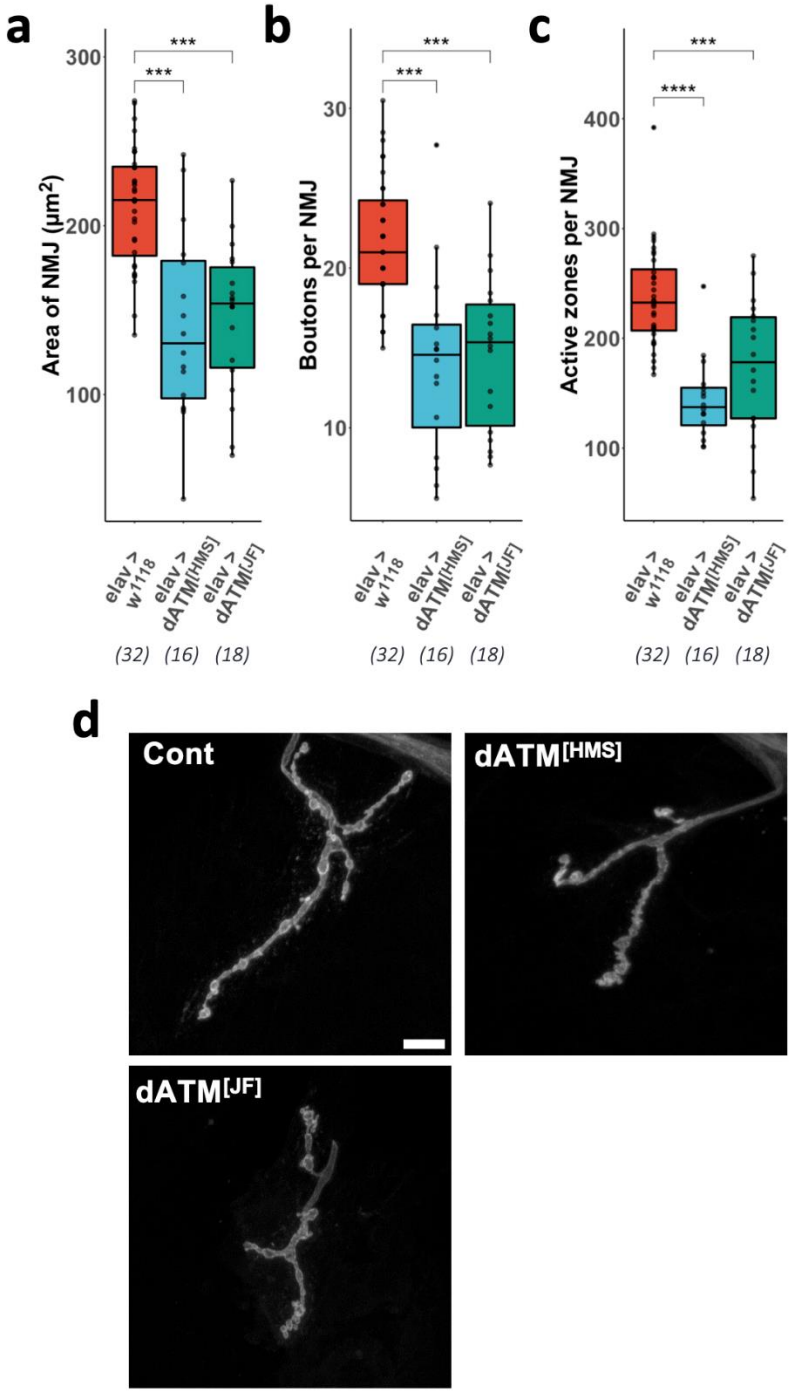

Figure 3.3: Pan-neuronal presynaptic knockdown of dATM through over-expression of dATM shRNA constructs using the *elav-gal4* driver leads to similar deficits in NMJ development as the heterozygous mutants. Knockdown larvae show a reduction in **a**) mean surface area of the NMJ, **b**) bouton count per NMJ, and **c**) number of active zones per NMJ, all scaled to mean surface area of muscle 4. Shown are adjusted p-values from a one-way ANOVA with Dunnett's multiple comparisons test using the *elav > w^{1118}* control as reference. N numbers indicated below genotypes. p≤0.05 *, p≤0.01 **, p≤0.001 ***, p≤0.0001 ****. **d**) Representative images of NMJs from the indicated genotypes. Scale bar = 10 µm. Anterior = up.

Figure 3.3 shows the effects of pan-neuronal knockdown of dATM on the structure of the 3I-NMJ. The effect of neuronal knockdown phenocopied that of carrying *dATM* heterozygous null alleles, with significant reductions in NMJ surface area, bouton number and active zone count, relative to muscle surface area, of both RNAi constructs. In terms of other developmental consequences of neuronal dATM knockdown, it was noted that the 2nd chromosome construct (TRiP[HMS02790]) produced pharate lethality at 25°C, whereas the 3rd chromosome (TRiP[JF01422]) did not. This effect persisted even if expression was confined to motor neurons using the *OK371-GAL4* driver and appeared to be contingent on the level of dsRNA expression; raising the crosses at lower temperatures (<21°C) abrogated the pharate lethality, consistent with a reduction in Gal4 activity at lower temperatures.

By contrast, overexpression of dATM dsRNA with either the pan-glial *repo-GAL4* driver or the muscle *mef2-GAL4* driver did not replicate this effect (figure 3.4a). One caveat of this was that the *repo > w^{1118}* control itself had significant deficits in NMJ development compared to the other GAL4 control lines, which albeit not exacerbated by dATM reduction, make it challenging to draw firm conclusions on the necessity of dATM in glial cells for NMJ development. Figure 3.4b shows the different tissue dATM knockdowns compared to the control line. From this, it is clear that pan-neuronal dATM knockdown is sufficient to phenocopy the effects of *dATM* null heterozygosity while glial and muscular knockdown is not, suggesting a clear presynaptic requirement for dATM during NMJ development.

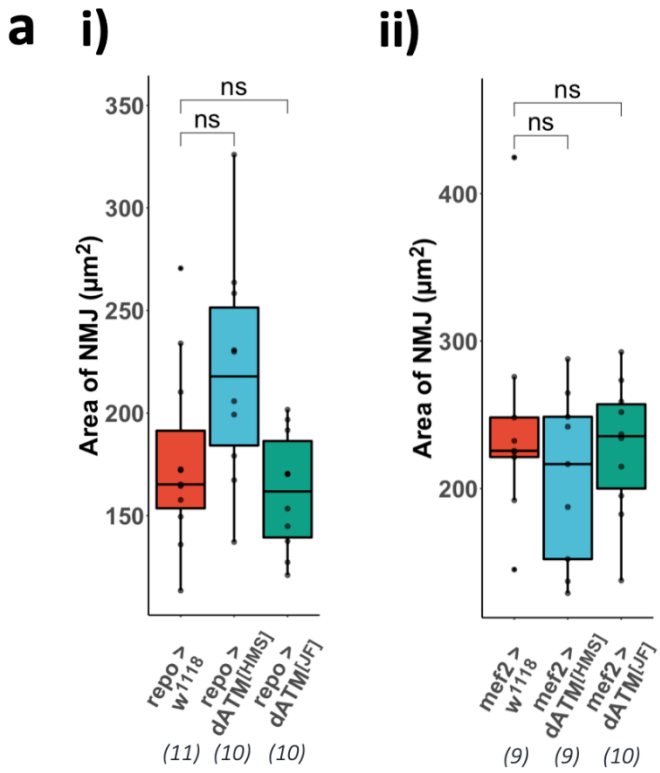

Figure 3.4: A screen of muscle, glial and neuronal dATM knockdown. **a**) Overexpression of dATM shRNA in either **i**) glia (repo-gal4) or **ii**) muscles (mef2-gal4), which represent the peri and postsynaptic compartments of the NMJ, respectively, do not lead to significant alterations in NMJ development. **b**) Summary of results of dATM knockdown in different compartments of the NMJ. **i**) mean surface area of the NMJ, **ii**) bouton count per NMJ, and **iii**) number of active zones per NMJ, all scaled to mean surface area of muscle 4. All p-values are adjusted-p values from a one-way ANOVA with Dunnett's multiple comparisons test using the control as reference. p≤0.05 *, p≤0.01 **, p≤0.001 ***. N numbers indicated below each genotype.

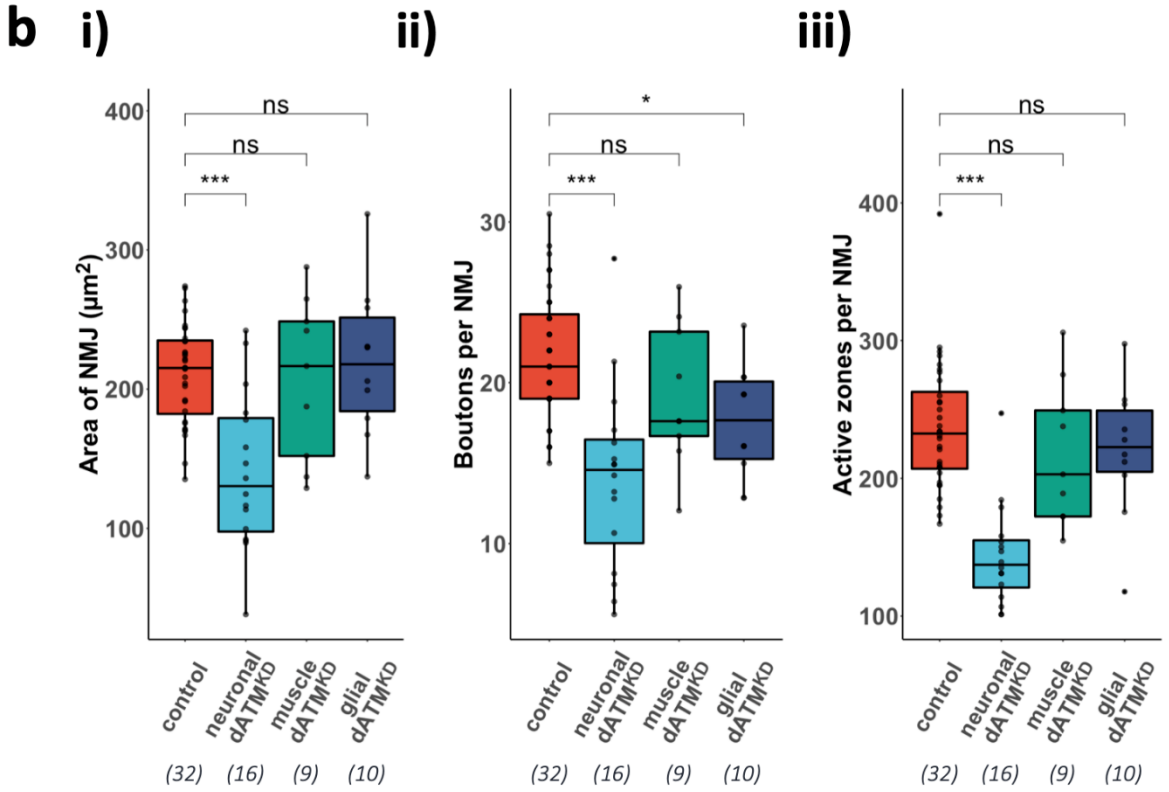

3.2.4 – Knockdown of dATM with different drivers

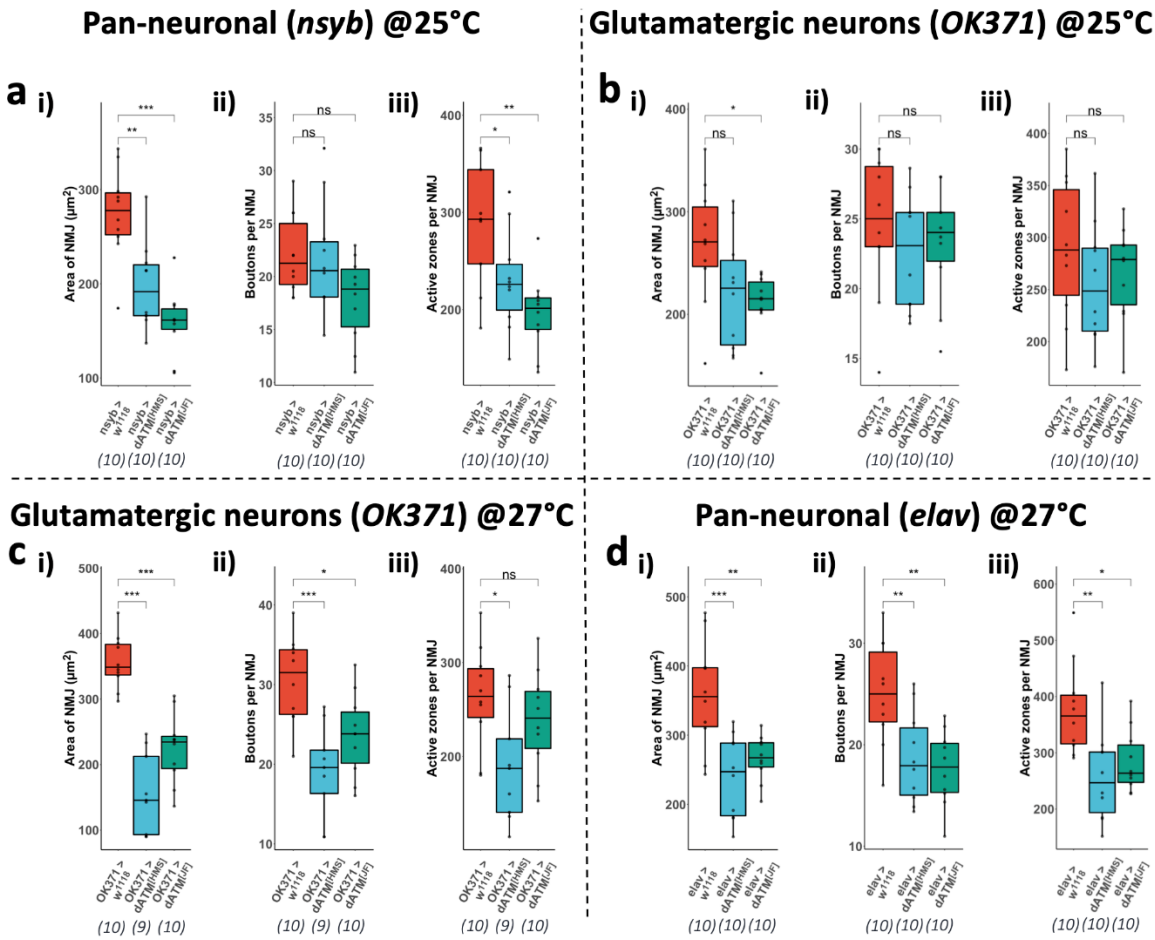

Figure 3.5: Overexpression of the 2 different dATM dsRNA constructs with different neuronal drivers at different temperatures. a) nsyb-GAL4 driver (pan-neuronal) at 25°C; **b)** OK371-GAL4 driver (motor neurons and some interneurons) at 25°C; **c)** OK371-GAL4 driver at 27°C; **d)** elav-GAL4 driver (pan-neuronal) at 27°C. **i)** NMJ surface area, **ii)** number of boutons per NMJ, and **iii)** number of active zones per NMJ, all scaled to muscle 4 surface area. All p-values are adjusted-p values from a one-way ANOVA with Dunnett's multiple comparisons test using the control conditions as reference. p≤0.05 *, p≤0.01 **, p≤0.001 ***. N numbers indicated below each genotype.

To validate that the effect of presynaptic dATM knockdown was not unique to the specific neuronal driver and dATM shRNA combination chosen, the experiments were repeated with two other neuronal drivers, and at different temperatures: one, *nsyb-GAL4*, is pan-neuronal like the *elav-GAL4;UAS-Dcr2* line; the other, *OK371-GAL4*, is a *VGlut* enhancer trap and is thus

expressed in glutamatergic motor-neurons and some interneurons. Fig 3.5 shows the results of these experiments.

For *nsyb-GAL4*, the data were comparable to that of the *elav-GAL4* knockdown at the same temperature, with presynaptic dATM RNAi resulting in significant reductions in the NMJ surface area (fig 3.5a-i) and active zone count (fig 3.5a-iii). By contrast, the bouton number was not significantly reduced with either dsRNA, although the 3rd chromosome construct was close to statistical significance (fig 3.5a-ii).

For *OK371-GAL4,* at 25°C, none of the NMJ metrics reached statistical significance, with the exception of NMJ surface area for the 3rd chromosome dsRNA (fig 3.5b). It was hypothesised that this could be due to one of 2 possible factors: either the effect of presynaptic dATM knockdown was non-cell autonomous, i.e., required dATM levels to be reduced across all neuronal cell types rather than just the presynaptic partners of muscle cells; or the expression of the dsRNA construct from *OK371-GAL4* was reduced compared to the other neuronal drivers. To test the second possibility, the experiment was repeated with the crosses raised at a higher temperature (27°C) as the expression levels of GAL4 is known to be temperature-dependent (Brand, Manoukian and Perrimon, 1994). At higher temperatures, larvae have increased activity levels, and this was reflected in a significant increase in the size of the NMJ in the controls compared to those at 25°C (t-test, $p<0.001$, not shown in figure). By contrast, at these temperatures, the *OK371*-driven dATM dsRNAs lead to significant deficits in NMJ development across all three metrics measured, except for the bouton count of the 3rd chromosome construct (fig 3.5c).

To confirm that the original *elav*-driven dsRNAs behaved in a similar fashion at higher temperatures, this experiment was also repeated at 27°C. Again, the controls significantly

expanded their NMJs compared to those at 25°C (t-test, $p<0.001$, not shown in figure) while in every metric, the dATM knockdowns showed significant deficits in NMJ development (fig 3.5d).

Taken together, despite in some conditions the failure of some of the measurements to reach statistical significance (particularly bouton count), the weight of the evidence suggests that presynaptic knockdown of dATM leads to significant structural deficits in the larval NMJ. This is true even if the knockdown is confined specifically to the presynaptic partners of the muscle cells, the motor neurons.

3.2.5 – The role of presynaptic dATM in neurodevelopment is independent of the DNA damage response

Because of the well-established role of ATM as the "master regulator" of the DNA damage response (DDR) to double-stranded DNA breaks (DSBs), there was the possibility that the NMJ phenotype observed from presynaptic dATM knockdowns was due to a general mis-regulation of the DDR resulting in deficient NMJ development. To test this possibility, a screen of dsRNA-mediated knockdowns to relevant upstream, downstream, and parallel DDR targets was performed. Fig 3.6a shows a simplified summary of the DDR: shown are the parallel single-stranded break response pathway with ATR as its key regulator alongside the DSB response pathway. The MRN complex sits upstream of ATM in the DSB response – therefore to test whether loss of upstream components influences the morphology of the NMJ, the *Drosophila* homologue of one of the components of the MRN complex, dMRE11, was knocked down in neurons using the *elav* driver and a TRiP shRNA construct as above. No significant changes were observed in the area, bouton count, or active zone count of the larval NMJ compared to

controls (fig 3.6b, i-iii, blue) suggesting that inhibition of upstream components of the DDR do not affect larval NMJ development.

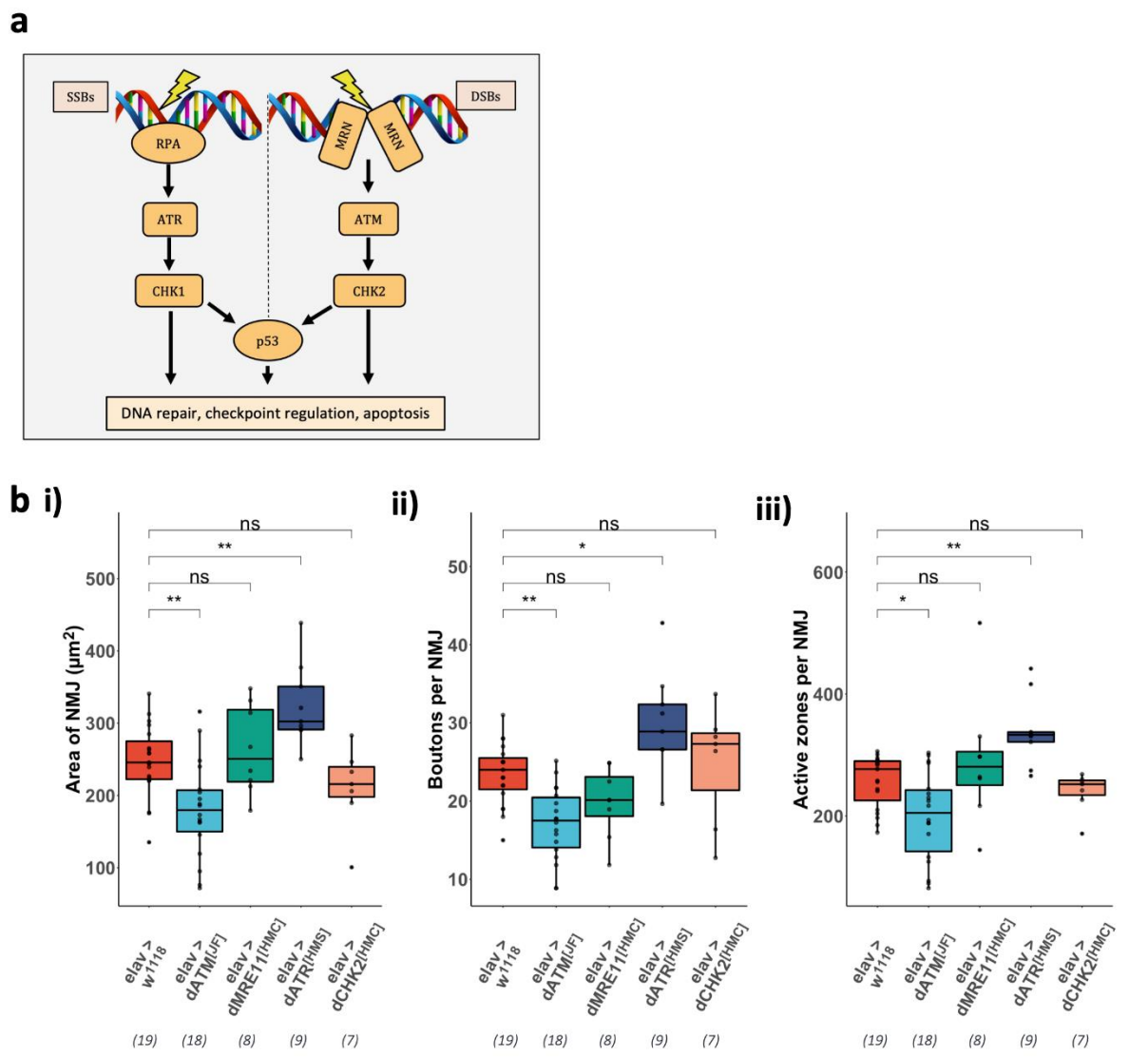

Figure 3.6: Pan-neuronal knockdown of other components of the DNA damage response (DDR). **a)** ATM is the "master regulator" of the DDR to double-strand breaks (DSBs). The upstream MRN complex recruits activated ATM to DSBs, where it phosphorylates downstream targets such as CHK2 to induce cell-cycle arrest and DNA repair. Shown also is the parallel single-strand break response pathway where ATM's sister kinase, ATR, plays a central role. **b)** Quantification of NMJ morphometrics following pan-neuronal RNAi of DDR components at 25°C: **i)** NMJ surface area, **ii)** number of boutons per NMJ, and **iii)** number of active zones per NMJ, all scaled to muscle 4 surface area. Shown are adjusted p-values from a one-way ANOVA with Dunnett's multiple comparisons test using the *elav* > w^{1118} control as reference. p≤0.05 *, p≤0.01 **, p≤0.001 ***. N numbers indicated below each genotype.

Likewise, the effect of knocking down downstream DDR components was tested. This pathway is conserved between *Drosophila* and mammals, with the *Drosophila* homologue of *checkpoint-kinase 2* (dCHK2) phosphorylated by dATM in response to DSBs to coordinate cell-cycle arrest. Pan-neuronal overexpression of a dCHK2 TRiP dsRNA did not significantly alter the morphology of the larval NMJ compared to controls (fig 3.6b, i-iii, yellow). This data implies that the phenotype observed with dATM knockdown is independent of the DDR as neither inhibition of directly upstream nor downstream components is sufficient to replicate the effect.

Since there is some data showing that ATM and its sister kinase, ATR, function together at the synapse in mammals (Li *et al.*, 2009; Cheng *et al.*, 2018), it begged the question of whether knockdown of dATR in neurons would have a similar effect to knockdown of dATM. By contrast, *elav*-driven dATR dsRNA led to a relative increase in the surface area and number of active zones (fig 3.6b-i and-iii respectively, green) compared to the controls, while the bouton count trended to an increase without quite reaching statistical significance (fig 3.6b-ii, green). However, it must be noted that all these metrics are quantified and then scaled to the surface area of muscle 4, the postsynaptic target of these motor neurons. Before scaling, the dATR results were not significantly different from controls but crucially, these larvae had significantly reduced mean muscle 4 surface area for an unknown reason (not shown). Therefore, the apparent overgrowth is relative to the reduced muscle size. While this may suggest an antagonistic role of presynaptic dATR (see *Discussion*), it is likely an artefact of the smaller larval size of this condition.

3.2.6 – The functional requirement of presynaptic dATM – Electrophysiology

The data above demonstrate that presynaptic reduction in dATM levels lead to morphological and structural deficits of the NMJ. To test whether this phenotype translated into functional consequences for neuronal signalling, electrophysiological recordings were taken from the postsynaptic muscle and the resulting miniature (mEJPs) and evoked excitatory junction potentials (EJPs) were quantified (see *Materials and methods*). Briefly, wandering third instar larvae were dissected as before, but maintained in HL3.1 saline without fixing, and the motor neurons transected at the base of the ventral nerve cord. A stimulus was applied via a suction electrode to a specific segmental motor neuron and the voltage change within the corresponding muscle segment recorded. mEJPs were recorded after the acquisition of EJPs by recording from the postsynaptic cell for a few minutes with no stimulation. Muscle resistance was measured from the voltage drop after injection of a -1nA current. Fig 3.7a shows representative traces from these experiments with the HL3.1 Ca^{++} concentration at 1.5 mM.

Figure 3.7: Example traces from electrophysiology experiments. a) Representative traces of the evoked EJP trains of the 3 genotypes tested, at 25°C in 1.5 mM Ca^{++}. **b)** Example of a paired-pulse stimulus, where the stimuli are separated by 100 ms. Note the stimulus artefacts preceding the evoked EJPs.

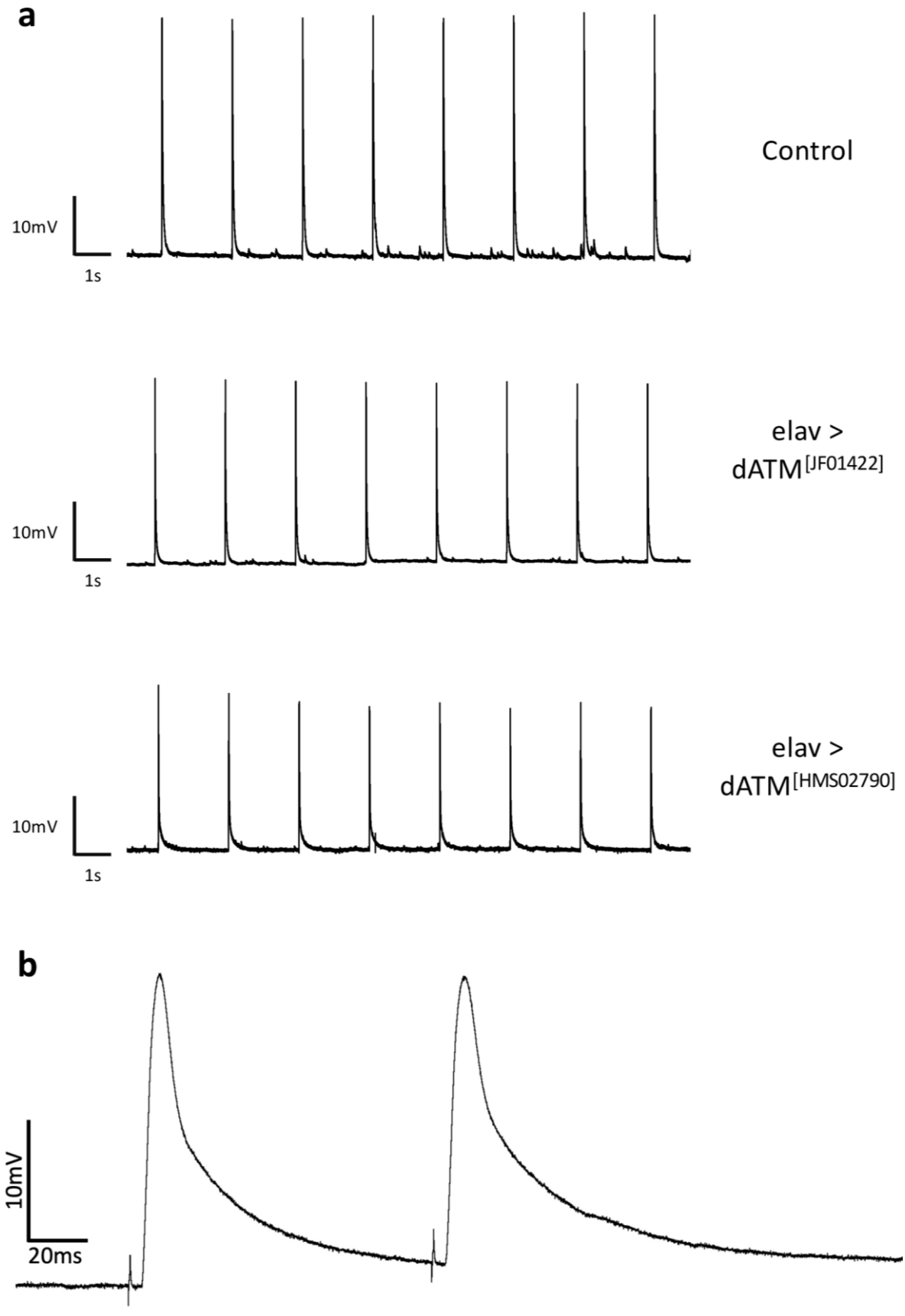
a
Control
10mV
1s
elav >
dATM[JF01422]
10mV
1s
elav >
dATM[HMS02790]
10mV
1s
b
10mV
20ms

For 1.5 mM Ca^{++} at 25°C, control larvae produced EJPs with a mean amplitude of 30.88 mV (SD=2.91 mV, N=11 larvae). The mean mEJP frequency of controls was 1.61 Hz (SD=0.84 Hz, N=11 larvae) while their amplitudes had a mean of 0.62 mV (SD=0.15 mV, N=11 larvae). This is consistent with other published *Drosophila* 3rd instar electrophysiology data (Zhang and Stewart, 2010a; Bykhovskaia and Vasin, 2017). Presynaptic knockdown of dATM using either the 2nd or 3rd chromosome RNAi constructs (TRiP[HMS02790] and TRiP[JF01422], respectively) resulted in a statistically significant decrease in the amplitudes of evoked EJPs (means of 19.07 mV and 27.05 mV, SDs=0.44 mV and 0.60 mV, respectively, fig 3.8a). The 2nd chromosome RNAi showed a strikingly stronger phenotype than the 3rd chromosome RNAi, which was unexpected given the comparatively similar results seen in the morphological experiments (fig 3.3). Similarly, this RNAi resulted in a significant reduction in mEJP amplitude (mean=0.44 mV, SD=0.10 mV), while the 3rd chromosome RNAi did not (mean=0.60 mV, SD=0.09 mV, fig 3.8b). Despite this, no significant changes in mEJP frequency (fig 3.8c) or quantal content (fig 3.8d) were observed.

The selection criteria for the experiments excluded any recordings from muscle fibres with resistances lower than 4 MΩ. However, because of the positive relationship between muscle resistance and the voltage response of the muscle cell, it was important to quantify any differences in muscle resistance across the tested genotypes to determine whether this was a factor in the observed changed in EJP amplitude. No significant difference in muscle resistance was detected across the different genotypes (fig 3.8e), suggesting that this played no role in the reduction of evoked EJP amplitude seen in the presynaptic dATM knockdown condition.

ATM has been shown elsewhere to be required in various forms of synaptic plasticity. One measure of short-term plasticity in *Drosophila* larval electrophysiology is the paired-pulse ratio (PPR), which is the difference in evoked EJP amplitudes in response to a pair of equally sized stimulations separated by a defined duration (see fig 3.7b for an example trace). The valence of this ratio is dependent on the concentration of Ca^{++} in the saline, as the evoked EJP amplitude is Ca^{++} dependent. At lower Ca^{++} concentrations, the second pulse is usually greater in amplitude than the first because of facilitation, whereby the second stimulus arrives at the synapse in a context of increased Ca^{++} concentration due to the first stimulus. Neurotransmitter release from the presynaptic bouton is positively correlated with calcium concentration; therefore, more neurotransmitter is released after the second stimulus and thus the postsynaptic response is greater. By contrast, at higher Ca^{++} concentrations, more neurotransmitter is released after the first stimulus than before and thus the pool of readily releasable vesicles is depleted, leading to a reduced response to the second stimulus (Hallermann, Heckmann and Kittel, 2010).

Fig 3.8f shows the results of paired-pulse experiments at high Ca^{++} concentrations (1.5 mM), with all PPRs scaled relative to the mean value of the PPR of the controls for ease of comparison. At this Ca^{++} concentration, a paired-pulse will usually produce a small depression in the response to the second stimulus, leading to a PPR of <1. While the controls and dATM knockdown larvae all show paired-pulse depression with PPRs <1 (not shown), the 2nd chromosome RNAi shows a significant increase in relative PPR compared to the controls, while the 3rd chromosome RNAi trends towards an increase (p.adj = 0.199).

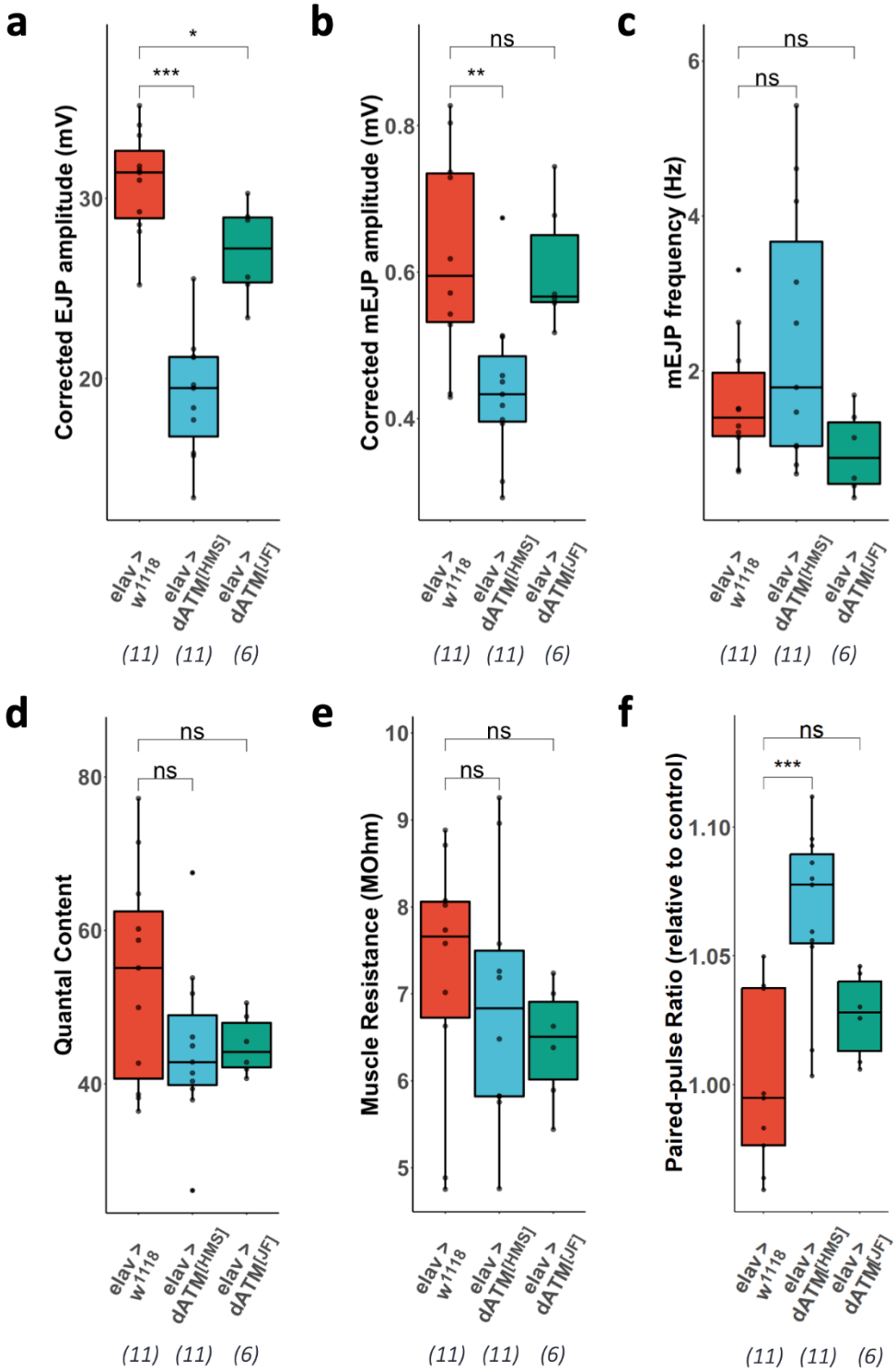

Figure 3.8: Quantification of electrophysiological properties of control vs pan-neuronal dATM knockdowns. a) Corrected evoked EJP amplitude; **b)** corrected mEJP amplitude; **c)** mEJP frequency; **d)** Quantal content (EJP/mEJP amplitudes); **e)** muscle resistance; **f)** paired-pulse ratio (relative to control). Shown are adjusted p-values from a one-way ANOVA with Dunnett's multiple comparisons test using the *elav > w^{1118}* control as reference. p≤0.05 *, p≤0.01 **, p≤0.001 ***. N=6-11 larvae per genotype, with 1-3 recordings from each larva averaged to give the displayed larval means. N numbers indicated below each genotype.

3.2.7 – The functional requirement of presynaptic dATM – Larval locomotion

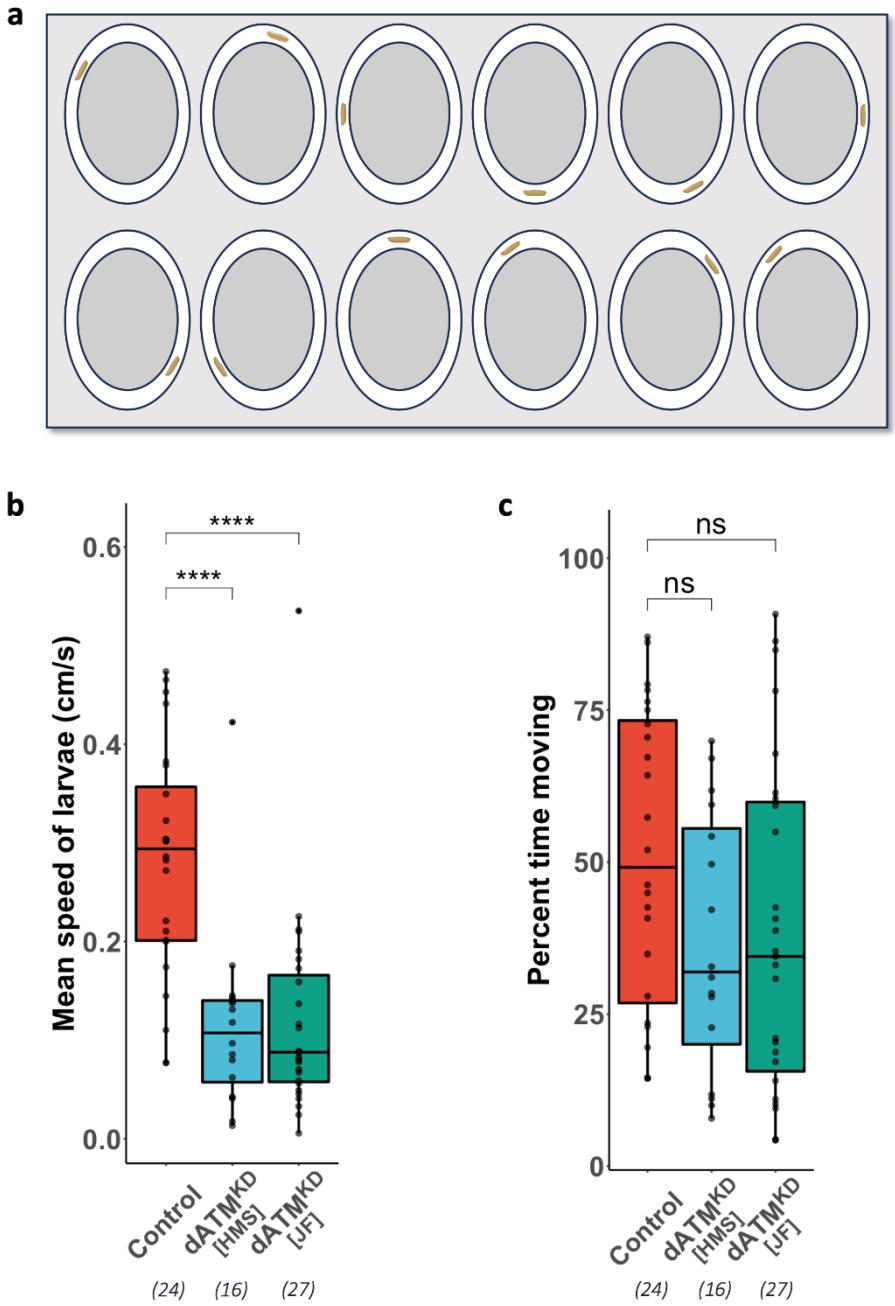

Figure 3.9: Presynaptic dATM knockdown negatively affects larval locomotor function. a) Schematic of larval tracking set-up. Larvae are individually placed into a 3D-printed arena with oval-shaped cut-outs lined with 2% agarose. Larval locomotion is tracked from above by a webcam and metrics such speed **(b)** and percentage time spent moving **(c)** are output. Shown is quantification of control vs glutamatergic dATM knockdown using *OK371-GAL4* at 27°C and the 2 different dsRNA constructs. All adjusted p-values are from Wilcox tests with the Holm-Bonferroni correction using the control as reference. p≤0.05 *, p≤0.01 **, p≤0.001 ***, p≤0.0001 ****. N=16-34 larvae per genotype. Locomotion experiments performed by D.P Bennett, S.A Ahmed and E Badenoch. N numbers indicated below each genotype.

In addition to electrophysiology, another assessment of neuronal function is larval locomotion. As shown above, confining knockdown of ATM to glutamatergic neurons using the OK371 driver is sufficient to induce NMJ structural deficits when the larvae are raised at 27°C. Given that motor neuron signalling to body wall muscles controls peristaltic movement, it stands to reason than any neurophysiological change in those neurons will be reflected in changes to locomotion.

To test this, larvae were tracked on an in-house larval locomotion monitoring platform, a schematic of which is shown in fig 3.9a (see *Materials and methods*). Briefly, individual wandering third instar larvae were placed into a 3D-printed "racetrack" arena containing 2% agarose coloured with a small amount of Orange-G dye. Larvae were allowed to freely crawl around the arena while their movement was tracked using EthovisionXT software, and metrics such as mean/median/max speed and percentage time moving were output.

Figure 3.9b summarises the results of an experiment using the OK371 driver at 27°C. Control larvae (*OK371-GAL4/+*) had a mean speed of 0.281 cm/s (SD=0.118 cm/s, N=23), while dATM knockdown larvae (*OK371-GAL4/dATM*$^{[HMS02790]}$ and *OK371-GAL4/+; dATM*$^{[JF01422]}$) were significantly slower, with a mean speed of 0.116 cm/s (SD=0.0956 cm/s, N=17) and 0.119 cm/s (SD=0104 cm/s, N=26), respectively. There was no statistically significant change in the percentage time spent moving between the three conditions. This result suggests that the structural and electrophysiological deficits seen with presynaptic dATM knockdown correlate with functional deficits in larval locomotion.

3.2.8 – The effect of temperature on locomotion and NMJ structural phenotypes

Neuronal activity has been established as a key factor in shaping the development of structural connectivity and plasticity in developing nervous systems, and the larval neuromuscular system is no exception. Given that *Drosophila* are poikilotherms, their developmental timing, ageing and activity levels are significantly influenced by external temperature. An increase in temperature abbreviates their developmental timeframe and increases their mobility, which is observable in both larval and adult stages. Consequently, there is an increase in neuronal activity with increased temperature. Because motor-neuronal knockdown of dATM failed to produce a structural phenotype at 25°C but produced a clear phenotype at 27°C, it was presumed that this could relate to one of two possibilities: either expression of the dsRNA is lower at 25°C than 27°C so the relative level of dATM knockdown is lower; or the level of neuronal activity influences the dATM knockdown phenotype.

To test the interaction between temperature and the consequences of presynaptic dATM knockdown, the *OK371-GAL4* experiment was repeated independently at 4 different rearing temperatures ranging from 19°C to 30°C, throughout embryonic and larval development. (Preliminary experiments indicated that raising crosses of control experiments consistently at temperatures of ≥32°C was severely detrimental to egg laying and larval survival). At each temperature, larval locomotion was tracked, and subsequent dissections were performed to quantify the structural phenotype of the NMJ. Figure 3.10 summarises these results.

For the controls, there was a 38.4% increase in mean crawling speed from 19°C (mean=0.203 cm/s, SD=0.145 cm/s) to 27°C (mean=0.281 cm/s, SD=0.118 cm/s). However,

this increase did not reach statistical significance when evaluated using a Tukey Honest Significant Differences test (p.adj=0.121). There was also a suggestive trend that increasing developmental temperature to 30°C had a detrimental impact on crawling speed with a 31% decrease compared to the 27°C group (mean=0.195 cm/s, SD=0.118 cm/s) but this similarly did not reach statistical significance. (Again, preliminary experiments supported this trend, indicating that a developmental temperature of 32°C negatively influenced the locomotor performance of the controls). For the dATM knockdown, the larvae showed poor performance at 19°C, and there were no statistically significant increases in motility as the temperature was elevated from 19°C to other tested temperatures except for 30°C (p.adj = 0.00162). By contrast, at 19°C and 27°C, there was a significant degradation of larval locomotion in the dATM knockdown group compared to the control, while in all except 19°C, there was no significant difference in the percentage time the larvae spent moving during the experiment (fig 3.10a ii).

The NMJ structural data is summarised in fig 3.10b. Notably, increasing developmental temperature from 19°C to 27°C resulted in a statistically significant 56% increase in NMJ surface area in the control group (Tukey, p.adj=1.51×10^{-7}). However, an increase in temperature beyond 27°C to 30°C resulted in a notable decrease in the NMJ surface area for the same group (Tukey, p.adj=0.00486). For the dATM knockdown larvae, there was a detectable increase in NMJ surface area as the developmental rearing temperature was raised from 19°C to 25°C (Tukey, p.adj=0.0434). Intriguingly, beyond this temperature range, the NMJ surface area remained stable, showing no significant changes at higher rearing temperatures. When compared to the control group, the dATM knockdown group exhibited a significant decrease in NMJ surface contact area (when scaled to muscle size) at all

temperatures, except at 25°C. This trend appeared to closely correspond with the locomotion data. With respect to bouton and active zone counts, a similar trend was observed. However, the variability of the data of these two other metrics resulted in fewer results reaching statistical significance. Of note, while bouton count for the controls significantly increased as rearing temperature was raised from 19°C to 27°C, bouton count was unchanged for dATM knockdowns across all rearing temperatures. Conversely, active zone number decreased in the controls from 19°C to 30°C but remained stable in the dATM knockdowns. Taken together, this evidence suggests that knockdown of dATM in glutamatergic neurons results in an overall block to temperature-regulated NMJ structural plasticity.

3.2.9 – Neurodegeneration of posterior motor neurons at higher temperatures

One question that remained from the structural and functional phenotype of presynaptic dATM knockdown was whether the effect was neurodevelopmental or neurodegenerative. Was the decrease synapse size and bouton count the result of failing to properly expand through development, or were these neurons vulnerable and degenerating? At higher developmental temperatures (≥27°C), it was notable that neuronal knockdown of dATM lead to pharate lethality, even if knockdown was confined to motor neurons, which potentially suggests that the 3rd instar model is on the threshold of degeneration. In addition, at these temperatures, posterior motor neurons (segment A7) of the dATM knockdown larvae showed significant “thinning out” compared to those of controls (see fig 3.11a for examples).

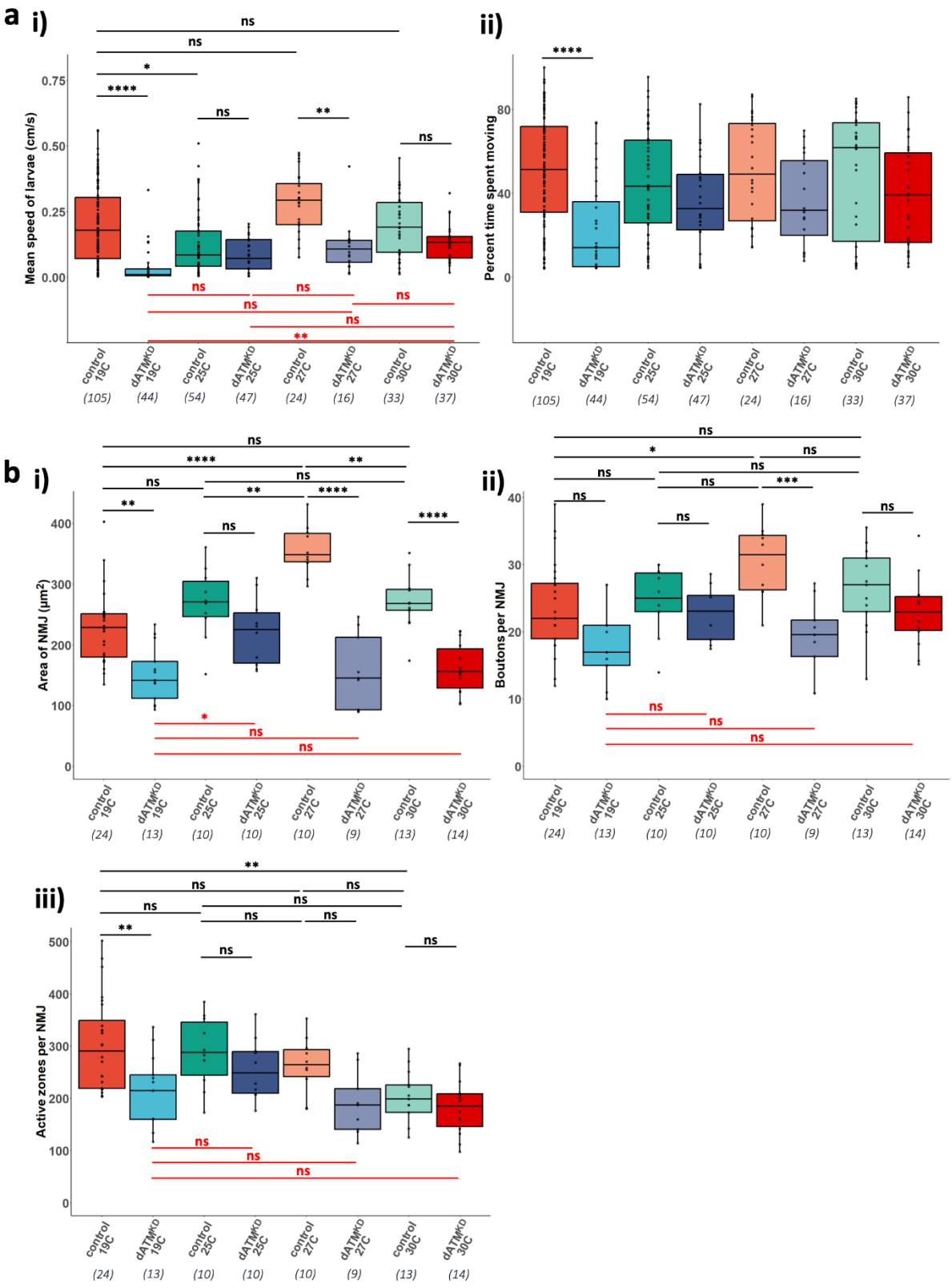
a
i)
ii)
Mean speed of larvae (cm/s)
Percent time spent moving
b
i)
ii)
iii)
Area of NMJ (µm²)
Boutons per NMJ
Active zones per NMJ
control 19C
dATMKD 19C
control 25C
dATMKD 25C
control 27C
dATMKD 27C
control 30C
dATMKD 30C
(105) (44) (54) (47) (24) (16) (33) (37)
(24) (13) (10) (10) (10) (9) (13) (14)
ns
*
**
***
****

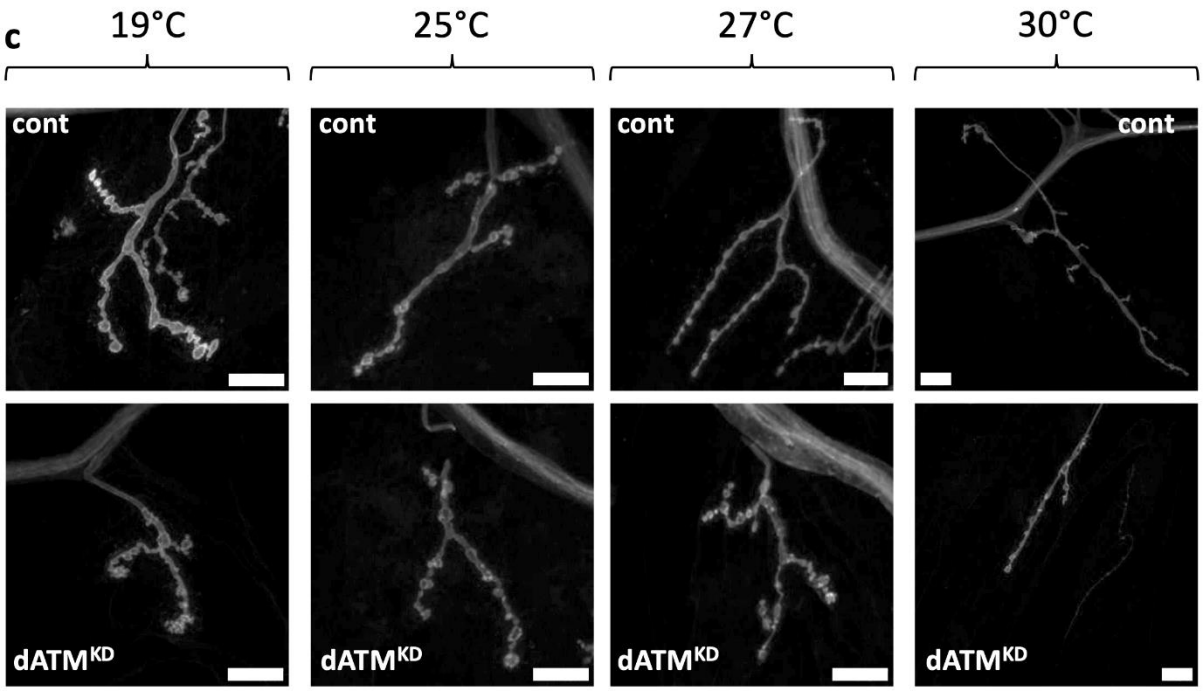

Figure 3.10: Quantification of the effect of developmental temperature on the locomotion and structural phenotypes of control vs motor-neuronal dATM knockdown. The driver line in all these conditions was *OK371-GAL4,* the dATM dsRNA was the 2nd chromosome construct, and the crosses were maintained at the indicated temperatures. **a) i)** Mean larval crawling speed and **ii)** percentage time spent moving when reared at the different indicated temperatures; **b)** NMJ morphometrics at different temperatures: **i)** area, **ii)** bouton count and **iii)** active zone count). All p-values are from Tukey HSD or Dunn's tests, depending on whether the data were significantly non-normal, as determined by Shapiro-Wilk normality testing. p≤0.05 *, p≤0.01 **, p≤0.001 ***, p≤0.0001 ****. N=8-16 larvae per genotype. N numbers indicated below each genotype. **c)** Representative images of muscle 4 NMJs from the indicated genotypes at the different temperatures. Scale bars = 15 µm. Anterior = up. Locomotion experiments performed by D.P Bennett, S.A Ahmed and E Badenoch.

An indication of neurodegeneration in the third instar larval model is the presynaptic membrane withdrawing from the postsynaptic density, which can be observed by a loss of presynaptic (HRP) staining from within regions of postsynaptic (DLG) staining, leaving synaptic "footprints" (Koch *et al.*, 2008). To test whether this was occurring, dATM dsRNA was again expressed either pan-neuronally (*elav-GAL4*) or in glutamatergic neurons (*OK371-GAL4*) at a rearing temperature of 27°C, wandering 3rd instar larvae dissected and co-stained with HRP and DLG, and their motor neurons imaged. While there were no obvious areas of DLG staining that completely lacked HRP signal, there was a clear difference in the intensity of HRP staining

compared to control larvae (fig 3.11b i). This was quantified in FIJI by using the HRP channel and thresholding to create a region of interest at the NMJ, calculating the average intensity of the HRP and DLG signal, and then from this calculating the ratio of the two. A decrease in the ratio of HRP to DLG signal would indicate loss of presynaptic structures from the end-plate. Both pan-neuronal (fig 3.11b ii) and motor neuronal (fig 3.11b iii) knockdown of dATM resulted in a significant decrease of the HRP to DLG ratio in neurons in segment A7, which is potentially an early indication of neurodegeneration.

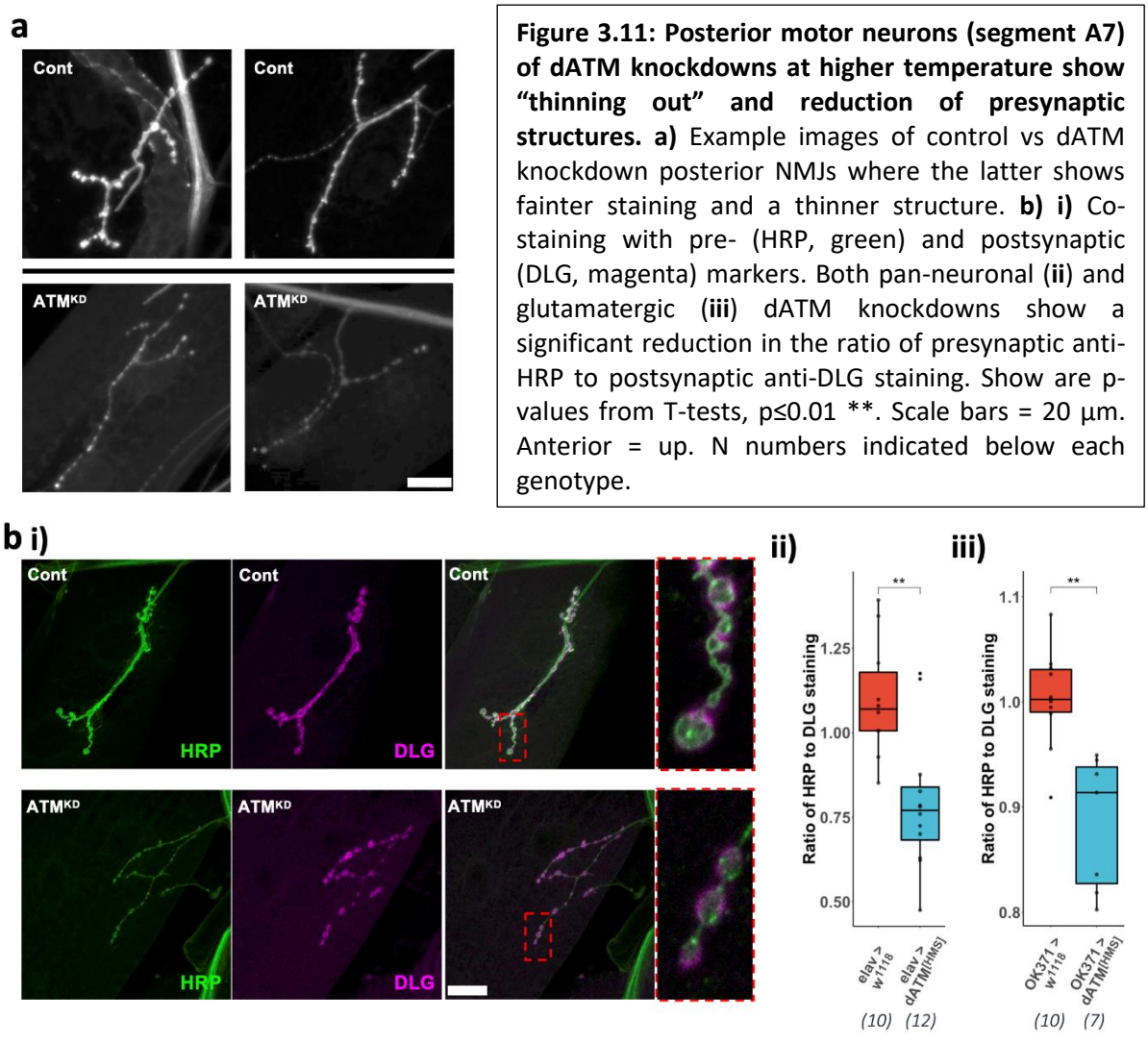

Figure 3.11: Posterior motor neurons (segment A7) of dATM knockdowns at higher temperature show "thinning out" and reduction of presynaptic structures. a) Example images of control vs dATM knockdown posterior NMJs where the latter shows fainter staining and a thinner structure. **b) i)** Co-staining with pre- (HRP, green) and postsynaptic (DLG, magenta) markers. Both pan-neuronal (**ii**) and glutamatergic (**iii**) dATM knockdowns show a significant reduction in the ratio of presynaptic anti-HRP to postsynaptic anti-DLG staining. Show are p-values from T-tests, p≤0.01 **. Scale bars = 20 µm. Anterior = up. N numbers indicated below each genotype.

3.2.10 – Detection of apoptosis using GC3Ai

If neurodegeneration is occurring, then one possible mechanism for this would be via apoptosis, which involves the upregulation of caspase activity. Various tools are available in *Drosophila* for monitoring changes in caspase activity, one of which is the GC3Ai system (Zhang *et al.*, 2013; Schott *et al.*, 2017). Briefly, this system involves expression of GFP molecules that contain a DEVD caspase cleavage site linking the C- and N-termini. In the absence of caspase activity, this linker remains intact and GFP fluorescence is quenched, but the protein is still amenable to antibody staining for localisation purposes. Upon caspase cleavage, the linker is removed and GFP fluorescence restored.

This system was therefore utilised to test for caspase activity within neurons where dATM had been knocked down. The *UAS-GC3Ai* construct was combined with the *OK371-GAL4* driver to give motor neuronal expression of the reporter, and this line was then crossed to the different dATM dsRNA constructs to assess the level of caspase activity. Larvae were dissected as for the NMJ dissections leaving the CNS in the preparation and stained for GFP. The immunofluorescent (αGFP) signal was used to mark the expression pattern of the GC3Ai reporter, and it matched what would be expected from the *OK371* driver (figure 3.12a). Caspase activity within cells was detected from the endogenous fluorescence of the GFP reporter, and the number of GC3Ai-positive cells per ventral nerve cord (VNC) were quantified. As a positive control, larvae were irradiated with a dose of 8 Gy of X-ray radiation, and this produced a significant increase in endogenous GFP signal within αGFP-positive cells (figure 3.12a second row, and 3.12b).

Both dsRNA constructs to dATM were tested, and GC3Ai-positive cells were observed in both conditions. However, only the dATM[HMS02790] dsRNA was significantly different from the control (fig 3.12b). Intriguingly, in some of the posterior neurons of the dATM knockdown larvae, endogenous GC3Ai fluorescence was faintly detectable within boutons (fig 3.12c and c'), implying local caspase activity which may be a further indication of early signs of neurodegeneration. Overexpression of the temperature-activated cation channel, TrpA1, was also tested, but this did not produce any change in caspase activity compared to controls (fig 3.12a bottom row, and 3.12b), which suggests that hyperactivating neurons alone is not sufficient to drive the cells into apoptosis. Altogether, these data give an indication that, at least at higher temperatures, dATM knockdown sensitises neurons to degeneration.

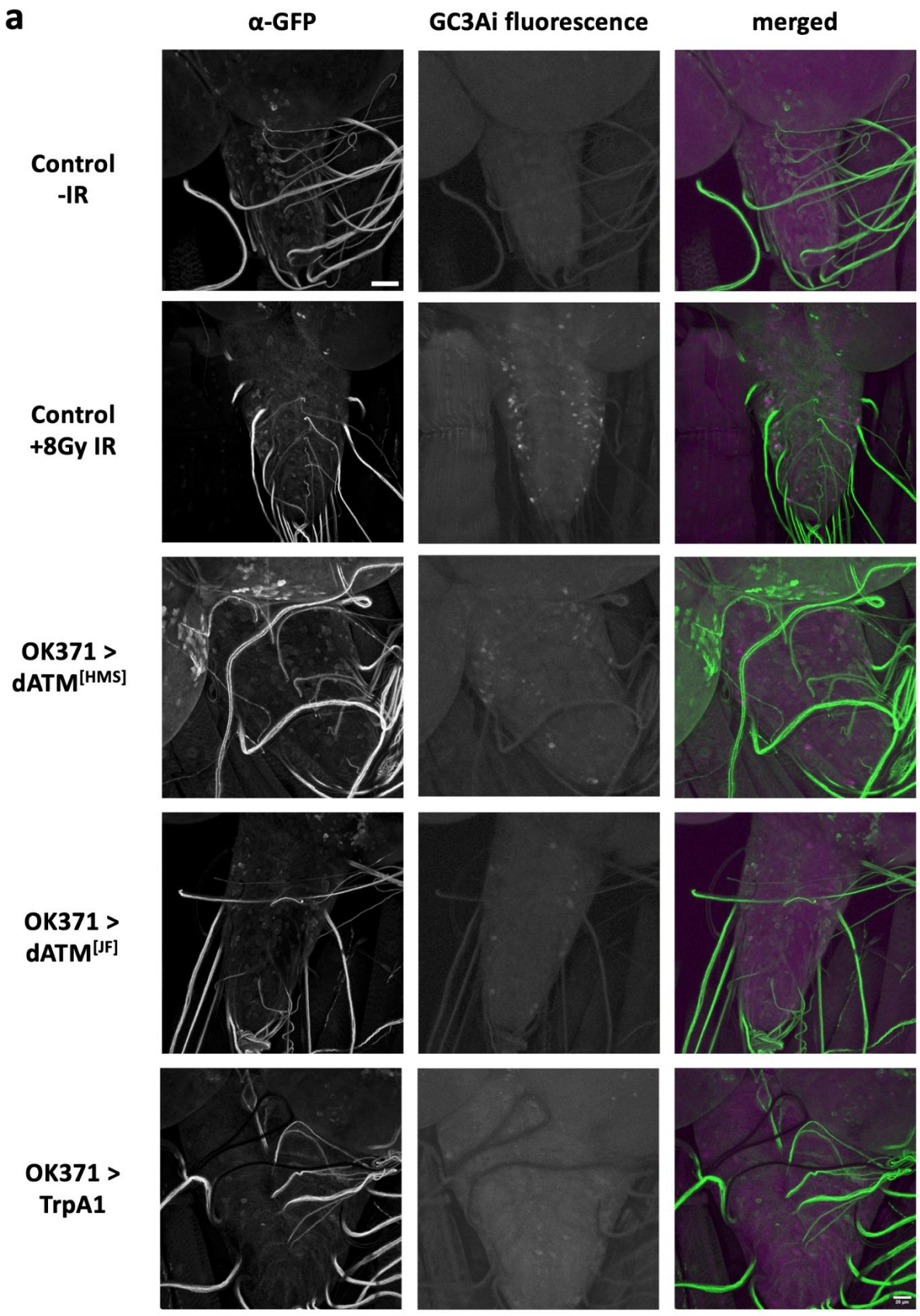
a
α-GFP
GC3Ai fluorescence
merged
Control
-IR
Control
+8Gy IR
OK371 >
dATM[HMS]
OK371 >
dATM[JF]
OK371 >
TrpA1

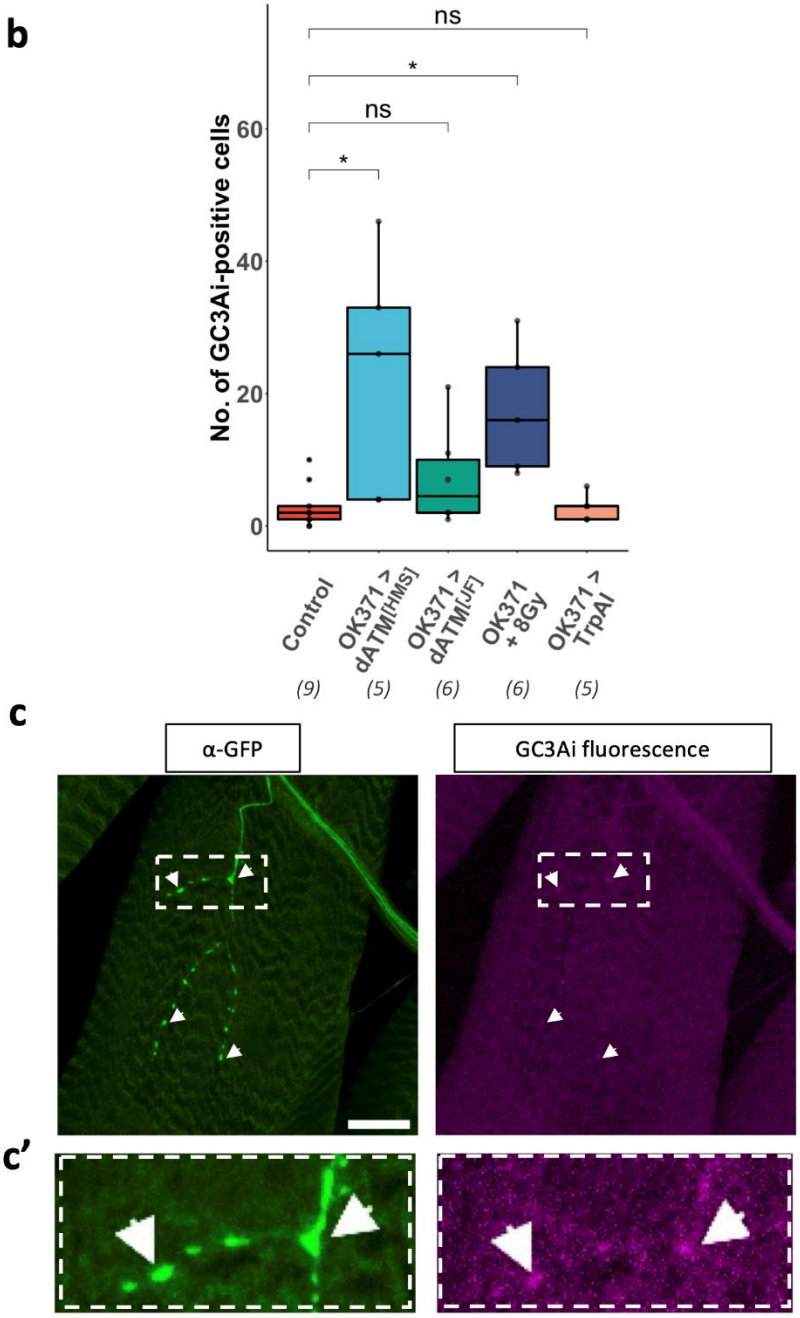

Figure 3.12: Using GC3Ai to detect caspase activity. a) Representative images of the different experimental conditions. The α-GFP column is the signal from immunolabelled GFP with an Alexa-594 secondary antibody, which will detect both active and inactive GC3Ai. The second column is the endogenous GC3Ai fluorescence, which will only occur in the presence of caspase activity. The final column shows the two merged, with α-GFP in green and endogenous GC3Ai in magenta. Scale bar = 30 µm. **b)** Quantification of the number of active GC3Ai positive cells per VNC in the different conditions. N numbers indicated below each genotype. Adjusted p-values are from Wilcox tests with the Holm-Bonferroni correction, p≤0.05 *. **c)** Example image of local GC3Ai fluorescence within synaptic boutons of dATM knockdown larvae, α-GFP in green and endogenous GC3Ai in magenta. Arrows and inset (**c'**) show foci of GC3Ai expression, some of which is endogenously fluorescent, indicating caspase activity. Scale bar = 20 µm. Anterior = up.

3.2.11 – Exploring the role of dATM in short-term structural plasticity

The block in long-term temperature-regulated NMJ structural plasticity seen as a result of presynaptic dATM knockdown begs the question as to whether dATM also has a role in shorter term structural plasticity induced by acute changes in temperature or neuronal activity. Upon hyperstimulation, the larval NMJ can undergo structural changes such as the addition of new boutons. This is achieved by budding or division of existing boutons, or the formation of new boutons *de novo* between existing boutons (Zito *et al.*, 1999). By co-staining for pre (HRP) and postsynaptic (DLG) markers, nascent "satellite" boutons can be detected by the presence of a HRP stain without DLG. This indicates that when the NMJ is undergoing short-term structural plasticity, first the presynaptic membrane "blebs" into a new process and then the postsynaptic density forms around it. If presynaptic dATM knockdown prevents the expansion of synapses when developmental temperature is increased, then perhaps these neurons would also fail to adapt structurally to short-term hyperstimulation.

Various techniques have been employed to induce structural plasticity of the *Drosophila* NMJ, which were evaluated in a study by Bruno Marie's lab (Maldonado-Díaz, Vazquez and Marie, 2021). The first method is achieved through K^+ "pulses", where intact NMJ preps are incubated sequentially in HL3.1 saline containing high and low concentrations of K^+. High K^+ in the extracellular media will depolarise neurons, causing them to fire tonically. The crucial step is to space these depolarisations apart with sufficient recovery time in-between. 5-6 depolarisations with increasing recovery time between each, using 90 mM K^+ for the high K^+ environment and 5mM K^+ for the low K^+ condition, has been shown to lead to the formation

of new boutons which eventually become specialised and filled with active zones (Ataman *et al.*, 2008; Vasin *et al.*, 2019).

Following the protocol outline in Maldonado-Diaz et al., 2021, w^{1118} control larvae were dissected and stimulated with bursts of high K^+ to induce structural plasticity (see *Materials and methods*), fixed and stained for HRP and DLG, and then imaged on a confocal microscope. In that study, stimulation resulted in an increase from a mean of ~1 nascent bouton per NMJ, to ~8, and they defined nascent boutons as those completely lacking postsynaptic DLG staining. Figure 3.13 shows representative images from muscle 6/7 of stimulated (b-c) and unstimulated (d) larvae, and muscle 4 of stimulated (e) and unstimulated (f) larvae. In these experiments, stimulation would produce a few boutons that appeared as if they were blebbing off from larger boutons. For example, in fig 3.13b in both insets, there are smaller boutons (marked with white arrowheads) that are growing out of a larger one, however there is faint DLG staining surrounding them, so it is unclear whether these are truly nascent boutons or have already become specialised. There were some, as indicated by fig 3.13c and its insets, where nascent boutons without DLG staining were apparent, but these were much less frequent than reported in the cited literature. Unstimulated neurons on muscle 6/7 did not show any evidence of nascent bouton formation (fig 3.13d).

As for muscle 4, stimulation with high K^+ produced a striking increase in the accumulation of small foci of extra-synaptic HRP staining (fig 3.13e, left panel). While it has been reported that fixation destroys the “stems” between nascent boutons and the NMJ (Maldonado-Díaz, Vazquez and Marie, 2021), this more closely resembles synaptic “debris” which has been shown to be shed from motor-neurons in an activity-dependent fashion (Fuentes-Medel *et al.*, 2009). This is supported by the fact that the unstimulated motor

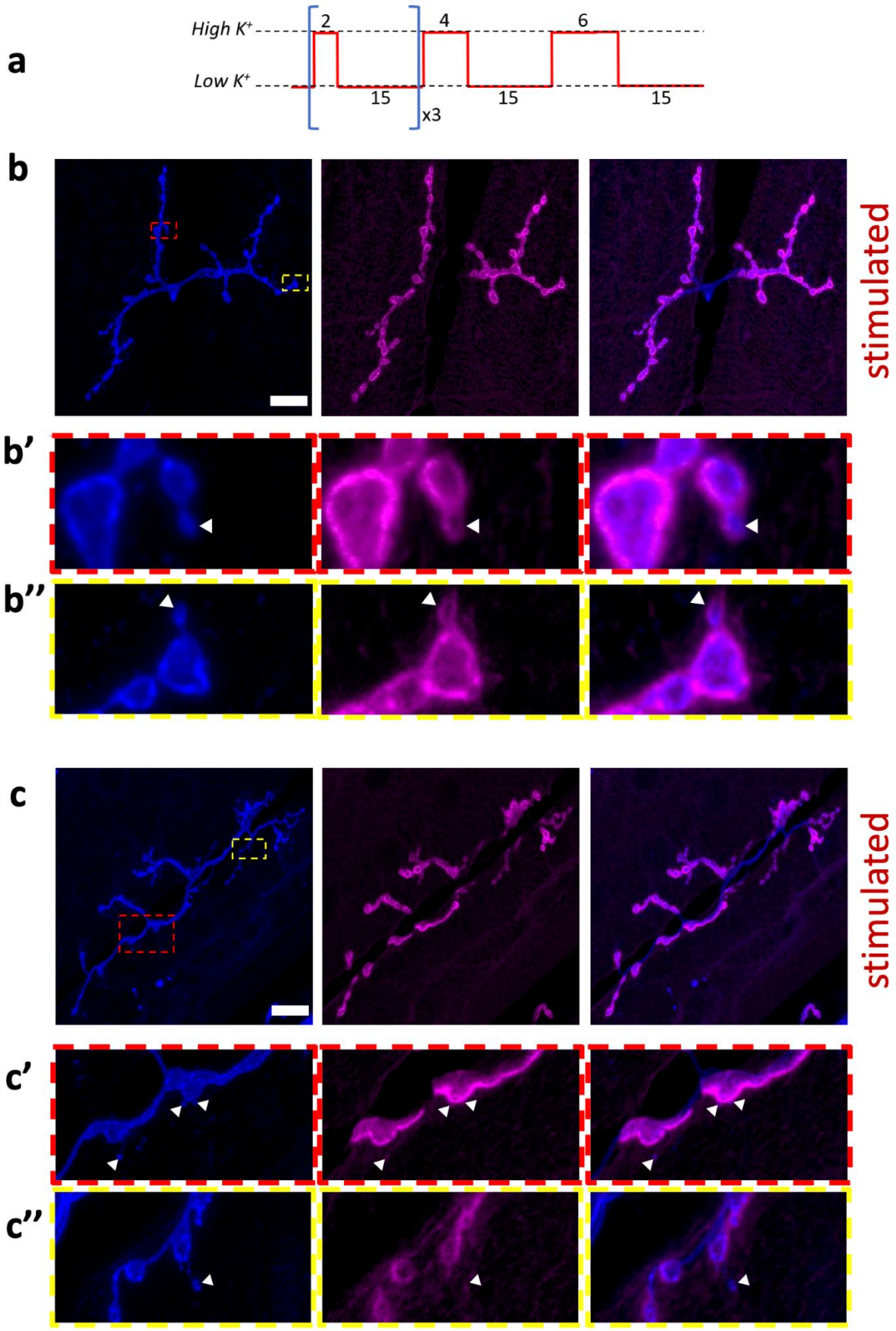
a
High K+
Low K+
2
4
6
15
15
15
x3
b
stimulated
b'
b''
c
stimulated
c'
c''

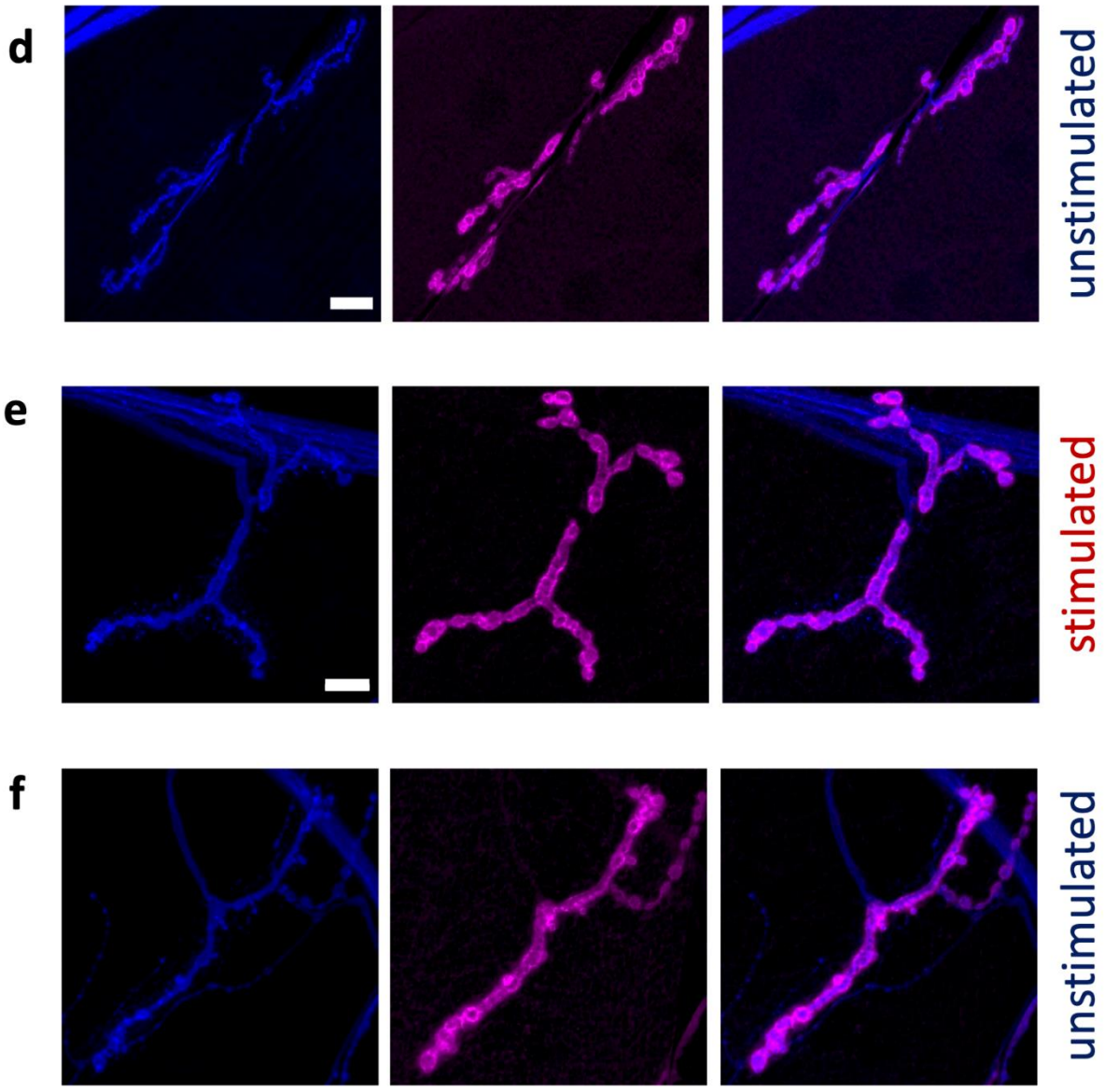

Figure 3.13: Attempting to induce structural plasticity via high K^+ pulses. a) Protocol for induction of plasticity, time shown in minutes. High K+ = 90 mM. Low K+ = 5 mM. **b-c)** NMJs on muscle 6/7 of stimulated larvae. Insets show examples of nascent boutons (arrows). **d)** NMJ on muscle 6/7 of unstimulated larva. **e)** NMJ on muscle 4 of stimulated larva. Arrows show examples of synaptic debris. **f)** NMJ on muscle 4 of unstimulated larva. In all panels, HRP (presynaptic) shown in blue, DLG (postsynaptic) shown in magenta, rightmost image is a composite. Scale bars: a-d = 15 µm; e-f = 10 µm. Anterior = up.

neurons did not have an accumulation of this debris (fig 3.13f). The lack of convincing increase in certifiably nascent boutons and the dramatic increase in synaptic debris elicited from this method, plus the concerns around muscle health following K^+-mediated depolarisation elucidated in Maldonado-Diaz et al., 2021, it was concluded that this method would not be viable for testing the role of dATM in short-term structural plasticity.

An alternative method to give spaced pulsed neuronal firing is through using temperature cycling combined with expression of the temperature-gated cation channel, TrpA1. Cycling between 21°C where the channel will be closed and 29°C where it will be open, with the same spacing as the K^+ protocol, should produce a pattern of high vs low neuronal firing sufficient to induce structural plasticity and nascent bouton formation (Maldonado-Díaz, Vazquez and Marie, 2021). The same study found that temperature shifting alone is also sufficient to give a small increase in nascent boutons.

Representative images from these experiments are shown in figure 3.14. Similar to the K^+ protocol, motor neurons on muscle 6/7 do show nascent bouton formation that lack a DLG signature (fig 3.14 b and c, plus insets). There are also some where the DLG signature is faint, as if fixation has captured the moment at which the postsynaptic density was beginning to form. For example, in fig 3.14 c', the most distal bouton from the main NMJ body shows a faint DLG signature while the more proximal ones do not. However, again these appear to be rare events, and while there are smaller boutons that may be budding from larger ones, the vast majority have a strong DLG signature which makes it difficult to class them as nascent.

With this protocol, motor neurons on muscle 4 show significantly less synaptic debris than with K^+ stimulation, and some evidence of infrequent nascent bouton formation when

stimulated (fig 3.14d and d'). In addition, there is evidence of a "satellite bouton" phenotype (e.g., the top rightmost structure in fig 3.14d) where a collection of smaller boutons surround a larger one, a phenotype often observed in NMJ overgrowth mutants (Menon, Carrillo and Zinn, 2013). TrpA1 overexpression is known to lead to an overgrowth of the NMJ, although in this experiment the channel was kept off during development as the larvae were raised at 21°C, only being switched on during the thermocycling protocol to induce structural plasticity. However, determination of "satellite boutons" is somewhat subjective, and they all showed a positive DLG signature, excluding them from the classification as nascent boutons.

Control larvae which were subject to the same temperature shift but lacking TrpA1 expression (fig 3.14e) did not show satellite boutons or any obvious nascent boutons, although there were infrequent cases of smaller boutons that appeared to be blebbing from larger ones (fig 3.14e'). However, these would always contain at least a faint DLG signature. In addition, co-expressing dATM dsRNA with TrpA1 in this thermocycling experiment was attempted (fig 3.14f and f'). There appeared to be a qualitative reduction in the frequency of nascent boutons compared to the TrpA1 alone condition; however, because there was such a small increase of nascent boutons with TrpA1 compared to controls which did not match the published literature, it was determined that this too was not a viable method for quantifying any differences in structural plasticity following presynaptic dATM knockdown.

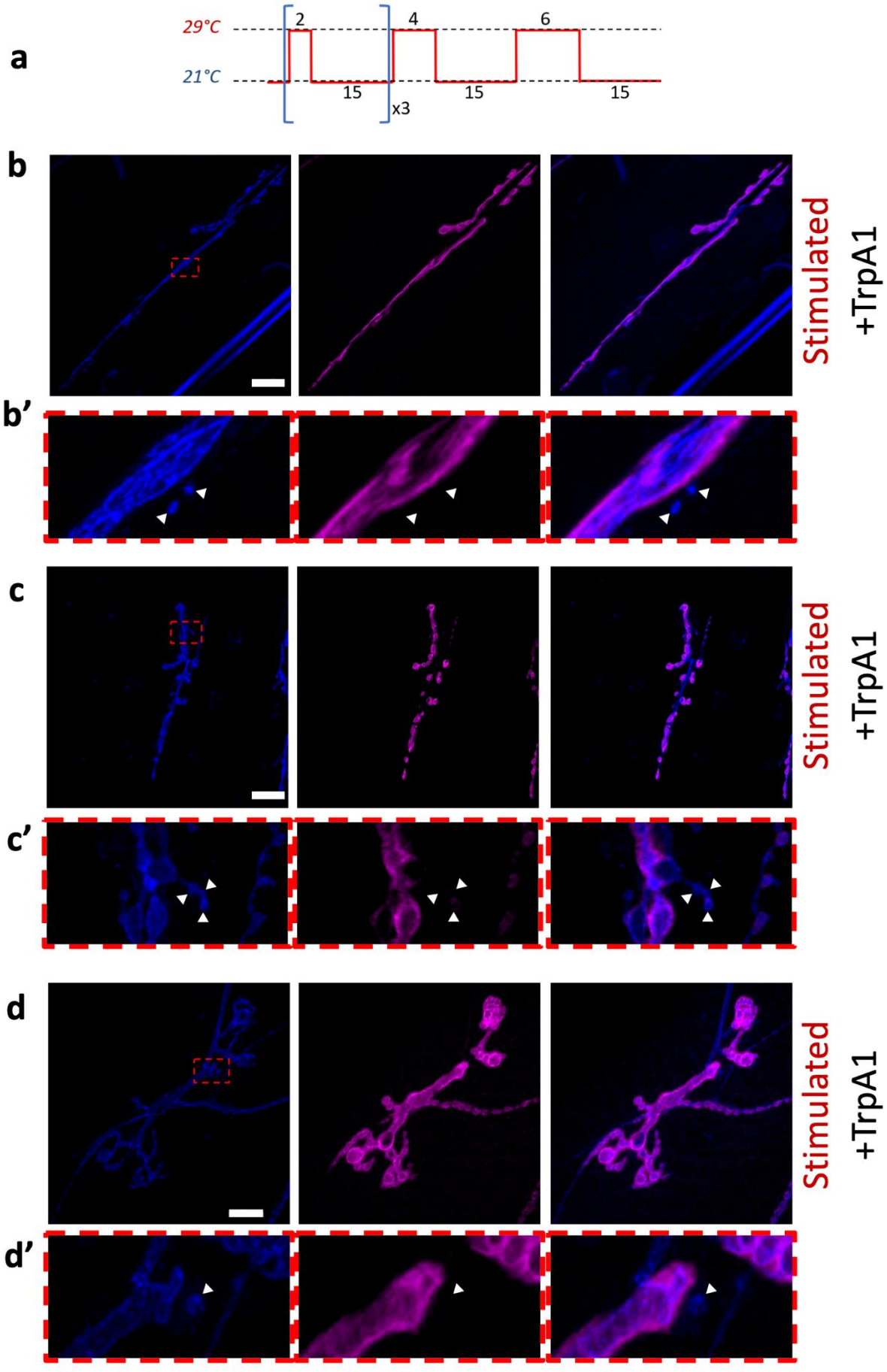
a
29°C
21°C
2
4
6
15
15
15
x3
b
b'
c
c'
d
d'
Stimulated
+TrpA1
Stimulated
+TrpA1
Stimulated
+TrpA1

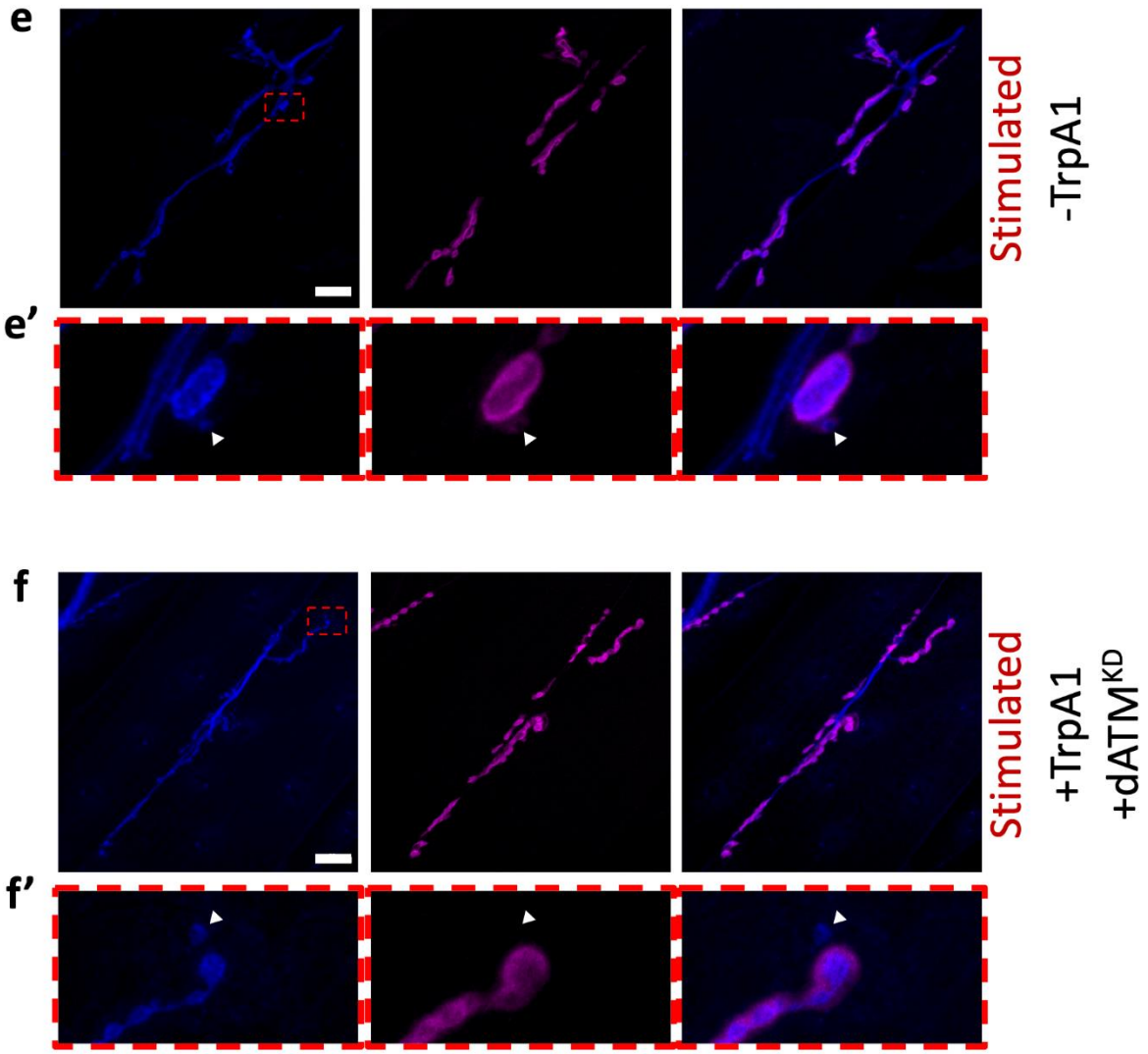

Figure 3.14: Attempting to induce structural plasticity via TrpA1 and temperature cycling. a) Protocol for induction of plasticity, time shown in minutes. Example images of NMJs on **b,c)** muscle 6/7 or **d)** muscle 4 of stimulated larvae expressing TrpA1. **e)** Muscle 6/7 NMJ of thermocycled larva lacking TrpA1 expression. **f)** Muscle 6/7 NMJ of stimulated larva with both TrpA1 expression and dATM knockdown. Insets show examples of nascent boutons which lack a postsynaptic signature (arrows). In all panels, HRP (presynaptic) shown in blue, DLG (postsynaptic) shown in magenta, rightmost image is a composite. Scale bars: b-c = 20 µm; d = 10 µm; e-f = 15 µm. Anterior = up.

3.3 – Discussion

The evidence that mammalian ATM kinase has an important role in the development of neurons and their function is convincing: mutations cause progressive cerebellar degeneration (Boder and Sedgwick, 1970) and cerebellar patterning defects (Vinters, Gatti and Rakic, 1985), Purkinje cells from A-T patients have deficits in calcium currents (Chiesa *et al.*, 2000), and ATM function is required for various forms of synaptic plasticity (Li *et al.*, 2009; Vail *et al.*, 2016). Using a well-established model synapse, the *Drosophila* larval NMJ, this chapter has provided evidence that presynaptic *Drosophila* ATM (dATM) is required for normal synapse development. In $dATM^{-/+}$ heterozygous larvae, the reduction of gene dosage is sufficient to result in smaller NMJs at wandering third instar even when muscle surface area is accounted for, and only presynaptic reduction of dATM using RNAi replicates this phenomenon. The importance of presynaptic dATM is consistent with mammalian experiments, in which high-resolution microscopy observes close ATM colocalization with presynaptic vesicle proteins (Vail *et al.*, 2016). However, at this stage, there is no evidence that dATM localises to synapses in the same way as its mammalian counterpart.

Neither muscle nor glial knockdown of dATM produced significant changes in NMJ morphology, potentially meaning that postsynaptic and peri-synaptic dATM is dispensable for synapse development. Intriguingly, it has been found elsewhere that in adult *Drosophila,* dATM knockdown in glial cells, but not neurons, leads to neurodegeneration and reduced survival (Petersen, Rimkus and Wassarman, 2012). However, this picture is complicated by the fact that in that study, the *repo-GAL4* (glial driver) alone caused significant reduction in survival, so it is possible that the extra reduction in survival in the dATM knockdown is related to a failure to respond to the glial GAL4 toxicity rather than a consequence of reduced glial

dATM *per se*. Further, the data presented here examines the consequence of dATM knockdown during embryonic and larval development, whether in the heterozygous condition or by selective manipulation of subsets of neurons, rather than the consequence on the adult fly. This focus on developmental stages respects the fact that the human disease is a neurodevelopmental one in which the maturing CNS is vulnerable, rather than a late-onset neurodegenerative disorder. It is also clear that, in *Drosophila* at least, ATM has differing roles in the mature *versus* developing nervous system – previously published work from the Tuxworth lab shows that confining neuronal knockdown of ATM to the adult fly improved lifespan and motor performance of a *Drosophila* model of Alzheimer's disease (Taylor *et al.*, 2022). In addition, chronic neuronal ATM knockdown at adult stage does not negatively impact survival, whereas knockdown of ATM through development (as seen above) causes significant neurophysiological deficits and with certain GAL4-dsRNA combinations leads to pharate lethality.

Because of the multifaceted role of ATM in the DNA damage response (DDR), there was a possibility that any structural NMJ phenotype could be due to defective DDR signalling during neurodevelopment. Mutations in DDR proteins, such as components of the MRE11-Rad50-NBS1 complex which sits upstream of ATM in the response to double-strand breaks (DSBs), are associated with microcephaly (Barbi *et al.*, 1991; Waltes *et al.*, 2009; Matsumoto *et al.*, 2011) and neurodegeneration (Digweed, Reis and Sperling, 1999; Stewart, 1999). Mutations in the downstream DDR component CHK2 increases cancer susceptibility (Stolarova *et al.*, 2020), although, other than the association of deficient DNA repair mechanisms with ageing, there is no concrete evidence linking CHK2 deficiency to neurodevelopmental or neurodegenerative disorders. In this work, presynaptic dMRE11 and dCHK2 were found to be

dispensable for NMJ development. The consensus as to the mechanism for microcephaly in these DDR-related conditions is the death of neuronal precursors, which should not be a factor in the above experiments; the shRNA to each component is almost exclusively being expressed in differentiated, post-mitotic neurons, although there is some evidence for transient *elav--GAL4* expression in embryonic neuronal precursors but not postembryonic neuroblasts (Berger *et al.*, 2007). It appears that there is a dissociation of the role of DDR proteins in dividing neuronal precursors *versus* differentiated neurons, further evidenced by the fact that knockdown of DDR components in some contexts can be neuroprotective (Tuxworth *et al.*, 2019; Taylor *et al.*, 2022). This contrasts with the role of ATM, which seems to be required in post-mitotic but still developing neurons (e.g., *Drosophila* larval motor neurons), pointing to the idea that the pathway in which neuronal ATM functions is separate from the DDR. A future test of this hypothesis would be to repeat the DDR knockdowns with a neuroblast driver, such as *dpn-GAL4* (Hara *et al.*, 2018), and observe whether this results in altered NMJ structure or reduced larval brain volume.

Microcephaly is also associated with mutations in ATR, the sister protein of ATM which regulates the response to single-stranded DNA breaks (O'Driscoll *et al.*, 2003). Intriguingly, when quantified and scaled relative to muscle size, presynaptic knockdown of dATR resulted in a small but significant overgrowth of the neuromuscular junction; the opposite effect of dATM knockdown. Work from the Herrup lab has shown that ATM and ATR are both associated with presynaptic vesicles, and in neurons they physically interact with each other in the cytosol and not the nucleus (Li *et al.*, 2009). Further, ATM associates with excitatory vesicles and ATR inhibitory vesicles; it is proposed that this helps to regulate excitatory/inhibitory homeostasis (Cheng *et al.*, 2018). It is tempting to interpret the

overgrowth seen with presynaptic dATR knockdown in this light – could there be a disruption to the excitatory/inhibitory balance in favour of excitation, leading to synapse expansion through activity-dependent growth? This line of reasoning must proceed with caution, however, since there was a significant and unusual reduction in the muscle surface area of the larvae in this condition compared to controls, which was the reason why the *scaled* NMJ surface area was larger. Because presynaptic dATM knockdown did not affect muscle surface area, it is possible that the result from dATR knockdown was an artefact from the unexplained decrease in larval body size. Nevertheless, developing motor neurons in *Drosophila* are shaped by the growing muscle and consequently grow to a size appropriate for maintaining synaptic strength on their target muscle, while excess boutons are "pruned" (Menon, Carrillo and Zinn, 2013). The fact that dATR knockdown neurons are inappropriately sized relative to their smaller muscles could therefore indicate a deficit in this process in favour of inappropriately expanded synapses; the opposite phenotype to dATM knockdown.

The method of knocking-down dATM levels in these experiments relied on the expression of dsRNA constructs complementary to dATM mRNA, under the control of the GAL4-UAS system. Various combinations of drivers, dsRNA constructs and temperatures were used since these will affect the level of reduction of dATM mRNA. As shown above, there was some variation in the results achieved under these different conditions. It seems likely that this is related to the level of knockdown, since it will never be 100% efficient, however qPCR would be needed to confirm this. As an example, with the glutamatergic *OK371-GAL4* (which includes motor neurons), overexpression of the 2nd chromosome dATM dsRNA at ≥25°C resulted in pharate lethality, while <22°C permitted eclosion. This could be due to the effect of temperature on

neuronal activity levels, GAL4 expression (and thus dsRNA expression) or a combination of the two. There was clearly sufficient knockdown of dATM to result in a structural and functional phenotype at 19°C. It is notable that the 3rd chromosome shRNA did not produce pharate lethality under these conditions, which could be related to the efficiency of the dsRNA constructs. Again, qPCR could confirm this although it is technically challenging to isolate mRNA from only the cells in which OK371 drives expression. Nevertheless, it has been shown elsewhere in a separate study that the 2nd chromosome construct is the more efficient of the dATM dsRNA constructs (Sopko *et al.*, 2014).

In terms of the electrophysiological properties of the neurons that are deficient in dATM, there was a clear reduction in the amplitude of the evoked excitatory junction potentials (EJPs) in response to a fixed stimulus. Since, from Ohm's law, voltage is proportional to resistance, it was possible that this could be due to decreased muscle resistance despite an exclusion criterion of muscles of <4 MΩm resistance. However, the muscle resistance of all 3 groups tested were not significantly different from each other. In addition, only muscles with a resting membrane potential of <-55 mV were selected, and any effect of differences in Vm were corrected for nonlinear summation using a derivation of Martin's relationship (Feeney et al., 1998, see *Materials and Methods*). Although both pan-neuronal dATM knockdown groups trend lower, there was no significant change in quantal content, which suggests that the amount of neurotransmitter released in response to a stimulus is unchanged. The two dsRNA constructs behaved differently in a couple of respects. The first was that the 2nd chromosome dsRNA produced a significant decrease in miniature excitatory junction potential (mEJP) amplitude while the 3rd chromosome dsRNA did not. This explains why no change in quantal content was observed – although there was a significant decrease in EJP amplitude,

the decrease in quantal *size*, i.e., the amount of postsynaptic depolarisation evoked from the spontaneous release of neurotransmitter from a single presynaptic vesicle, which is equivalent to the mEJP, balanced this out. Therefore, for this construct, there was a significant decrease in both evoked response amplitudes and spontaneous event amplitudes.

In the context of the structural phenotype (reduced NMJ size, bouton count and active zones) and the locomotor phenotype (slower crawling), the electrophysiological results are consistent. One would expect that a reduction in active zone number per NMJ would lead to a reduction in vesicle release, but the lack of quantal content change weighs against this conclusion. Likewise, the phenotype could result from a postsynaptic disruption, such as reduced glutamate receptor clustering/density, but this too would be reflected in a change in muscle resistance. Although the knockdown of dATM is confined to the presynaptic side, there is a plethora of evidence for the involvement of anterograde presynaptic signalling in shaping the postsynaptic density (e.g., Packard et al., 2002). Nevertheless, given the work showing that mammalian ATM localises to presynaptic vesicles, it seems more plausible that the phenotype is being conferred in the neuron.

Quantal size in *Drosophila* is regulated at both the pre and postsynaptic levels (Cunningham and Littleton, 2019). Post-synaptically, glutamate receptor expression and subunit composition significantly impact the amplitude of spontaneous mEJPs; for example, increasing expression of DGluRIIA increases quantal size, whereas overexpression of DGluRIIB reduces it (DiAntonio *et al.*, 1999). Similarly, postsynaptic PKA expression shows a reciprocal relationship to quantal size (Davis *et al.*, 1998). Presynaptically, there is evidence that vesicle size contributes to quantal size – the 1s synapse shows a larger mean quantal size than the 1b synapse, which correlates with increased vesicle volume (Karunanithi *et al.*, 2002). One key

observation from these experiments is that a decreased quantal size, e.g., in *DGluRIIB* mutants, does not always lead to a reduction in evoked EJPs, i.e., there can be a reduction in mEJP amplitude without a reduction in EJP amplitude. This is achieved through a compensatory increase in quantal content, i.e., the probability of vesicle release in response to a given stimulus (DiAntonio *et al.*, 1999). The phenomenon can also occur in the inverse, for example *NF1* mutants exhibit a striking increase in mEJP amplitude compared to controls, but no overall change in EJP amplitude, which is due to a decrease of quantal content (Dyson *et al.*, 2022). This phenomenon is known as *presynaptic homeostatic plasticity (PHP).* Because presynaptic dATM knockdown shows a decrease in quantal size without a corresponding compensatory increase in quantal content, this could demonstrate a failure to induce PHP. However, the 3rd chromosome RNAi construct only showed a smaller drop in EJP amplitude without any significant change in mEJP amplitude (quantal size) or quantal content, so it is also possible that deficits in neurotransmission are evidence merely of an under-developed (or even degenerating) NMJ. It is unclear why there was such a disparity in the electrophysiological properties of the two dATM knockdown conditions given how similar the structural and locomotor phenotypes were.

It is nevertheless surprising that homeostatic compensatory processes are not functioning in this system where in other cases, significant changes in synapse area and AZ number do not result in changes to evoked potentials or currents, such as with the *endo* or *rab3* mutants (Graf *et al.*, 2009; Goel *et al.*, 2019). The authors of the latter study found that this homeostatic compensation is achieved *via* changes to the architecture of the AZs themselves – *endo* mutants showed an increased number of smaller BRP puncta than controls, and high-resolution stimulated emission depletion microscopy revealed BRP ring diameter

was decreased in *endo* mutants and increased in *rab3* mutants (Goel *et al.*, 2019). This AZ component adjustment was mediated through *arl8*-dependent anterograde axonal transport (Goel *et al.*, 2019). Others have hypothesised that increasing the release probability of individual active zones serves as a mechanism to adjust synaptic output to compensate for different perturbations (Akbergenova *et al.*, 2018; Wang *et al.*, 2021). Therefore, it would be informative to use higher-resolution microscopy to interrogate the ultrastructure of individual AZs in dATM knockdown neurons, examine the release probabilities of individual AZs using calcium sensors, and alternatively observe whether there are changes in postsynaptic glutamate receptor composition. This would help to determine whether deficiencies in these homeostatic compensatory processes exist, whether they occur trans-synaptically or are confined to either the pre or postsynaptic side, and consequently how they contribute to the functional dATM knockdown phenotype.

The 2nd chromosome RNAi construct also showed a difference in paired-pulse ratio compared to the controls, while the other construct did not quite reach statistical significance. Normally, at 1.5 mM Ca^{++}, the larval NMJ will undergo paired-pulse depression because of a reduction in the readily-releasable pool (RRP) of neurotransmitter-containing vesicles after the first stimulation (Hallermann, Heckmann and Kittel, 2010). The relative increase in PPR in the dATM knockdown case is therefore likely due to the overall reduction in EJP amplitude, which means the RRP is not as depleted as in the controls after the first stimulus.

As the larva grows from 1st to 3rd instar, the nervous system must also expand alongside. In addition, from feeding 3rd instar to wandering 3rd instar, the larva grows without moulting, its muscles enlarge by up to 100-fold, and the NMJs consequently need to expand to maintain

appropriate synaptic performance (Schuster *et al.*, 1996a; Menon, Carrillo and Zinn, 2013). Various studies across multiple different systems have suggested that the maturing NMJ exists in a dynamic equilibrium between expansion and retraction, related in a large part to the amount of neuromuscular activity (Schuster *et al.*, 1996b; Wilson and Deschenes, 2005). The effect of neuronal activity on the dATM knockdown phenotype was tested in this study through the utility of different rearing temperatures of the experimental crosses since neuronal activity in poikilothermic animals such as *Drosophila* can be modulated by temperature. The effects seen above of rearing temperature on larval locomotion broadly matches what has been documented previously, with increasing temperatures leading to increased crawling speed (Sigrist *et al.*, 2003). Further, increased temperature increases NMJ size and arborisation, a process which is dependent on increased neuronal activity (Sigrist *et al.*, 2003; Zhong and Wu, 2004). That second study also found a reversal point at which neuronal activity would then promote a decline in NMJ size and arborisation, suggesting a balance in the relationship between synapse growth and neuronal activity.

Within this context, it is striking that dATM knockdown larvae fail to expand their synapses appropriately to increasing rearing temperature, i.e., they were insensitive to temperature-regulated developmental processes. This could reflect a failure in PHP as suggested earlier, since structural plasticity of synapses in response to both neuronal activity and larval growth is a feature of this phenomenon. While the possibility of different levels of knockdown having different effects cannot be ruled out from these experiments, the fact that at lower temperatures there is a striking phenotype where one would expect knockdown to be weaker suggests that temperature/neuronal activity is a significant factor on the dATM knockdown NMJ phenotype. The observed phenotype also leads to the question of whether

there is a failure in neurodevelopment, or if the neurons are degenerating, with the NMJs sensitive or vulnerable to increases in temperature or neuronal activity.

One caveat to the experiments in this Chapter is that the indicated rearing temperatures were applied throughout embryonic and larval development. This means that the recently identified embryonic "critical period" (17-19 h AEL) will be included in these manipulations (Giachello and Baines, 2015) and confining certain stimuli to this period is known to produce neurobiological changes which persist long after the stimulus is withdrawn, including increased synaptic excitability (Giachello *et al.*, 2021). Further, rearing larvae predominantly at low temperatures with a shift to higher temperatures solely during the critical window leads to increased larval locomotion and expanded NMJ structure compared to controls reared exclusively at lower temperatures (private communication of unpublished data). It would be interesting to test whether this phenomenon is dependent on presynaptic dATM; or, by confining knockdown of dATM to solely during or post critical period, whether the synaptic phenotypes in this Chapter are still observed. One future experiment could be to shift dATM knockdown larvae, reared at 19°C, to 30°C during the critical window then return them to 19°C until wandering third instar and test their crawling speed, electrophysiological properties and NMJ anatomy. If the phenotypes were rescued then this would suggest this brief burst of increased temperature during embryonic development sensitised the NMJ to increases in neuronal activity sufficient to overcome the desensitisation of dATM knockdown neurons. Because the remainder of development then occurs at lower temperatures in this example, the sensitisation may not lead to degeneration. In this way, the interplay of the embryonic critical period and dATM signalling in synaptic development and homeostasis could be uncovered.

In addition to the developmental expansion of the synapse, the structure of the NMJ can change on shorter timescales in response to acute stressors. Previous work has shown that pulses of high extracellular K+ concentration or temperature cycling with or without the motor neuronal expression of TrpA1 can induce the appearance of nascent boutons, which form both between and from pre-existing boutons, and are characterised by a lack of postsynaptic (DLG) signature (Ataman *et al.*, 2008; Vasin *et al.*, 2019; Maldonado-Díaz, Vazquez and Marie, 2021). However, detection of these nascent boutons in the above experiments was infrequent – smaller "satellite" boutons were observed, but rarely was there a presynaptic signature (HRP) without the DLG signature. It appeared that a timepoint was being captured where postsynaptic specialisation and stabilisation of nascent boutons was beginning to occur, which made classification subjective and quantification difficult. This limited the utility of the assay in quantifying structural plasticity with any confidence.

The K^+ stimulation protocol led to a clear accumulation of synaptic debris, i.e., the shedding of presynaptic membrane into the synaptic cleft. Previous work has found that increasing synaptic debris correlates with neuronal activity, and both peri-synaptic glia and the postsynaptic muscle play a role in its clearance (Fuentes-Medel *et al.*, 2009). That study determined that one of the sources of the debris were nascent boutons which failed to acquire a postsynaptic signature and become stabilised and were thus shed from the presynaptic arbor. This may suggest that the K^+ protocol above was successful in inducing structural plasticity, but the NMJ environment was unsuitable for the stabilisation of nascent boutons. In support of this conclusion, there is evidence that K^+ stimulation is detrimental to muscle health (as measured by input resistance in electrophysiology experiments) (Maldonado-Díaz,

Vazquez and Marie, 2021) which may impair the ability of postsynaptic densities to form and stabilise nascent boutons.

Often, small budding boutons were observed which still had a faint DLG signature. Expressing TrpA1 in motor neurons and cycling the temperature between the channel's ON and OFF states was the most reliable way to induce nascent bouton formation without DLG staining, albeit still rarely. Temperature cycling control larvae in the same way would also produce small budding boutons, but almost exclusively these had postsynaptic staining. Perhaps one reason for this difference is that while increasing temperature will increase neuronal firing, this increase will be significantly milder relative to the tonic hyperstimulation induced by TrpA1 channel activation. Thus, activity-dependent structural plasticity in TrpA1-expressing neurons will be occurring rapidly with nascent boutons forming more quickly before there is a chance for the postsynaptic specialisation to form. It is also clear that the thermocycling/TrpA1 protocol leads to significantly less synaptic debris accumulation than the K^+ protocol, suggesting that the muscle is in better health and can both stabilise nascent boutons and clear destabilised boutons' debris more efficiently.

Going forward, a more optimal method for studying the effects of dATM knockdown on short-term structural plasticity would be to use an optogenetic system. In the above experiments, both expression of TrpA1 (to induce neuronal hyperactivity) and knockdown of dATM (through overexpression of a dsRNA) were GAL4 and temperature dependent. Co-expression of TrpA1 and dATM dsRNA at the ON state of the channel is lethal; therefore, the experiment was performed by raising the larvae in the channel OFF state (21°C) and only shifting to higher temperatures during the thermocycling protocol. However, this means that dATM knockdown is not controlled at a constant level (since GAL4 expression is temperature-dependent). With

an optogenetic approach, the larvae could be maintained at a constant temperature, meaning dATM knockdown is consistent, while hyperactivity is induced in short bursts using light. For example, this approach has been used successfully with CsChrimson, a red-light gated cation channel (Klapoetke *et al.*, 2014). Patterned stimulation using bursts of red light followed by resting periods has been shown to be sufficient to induce structural and electrophysiological plasticity without detrimental effects to the postsynaptic muscle (Maldonado-Díaz, Vazquez and Marie, 2021). It is also far more precise than temperature-shifting, since the amount of neuronal firing correlates precisely to the intensity of the light source, and this can be switched on and off immediately in contrast to the slow ramping up and down of temperature. In addition, recent work from the Theodoro lab identified a requirement for muscle contraction and membrane blebbing, the latter a process driven by pressure rather than actin-myosin interactions, in order for nascent boutons to form – by overstretching larval preparations during the K^+ stimulation protocol, the amplitude of muscle contractions were reduced and rhythmic contractions eliminated, which significantly decreased nascent bouton formation (Fernandes *et al.*, 2023). It is possible that the lack of nascent bouton formation in *3.2.11* was therefore due to an overstretching of the preparations during each stimulation protocol.

It is challenging to distinguish between neurons that have failed to develop properly *versus* neurons which are in an early stage of neurodegeneration. Smaller, poorer performing synapses could be indicative of either, perhaps as a failure to respond correctly to growth signals, or a vulnerable synapse on the cusp of degenerating. In support of the latter, it was apparent that higher developmental temperatures lead to a striking structural phenotype in the dATM knockdown larval NMJ, particularly in the more posterior motor neurons. These

neurons are necessarily longer and thus more energy consuming than the anterior motor neurons which may explain the antero-posterior gradient of phenotype severity. In models of neurodegeneration, it is common to observe a bright fluorescent signal from the presynaptic neuron as it starts to degenerate and pulls away from the end-plate, which has been termed the "retraction bulb" (Riley, 1977). This creates regions of postsynaptic density without presynaptic membrane, described as synaptic "footprints" (Koch *et al.*, 2008). Whilst there was no clear evidence of a retraction bulb in the experiments above, some of the boutons in the dATM knockdown larvae would appear brighter than the others, the HRP signal overall would be fainter, and the NMJ appear "thinner." Quantifying the ratio of presynaptic HRP to postsynaptic DLG signal can stand in as a measure of how much the neuron is degenerating away from the end-plate, and there was a significant reduction of this ratio in the dATM knockdown at higher rearing temperatures. It would be interesting to see if this also holds true at lower rearing temperatures, where the NMJs were significantly smaller but didn't seem to be thinning or breaking up. If at lower temperatures there is no evidence of degeneration, then this presents a scenario in which dATM is required both for the normal expansion of the synapse during neurodevelopment and as a guardian against neurodegeneration when the neuron is under stress e.g., from increased activity.

3.4 – Conclusion

In conclusion, this chapter has demonstrated a clear requirement for presynaptic dATM for the development of the larval neuromuscular junction. Loss of dATM from the presynaptic compartment leads to clear structural, functional, and electrophysiological deficits. There is also a potential role for dATM in the activity-dependent expansion of the neuromuscular

junction, as dATM knockdown synapses fail to expand in response to increasing temperature. Further, dATM deficiency appears to leave neurons vulnerable to stressors such as increased rearing temperature. At this point, the data suggest a model in which ATM is involved in sensing the activity level of a neuron and translating this into a growth signal, while also potentially protecting the neuron from the toxic effects of increased neuronal activity. This model will be refined and tested further in the next chapter.

Chapter 4 – Localisation of endogenous and overexpressed GFP-tagged dATM

4.1 – Introduction

In the preceding chapter, the data suggest that presynaptic *Drosophila* ATM kinase (dATM) is required for synapse development and maintenance. In summary, heterozygous whole organism mutants showed an undergrowth of the neuromuscular junction (NMJ). From cell-type specific knockdowns in presynaptic (neuronal), postsynaptic (muscle) and peri-synaptic (glial) compartments, only presynaptic knockdown replicated the NMJ undergrowth phenotype.

However, without localisation data, the evidence for a neuron-specific role of dATM during development is circumstantial. As there is no available antibody targeting dATM, an alternative solution is to overexpress a recombinant dATM tagged with a fluorescent protein or epitope tag, such as FLAG, using the GAL4-UAS system (Brand and Perrimon, 1993). Previous work studying localisation of dATM was performed using overexpression of transgenic FLAG-dATM in S2 cells (Hong and Choi, 2013). The results demonstrated nuclear localisation of the transgenic construct and foci formation upon irradiation. However, this study was limited to *in vitro* dATM overexpression in a single cell type. There is therefore a lack of understanding of *in vivo* endogenous dATM localisation within neurons.

CRISPR/Cas9 technology has enabled the targeting of a greater range of DNA sequences for gene editing than ever before. The process relies on small motif sequences that are widespread throughout the genome that can be recognised by CRISPR RNA (crRNA), which

consists of a guide RNA (gRNA) and transactivating CRISPR RNA (tracrRNA). These interspersed sequences end in a 3' protospacer adjacent motif (PAM) N(G/A)G, to which the Cas9 nuclease can be recruited by complementary crRNA to induce a double strand break (Jinek *et al.*, 2012). This can be used for targeted mutagenesis, or if a homology-directed repair (HDR) construct is provided, to edit the locus of interest with a new DNA sequence, e.g., to insert a fluorescent reporter (Bassett *et al.*, 2013; Gratz *et al.*, 2015).

When designing a CRISPR/Cas9 gene edit *in vivo*, there are two key factors to consider:

1) Efficiency of the edit
2) Marking progeny with successful incorporation of the edit.

Efficiency depends on design of the gRNAs such that off-target effects are limited, and web-based tools have been developed to aid this design *in silico*, such as e-CRISP and TargetFinder (Gratz *et al.*, 2014; Heigwer, Kerr and Boutros, 2014). Also crucial for efficiency is an optimal HDR construct. When CRISPR-based systems were first being adapted to *Drosophila*, single-stranded oligodeoxynucleotide (ssODN) donors were used with small homology arms of <100 nucleotides (Gratz *et al.*, 2013), but these were only applicable for small insertions. For larger insertions, injection of double stranded DNA (dsDNA) donors with larger homology arms of ~1kb were required (Beumer *et al.*, 2013; Gratz *et al.*, 2014). More recently, a system was developed where the HDR template is provided in a circular plasmid vector, with gRNA recognition sites specific to that vector (and absent in the genome) flanking the template. By co-injecting with gRNAs targeting the HDR vector, Cas9 linearizes the construct *in vivo*. This

method was found to only require homology arms of ~100nt for efficient integration (Kanca *et al.*, 2019).

Marking successful transformants is usually achieved through the incorporation of a dominant marker within the HDR construct and injecting into a recessive mutant background (e.g., w+ marker in HDR, injected into w- background – successful insertion marked by red-eye phenotype). This is particularly useful when the goal is to create a new mutation within a gene, or to insert a cassette which will drive GAL4 expression in the same pattern as the gene of interest while knocking-out the gene's expression (P.-T. Lee *et al.*, 2018).

In theory, it is now possible to generate a marked mutant for the gene of interest with the ability to induce rescue *within the same construct*. The O'Connor-Giles lab have developed a CRISPR-based method in which the HDR construct contains both the protein tag (e.g., HA or GFP) and 3xP3-promoter-driven DsRed flanked by piggyBac transposase recognition sequences (Berghammer, Klingler and A. Wimmer, 1999; Horn *et al.*, 2003; Li *et al.*, 2013; Bruckner *et al.*, 2016). Initial insertions are marked by strong red fluorescence in the eye and ocelli, and the presence of a stop codon within the first piggyBac inverted repeat leads to a non-functional protein product (depending on if the site of insertion leads to a truncated protein product). PiggyBac-mediated footprint-free removal of DsRed restores tagged-protein expression allowing precise localisation of the protein at endogenous levels of expression (Bruckner *et al.*, 2016; Gratz *et al.*, 2019; Revaitis *et al.*, 2020).

With these considerations, this chapter employs a novel combination of the Oguz Kanca and Kate O'Connor-Giles methods to generate a CRISPR-mediated knock-in of superfolder GFP (sfGFP) into the endogenous dATM locus in *Drosophila.* The initial insertion of the full s*carless*-

sfGFP-DsRed construct is, as predicted, a loss-of-function mutant of dATM. Following PCR and sequence validated piggyBac-mediated excision of DsRed to generate sfGFP-tagged dATM, there is clear evidence of restoration of functionality. Despite this, localisation of the construct has mixed results. To address this localisation issue and to test whether human ATM (hATM) can complement dATM function, tagged forms of hATM and dATM were overexpressed using the GAL4/UAS system. Both constructs display predominantly cytosolic expression within neurons, while msGFP2-tagged dATM also shows focal expression within distal axons and presynaptic boutons of the NMJ. These constructs open new possibilities for studying the role of neuronal dATM during synapse development and plasticity.

a

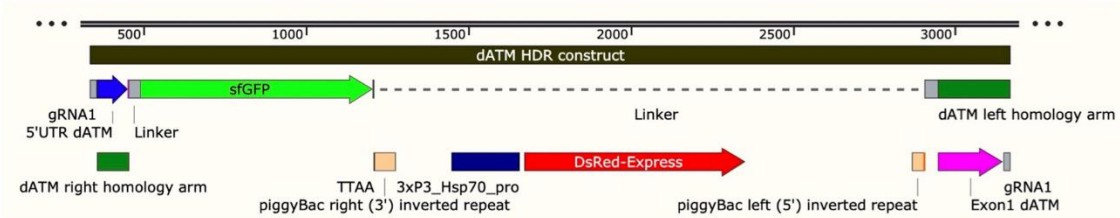
500
1000
1500
2000
2500
3000
dATM HDR construct
sfGFP
gRNA1
5'UTR dATM
Linker
Linker
dATM left homology arm
dATM right homology arm
TTAA
3xP3_Hsp70_pro
piggyBac right (3') inverted repeat
DsRed-Express
piggyBac left (5') inverted repeat
gRNA1
Exon1 dATM

b

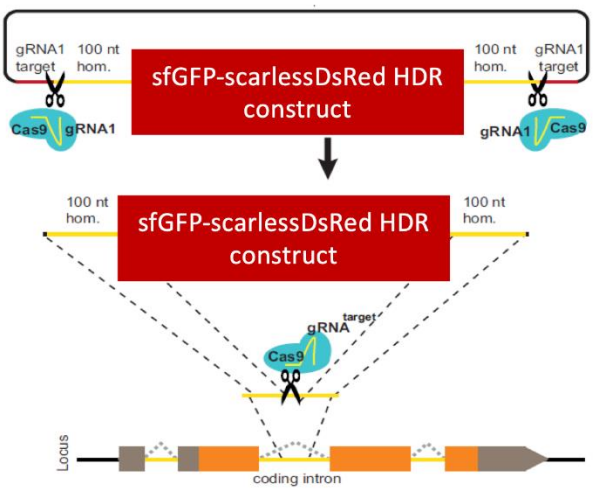
gRNA1 target
100 nt hom.
sfGFP-scarlessDsRed HDR construct
100 nt hom.
gRNA1 target
Cas9
gRNA1
gRNA1
Cas9
100 nt hom.
sfGFP-scarlessDsRed HDR construct
100 nt hom.
gRNA target
Cas9
Locus
coding intron

c

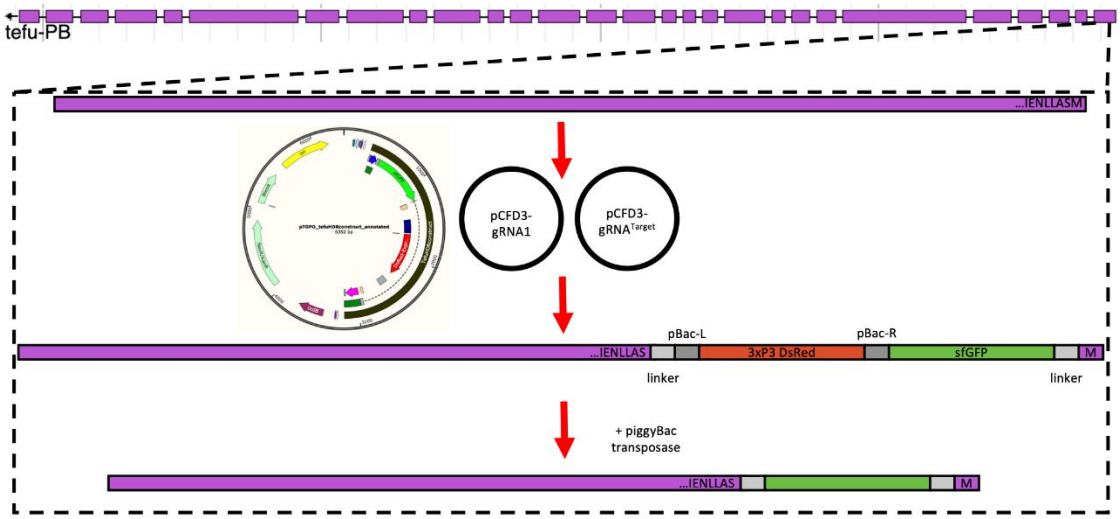
tefu-PB
...IENLLASM
pCFD3-gRNA1
pCFD3-gRNA Target
pBac-L
pBac-R
...IENLLAS
3xP3 DsRed
sfGFP
M
linker
linker
+ piggyBac transposase
...IENLLAS
M

Figure 4.1: Strategy for CRISPR-mediated knock-in of *scarless-sfGFP::DsRed* into *dATM* locus. a) Schematic of homology-directed repair (HDR) construct for CRISPR/Cas9-mediated knock-in of superfolder GFP into the *dATM* locus, with key features annotated. **b)** Summary of the *in vivo linearisation* protocol. HDR construct contains unique gRNA target sites (gRNA1). Co-injection with gRNA1 allows Cas9 to cut the HDR template away from the plasmid vector. $gRNA^{target}$ then guides Cas9 to the site in the genome for the CRISPR-edit. Modified from Kanca et al., 2019. **c)** Diagram of the logic of using *Scarless-sfGFP::DsRed* to generate the initial DsRed-labelled *dATM* mutant, and following piggyBac-mediated excision of 3xP3::DsRed, the sfGFP-tagged dATM construct. At the top is the dATM coding sequence. Protocol involves: Injection of 3 plasmids into *vas::cas9* (HDR plus 2 gRNAs), screening for 3xP3::DsRed, followed by crossing to line containing piggyBac transposase. *Note that dATM is encoded from the antisense strand so the diagram should be read from right-to-left.*

4.2 – Results

4.2.1 - Design and generation of CRISPR-mediated insertion into dATM *locus*

To address the lack of localisation data for *Drosophila* ATM (dATM), a CRISPR/Cas9-mediated knock-in of superfolder green fluorescent protein (sfGFP) into the *dATM* locus was generated. The process is summarised in fig 4.1. A homology-directed repair (HDR) cassette was cloned into the pCR-Blunt II-TOPO vector, with a unique gRNA recognition and protospacer-adjacent motif (PAM) site on either side the cassette. This gRNA site is not present in the *Drosophila* genome. The construct contains (fig 4.1a): short (~100 nt) homology arms targeting the N-terminus of dATM; sfGFP; DsRed downstream of a 3xP3 promoter (to mark successful integration); and piggyBac recognition sequences flanking the DsRed (Bruckner *et al.*, 2016; Revaitis *et al.*, 2020). Due to the stop codon immediately following sfGFP (within a pBac inverted repeat), the initial insert should produce a null dATM mutant, as the single exon transcribed should be degraded by nonsense-mediated decay. Theoretically, this mutant should be “cleaner” (i.e., more specific) than other dATM mutants that were generated using ethyl methanesulfonate mutagenesis, given that the *dATM* locus was being specifically targeted by the gRNA.

To increase integration efficiency, a "linearisation *in vivo*" method was used (fig 4.1b), in which co-injection of gRNAs specific to a plasmid carrying the HDR construct has been shown to be more efficient than injecting linear DNA (Kanca *et al.*, 2019). Cas9 expressed in the germline of injected flies from the *vas* promoter then cuts these sites flanking the HDR construct, and a second gRNA specific to the *dATM* locus induces a double-strand break. The linearised HDR construct then provides a template for homologous recombination. This method eliminated the need for cloning long homology arms (only 100 nucleotides are required rather than ~1000), which was particularly useful given the putative promoter sequences for the neighbouring gene at the 5' end of the *dATM* locus. Despite this experimental design, the efficiency was poor, with only 1 positive insertion from the ~280 larvae that survived microinjection.

Diagnostic PCRs and sequencing of excised bands confirmed correct CRISPR-editing of the *dATM* locus from the HDR construct (fig 4.2). Red-circled bands in fig 4.2b are products amplified from the *dATM[sfGFP::STOP::pBac::ScarlessDsRed::pBac]* locus: the first is ~2800 bp which corresponds to amplification between primers which flank the insertion site and thus the entire *scarless-sfGFP::DsRed* insert (this lane also contains a band for wild-type *dATM* which is on the balancer chromosome of the heterozygote); the second uses the same reverse primer within *dATM* intron 1, and a forward primer 5' of the first piggybac TTAA recognition sequence in the insert, giving an expected product size of 2000 bp, and no wild-type band. From this, it was determined that, at the genetic level, the CRISPR-mediated gene-editing was successful, and the presence of a STOP codon within the insert should lead to a null dATM allele.

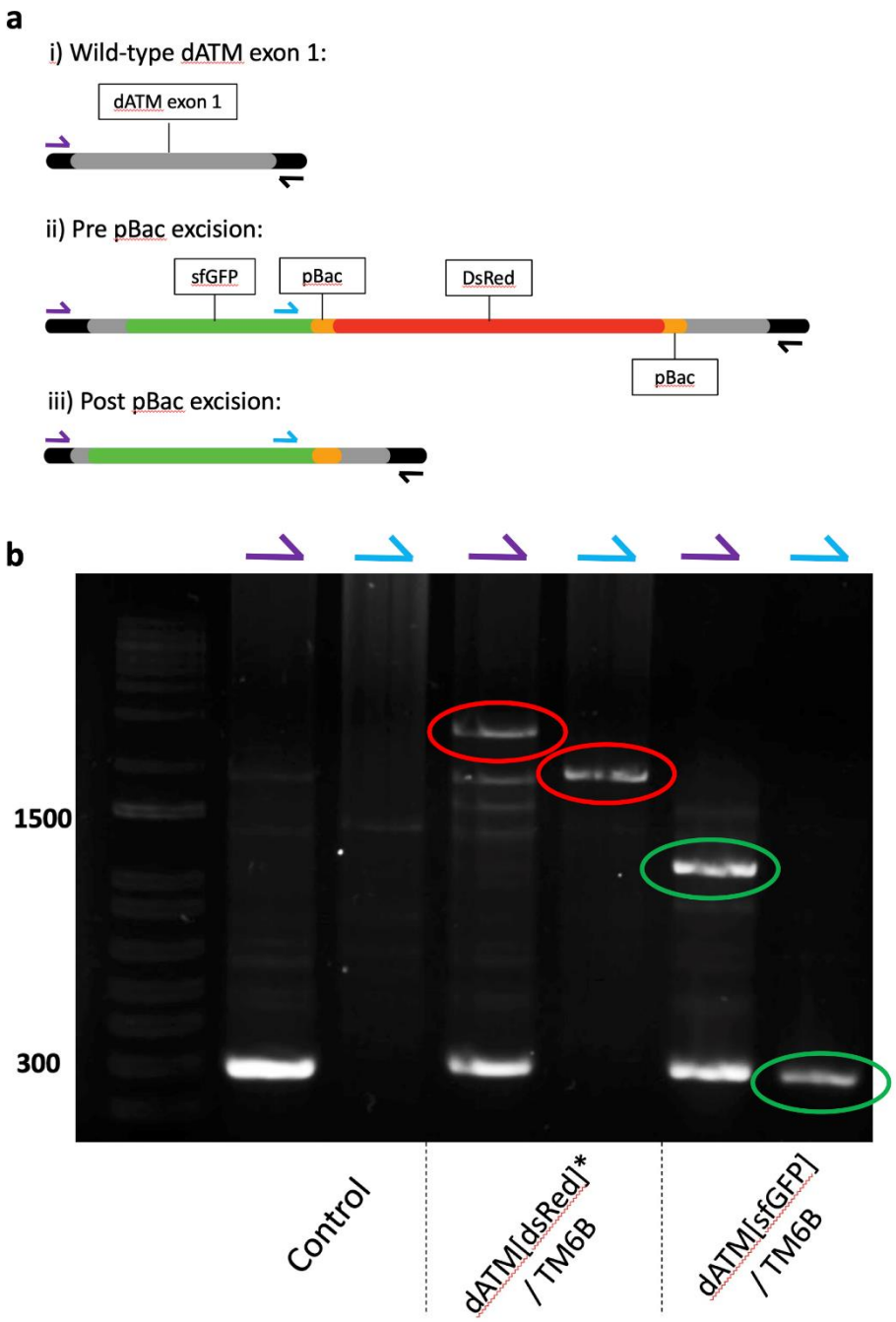

Figure 4.2: PCR screening of successful CRISPR/Cas9-mediated insertions and piggyBac transposase-mediated excision events. **a)** Schematic of PCR amplifications from different primer sets. Reverse primer identical between reactions. Purple forward primer upstream of 5' end of *dATM* with the reverse primer produces: **i)** 300 bp band for wild-type *dATM*; **ii)** 2800 bp band for the CRISPR insertion before piggyBac excision; **iii)** 1100 bp band after piggyBac excision. Blue forward primer with the reverse primer produces: **i)** no band; **ii)** 2000bp band before excision; **iii)** 300bp band after excision. **b)** DNA gel with purple and blue forward primers. Coloured rings indicate products associated with the CRISPR insert. *Note: CRISPR lanes are heterozygous for wild-type dATM.*

4.2.2 – Validation of initial CRISPR knock-in as a bona-fide dATM mutant

Initial outcrossing to a third-chromosome balancer line and subsequent sibling cross revealed that the *dATM[sfGFP::STOP::pBac::ScarlessDsRed::pBac]* transgene (referred to as *dATM[DsRed]**) was inviable as a homozygous stock, which is to be expected if it is a null allele of *dATM*. Given the fact that heterozygous dATM mutant larvae showed an NMJ undergrowth phenotype (see previous chapter), it posed the question of whether this would also be true for *dATM[DsRed]** heterozygous larvae. Crossing *dATM[DsRed]** males to control w^{1118} females and dissection of third instar progeny revealed haploinsufficiency of the CRISPR transgene in NMJ development, with significant reductions in NMJ surface area, bouton count, and active zones (fig 4.3a i-iii, blue vs red boxplots).

In addition, like its mammalian counterpart, the dATM protein is involved in the phosphorylation of histone H2AX (in flies, this is γH2Av) in response to DNA double-stranded breaks. Third-instar larvae were X-ray irradiated with an accumulated dose of 8 Gy, followed by a recovery period of 30 minutes, before protein extraction and Western blotting. Control larvae showed a significant upregulation of γH2Av post irradiation (fig 4.3c i-ii, first 2 columns). Because homozygous *dATM[DsRed]** larvae were not present at third instar, the *dATM[DsRed]*/TM6B* stock was first crossed to another dATM mutant stock, $dATM^{-6}$*/TM6B,* and non-tubby third instar larvae selected. These, therefore, contained trans-heterozygous *dATM* null alleles, and theoretically no functional dATM protein. After irradiation, it was observed that these larvae failed to upregulate γH2Av (fig 4.3c i-ii, middle two columns). In summation, these data suggest that *dATM[DsRed]** is a legitimate mutant of dATM.

4.2.3 - Rescue of dATM function after piggyBac-mediated excision of DsRed and backcrossing

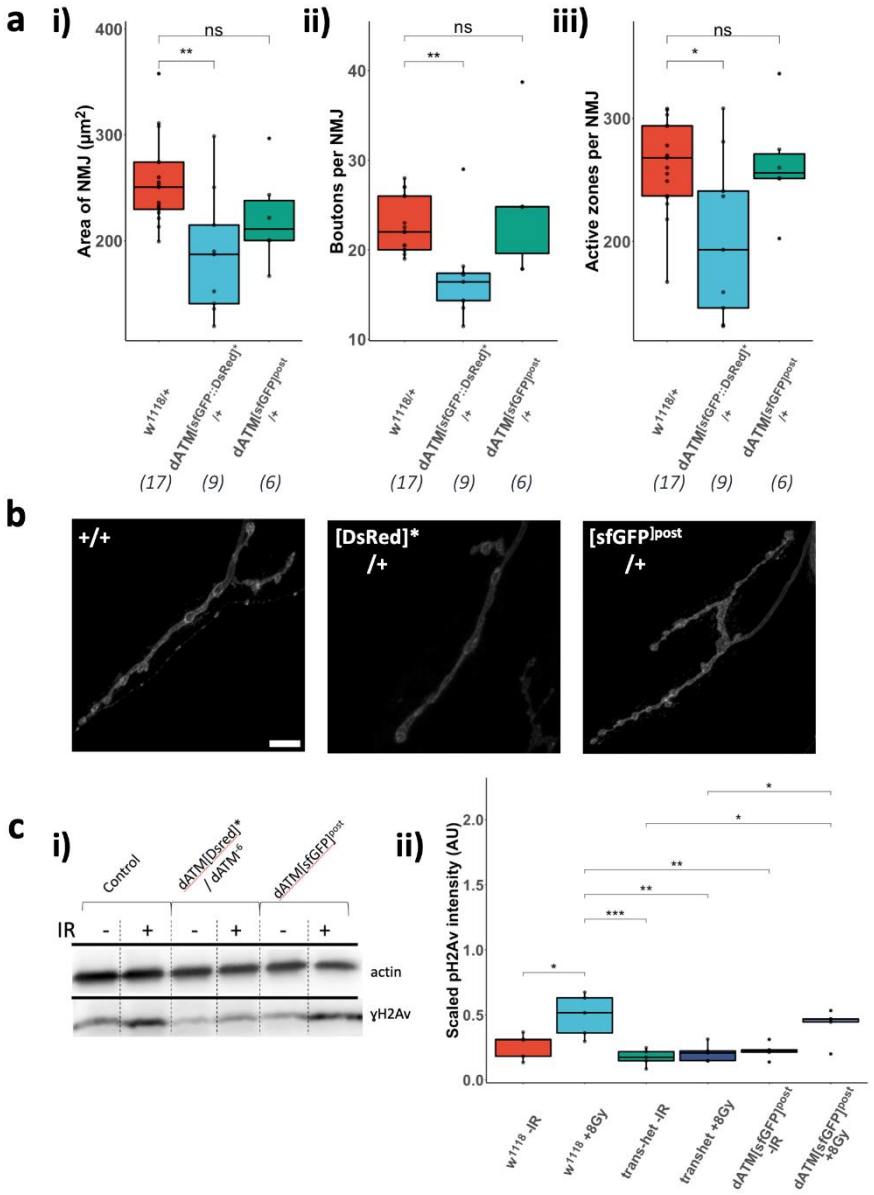

Figure 4.3: Characterisation of CRISPR-generated DsRed dATM mutant and sfGFP "rescue". Heterozygous *dATM[DsRed]** mutants (blue) show deficits in NMJ development. *dATM[DsRed]** mutants have undergrown synapses **(i)**, with fewer "boutons" **(ii)** and active zones **(iii)**. PiggyBac-mediated excision of 3xP3-DsRed to leave sfGFP-tagged dATM significantly rescues all 3 metrics (green). Data all scaled to muscle surface area. **b)** Representative images of NMJs from the respective genotypes. Scale bar = 10 µm. Anterior = up. **c) i)** Representative western blot showing failure to induce γH2Av upon irradiation in transheterozygous *dATM* mutant larvae, which is rescued in homozygous *dATM[sfGFP]*^{post} larvae; **ii)** Quantification of γH2Av intensities scaled to actin levels from N = 3 experiments. All adjusted p-values from one-way ANOVA with Dunnett's test for multiple comparisons, p≤0.05 *, p≤0.01 **, p≤0.001 ***, with non-significant comparisons not shown.

To rescue expression of dATM from *dATM[DsRed]** by removal of the stop codon and 3xP3-driven DsRed, this 3rd chromosome construct was combined with a tubulin-driven piggyBac transposase on the 2nd chromosome by means of a simple crossing scheme (shown below):

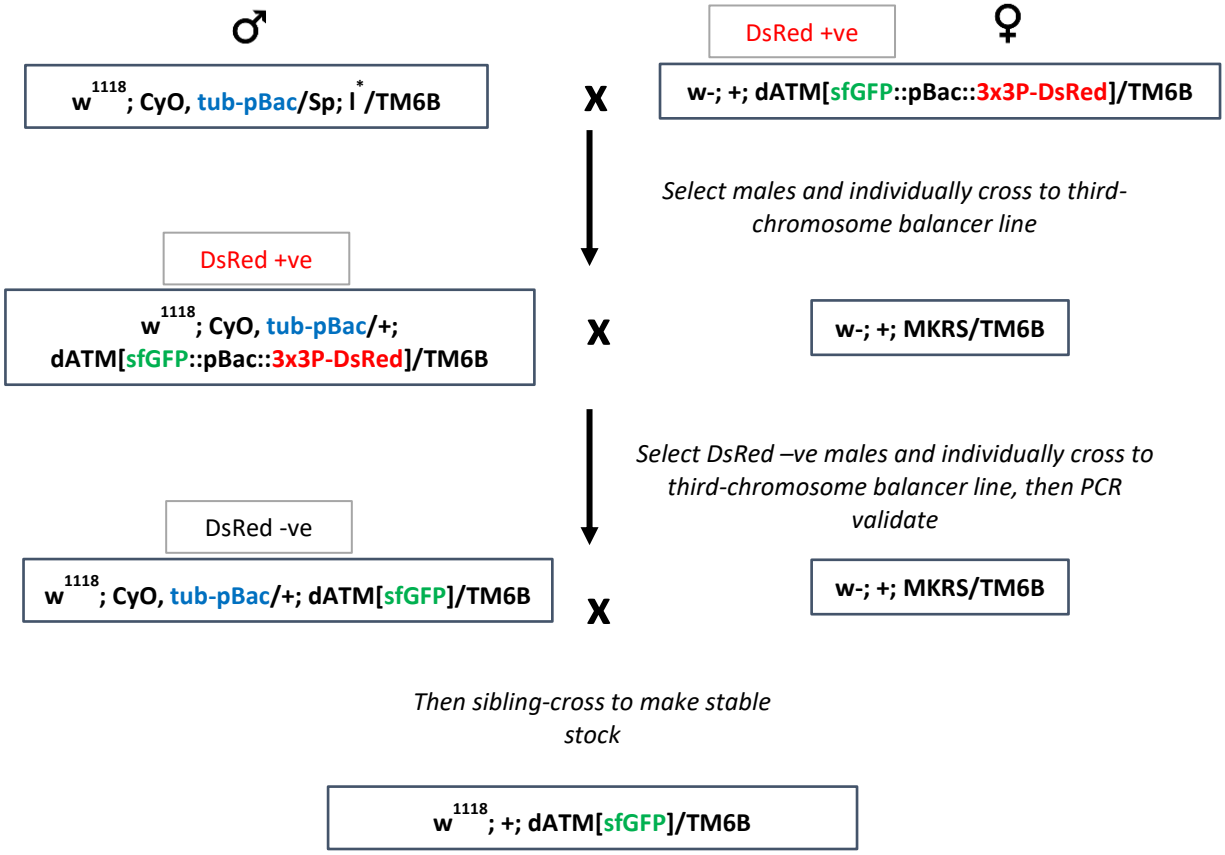

Diagnostic PCRs from genomic DNA of the piggybac-excised lines were used to verify the excision of 3xP3-DsRed, as seen by a reduction in the size of bands using the same primers as above. The green-circled bands in fig 4.2b represent a positive 'hit' of piggybac excision – the first, using the same primers as lane A of the *dATM[DsRed]** line, shows an expected product of ~1100 bp, which corresponds to the entire remaining CRISPR consisting only of sfGFP plus

the linker sequences and the flanking dATM sequence; the second using lane B primers is a product size of just 300 bp, which contains one TTAA site (the other is removed during piggybac transposition – see (Chen *et al.*, 2020) the 3'linker and the remainder of dATM exon 1. These results and the resulting loss of DsRed expression are consistent with correct piggybac-mediated excision of 3xP3-DsRed. Further, sequencing of the excised bands returned 100% of the expected sequence with no indels or frameshifts. However, upon sibling crossing, the resultant *dATM[sfGFP]* construct failed to become homozygous. This suggested either a) functional dATM expression had not been restored, or b) the original CRISPR/Cas9 HDR construct had inserted at other sites in the genome or had off-target effects, causing secondary recessive lethal mutations.

To help distinguish these possibilities, the initial *dATM[sfGFP]* line was subjected to a series of backcrosses to a control w^{1118} stock, following the *sfGFP* insert by PCR at each step. After the 6th backcross, dATM[sfGFP]-positive males were crossed to a third chromosome balancer, then *dATM[sfGFP]/TM6B* progeny were sibling-crossed. Out of ~20 backcross lines tested, one was able to become homozygous upon sibling crossing, suggesting the second mutation had been outcrossed. Hereon, the initial *dATM[sfGFP]* line pre-backcrossing will be referred to as $dATM[sfGFP]^{pre}$ while the post-backcrossing line will be referred to as $dATM[sfGFP]^{post}$.

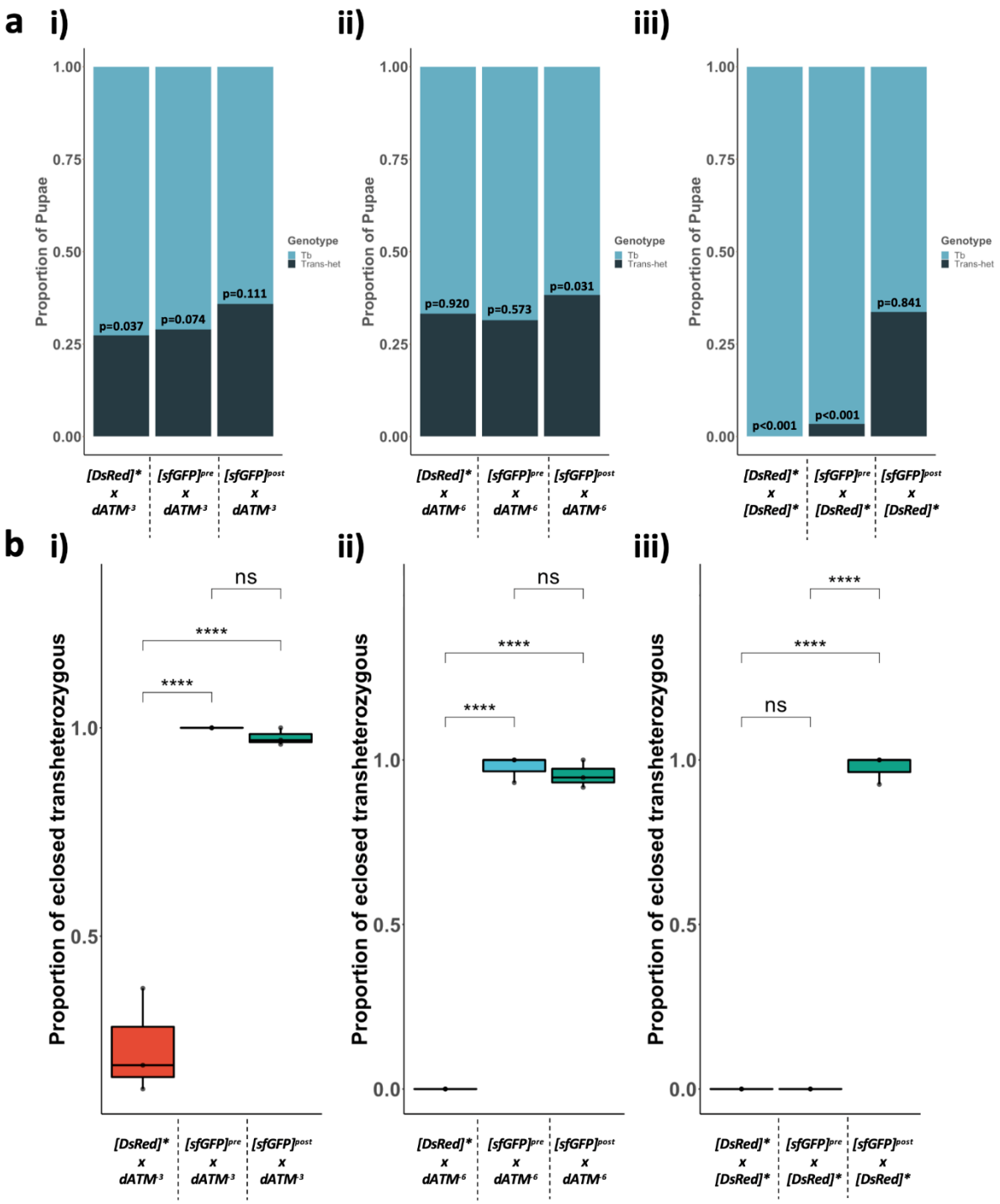

Figure 4.4: Complementation crosses. **a)** Proportion of pupae of either "tubby" (Tb) phenotype indicating inheritance of only one of the *dATM* mutant/transgenic alleles, or transheterozygous (Trans-het) phenotype; **i)** crosses to $dATM^{-3}$; **ii)** crosses to $dATM^{-6}$; **iii)** crosses to *dATM[DsRed]**. P values are from χ^2 tests of Mendelian inheritance. **b)** Proportion of adult flies that successfully eclose of the 2 different genotypes; **i)** crosses to $dATM^{-3}$; **ii)** crosses to $dATM^{-6}$; **iii)** crosses to *dATM[DsRed]**. Shown are adjusted p-values from a one-way ANOVA with Tukey's Honest Significant Differences test for multiple comparisons. p≤0.05 *, p≤0.01 **, p≤0.001 ***, p≤0.0001 ****. The mean of 3 repeat experiments is plotted.

To test whether secondary recessive lethal mutations or off-target CRISPR effects were the cause of the failure of the initial *dATM[sfGFP]^{pre}* line to become homozygous, all three CRISPR stocks were crossed to other *dATM* mutant lines and subjected to complementation analysis. Previous evidence (Pedersen, Tiong and Campbell, 2010) and preliminary work suggested that the various *dATM* null alleles, while obligate heterozygotes as stocks, were trans-heterozygous viable up to the pupal stage when combined with each other, where they would then fail to eclose, indicative of pharate lethality. Fig 4.4 quantifies the results of these crosses. Up to the pupal stage, *dATM[DsRed]** was trans-heterozygous viable with *dATM^{-3}* (fig 4.4a i, left column) and *dATM^{-6}* (fig 3.4a ii, left column), but was not homozygous viable (fig 3.4a iii, left column). With *dATM^{-3}*, it was observed that the ratio of trans-heterozygous larvae to heterozygous larvae was significantly different from the expected Mendelian ratio: (χ2, df=1 N=300), 4.357, p=0.037. In all cases*, dATM[DsRed]** trans-heterozygous or homozygous adults either failed to eclose or rarely eclosed, indicating pharate lethality (fig 3.4b i-iii, left columns).

For *dATM[sfGFP]^{pre}*, when crossed to *dATM^{-3}* and *dATM^{-6}*, there was no significant deviation from the expected Mendelian ratio of trans-heterozygous to heterozygous larvae (fig 4.4a, i-ii, middle columns). There was a significant rescue of the lethality of both of these mutations compared to *dATM[DsRed]**, with most trans-heterozygous flies eclosing from pupae (fig 4.4b i-ii, middle columns). By contrast, *dATM[sfGFP]^{pre}* was unable to rescue the *dATM[DsRed]** mutant: very few third instar larvae were trans-heterozygous (significantly lower than the predicted Mendelian ratio: (χ2, df=1 N=59), 23.396, p<0.001) and those that pupated never eclosed (fig 4b iii, middle column).

The post-backcross *dATM[sfGFP]^{post}* allele was viable in-trans with all of the tested dATM mutants (fig 4.4a i-ii, right columns), but was also able to rescue Mendelian trans-heterozygous larval inheritance with the *dATM[DsRed]** CRISPR mutant (fig 4.4a iii, right column): (χ2, df=1 N=193), 0.040216, p=0.841). Like *dATM[sfGFP]^{pre}*, flies trans-heterozygous for this allele with either *dATM^{-3}* or *dATM^{-6}* were viable to the adult stage (fig 4.4b i-ii, right columns). However, this time the viability of adult *dATM[DsRed]** trans-heterozygotes was also restored (fig 4.4b iii, right column).

To test whether *dATM[sfGFP]^{post}* is a functional rescue beyond rescue of survival, heterozygous third instar larvae were dissected to confirm whether deficits in NMJ development seen with *dATM[DsRed]** were abrogated. *dATM[sfGFP]^{post}* heterozygotes compared to *w^{1118}* controls showed no significant differences in the surface area, bouton count or active zone number of their NMJs (fig 4.3a i-iii). Further, using the same irradiation protocol as above, homozygous *dATM[sfGFP]^{post}* larvae showed a significantly greater γH2Av response than *dATM[DsRed]*/dATM^{-6}* larvae (fig 4.3c i). There was an upward trend of γH2Av intensity in the post-irradiation compared to pre-irradiation *dATM[sfGFP]^{post}* condition, although the variability of this experiment resulted in the values not quite reaching statistical significance (fig 4.3c ii).

Taken together, the weight of evidence suggests that both *dATM[sfGFP]* alleles pre- and post-backcross are functional dATM alleles, but an off-target CRISPR mutation prevents the ability of the *dATM[sfGFP]^{pre}* allele to both become homozygous and rescue *dATM[DsRed]**. Successive backcrosses have thus succeeded in eliminating the off-target mutation in *dATM[sfGFP]^{post}* enabling it to be viable both as a homozygote and in trans with *dATM[DsRed]**. This allele is capable of rescuing both NMJ structural phenotypes and

phosphorylation of γH2Av. Presumably, given that other *dATM* mutants are viable in trans and *dATM[DsRed]** is viable in trans with them, a true "clean" *dATM* null mutant e.g., the CRISPR mutant generated here but without the off-target effect, would be homozygous viable as a larva, before failing to eclose as an adult.

4.2.4 - Localization of dATM[sfGFP]

Following the evidence which suggested that the *dATM[sfGFP]^{post}* construct produced functional dATM protein, the next step was to validate whether this could be used for localisation studies. During the piggybac-mediated DsRed excision step, it was noted that endogenous sfGFP fluorescence under a standard fluorescence dissection microscope was not a reliable marker of a positive excision event (rather, loss of 3xP3-DsRed was much more obvious). To test whether dATM[sfGFP] could be detected under endogenous fluorescence, homozygous *dATM[sfGFP]^{post}* larvae were dissected, fixed briefly in 4% formaldehyde, co-stained with the DNA dye TO-PRO3, and imaged on a confocal microscope. Various tissues were imaged, but the clearest signal was observed in the salivary glands (fig 4.5a). These tissues are somewhat autofluorescent even in control larvae; however there appeared to be diffuse dATM[sfGFP] in the cytosol of salivary gland cells with more punctate staining in the nuclei (fig 4.5a i), which was not present in controls (fig 4.5a ii). After irradiation, this nuclear localisation becomes more distinct, and there is broad co-localisation with γH2Av puncta, which would be expected from functional dATM (fig 4.5b). At the NMJ, the picture is less clear. The muscle shows diffuse green staining, although the striated pattern is likely muscular autofluorescence. The axon (indicated with a white arrowhead) seems to contain a mixture of

diffuse and punctate GFP staining, however there is no clear evidence of GFP localization to the NMJ itself (fig 4.5c).

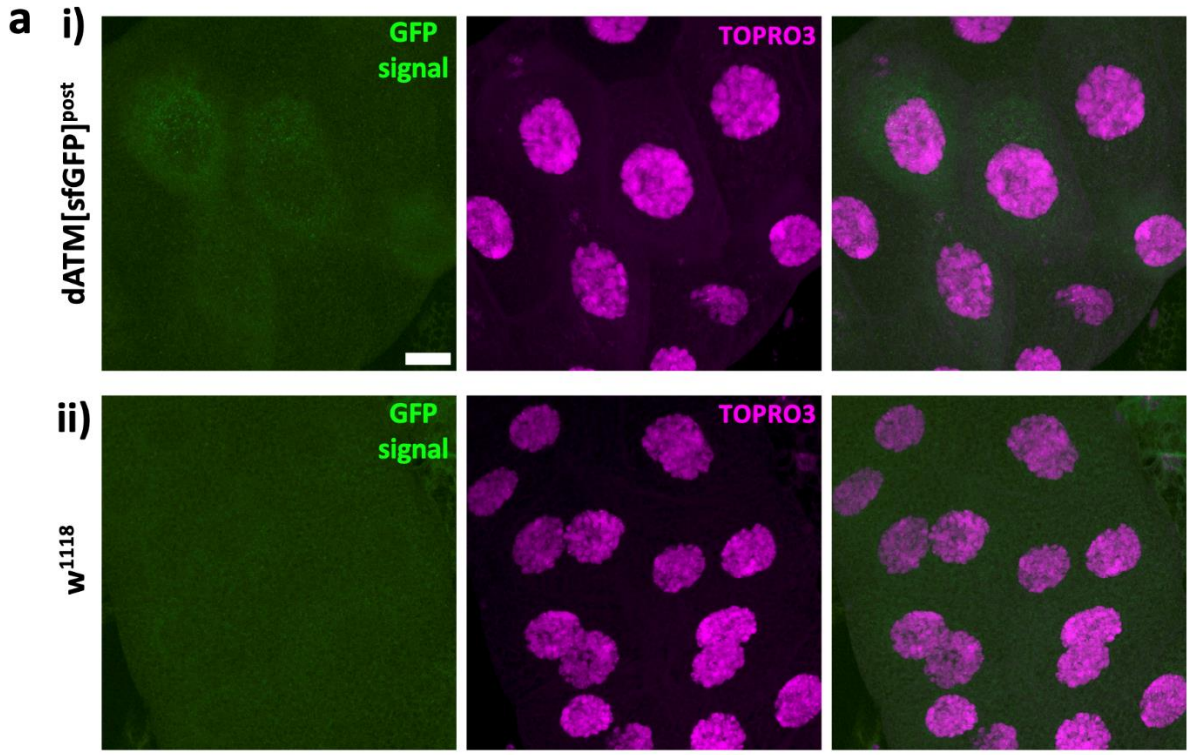

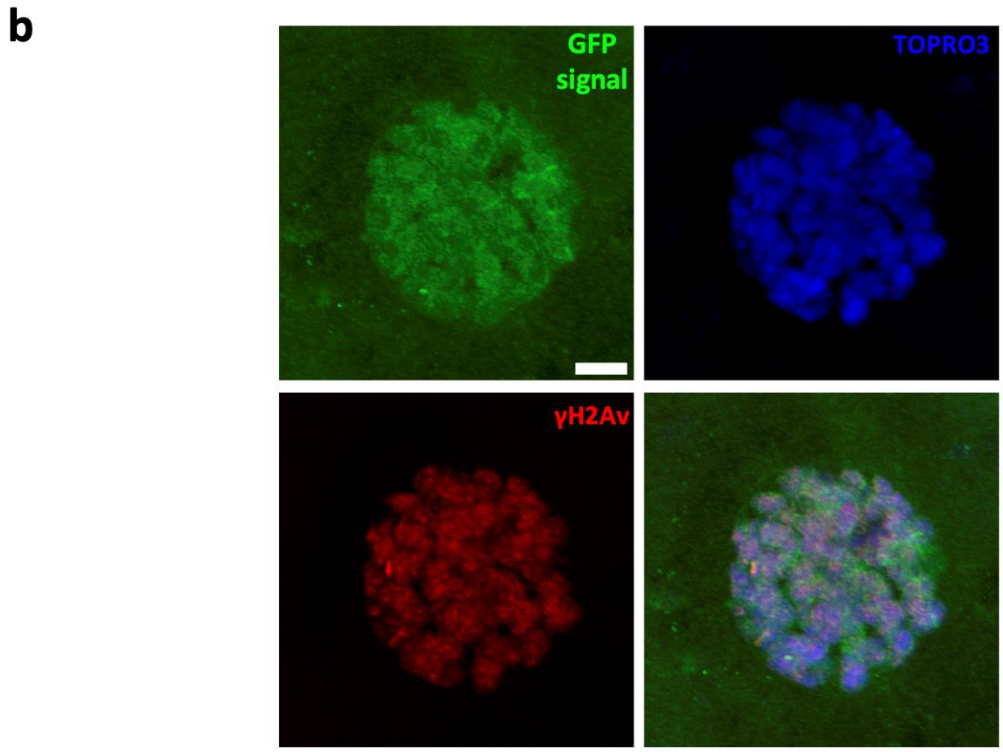

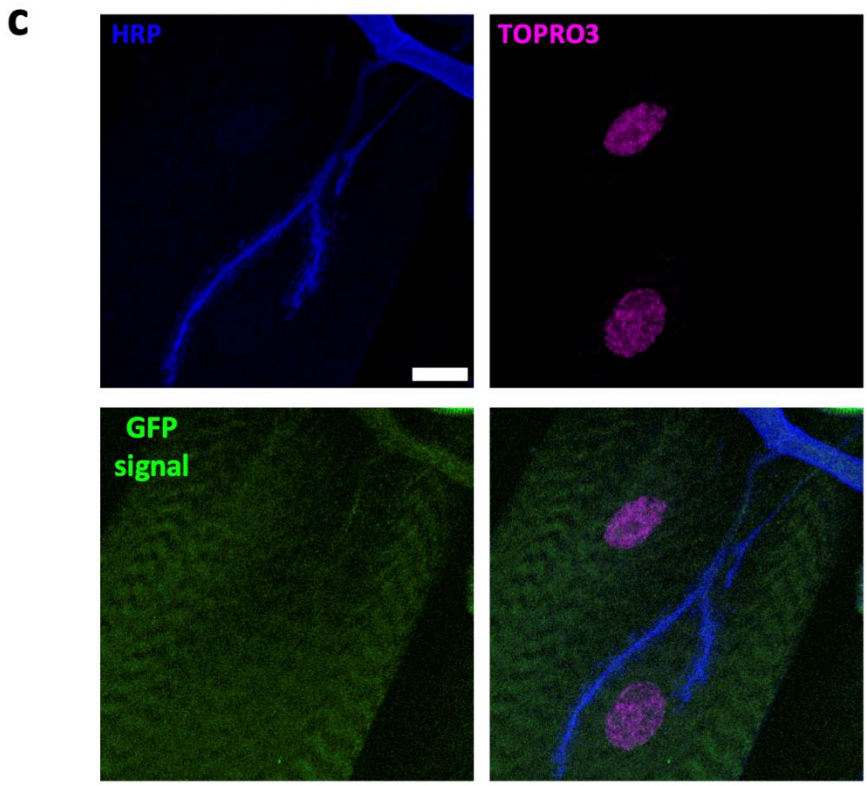

Figure 4.5: Localisation of dATM[sfGFP] protein using endogenous fluorescence. a) Confocal images of fixed salivary glands from **i)** homozygous *dATM[sfGFP]*^{post} and **ii)** w^{1118} negative controls, using the same microscope settings. Scale bar = 30 µm. Rightmost image is a composite of the other two. **b)** *dATM[sfGFP]*^{post} salivary gland nucleus post 8 Gy irradiation. Scale bar = 10 µm. Bottom right image is a composite of the others. **c)** Muscle 4 NMJ from *dATM[sfGFP]*^{post}. Arrows indicate motor neuron axon. Scale bar = 15 µm. Bottom right image in panel is a composite of the others. All images are 2D max intensity projections from 3D z-stacks.

Attempting to localize sfGFP-tagged dATM using its endogenous fluorescence has limitations. Firstly, fixation has the potential to destroy GFP fluorescence by altering its tertiary structure. In addition, evidence from the FlyAtlas and ModEncode data sets suggests that dATM is expressed at low levels, which may make it challenging to detect endogenous dATM[sfGFP] above background autofluorescence in larval tissues. Immunofluorescence using anti-GFP antibodies can overcome these issues since they can still bind to GFP after fixation, and the signal is amplified following secondary antibody incubation.

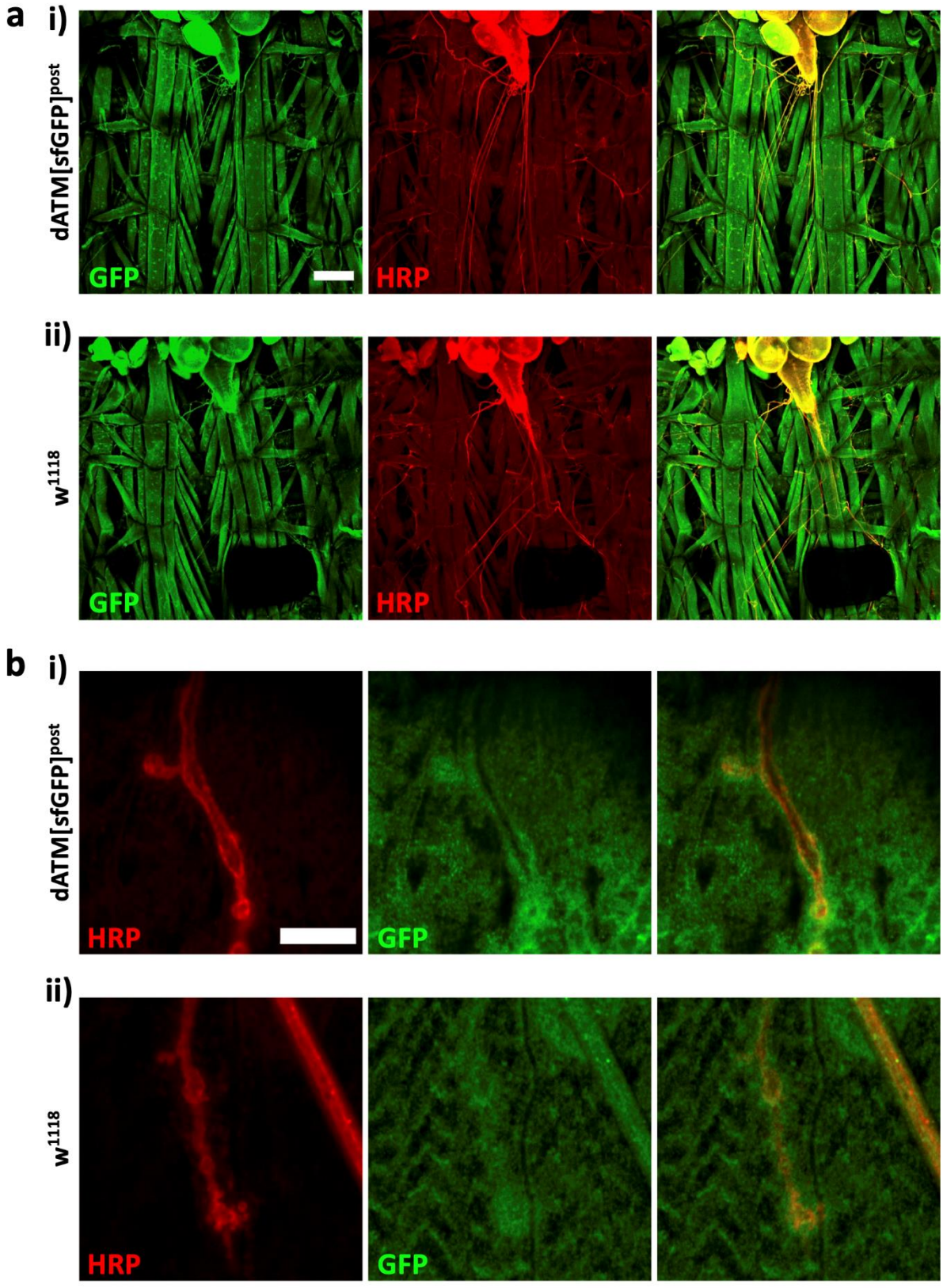
a
i)
dATM[sfGFP]post
GFP
HRP
ii)
w1118
GFP
HRP
b
i)
dATM[sfGFP]post
HRP
GFP
ii)
w1118
HRP
GFP

Figure 4.6: Attempt to localise dATM[sfGFP] using rabbit-GFP antibody. a) Larval "fillet" preparations exposing the CNS and body wall musculature, stained for rabbit anti-GFP (green) and goat anti-HRP (red, neuronal membranes): **i)** Homozygous *dATM[sfGFP]^{post}* larvae; **ii)** *w^{1118}* control larvae. Scale bar = 200 μm. **b)** Representative NMJ images of (**i**) *dATM[sfGFP]^{post}* and (**ii**) *w^{1118}* larvae. Scale bar = 10 μm. In both cases, the control larvae show significant background GFP staining with the same microscope settings. Rightmost image in each row is a composite of the previous two. Anterior = up.

Therefore, localisation experiments with homozygous *dATM[sfGFP]^{post}* larvae were repeated using rabbit anti-GFP (ab290) and 488-donkey anti-rabbit to amplify the GFP signal. Larval "fillet" preps revealed broad staining in the pattern one would expect from a ubiquitously expressed protein such as dATM (fig 4.6a i) – however, wild-type *w^{1118}* control larvae displayed broadly the same staining pattern (fig 4.6a ii). At the NMJ, there looked to be an accumulation of GFP staining surrounding presynaptic boutons with some punctate staining within (fig 4.6b i) but again, control larvae had significant non-specific background staining.

As an alternative, chicken anti-GFP was also tested for dATM[sfGFP] localization. Overall background levels were reduced compared to the rabbit antibody – however, there were similar staining patterns in both the control and *dATM[sfGFP]^{post}* samples in both whole "fillet" preparations and at the NMJ. To test whether these two anti-GFP antibodies had the same off-target background staining, larval preparations were incubated in both together, with different secondary fluorophores for subsequent detection. Once again, controls and *dATM[sfGFP]^{post}* had broadly similar staining patterns, while composite images of the two channels showed significant overlap in the signals (fig 4.7a i-ii). Crucially, this background staining was not a result of non-specific binding of the secondary antibodies as no-primary

controls had only weak levels of fluorescence, with the exception of salivary gland nuclei which were mildly autofluorescent in the 594nm channel (fig 4.7a iii).

Western blots of protein extracts from control and homozygous *dATM[sfGFP]^{post}*, in addition to *dATM[DsRed]*/dATM^{-6}* trans-heterozygotes, incubated in the rabbit anti-GFP primary, showed strong non-specific bands across all samples (fig 4.7b). This may explain the strong background staining in control larvae in the immunofluorescence experiments, particularly when the target construct is expressed at low levels. Note that this is the same antibody used in the previous chapter for the GC3Ai experiments; however, in those experiments, the construct is overexpressed, reducing the relative level of low affinity antibody binding to non-specific background. These results suggest that both rabbit and chicken anti-GFP primaries were unreliable for the detection of tagged proteins with low endogenous expression, as is likely the case with dATM[sfGFP].

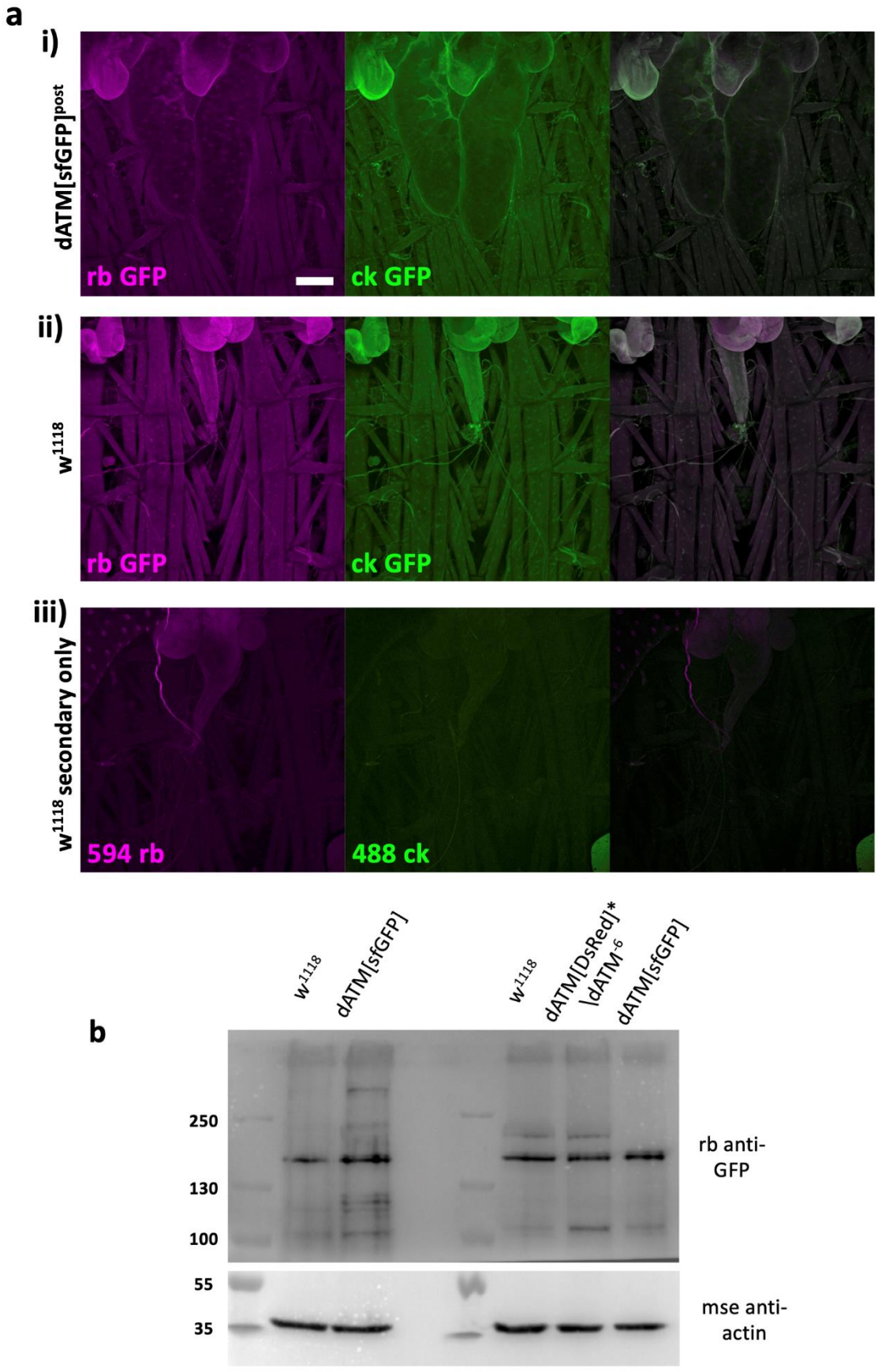
a
i)
dATM[sfGFP]post
rb GFP
ck GFP
ii)
w1118
rb GFP
ck GFP
iii)
w1118 secondary only
594 rb
488 ck
b
w-1118
dATM[sfGFP]
w-1118
dATM[DsRed]*
\dATM-6
dATM[sfGFP]
250
130
100
55
35
rb anti-
GFP
mse anti-
actin

Figure 4.7: Comparison of rabbit and chicken GFP antibodies. a) "Fillet" preparations from an experiment using both chicken- and rabbit-anti-GFP simultaneously, 488-rabbit (green) and 594-chicken (magenta) secondary antibodies: **i)** Homozygous *dATM[sfGFP]*^{post} larvae; **ii)** *w*^{1118} control larvae; **iii)** control with secondary antibodies only. Rightmost images of each panel are a composite of the previous two. Scale bar = 200 µm. Anterior = up. **b)** Western blot of whole larval protein extracts with rabbit-GFP (upper) and mouse-actin (lower), showing strong non-specific GFP bands (monomeric dATM[sfGFP] should be ~350 kDa). Size markers in kDa shown on the left.

A more recent development in immunohistochemistry is the use of camelid heavy chain-only IgGs, which are distinct in their lack of both the light chain and the heavy chain C_H1 domain. The antigen-binding domain of these IgGs can be harnessed separately from the rest of the chain, termed the nanobody due to its small size. These nanobodies are highly specific and sensitive with low background, which made them an ideal candidate for reattempting dATM[sfGFP] localisation. Therefore, the experiment was repeated using an anti-GFP alpaca nanobody, with a 488 anti-alpaca secondary antibody. NMJ preparations displayed reduced background muscle staining compared to the other primary antibodies used (fig 4.8). However, this time there was an unexpected postsynaptic signal reminiscent of DLG staining in both controls and *dATM[sfGFP]*^{post} larvae (fig 4.8a-b). Incubating control preparations in just the 594-HRP and 488 anti-alpaca antibodies revealed that this was an off-target effect of the 488 anti-alpaca secondary, rather than any issue with the nanobody (fig 4.8c). However, no other anti-alpaca secondary was available, which again meant that this paradigm was unreliable for dATM[sfGFP] localization.

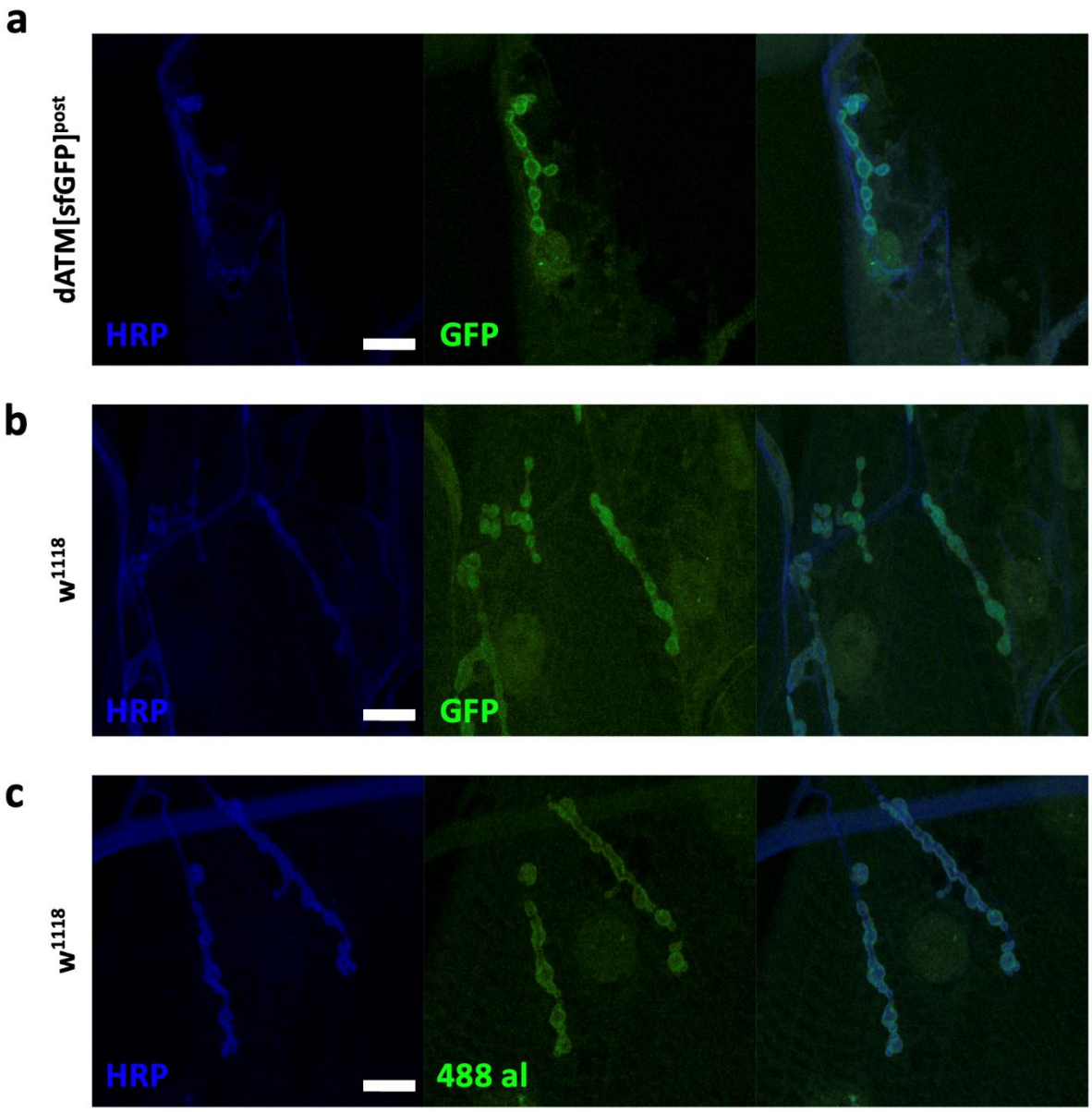

Figure 4.8: Attempt to localise dATM[sfGFP] using alpaca-GFP nanobody. Both **a)** *dATM[sfGFP]*^{post} NMJs and **b)** *w*^{1118} control NMJs show GFP staining in postsynaptic structures. **c)** Control NMJs lacking the alpaca-GFP nanobody and stained with the 488-alpaca secondary still show postsynaptic staining with the same microscope settings. Rightmost images of each panel are composites of the previous two. Scale bars = 15 µm. Anterior = up.

4.2.5 – Structural prediction of dATM[sfGFP]

Although the complementation, NMJ experiments and rescue of the DNA damage response to double-strand breaks all suggest that dATM[sfGFP] is functional, the difficulty in localising the protein with any confidence could imply that sfGFP insertion has subtle effects on dATM structure affecting its folding, function, or expression. In addition, there is the possibility that sfGFP is cleaved from the protein, leading to a functional dATM which is impossible to localize. The lack of published structure of dATM means that it is challenging to predict the effects of inserting a GFP tag in any specific location. However, building upon work above (*Structural comparison of hATM and dATM*), *ColabFold* was used to make a reasonable estimate of any structural changes. These structural predictions are summarized in fig 4.9**.** Briefly, the amino acid sequence of sfGFP after the start codon of dATM, plus the original 1000 N-terminal amino acids that were used to make the previous N-terminal prediction, were input into *Colabfold* and models were generated. The "best rank prediction" was imported into *PyMol* and aligned with the original dATM structural prediction (RMSD = 0.421), to give a reasonable estimate of monomeric dATM[sfGFP] (fig 4.9a). In addition, the dATM[sfGFP] N-terminal fragment was aligned with each chain of the published hATM dimeric crystal structure (7SIC, RMSD = 5.172), using *PyMol's* built-in *cealign* function (fig 4.9b). Subsequently, the dATM structural prediction was aligned onto the stationary dATM[sfGFP] N-terminal fragment to give an estimate of the structure of dimeric dATM[sfGFP] (fig 4.9c), assuming that dATM dimerises in a similar way to hATM.

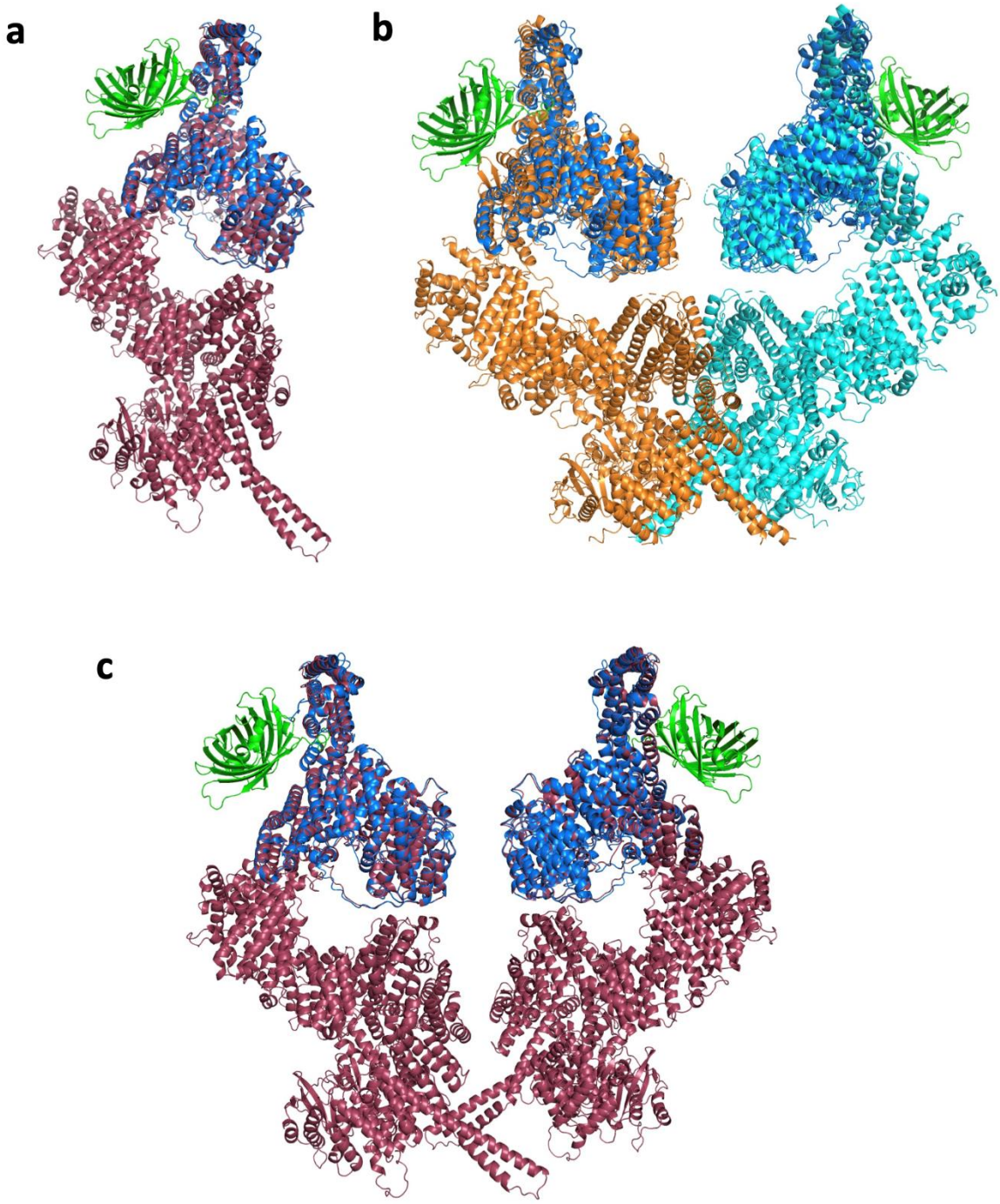

Figure 4.9: Structural prediction of dATM[sfGFP]. a) Predicted location of sfGFP (green) in dATM monomer. Blue is the alphafold predicted N-terminal 1000 residues with sfGFP located after the start codon. Predicted monomeric structure of wild-type dATM shown in maroon. RMSD of alignment = 0.421. **b)** dATM[sfGFP] alphafold prediction aligned (cealign) onto hATM (7SIC) dimer (RMSD = 5.172). Chain A of dimer shown in orange, chain B shown in cyan. **c)** sfGFP dATM aligned onto a putative dATM dimer, based on alignments of the predicted dATM monomeric structure onto the hATM dimer.

The predicted structures and alignments suggest that sfGFP would sit on the outside of the dimer and is therefore unlikely to interfere with dimer formation. In addition, the key functional domains of dATM are in the C-terminal half of the protein and are a significant distance from the insertion of sfGFP. It is not possible to predict the entire structure of dATM[sfGFP] in one attempt using *Colabfold*, so the effects of sfGFP on the folding of the remainder of the protein cannot be predicted. However, it seems more likely that the difficulties in localization of dATM[sfGFP] are either due to low expression of the construct, or cleavage of sfGFP.

4.2.6 – Attempting to rescue dATM with overexpression of hATM

In addition to localizing endogenous dATM, FLAG-tagged human ATM cDNA from the *pcDNA3.1(+)Flag-His-ATM wt* vector (AddGene #31985) was cloned into the pUAST-attB vector to enable expression using the GAL4/UAS system. Initial testing was performed in S2 cells by co-transfecting pUAST-attB-hATM along with pMT-GAL4 and incubating in 500 µM $CuSO_4$ for 12 hours. Staining for anti-FLAG revealed that transfection and expression of the construct was successful, with hATM expression seen predominantly in the cytosol and not associated with DNA (fig 4.10). Subsequently, pUAST-attB-hATM was injected into embryos and incorporated into the attP40 and attP2 phiC31 landing sites to make a second and third chromosome UAS-hATM stock, respectively.

Overexpression of Flag-hATM using the pan-neuronal Elav-GAL4 driver revealed diffuse staining throughout the nuclei and cytosol of ELAV-positive cells (fig 4.11a-c). Larger surface cells which are likely larval neuroblasts showed a particularly strong expression of Flag-hATM. Axons leaving the CNS showed a faint Flag signal, although control larvae also had

a faint signal, so this was likely background fluorescence. No Flag-hATM was observed at the NMJ (fig 4.11d).

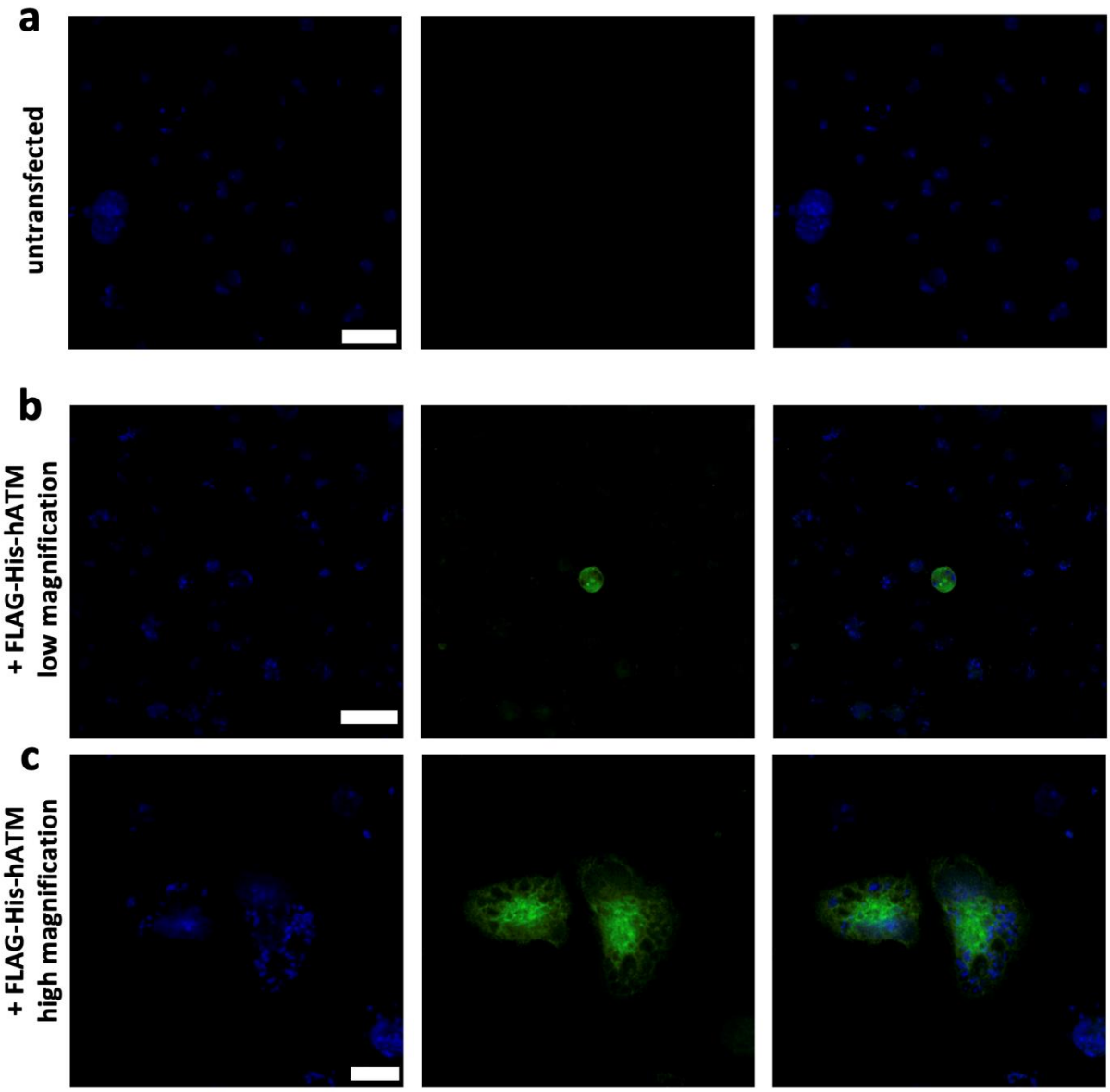

Figure 4.10: Expression of FLAG-tagged human ATM in S2 cells. a) Untransfected cells. **b)** S2 cells transfected with FLAG-His-hATM cDNA, low magnification (scale bars = 30 µm). **c)** S2 cells transfected with FLAG-His-hATM cDNA, higher magnification (scale bar = 10 µm). Rightmost images in each set are a composite of the previous two.

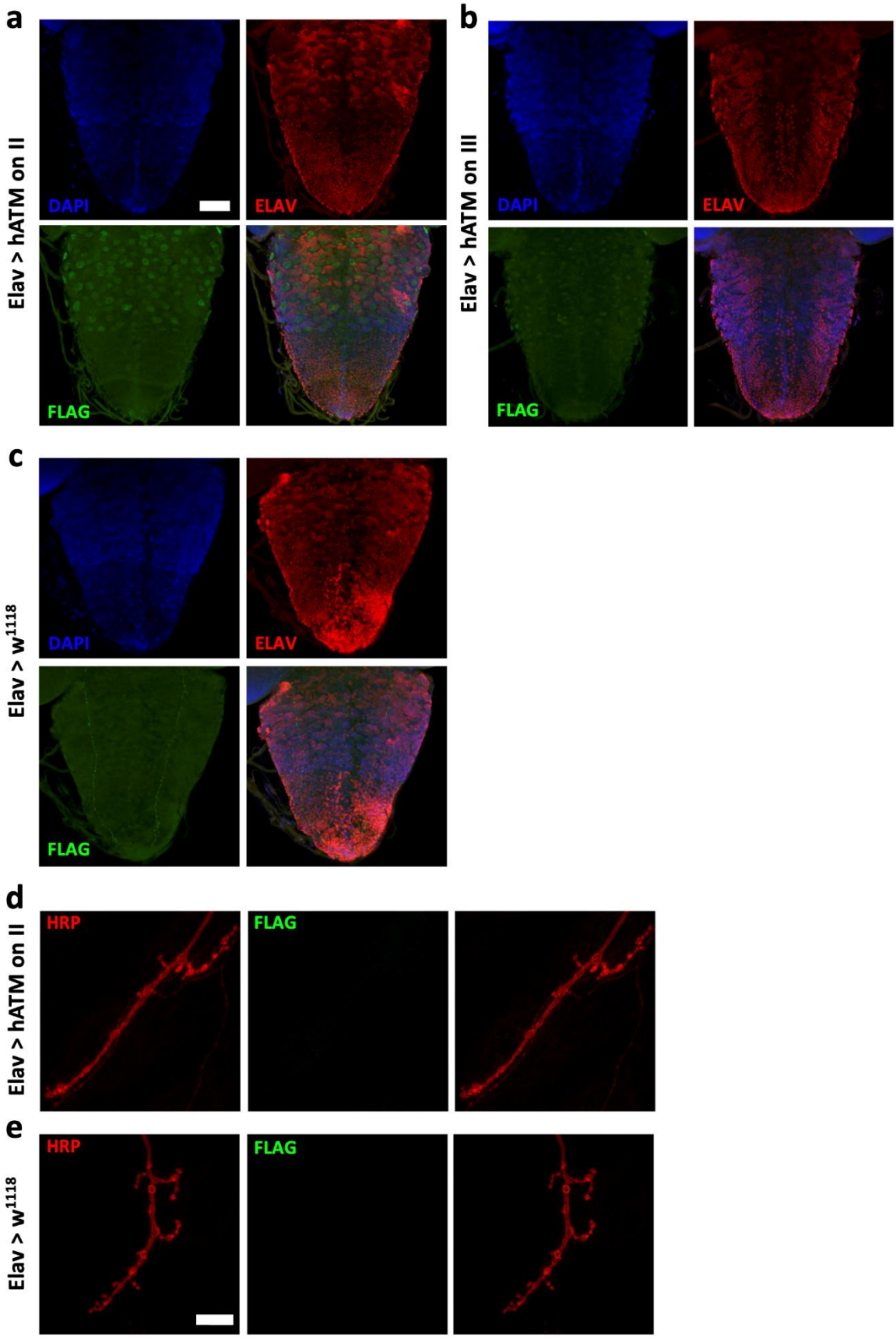
a
Elav > hATM on II
DAPI
ELAV
FLAG
b
Elav > hATM on III
DAPI
ELAV
FLAG
c
Elav > w1118
DAPI
ELAV
FLAG
d
Elav > hATM on II
HRP
FLAG
e
Elav > w1118
HRP
FLAG

Figure 4.11: Expression of FLAG-tagged hATM in the larval nervous system. *Upper:* Elav-GAL4 was used as the pan-neuronal driver line crossed to **a)** *UAS-hATM on II*, **b)** *UAS-hATM on III*, and **c)** w^{1118} as the negative control. The bottom-right image in each panel is a composite of the others. Scale bar = 50 µm. *Lower:* larval NMJ preps from Elav-GAL4 crossed to **d)** UAS-hATM on II and **e)** w^{1118} as the negative control. Rightmost image is a composite of the previous two. Scale bar = 15 µm. All images are max intensity 2D projections of 3D z-stacks. Anterior = up.

To test whether hATM could functionally complement dATM in larval NMJ development, dsRNA-mediated knockdown of dATM at 27°C was repeated +/- UAS-hATM, using the OK371-GAL4 driver. The results from the NMJ dissections were mixed (fig 4.12a). Overexpressing hATM alone with OK371-GAL4 was sufficient to lead to a reduction in surface area, while for both surface area and bouton count, the combined dATM knockdown with hATM overexpression had an intermediate phenotype that was not significantly different from either the control or dATM knockdown alone (fig 4.12a i-ii). For active zone count, both alone and in combination with dATM knockdown, overexpression of hATM resulted in a significant reduction compared to the controls (fig 4.12a iii). Taken together, the results suggest that hATM may be able to complement certain aspects of NMJ development and maturation but is detrimental to others.

4.2.7 – Overexpression of dATM[msGFP2]

An alternative strategy for protein localization in *Drosophila*, rather than knock-in of a tag into the endogenous gene, is to express ectopically a tagged version of the protein of interest. To achieve this, a construct was synthesized containing the full-length cDNA of *dATM* with a codon-optimized *monomeric superfolder GFP2 (msGFP2)* inserted after Thr485. msGFP2 was chosen due to its ability to maintain fluorescence even in highly oxidizing environments, and for the point mutations in the dimerization interface (Valbuena *et al.*, 2020). This latter point

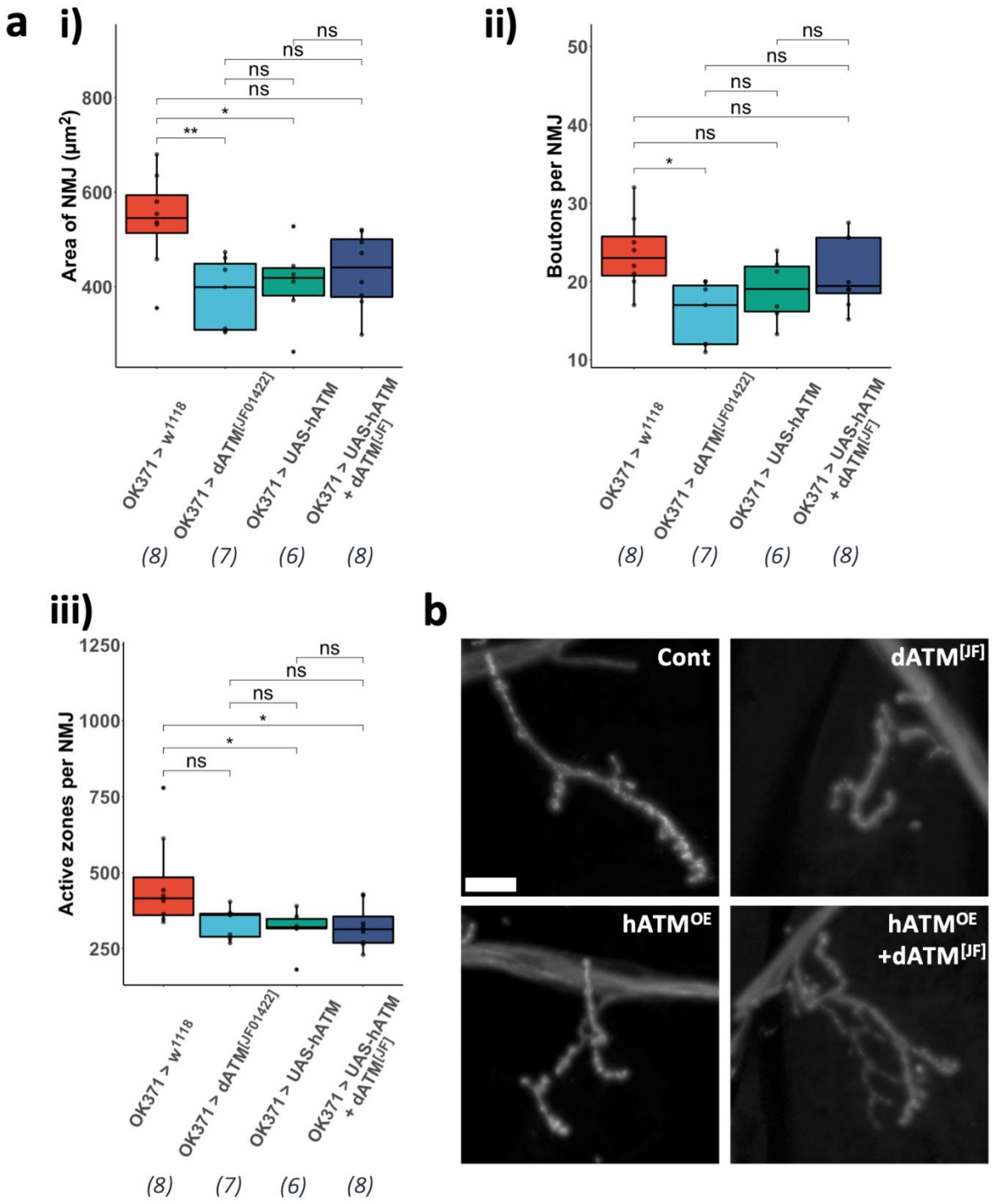

Figure 4.12: Overexpression of hATM +/- dATM knockdown. a) Quantification of NMJ morphometrics - **i)** NMJ surface area, **ii)** bouton count, and **iii)** active zone number. All data scaled to mean surface area of muscle 4. N numbers indicated below each genotype. Adjusted p-values from one-way ANOVA with Tukey's Honest Significant Difference multiple comparisons test, p≤0.05 *, p≤0.01 **. **b)** Representative images of NMJs of the indicated genotypes. Scale bar = 15 µm. Anterior = up.

was particularly important for labelling a protein such as dATM which, if its function is truly paralogous to hATM, will have different downstream targets dependent upon its dimerization status.

Thus, it was important to avoid forced dimerization through interactions between GFP molecules. The location of the insertion (Thr485) was chosen with reference to other work being performed in the lab – attempting to make a CFP/YFP hATM FRET sensor of dimeric hATM – where the location of fluorescent protein insertion was chosen to result in predicted close interaction between the fluorophores, enabling FRET. *ColabFold* predictions of dATM structure were aligned to the published hATM structure, and it was determined that Thr485 was the closest-in-space residue in dATM to the residues chosen for the CFP/YFP insertion into hATM.

Subsequently, the cDNA of *dATM[msGFP2]* was subcloned into pUAST-attB and injected into phiC31 landing sites as in the above UAS-hATM experiments. Expression of UAS-dATM[msGFP2] was driven by *OK371-GAL4* to generate larvae of the following genotype: *+/+;OK371-GAL4/UAS-dATM[msGFP2];+/+*. Unlike with *dATM[sfGFP]*^{post} larvae, green fluorescence was observable using a standard fluorescence dissection scope, in both the CNS and salivary glands (*OK371-GAL4* is known to also drive expression within salivary gland tissues and some interneurons, as well as motor neurons). To enhance the signal, larval preparations were incubated in chicken anti-GFP, as well as anti-HRP and TOPRO3 for visualization of neuronal membranes and nuclei, respectively. 2 examples of the “fillet” preparations are shown in fig 4.13a-b, where there is clear GFP expression within the CNS along the ventral nerve cord (VNC), in addition to salivary glands. GFP can also be seen along axons leaving the

VNC. Closer inspection of the VNC reveals strong GFP expression within rows of midline motor neurons' cell bodies and within more peripheral motor neurons, in addition to the axons (fig 4.13c). There appears to be fainter, diffuse green staining throughout the CNS which could be dATM[msGFP2] expression in interneurons and connections between neurons, however it is possible that this is also off-target background staining given the issues with the anti-GFP antibodies described above. Higher magnification of motor neuron cell bodies reveals that dATM[msGFP2] expression is predominantly cytosolic.

At the NMJ, OK371-driven dATM[msGFP2] expression is less diffuse and far more punctate (fig 4.14). There is some low-level fluorescence within muscles, with punctate staining particularly within muscle nuclei (fig 4.14a, white arrowhead), which could be due to "leaky" expression of the construct. The axon (fig 4.14b) displays very bright puncta of dATM[msGFP2]. Comparing the region of the axon leaving the VNC in fig 4.13c with the axon region proximal to the NMJ in fig 4.14b, it appears that the msGFP2 signal becomes more punctate in the more distal parts of the neuron. At the NMJ itself, presynaptic boutons contain a particularly high concentration of msGFP2 puncta than the rest of the synapse (fig 4.14c, white arrowheads). Taken together, this would suggest that neuronal dATM is primarily cytosolic and localises to axonal and presynaptic vesicular structures.

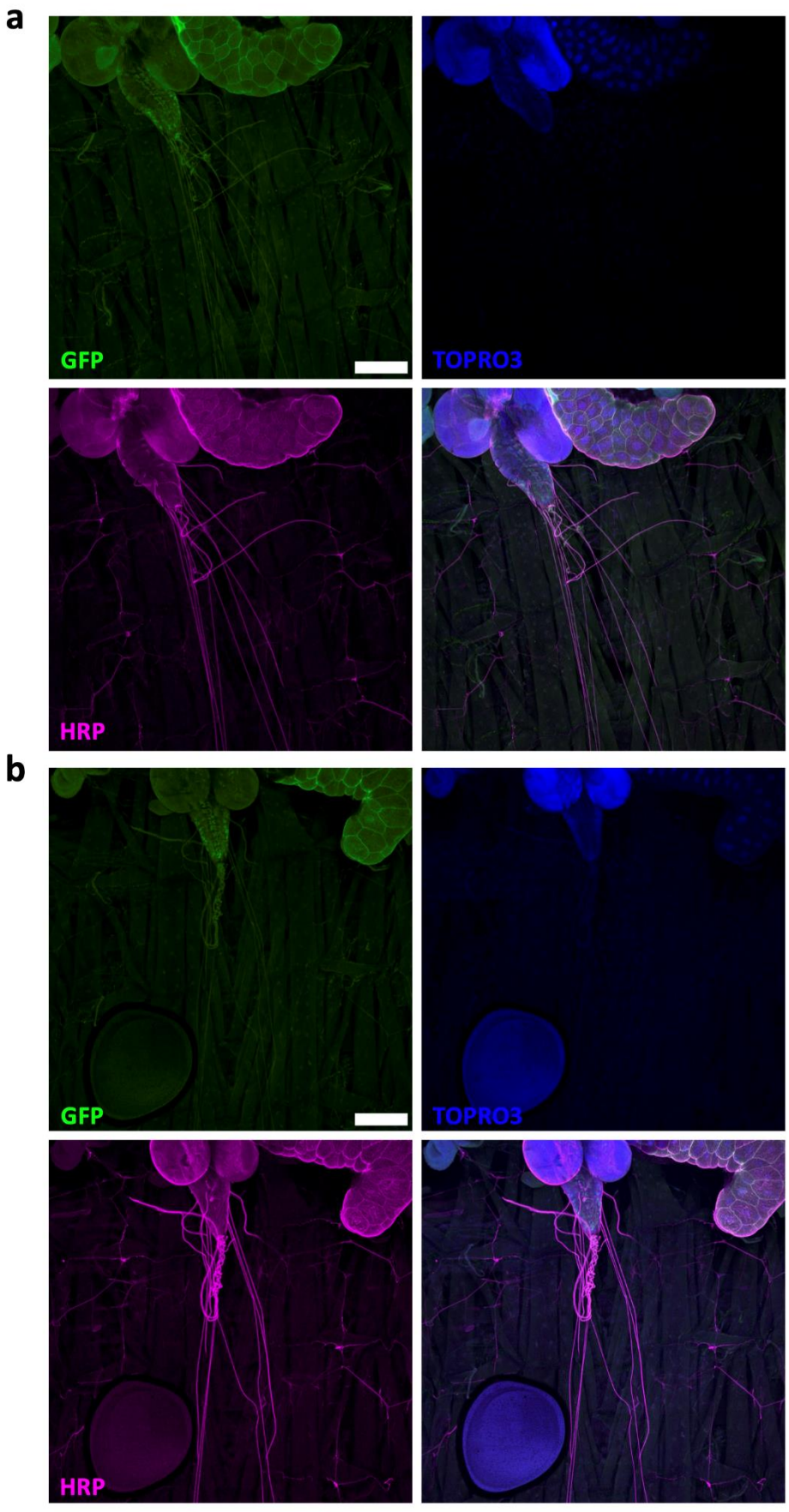
a
GFP
TOPRO3
HRP
b
GFP
TOPRO3
HRP

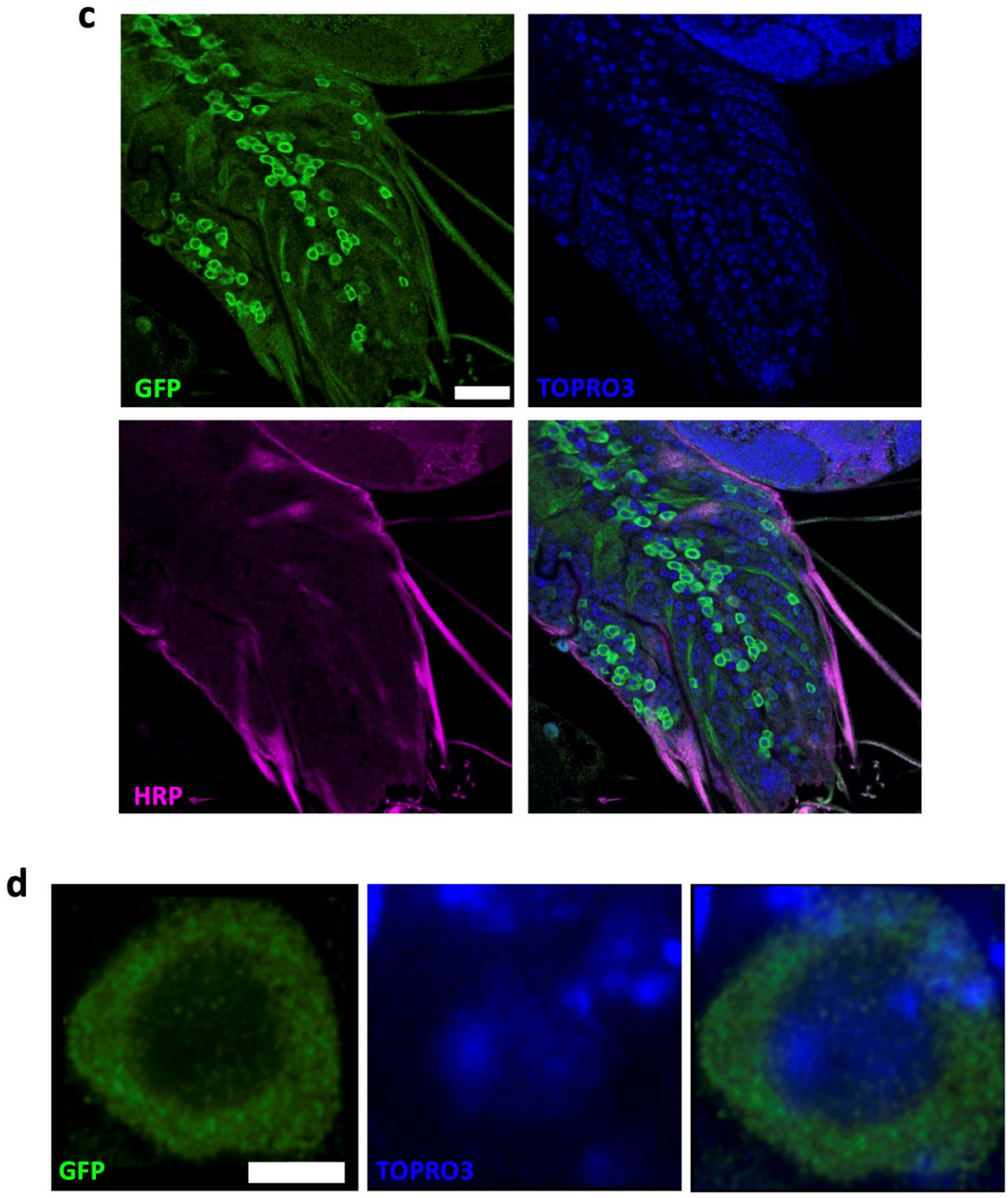

Figure 4.13: Overexpression of dATM[msGFP2] using *OK371-GAL4* driver. a, b) Larval "fillet" preparations of the genotype *+/+;OK371-GAL4/UAS-dATM[msGFP2];+/+.* Anterior = up. **c)** Larval ventral nerve cord, showing expression of dATM[msGFP2] in pattern of OK371-GAL4 expression (primarily motor neurons, e.g., red dashed box) – **d)** Higher magnification image of dATM[msGFP2]-positive neurons showing primarily cytosolic localisation. Scale bars: a,b = 200 µm; c = 30 µm; d = 2 µm. Bottom right or rightmost image is a composite of the others in each panel.

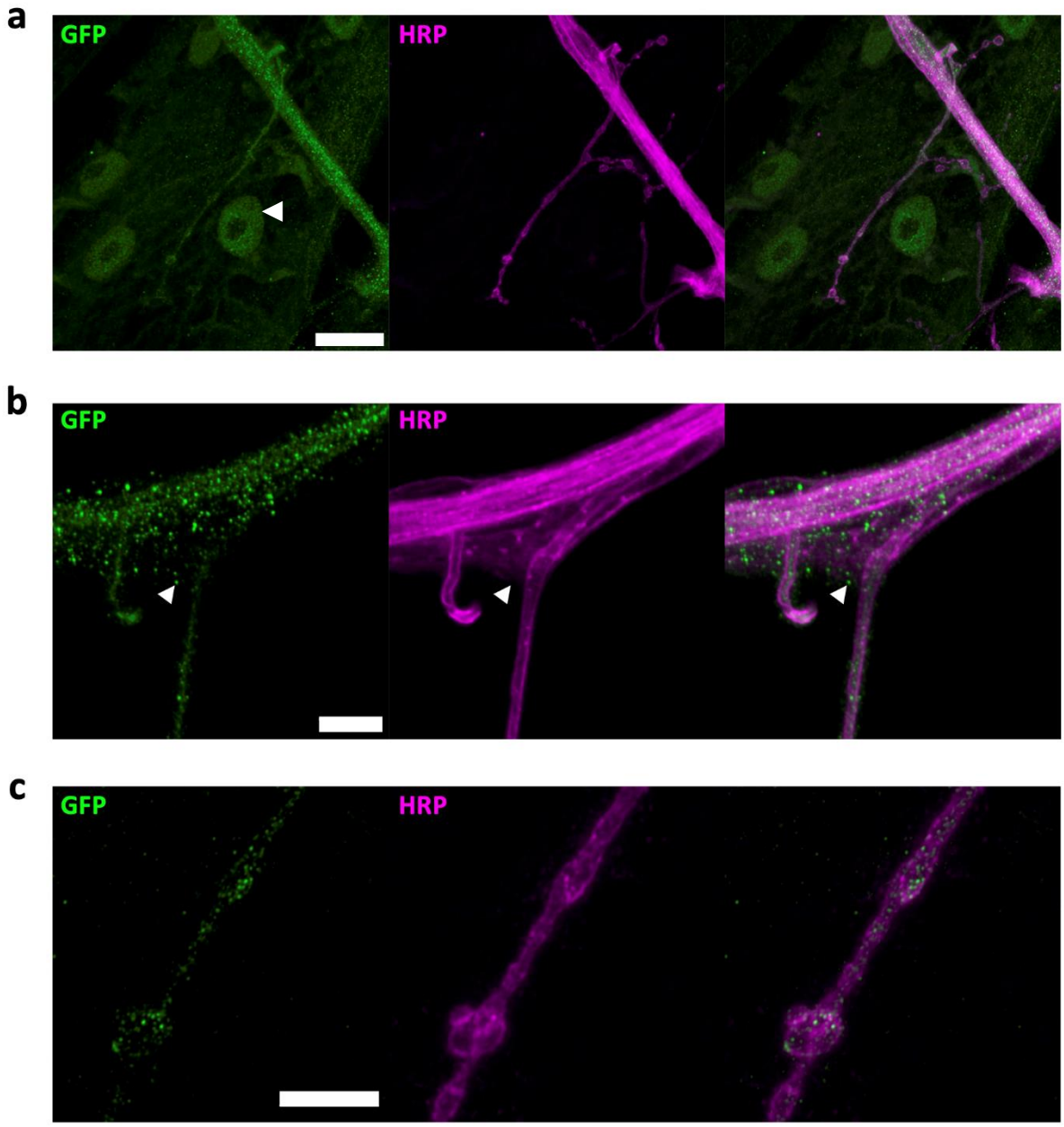

Figure 4.14: Punctate staining of dATM[msGFP2] in axons and the NMJ. a) Lower magnification image of whole muscle 4 NMJ of *+/+;OK371-GAL4/UAS-dATM[msGFP2];+/+* larvae. White arrowhead indicates a muscle nucleus. **b)** Higher magnification of motor neuron axon. Some foci of GFP appear outside of neuronal membrane (white arrowheads). **c)** Higher magnification image of NMJ, generated by manually selecting a ROI around the NMJ – puncta of GFP appear to be denser within "boutons" (white arrowheads). Scale bars: a = 20 µm; b,c = 5 µm. Rightmost image of each panel is a composite of the others. Anterior = up.

4.3 – Discussion

In this chapter, CRISPR/Cas9 gene editing was used to successfully introduce *scarless DsRed::sfGFP* into the endogenous *dATM* locus. The initial *dATM[DsRed]** null mutant behaves as expected, with disruptions to NMJ structure, trans-heterozygous pharate lethality with other *dATM* null mutants and failure of those trans-heterozygous flies to phosphorylate H2Av upon induction of DNA damage by ionising radiation. Interestingly, it was observed during the complementation crosses that most combinations of the different *dATM* mutations are trans-heterozygous pharate lethal, while they are all homozygous inviable before the 3rd instar larval stage (with the exception of dATM^{-8} at lower temperatures as seen elsewhere (Petersen, Rimkus and Wassarman, 2012; Rimkus and Wassarman, 2018)). Pharate lethality is commonly seen in fly models of locomotor disorders such as ALS and Huntington's (Krench and Littleton, 2013; Frickenhaus *et al.*, 2015; Layalle *et al.*, 2021), which is further evidence for the role of dATM in the development of the *Drosophila* nervous system.

Linearisation of the CRISPR HDR construct *in vivo* has been reported elsewhere to increase CRISPR/Cas9 gene editing efficiency, even with homology arms as short as 100 nucleotides (Kanca *et al.*, 2019). However, in this case, the method was inefficient, with only 1 positive integration of *scarless-DsRed-sfGFP* from the ~280 larvae that survived microinjection. More recent analysis of the secondary structure of the gRNA targeting the *dATM* locus using the Platinum CRISPR tool (Arnold & Soller, unpublished; https://platinum-crispr.bham.ac.uk/predict.pl) revealed that the gRNA structure was "compromised," which may account for the inefficiency of the edit. To address this going forward, the gRNA can be redesigned such that Platinum CRISPR predicts "high" efficiency. In addition, a Cas9-

expressing fly line with a *lig4* mutant background could be used for injections. The *lig4* mutation has been shown to inhibit non-homologous end joining, increasing the likelihood that the Cas9-generated double strand break will be repaired by homologous recombination, increasing integration efficiency (Beumer *et al.*, 2008; Cao *et al.*, 2020).

Compounding the inefficiency issues, there was also reason to believe that the *dATM[DsRed]** stock contained either a second insertion site of the CRISPR construct, or an off-target mutation. After combining *dATM[DsRed]** with piggyBac transposase and excision of the *scarless-DsRed* motif, the resultant *dATM[sfGFP]*^{pre} stock was able to rescue the lethality of other *dATM* mutant lines, suggesting it was a functional allele of *dATM*. However, its inability to rescue *dATM[DsRed]** or become homozygous is evidence of off-target CRISPR effects. The fact that by backcrossing the *dATM[sfGFP]*^{pre} line to a control line (to generate *dATM[sfGFP]*^{post}) restored homozygous viability and allows complementation of *dATM[DsRed]** suggested any extraneous mutations were successfully outcrossed.

Multiple diagnostic PCRs and rounds of sequencing confirmed, at least at the genetic level, correct scarless excision of 3xP3::DsRed post piggyBac expression. The resultant dATM[sfGFP] protein product rescued pharate lethality and phosphorylation of γH2Av in the DNA damage response. Within larval salivary glands, the construct also seemed to localize to sites of DNA damage following irradiation, as would be expected from functional dATM, and supports previous observations using overexpressed FLAG-dATM in S2 cells (Hong and Choi, 2013). However, further efforts to localize the protein using endogenous sfGFP fluorescence were hampered by the likely low levels of protein expression, resulting in a level of fluorescence that was hardly distinguishable above typical larval tissue autofluorescence. Attempts to overcome this with immunohistochemistry were problematic with every

attempted combination of anti-GFP primary and their concomitant secondaries. For some reason, these commonly used anti-GFP antibodies, when used on larval preparations to detect low levels of protein expression, lead to significant background staining even in control larvae. Inexplicably, the anti-alpaca secondary alone immunoreacted with a target in the postsynaptic density, reminiscent of DLG staining (see previous chapter). Western blotting using the rabbit-GFP antibody revealed strong non-specific bands in control lanes. This antibody is the same as that used for the GC3Ai staining in the previous chapter, which suggests that an overexpressed GFP construct leads to less binding of the antibody to lower-affinity background targets.

An alternative explanation for the difficulty in localizing dATM[sfGFP] could be that insertion of sfGFP leads to misfolding of the protein, and its subsequent degradation. However, there was clear evidence for the restoration of protein function. As discussed previously, there is no published structure for dATM, let alone dATM[sfGFP]. However, using Colabfold, it is possible to generate a reasonable estimate of the effects of sfGFP insertion on the predicted structure of dATM. The results above showing the location of sfGFP within dATM[sfGFP] do not give any clear indication that sfGFP would cause any issues for dATM's function, interactions with other proteins or putative dimerization. It also leaves open the HEAT repeat region of the N-terminus which are known to be required for protein-DNA interactions (Piazza *et al.*, 2014; Lau *et al.*, 2016). There is some potential steric hindrance of the TAN motif required for recruitment of ATM to double-strand breaks (Seidel, Anderson and Blackburn, 2008) and of the p53 binding domain (Baretić *et al.*, 2017), although the linkers attaching sfGFP to the rest of dATM should allow for flexibility – the structural prediction from Colabfold is just a snapshot of one conformation and does not take flexibility into account. Further, the results above suggested dATM[sfGFP] could still be recruited to sites of DNA

damage. Nevertheless, there are two possibilities that cannot be fully ruled out. The first is the potential for sfGFP to be cleaved leading to functional dATM lacking the sfGFP tag. The other is that insertion of sfGFP in the N-terminus could have disrupted putative promoter sequences, leading to misexpression or outright reduced expression. Generally, N-terminal GFP fusions are avoided because of the possibility of aberrant subcellular localization brought on by inappropriate masking of signal sequences (Palmer and Freeman, 2004). The reasons for inserting sfGFP at the N-terminus of dATM in this thesis arose from the fact that dATM's functional domains are at the C-terminus, as is dimerization interface for hATM (Lau *et al.*, 2016; Baretić *et al.*, 2017). Additionally, the N-terminal insertion using the Scarless-sfGFP::DsRed system allowed first for the generation of a null allele due to the presence of the STOP codon downstream of first piggBac repeat. Regarding aberrant localization, based on structural predictions discussed earlier, the predicted dATM nuclear localization sequence should not be masked by insertion of sfGFP at the N-terminus. Another more technical reason for the difficulty in localizing endogenous dATM[sfGFP] are reports of increased susceptibility to photobleaching of engineered sfGFP constructs (Pédelacq *et al.*, 2006; Valbuena *et al.*, 2020). Taken together, it was determined that localisation studies necessitated the creation of tagged overexpression constructs.

A common goal when using *Drosophila* to model human disorders is to test whether the human protein in question can complement the function of the orthologous *Drosophila* protein, known as *heterologous rescue* (Ecovoiu *et al.*, 2022). This is generally achieved through the overexpression of human protein cDNA under UAS control using GAL4 drivers either ubiquitously or in relevant tissues, e.g., pan-neuronally for neurodegenerative disorders. Human ATM has not previously been introduced into flies to test heterologous

rescue. For this chapter, the aim was to kill two birds with one stone – by overexpressing a tagged form of hATM, both complementarity and localisation could be studied. Like dATM[msGFP2] (*see below*), FLAG-hATM showed predominantly cytosolic localization, whether tested *in vitro* in S2 cells or *in vivo* being expressed pan-neuronally using Elav-GAL4. Unlike dATM[msGFP2], no expression of FLAG-hATM was detected at the NMJ. Ubiquitous overexpression of hATM was unable to restore adult viability to transheterozygous dATM mutants (not shown), while rescue of the NMJ structural phenotype of dATM knockdowns was mixed. This is not entirely unexpected. There are various examples of like-for-like gene replacement almost completely abrogating the *Drosophila* mutant phenotype (reviewed in (Ecovoiu *et al.*, 2022), such as ALS-associated *dSod1* being rescued by expression of hSOD1 (Parkes *et al.*, 1998; Mockett *et al.*, 2003), or expression of human Huntingtin (Htt) rescuing autophagy, longevity and locomotor defects of *Drosophila Htt* nulls (Rui *et al.*, 2015). However, with a "master regulator" such as ATM having a wide variety of downstream targets contingent on its localization and mechanism of activation, a complete rescue was improbable, and there are no examples of heterologous rescue of mutations in proteins associated with the DNA damage response. In addition, FLAG-hATM was overexpressed from a single, non-codon-optimized, 9.2kb cDNA rather than at endogenous levels, and there was no guarantee of it being correctly folded. Another consideration is that, although dATM and hATM are predicted to have similar structures, there is a significant divergence in the actual protein sequence, with only ~30% sequence similarity overall between the two proteins, with no similarity at all in the FATC domain. Note that in $dATM^{-8}$, the sole amino acid substitution occurs within the FATC domain, and this is sufficient to confer it as a temperature-sensitive null allele. In addition, the structural comparisons suggested that the likeliest candidate of a

homologous residue to hATM C2991, required for its redox activation (Guo *et al.*, 2010), is contained within the dATM FATC domain. A future approach may be to generate a chimeric hATM protein with the FATC domain replaced with that of dATM, and rather than overexpress the protein, to perform endogenous gene replacement whereby the sequence for hATM is cloned into the *dATM* locus. This would enable hATM to be expressed in the same pattern as dATM at endogenous levels, as has been performed elsewhere such as with TDP-43 (Chang and Morton, 2017).

Glutamatergic overexpression of dATM tagged with msGFP2 (dATM[msGFP2]) suggested that, consistent with the findings of ATM in mammalian neurons (Barlow *et al.*, 2000; Li *et al.*, 2009), dATM in *Drosophila* neurons displays significant cytosolic localisation. The pattern of expression within cell bodies and axons leaving the VNC was diffuse but became more punctate at distal points along the axon, while at the synapse, it was particularly punctate with higher densities within presynaptic boutons. Previous work looking at dATM localization has been limited to studying overexpression of a FLAG-tagged construct in S2 cells (Hong and Choi, 2013), so the identification of dATM localizing to synaptic boutons in *Drosophila* is novel. It nevertheless supports observations from mammalian models which have observed ATM co-localizing with presynaptic vesicle markers (Vail *et al.*, 2016), which supports the use of *Drosophila* as a model for the biology of neuronal ATM. However, it has not yet been tested whether UAS-dATM[msGFP2] is able to complement *dATM* mutations, rescue survival or other dATM functions. Future work would be to characterise what the foci of dATM are, e.g., whether they correspond to synaptic vesicles, and to answer the question as to what the functional role of presynaptic dATM is. The latter of those aims is the subject of the next chapter.

Chapter 5 – How does presynaptic dATM regulate neurodevelopment and homeostasis?

5.1 – Introduction

Chapter 3 demonstrated the requirement of presynaptic dATM in larval NMJ development at the structural, functional, and behavioural level. In *Chapter 4,* evidence was presented that showed GFP-tagged dATM shows predominantly cytosolic expression in neurons and localises to presynaptic puncta. As a master regulator of the DNA damage response, the synaptic localisation of ATM, which has also been observed in mammalian models (Vail *et al.*, 2016), is curious. However, increasing evidence is accumulating for a cytosolic role of ATM, such as its ability to upregulate autophagy (Hwang *et al.*, 2023), particularly in response to oxidative stress (OS) signalling (Alexander *et al.*, 2010), and the role it plays in mitophagy (Qi *et al.*, 2016). Whether dATM interacts with these pathways in a similar way to hATM is not known.

As shown in *Chapter 1*, while the sequence of dATM overall is poorly conserved with hATM, the functional domains (e.g., FAT, PI3K) are well conserved and the *ColabFold* predicted structure maps well onto the published hATM structure. Some of the key residues for hATM's function in different contexts have been established, including the nuclear localisation sequence (Young *et al.*, 2005), the phosphorylation site on S1981 (Bakkenist and Kastan, 2003) and acetylation site on K3016 for DDR activation (Sun *et al.*, 2007), and the C2991 site for intermolecular disulphide bond formation in the dimer induced by redox activation (Guo *et al.*, 2010; Baretić *et al.*, 2017). While the evidence of like-for-like equivalent residues in dATM is ambiguous, *Chapter 1* elucidated potential homologous residues in dATM using the structural alignments. Given the overall conservation of structure and the sequences of the functional domains, it is likely that dATM is activated in a similar way in equivalent pathways.

The interplay of OS signalling and autophagy in *Drosophila* NMJ development is well established (Milton and Sweeney, 2012). Both oxidative stress and autophagy can act as positive regulators of NMJ growth (Shen and Ganetzky, 2009; Milton *et al.*, 2011), but these processes must be held in balance as either in excess can lead to neurodegeneration (Liu and Levine, 2015; Fracassi *et al.*, 2021). An additional factor explored in *Chapter 3* is the role for neuronal activity, since larvae reared at increasing temperatures saw a concomitant expansion of the NMJ and increase in locomotor activity, up to a point at which it also became deleterious; while dATM knockdown larvae failed to respond appropriately to increasing rearing temperature. The dATM knockdown larval NMJ structural phenotype could be a result of several scenarios:

1. Reduction of developmental neuronal activity levels or failure to respond appropriately to neuronal activity.
2. Reduction of autophagic flux.
3. Failure to respond to ROS signalling – or excessive ROS leading to degeneration.

The initial hypothesis for how dATM functions in NMJ development and homeostasis is summarised in *Model summary 1* (below). In summary, the hypothesis is that under normal conditions, modest increases of ROS lead to redox-activation of synaptic dATM, where it upregulates autophagy through the AMPK-TORC1 pathway, leading to NMJ expansion. This process is held in balance with other dATM downstream targets, such as p53 and the pro-apoptotic machinery, and thus the hypothesis is that under conditions of excessive ROS, this pathway predominates leading to apoptosis and neurodegeneration. In the case of presynaptic dATM knockdown, there are two possibilities under this model. The first is that the NMJ fails to respond to moderate increases in ROS – which could be a readout of neuronal

activity – and thus fails to induce autophagy and expand properly. The second is that the dATM knockdown NMJ is constitutively oxidatively stressed or has a lower threshold at which ROS levels become toxic, and thus the NMJ shows signs of degeneration. These hypotheses are not mutually exclusive: they may both be true depending on the cellular context. The latter has some support from evidence in *Chapter 3* where posterior motor neurons in the dATM knockdowns showed signs of degeneration at higher rearing temperatures. However, the response of these neurons to manipulations of neuronal activity, ROS levels, and the autophagy machinery is not known.

This is the model tested and refined throughout this chapter. Given that the expression of GFP-tagged dATM was primarily cytosolic, and that knockdown of other DNA damage response proteins both upstream and downstream of dATM had no effect on NMJ development, it made sense therefore to focus on the known cytosolic interactors of ATM. A targeted screen of modifiers of the dATM knockdown phenotype was performed by combining dATM dsRNA lines with overexpression or knockdown of proteins involved in ROS generation and scavenging, and autophagy regulators. Any epistatic enhancer/suppressor interactions that come from this screen should give an indication whether ATM signalling occurs through these pathways and thus how presynaptic dATM regulates NMJ development and homeostasis. In addition, since the model would predict deficits in autophagy, mitophagy or OS regulation, various techniques were employed to establish whether these existed and therefore could explain the dATM knockdown phenotype.

Model summary 1

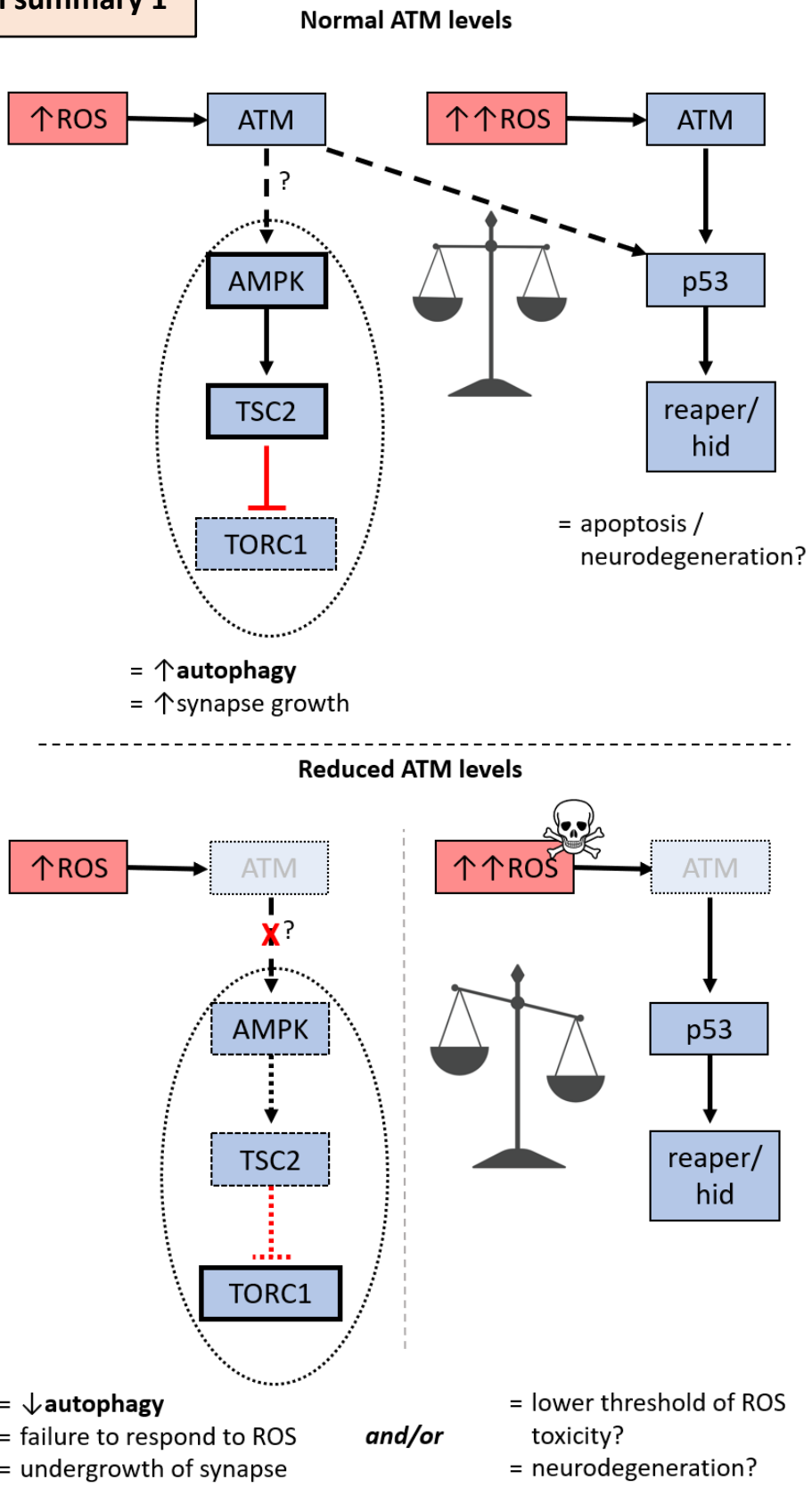

Model summary 1: *Top* – Under normal conditions, ATM may help mediate the balance between ROS-induced growth and toxicity. Redox-activated ATM can phosphorylate AMPK leading to downregulation of TORC1 activity, upregulation of autophagy and NMJ growth. ATM can also signal through p53 to upregulate apoptosis in response to excessive oxidative and genotoxic stress. These processes are held in a fine balance. *Bottom* – Reduction of ATM could result in a failure to induce autophagy upon ROS signalling, leading to synaptic undergrowth. Alternatively, the threshold for ROS toxicity could be reduced in ATM-deficient neurons. These hypotheses are not mutually exclusive.

5.2 – Results

5.2.1 – Presynaptic dATM knockdown sensitises the NMJ to excitotoxicity

Neuronal overexpression of the temperature-gated cation channel, TrpA1, and activation of the channel by rearing larvae at ≥27°C leads to an overgrowth of the third instar NMJ as measured by bouton number (Oswald *et al.*, 2018). Activation of this channel at 27°C leads to tonic stimulation of neurons at frequencies of ~20-30 Hz, even when cell bodies are disconnected by severing the axons (Pulver *et al.*, 2009). It was also shown that hyperstimulation of motor neurons in this way leads to an increase of mitochondrial ROS at the NMJ, and that scavenging this extra ROS through overexpression of catalase abrogates the TrpA1-induced overgrowth (Oswald *et al.*, 2018). However, in addition to acting as a positive regulator of synapse growth, excessive ROS can lead to excitotoxic neurodegeneration (Rego and Oliveira, 2003) – thus a balance between these two processes must be held. The dATM knockdown phenotype of undergrown synapses could therefore be explained by one of two possibilities: either the neurons are hypersensitive to ROS and are thus showing signs of degeneration (as seems to be the case with the posterior neurons in dATM knockdown larvae explored in *Chapter 3*); or the neurons fail to sense normal fluctuations in ROS during synapse development and homeostasis and thus fail to expand appropriately – summarised in *Model summary 1* above.

If the latter is true, and if this ROS-induced growth is at least partially mediated by dATM signalling, then combining dATM knockdown with tonic activation of TrpA1 may lead to a rescue of the phenotype, by providing a stronger ROS signal to overcome the "undergrowth." To test this, motor neuron knockdown of dATM driven by OK371-GAL4 and dATM dsRNA was combined with overexpression of UAS-TrpA1 and larvae reared at 27°C. Consistent with other published work (Oswald *et al.*, 2018), overexpression of TrpA1 and tonic activation of motor neurons was sufficient to induce overgrowth of the NMJ as measured by normalised surface area and bouton count, although the data were highly variable (fig 5.1a i-ii). There was no significant increase in active zone number per NMJ (fig 5.1a iii). Combining dATM knockdown with TrpA1 overexpression and activation was lethal prior to wandering third instar, suggesting that dATM knockdown sensitises larvae to excitotoxic neurodegeneration. This lethality was dependent on activation of TrpA1, since raising larvae at 21°C restored viability of this genotype (not shown).

It was possible that the lethality of dATM knockdown in the presence of TrpA1 expression was due to overwhelming DNA damage as a result of the oxidative stress generated by neuronal hyperstimulation. To test whether hyperstimulation leads to a detectable DNA damage response, CNSs were dissected from larvae of the genotype *OK371-GAL4, UAS-mCD8::GFP/UAS-TrpA1* raised at 21°C ($TrpA1^{OFF}$) or 27°C ($TrpA1^{ON}$) through embryonic and larval development, and stained for a marker of double-strand breaks, γH2Av. Expression of mCD8::GFP marked cells in which TrpA1 was being co-expressed, so accumulation of γH2Av within these cells specifically would indicate a cell-autonomous increase in DNA damage as a result of neuronal hyperactivation. However, no detectable increase in DNA damage was observed (fig 5.1c ii), suggesting that the vulnerability of these neurons lay elsewhere.

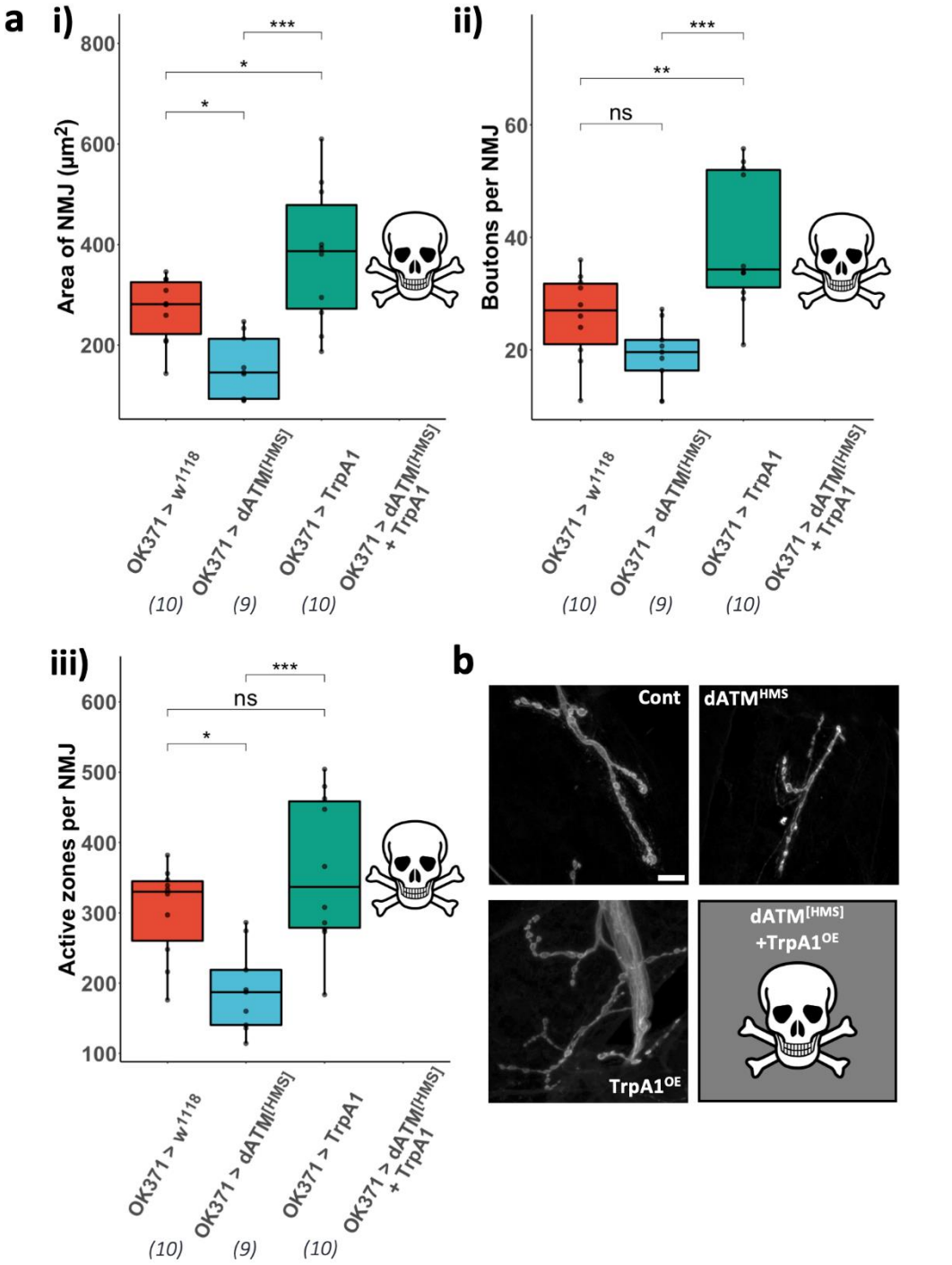
a
i)
ii)
iii)
b
c
i)
ii)
Area of NMJ (µm²)
Boutons per NMJ
Active zones per NMJ
ns
*
**
***
OK371 > w1118
OK371 > dATM[HMS]
OK371 > TrpA1
OK371 > dATM[HMS] + TrpA1
(10)
(9)
(10)
Cont
dATMHMS
TrpA1OE
dATM[HMS] +TrpA1OE
Cont +IR
TrpA1OFF
TrpA1ON

Figure 5.1: dATM knockdown sensitises larvae to excitotoxicity. a) Quantification of **i)** NMJ surface area; **ii)** Bouton count; **iii)** Active zone number – all scaled to muscle 4 surface area. Larvae reared at 27°C. Note that *OK371 > dATM$^{[HMS]}$+TrpA1* larvae did not survive to 3rd instar. N numbers indicated below each genotype. Shown are adjusted p-values from a one-way ANOVA with Dunnett's multiple comparisons test using the *OK371 > w^{1118}* control as reference. p≤0.05 *, p≤0.01 **, p≤0.001 ***. **b)** Representative NMJ images of the indicated genotypes (OE = overexpression). Scale bars: b = 10 µm, c = 20 µm. **c i)** Control larval CNS γ-irradiated with a dose of 8 Gy, dissected and stained for γH2Av (magenta) and DAPI (blue). **ii)** Larvae of the genotype *OK371-gal4,UAS-mCD8::GFP/UAS-TrpA1* raised at 19°C (TrpA1^{OFF}) and 27°C (TrpA1^{ON}) and stained with the same as previous. OK371-expressing cells shown in green due to inclusion of UAS-mCD8::GFP in the driver.

5.2.2 – Interaction of dATM with OS machinery

In *Chapter 3*, the possibility that the dATM knockdown larvae were showing indications of an early stage of neurodegeneration was explored. At higher temperatures, the posterior larval motor neurons displayed a "thinning-out" phenotype, with a reduction of their presynaptic/postsynaptic staining ratio, suggesting a retraction of the presynaptic membrane away from the end plate. At 30°C, this phenotype was even more pronounced, and OK371-driven dATM knockdown adults failed to eclose after metamorphosis, suggesting they were on the cusp of degeneration. If the toxicity produced by constitutive motor neuronal TrpA1 overexpression and activation is mediated by ROS, then combining dATM knockdown with knockdown or overexpression of ROS scavengers should provide insight about any heightened sensitivity to oxidative stress. Others have shown that dsRNA-mediated neuronal knockdown of ROS scavengers, such as Catalase, SOD1 and SOD2, lead to increase in NMJ bouton number (Oswald *et al.*, 2018). Again, there must exist a balance between the overgrowth and degenerative potential of ROS, since excessive ROS leads to degeneration, and the effect of knockdown of ROS scavengers at higher rearing temperatures where larvae are potentially more sensitive to the effects of perturbations of the OS machinery has not been tested.

To address this possibility, dATM dsRNA lines were combined with catalase dsRNA lines (Cat[JF02173], abbreviated to Cat[JF]) to generate a double knockdown. Catalase catalyses the breakdown of H_2O_2 into O_2 and H_2O, thus protecting the cell from the toxic effects of excessive H_2O_2 (Deisseroth and Dounce, 1970). Crosses to *OK371-GAL4* were subsequently performed at 30°C and larvae dissected at wandering third instar. The first observation was that very few larvae of the double-knockdown condition survived to third instar, to the point where it was initially assumed that, like the TrpA1 co-expression at 27°C, this combination was lethal. The survival of a few "escapers" meant that this combination was deemed semi-lethal. The few that were able to be dissected were included in the analysis. The results are summarised in figure 5.2. At 30°C, OK371-driven dATM[HMS] dsRNA results in significantly reduced NMJ surface area, but not bouton count or active zone number, possibly due to the control showing signs of toxic GAL4 overexpression (Rezával, Werbajh and Ceriani, 2007). At this rearing temperature, catalase knockdown does not produce an overgrowth – rather there is a significant reduction in all 3 metrics compared to the controls (fig 5.2a, green), a phenotype which is exacerbated by co-expression of dATM[HMS] dsRNA (fig 5.2a, dark blue). The co-expression group, in addition to reduced numbers available, also had a weaker HRP signal which required adjustment of the microscope settings, which may imply degenerating neurons. This evidence suggests that decreased ROS scavenging at higher temperatures is sufficient to disrupt NMJ development, and potentially sensitises the dATM knockdown condition to higher ROS levels.

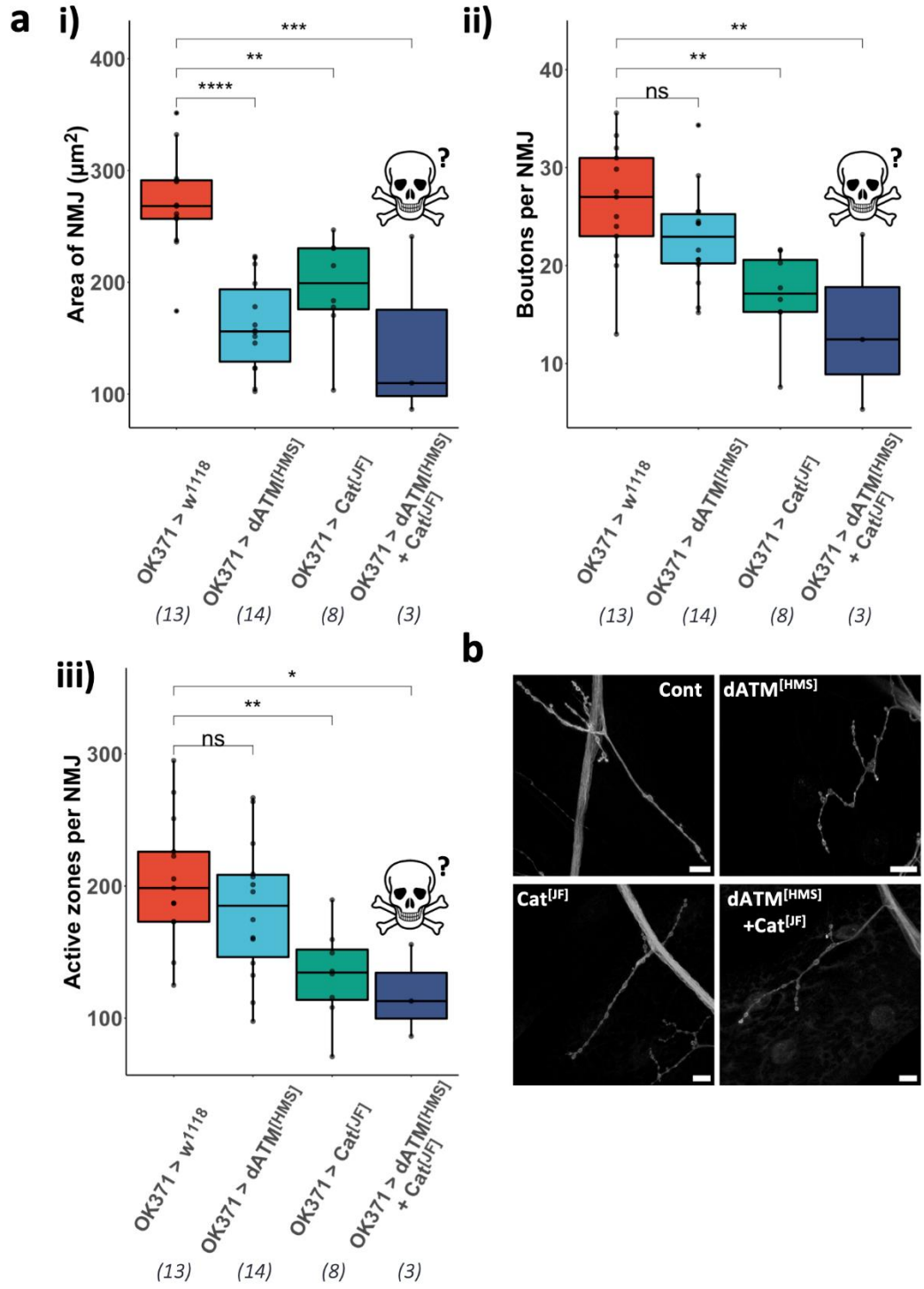

Figure 5.2: Knockdown of OS scavengers (catalase) at higher rearing temperatures (30°C) phenocopies dATM knockdown. a) Quantification of **i)** NMJ surface area; **ii)** Bouton count; **iii)** Active zone number – all scaled to muscle 4 surface area. Note that only a few escaping *OK371 > dATM[HMS]+Cat[JF]* larvae survived to 3rd instar. All adjusted p-values are from a one-way ANOVA with Dunnett's multiple comparisons test using the *OK371 > w1118* control as reference. p≤0.05 *, p≤0.01 **, p≤0.001 ***, p≤0.0001 ****. **b)** Representative NMJ images of the indicated genotypes. Scale bars = 10 µm (not all images are at the exact same magnification, so scale bars included for reference). Anterior = up.

If catalase knockdown is sufficient to increase sensitivity and exacerbate the dATM phenotype, the next question was whether the converse was true – could overexpression of ROS scavengers rescue the phenotype? For catalase overexpression, this does not appear to be the case. OK371-mediated overexpression of catalase alone had no significant effect on NMJ area or bouton count (fig 5.3a, i-ii green), although there was a small reduction in active zone number (fig 5.3a, iii green). Combining catalase overexpression with dATM knockdown (dATM[JF01422] dsRNA) phenocopied the dATM knockdown alone (fig 5.3a, dark blue). Overexpression of SOD2 was not attempted because it was shown previously that this actually exacerbates ROS-induced NMJ overgrowth rather than rescuing it (Oswald *et al.*, 2018). Taken together, while increasing ROS is sufficient to exacerbate the dATM phenotype, increased ROS scavenging fails to rescue it.

5.2.3 – Comparing ROS sensitivity at lower and higher rearing temperature

Returning to the competing hypotheses that explain the dATM knockdown phenotype at the NMJ, two main possibilities were considered. First, structural changes may result from a failure to respond to ROS positive-growth signals. Second, they may be a sign of excitotoxic neurodegeneration. Interestingly, these explanations could co-exist, and the temperature-dependence of the phenotype supports this notion. In *chapter 3*, at lower rearing temperatures (19°C) and higher rearing temperatures (27-30°C), there was a clear difference between controls and dATM knockdown. However, at 25°C, no difference was apparent. This finding is not likely to represent normal experimental variation, or lack of sensitivity of the assay, as both structural and functional (locomotion) phenotypes are the same.

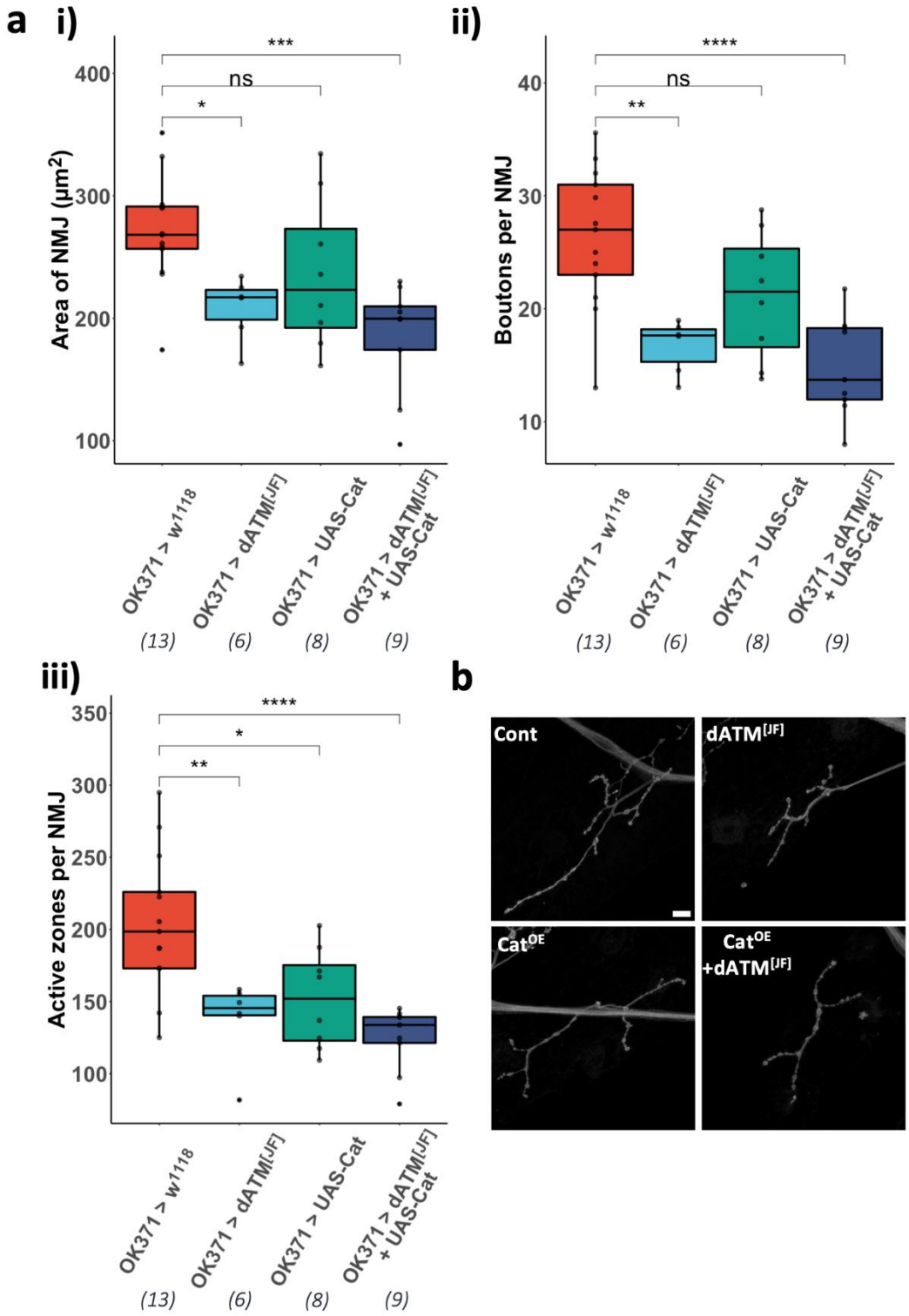

Figure 5.3: Overexpression of OS scavengers (catalase) at higher rearing temperatures (30°C) fails to rescue dATM knockdown. a) Quantification of **i)** NMJ surface area; **ii)** Bouton count; **iii)** Active zone number – all scaled to muscle 4 surface area. N numbers indicated below each genotype. All adjusted p-values are from a one-way ANOVA with Dunnett's multiple comparisons test using the *OK371 > w^{1118}* control as reference. p≤0.05 *, p≤0.01 **, p≤0.001 ***, p≤0.0001 ****. **b)** Representative images of the indicated genotypes. Scale bar = 10 µm. Anterior = up.

A model which encapsulates this posits that at lower temperatures, ROS levels are within a lower range with less toxic potential and, in this context, dATM knockdown results in a failure to respond to normal levels of ROS-mediated growth signals; at higher temperatures, increased neuronal activity results in ROS levels which are constitutively higher, meaning neurons are closer to the threshold of ROS-induced toxicity, and dATM knockdown reduces this threshold. If true, then at some midpoint rearing temperature these competing effects might cancel out and there would be no phenotype from dATM knockdown, which is what is seen at 25°C.

If true, this leads to two predictions: firstly, that moderately increasing ROS at lower temperatures in the dATM knockdown condition would increase the ROS-mediated growth signal below the threshold for excitotoxicity and rescue the phenotype; secondly, that increasing ROS at higher rearing temperatures would be deleterious, as may be the case with TrpA1 overexpression and with catalase knockdown. One issue is that TrpA1 activation is temperature-sensitive, and the channel is silent at rearing temperatures of 19°C, so an alternative method for ROS generation was required. Overexpression of the NADPH oxidase Dual Oxidase (DuOx) is known to be sufficient to induce NMJ structural overgrowth as measured by bouton count (Oswald *et al.*, 2018; Sobrido-Cameán *et al.*, 2023). As a transmembrane protein, this enzyme generates extracellular ROS in the form of superoxide radicals and H_2O_2 (Fischer, 2009), and due to the poor membrane permissibility of H_2O_2, aquaporin channels are required for the intracellular effects on structural plasticity (Sobrido-Cameán *et al.*, 2023).

Here, the human form of DuOx, hDuOxII, was overexpressed from a UAS construct alone and in combination with dATM knockdown, at 19°C and 27°C rearing temperatures.

Surprisingly, at low temperatures, hDuOxII alone did not produce any detectable structural overgrowth of the NMJ and was deleterious to bouton count and active zone number (fig 5.4a ii-iii, dark blue). Co-expression of hDuOxII with dATM[HMS] dsRNA was sufficient to rescue NMJ surface area (fig 5.4a i, dark blue) – however it exacerbated the decrease in active zone number, suggesting a disconnect between these two aspects of NMJ structural development, and that even at lower rearing temperatures, dATM knockdown larvae are in some respects sensitive to ROS increases. At higher temperatures, co-expression of hDuOxII did not suppress or enhance any aspects of NMJ development compared to dATM knockdown alone, although there was a small but not significant exacerbation of bouton and active zone number decrease (fig 5.5a, dark blue). hDuOxII overexpression alone had no effect on NMJ development compared to controls except for a reduction in active zone number (fig 5.5a, green).

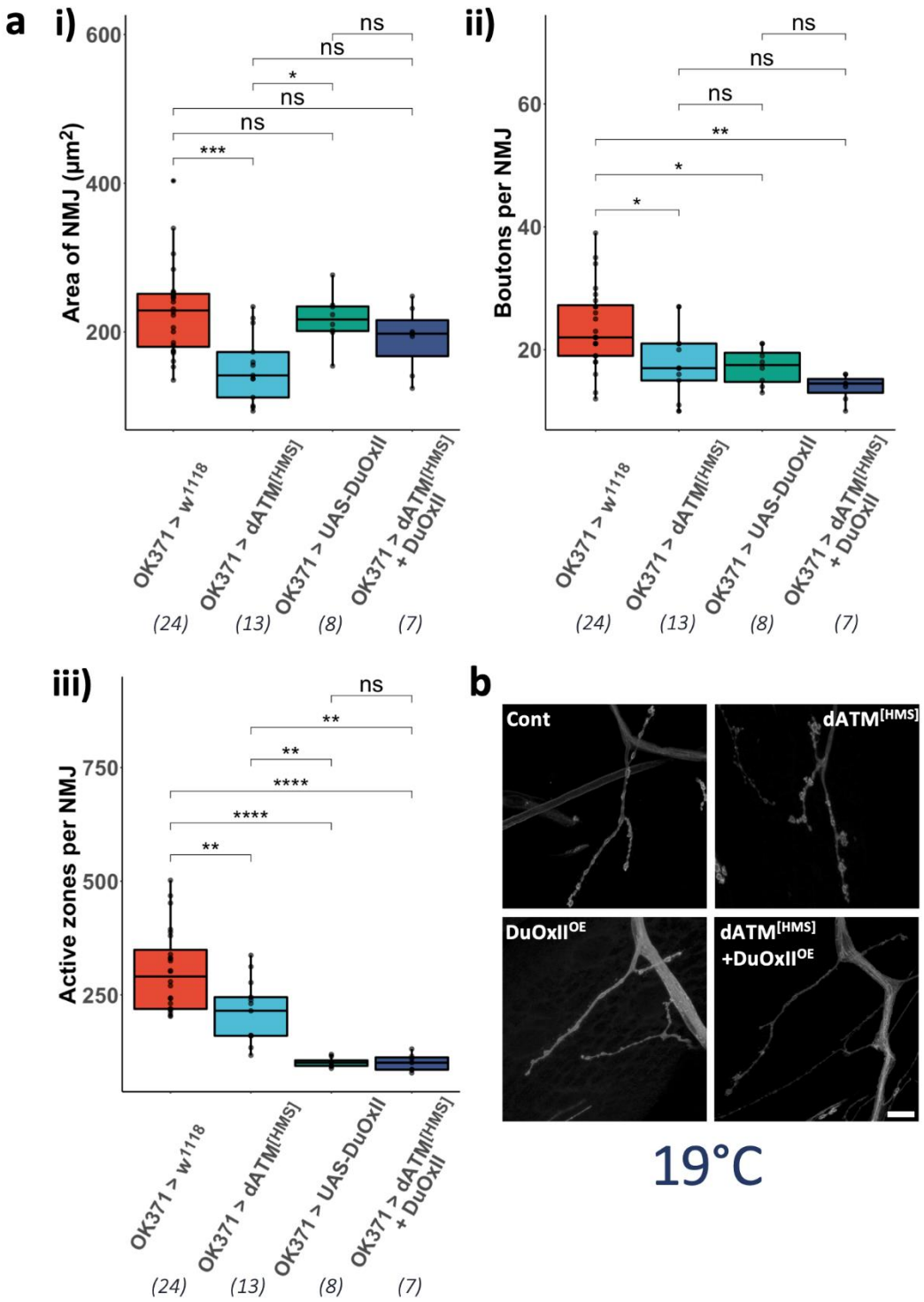

Figure 5.4: Increasing ROS at lower rearing temperatures (19°C) rescues some aspects of NMJ development but is deleterious to others. a) Quantification of **i)** NMJ surface area; **ii)** Bouton count; **iii)** Active zone number – all scaled to muscle 4 surface area. Larvae reared at 19°C. N numbers indicated below each genotype. Shown are adjusted p-values from Tukey's Honest Significant Differences test. p≤0.05 *, p≤0.01 **, p≤0.001 ***, p≤0.0001 ****. **b)** Representative images of the indicated genotypes. Scale bar = 15 µm. Anterior = up.

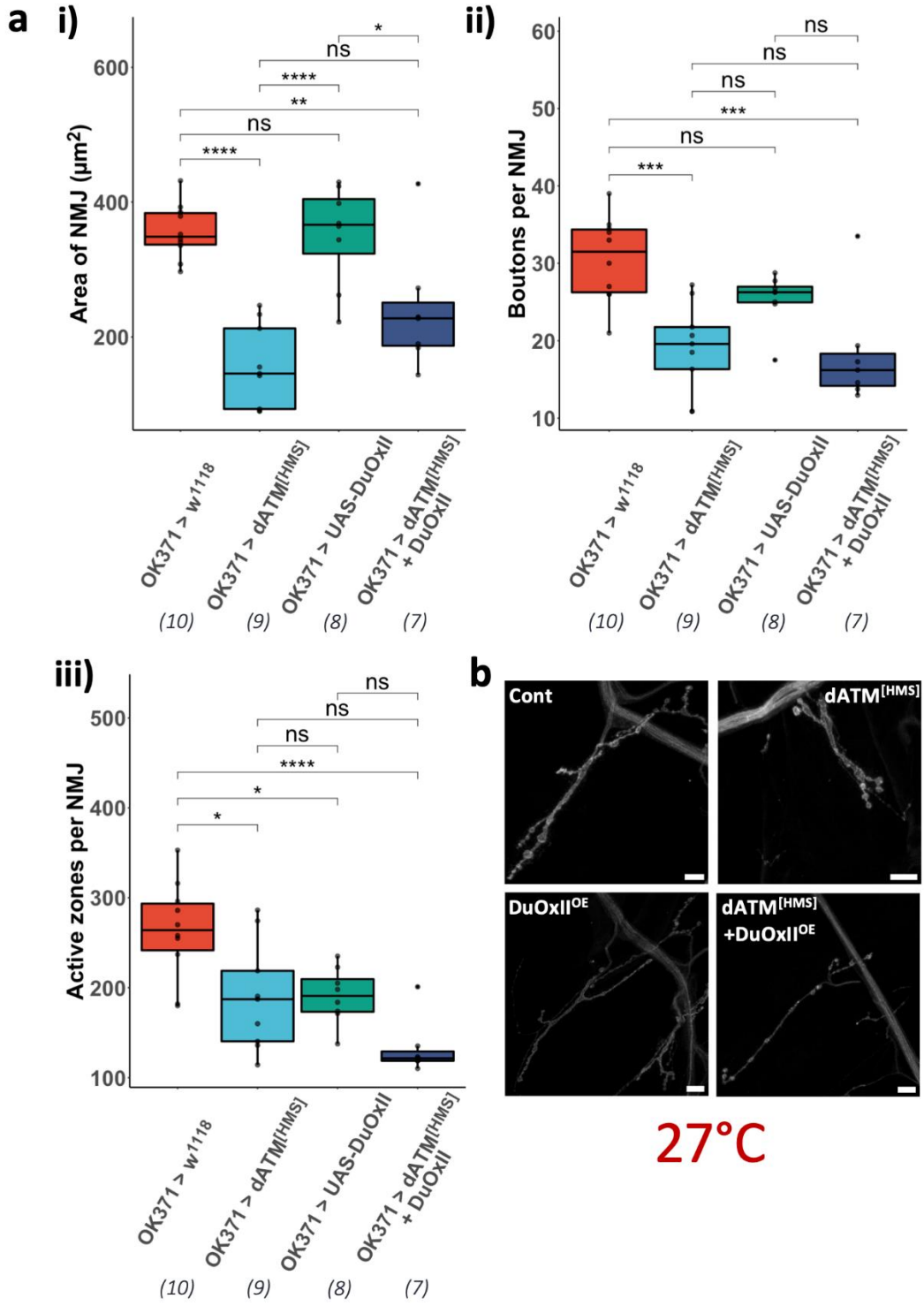

Figure 5.5: Increasing ROS at higher rearing temperatures (27°C) independently of neuronal activity has no effect on the dATM knockdown phenotype. a) Quantification of **i)** NMJ surface area; **ii)** Bouton count; **iii)** Active zone number – all scaled to muscle 4 surface area. Larvae reared at 27°C. N numbers indicated below each genotype. Shown are adjusted p-values from Tukey's Honest Significant Differences test. p≤0.05 *, p≤0.01 **, p≤0.001 ***, p≤0.0001 ****. **b)** Representative images of the indicated genotypes. Scale bars = 10 µm. Anterior = up.

5.2.4 – Interaction of dATM and autophagy machinery

It has been shown previously that another key regulator of synapse size in *Drosophila* is autophagy. *Atg* mutants have decreased NMJ surface area and bouton number, while overexpressing ATG proteins (e.g., ATG1) leads to synaptic overgrowth (Shen and Ganetzky, 2009). Given the known involvement of mammalian ATM in promoting autophagy upregulation under conditions of oxidative stress (Alexander *et al.*, 2010), it made sense therefore to test whether dATM interacted with the autophagic machinery during synapse development. Firstly, an attempt was made to replicate the findings of other previous studies. *Atg18* heterozygous mutants, like dATM, are known to result in NMJ undergrowth (Shen and Ganetzky, 2009) although it was not tested whether this was due to reduction of neuronal ATG18 *per se*. Pan-neuronal knockdown of ATG18 using the dsRNA Atg18[HMS01193] resulted in third instar NMJ morphology which phenocopied dATM knockdown, with reduced normalised NMJ surface area, bouton count and active zone number (fig 5.6a i-iii, green). Overexpression of ATG1 produced mixed results. Two different UAS-constructs were utilised, one on chromosome 2 and the other on chromosome 3. Pan-neuronal overexpression of ATG1 from the chromosome 2 *UAS-ATG1* was repeatedly lethal before third instar. In case homozygosity of *UAS-ATG1 on II* resulted in infertile male adults, the cross was repeated with males that contained a marked 2nd chromosome *CyO, Dfd::YFP* balancer. In this scenario, the progeny of the cross with *elav-GAL4;UAS-Dcr2* females were exclusively YFP-positive, indicating inheritance of the balancer rather than the UAS-ATG1 construct. However, combining *UAS-ATG1 on II* with the dATM dsRNA on chromosome 3 restored viability of 3rd instar larvae, which was the first suggestion of an interaction between dATM and the

autophagy machinery. This was not simply due to dilution of the GAL4, as the effect was not seen in combination with a *UAS-GFP dsRNA* on chromosome 3.

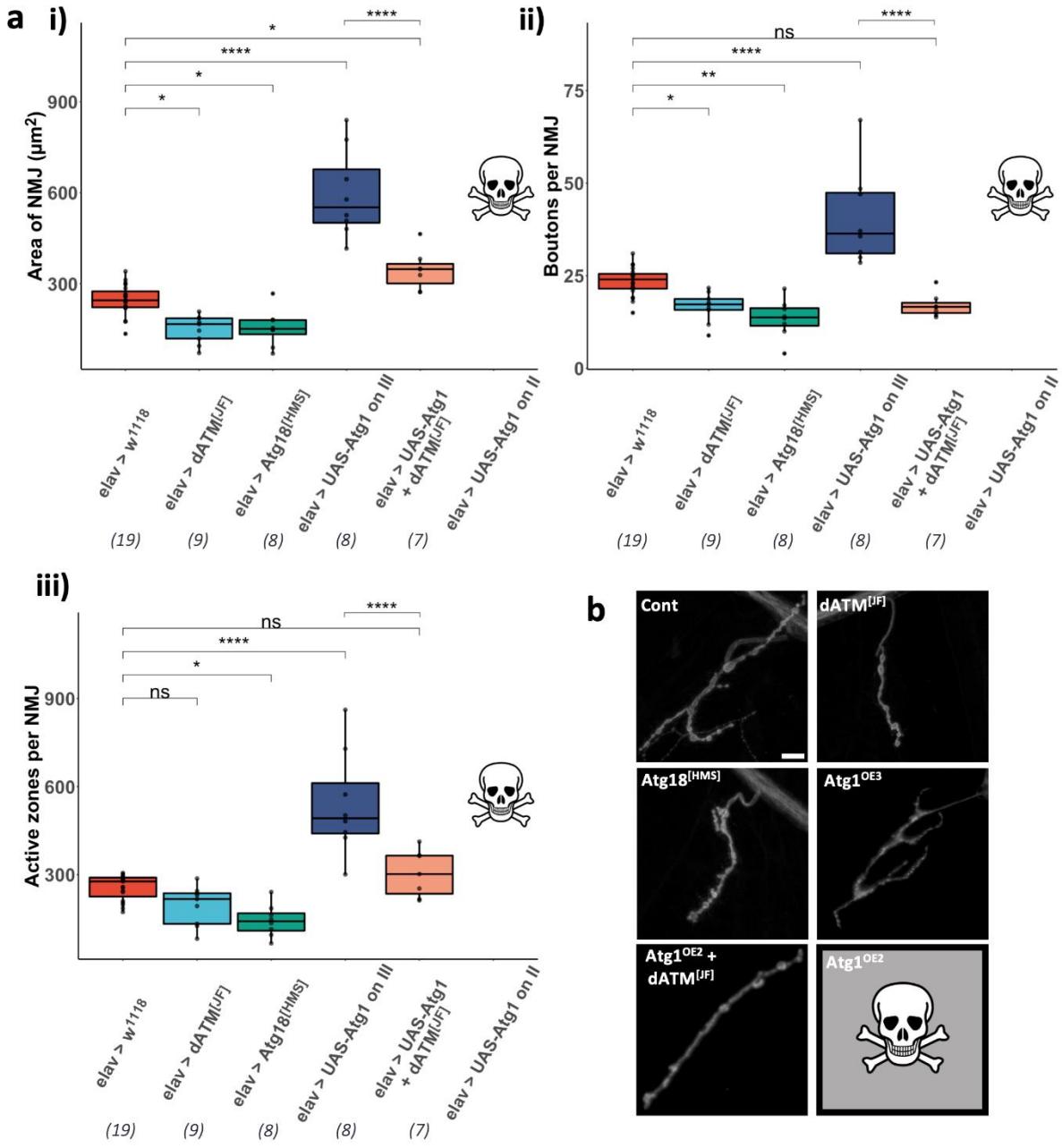

Figure 5.6: Assessing the interaction of dATM with autophagy regulators in NMJ development. **a)** Quantification of **i)** NMJ surface area; **ii)** Bouton count; **iii)** Active zone number – all scaled to muscle 4 surface area. Larvae reared at 25°C. Note that *elav > UAS-Atg1 on II* larvae did not survive to 3rd instar. N numbers indicated below each genotype. Shown are adjusted p-values from a one-way ANOVA with manually selected multiple comparisons and the Holm-Bonferroni correction. p≤0.05 *, p≤0.01 **, p≤0.001 ***, p≤0.0001 ****. **b)** Representative images of the indicated genotypes (OE = overexpression, 2 or 3 corresponding to the chromosome of the *UAS-Atg1* construct). Scale bars = 10 µm. Anterior = up.

By contrast, *UAS-ATG1 on III* produced a few escaping third instar larvae when crossed to *elav-GAL4;UAS-Dcr2* females, so these were used for NMJ structural analysis. These larvae were smaller than those from the other tested genotypes. As such, the muscle surface area normalised data from the NMJs revealed significant synaptic overgrowth relative to the size of the muscle in all 3 metrics obtained (fig 5.6a i-iii, dark blue). Combination of UAS-ATG1 with dATM knockdown resulted in a somewhat intermediate phenotype. For surface area, the magnitude of the overgrowth induced by UAS-ATG1 was lessened by co-expression of dATM dsRNA, but it was still significantly increased compared to the controls (fig 5.6a i, pink). Active zone count was restored to control levels (fig 5.6a iii, pink). Bouton count, however, trended towards the same reduction seen with dATM or ATG18 knockdown alone, without quite reaching statistical significance (fig 5.6a ii, pink) Taken together, the data suggest an interaction between dATM and the autophagy machinery during NMJ development and maturation.

5.2.5 – Interaction of dATM with AMPK in NMJ development

The AMP-activated protein kinase (AMPK) senses the intracellular AMP:ATP ratio through competitive binding of the two species to residues in the ɣ domain of the protein (Xiao *et al.*, 2007). Increases in the AMP:ATP ratio stimulates the kinase activity of AMPK leading to upregulation of ATP catabolism (Hardie, Carling and Carlson, 1998). AMPK is particularly highly expressed in the brain and is activated during prolonged synaptic activity, where it upregulates glycolysis and neuronal mitochondrial respiration (Marinangeli *et al.*, 2018), which in turn will generate increased ROS. In addition, AMPK has been shown to be downstream of ATM signalling under conditions of oxidative stress, where it then phosphorylates TSC2, leading to

repression of mTORC1 and upregulation of autophagy (Alexander *et al.*, 2010). This posed the question of whether dATM and AMPK interact in regulating the development of the NMJ.

Unlike reduction of ATG18, pan-neuronal knockdown of AMPK alone had no significant effect on the morphology of the synapse, while combined dATM and AMPK knockdown broadly resembled dATM knockdown alone (fig 5.7a). Qualitatively, however, the double knockdown condition NMJs had an appearance which was suggestive of a more severe phenotype – there were many examples of a fragmented presynaptic membrane along with what resembled a bright "retraction bulb" (see fig 5.7b for examples), or a thinning-out of the membrane which resembled the posterior phenotype described in *Chapter 3*. These differences were not picked up by the FIJI algorithm when performing the analysis, and consequently there were no statistically significant differences in the quantified NMJ metrics between the dATM knockdown and combined knockdown conditions.

Pan-neuronal overexpression of AMPK at 25°C rearing temperature had no effect on NMJ surface area or active zone number (fig 5.8a i, iii), but resulted in a significant decrease in bouton number compared to controls (fig 5.8a ii). Concomitantly, AMPK overexpression masked the effect of dATM knockdown, as the combined condition phenocopied AMPK overexpression alone. This suggests that increasing available AMPK is sufficient to overcome the decrease in dATM signalling, indicating an interaction of the two in NMJ development.

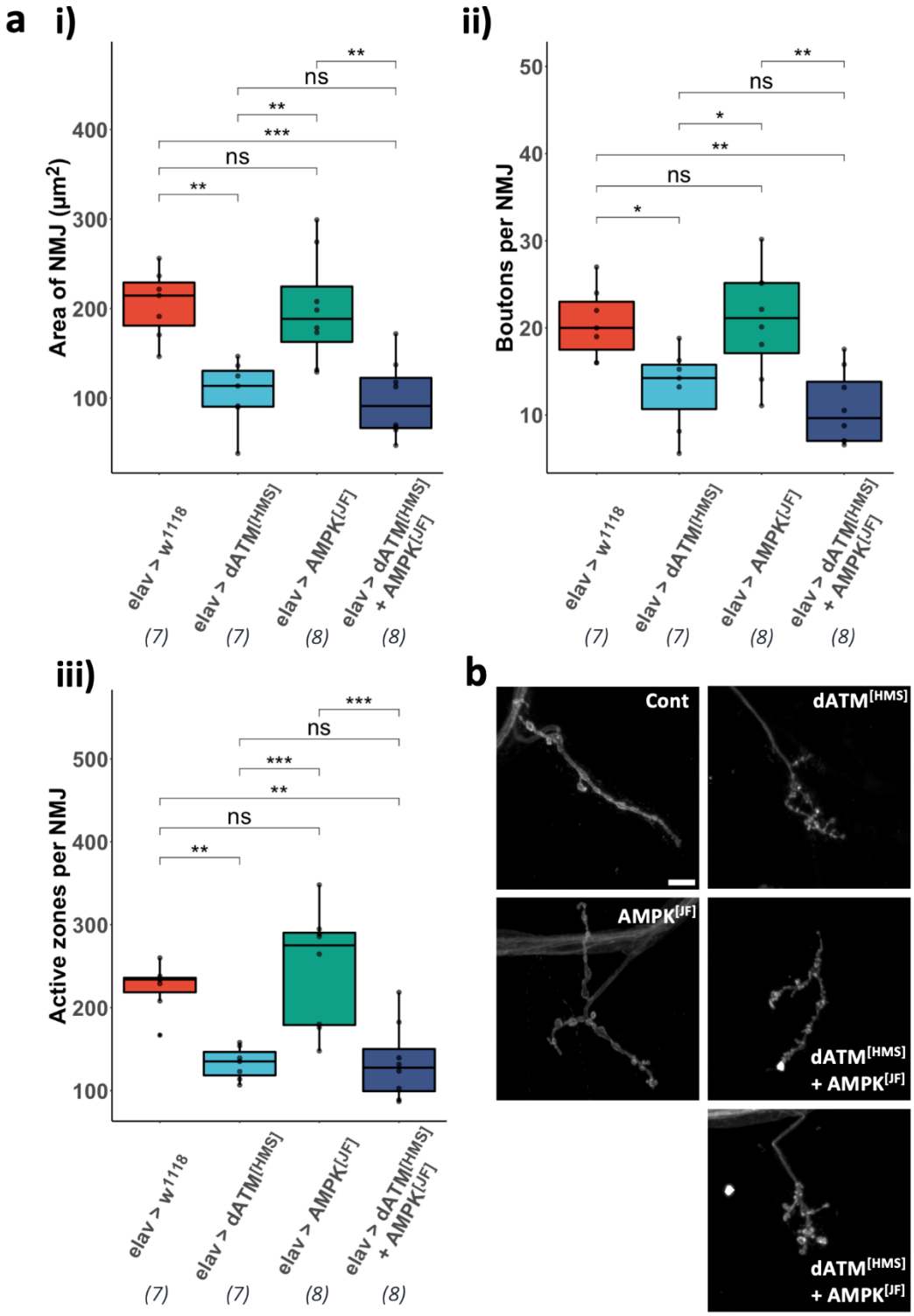

Figure 5.7: Knockdown of AMPK has no effect on NMJ development and qualitatively exacerbates the dATM knockdown phenotype. a) Quantification of **i)** NMJ surface area; **ii)** Bouton count; **iii)** Active zone number – all scaled to muscle 4 surface area. Larvae reared at 25°C. N numbers indicated below each genotype. Shown are adjusted p-values from Tukey's Honest Significant Differences test. p≤0.05 *, p≤0.01 **, p≤0.001 ***. **b)** Representative images of the indicated genotypes, with two examples of the *elav > dATM[HMS]+AMPK[JF]* genotype. Scale bar = 10 µm. Anterior = up.

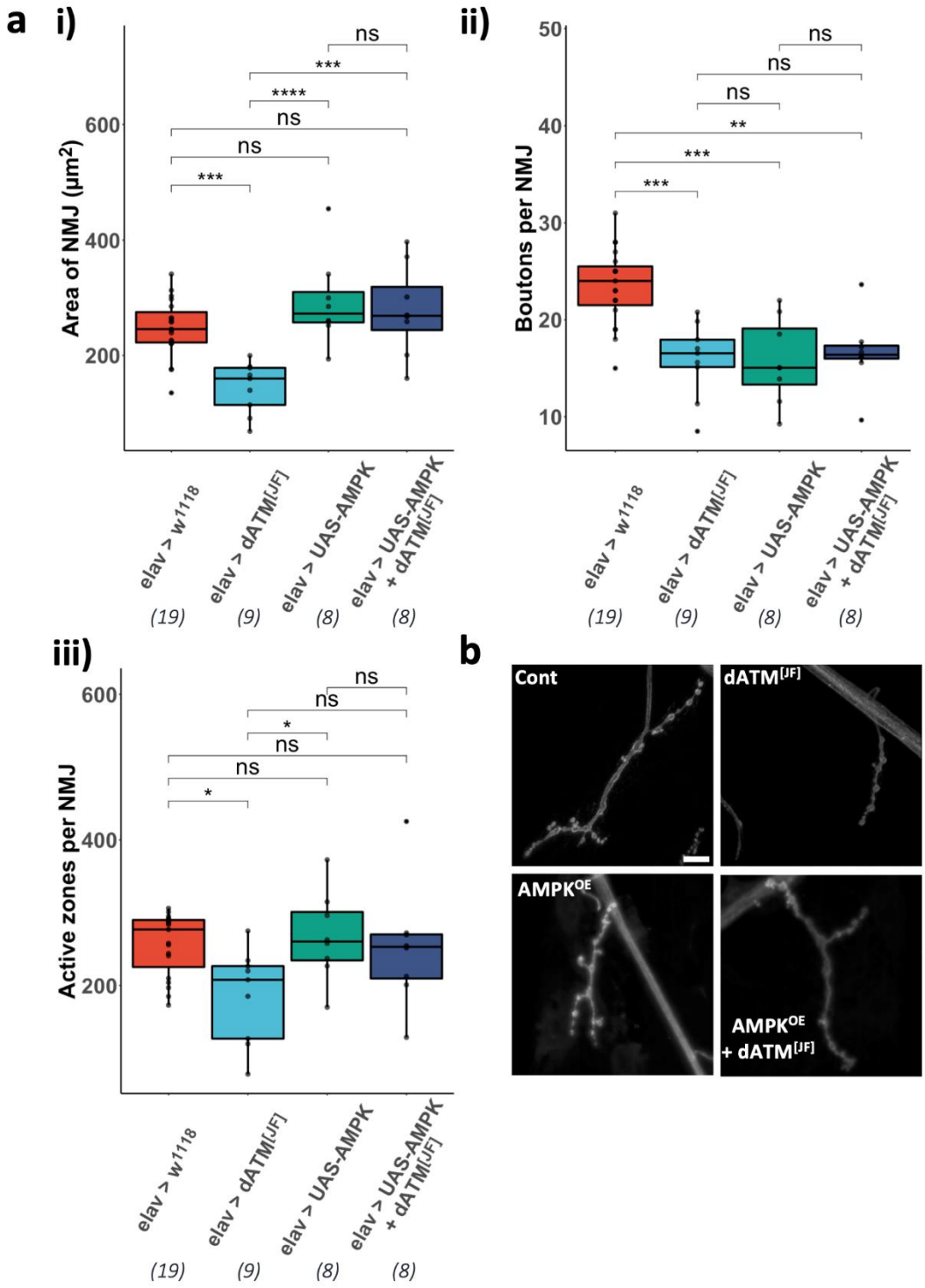

Figure 5.8: Overexpression of AMPK rescues NMJ surface area and active zone number, but not bouton count. a) Quantification of **i)** NMJ surface area; **ii)** Bouton count; **iii)** Active zone number – all scaled to muscle 4 surface area. Larvae reared at 25°C. N numbers indicated below each genotype. Shown are adjusted p-values from Tukey's Honest Significant Differences test. p≤0.05 *, p≤0.01 **, p≤0.001 ***, p≤0.0001 ****. **b)** Representative images of the indicated genotypes. Scale bar = 10 µm. Anterior = up.

5.2.6 – Quantification of autophagy

The putative interaction between dATM and the autophagy machinery in NMJ development demonstrated above led to the question of whether impaired autophagic flux would be detectable in neurons with reduced dATM levels. To achieve this, the dual-colour *mCherry-GFP-Atg8a* reporter was overexpressed using the *OK371-GAL4* driver. This reporter monitors autophagic flux by utilising the pH sensitivity of the GFP component and the pH stability of the mCherry component, both fused in tandem to the autophagosome-associated protein ATG8a. In neutral pH, both GFP and mCherry can fluoresce, leading to yellow puncta. Upon autophagosome fusion with acidic lysosomes, GFP signal is quenched while mCherry fluorescence is maintained, leading to the formation of red puncta (Nezis *et al.*, 2010; Klionsky *et al.*, 2021). As a positive control to induce autophagy in these experiments, larvae were starved in 20% sucrose solution for 3-24 hours.

The experiment required the tissues to be imaged live as fixation would alter the intracellular pH environment. This presented some challenges, as isolated CNSs were not fixed in place and thus were often in different planes of orientation during imaging (see fig 5.9a-b). Throughout the OK371-expressing cells of the CNS, in both the feeding and 3-hours starved state, diffuse GFP signal and both diffuse and punctate mCherry signal was observed in control (fig 5.9a) and dATM knockdown (fig 5.9b) feeding third instar larvae. It was clear that in the CNS there was a high basal level of autophagy given the number of red puncta observed within each cell. This is consistent with both the high metabolic demand of neurons and the lack of cell division to dilute out damaged cellular components. The high level of autophagy, plus the additional issue with the plane of orientation, made puncta quantification challenging and any differences between the genotypes and conditions impossible to quantify.

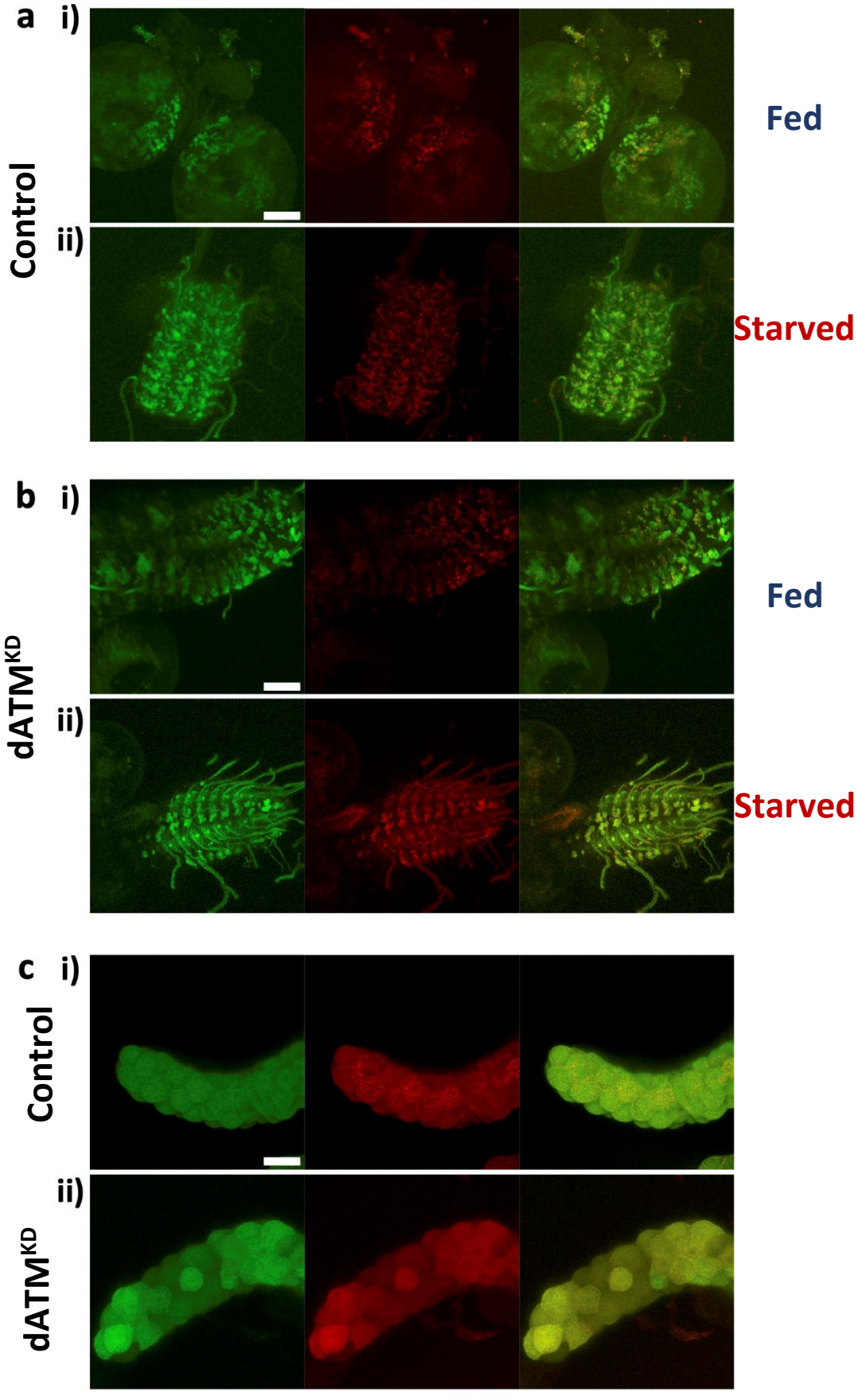
a
i)
Control
ii)
Fed
Starved
b
i)
dATM^KD
ii)
Fed
Starved
c
i)
Control
ii)
dATM^KD

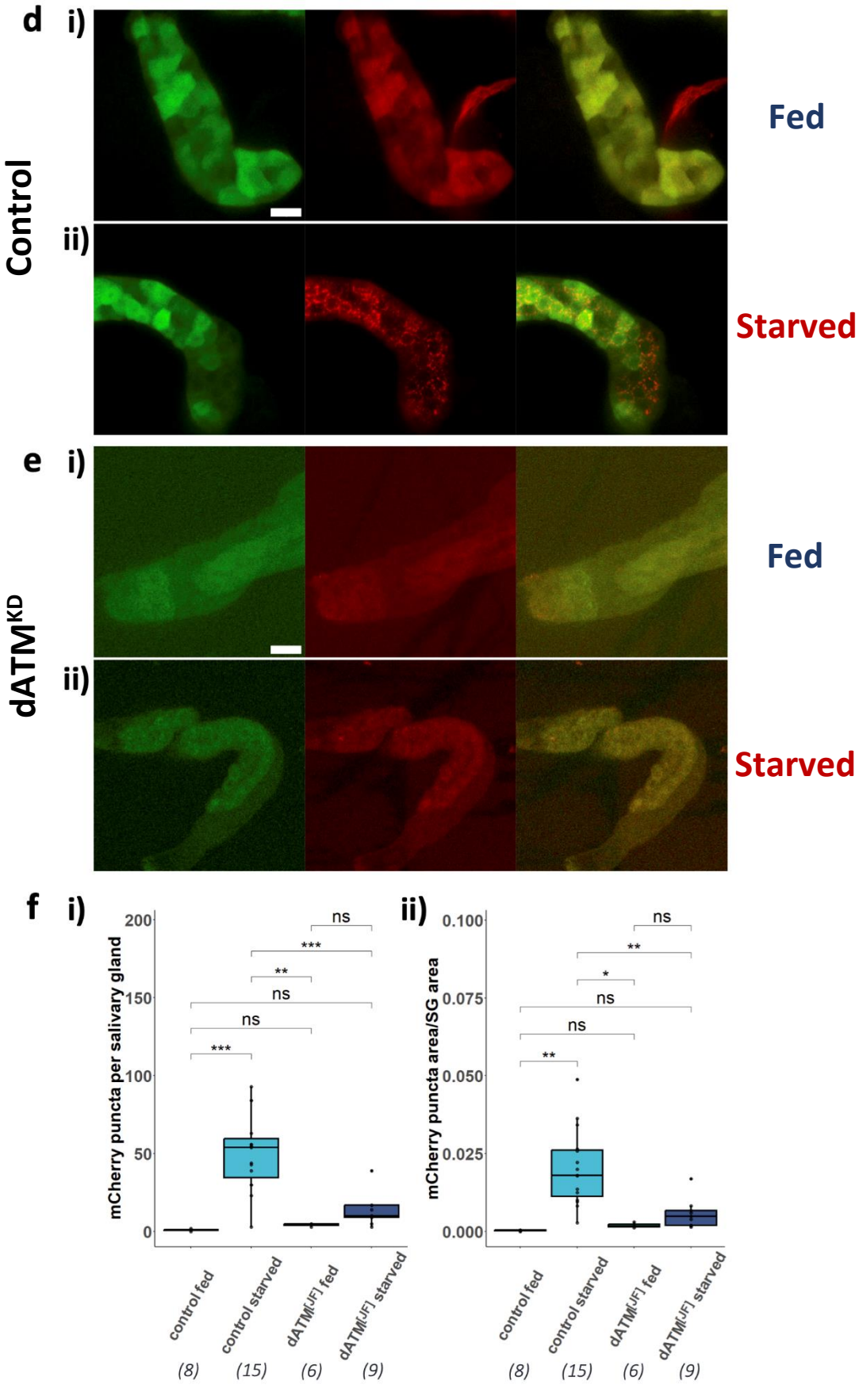
d
i)
ii)
Control
Fed
Starved
e
i)
ii)
dATM^KD
Fed
Starved
f
i)
ii)
mCherry puncta per salivary gland
mCherry puncta area/SG area
ns
***
**
*
control fed
control starved
dATM[JF] fed
dATM[JF] starved
(8)
(15)
(6)
(9)

Figure 5.9: Quantification of autophagic flux using *mCherry-GFP-atg8a* reporter. All images are from live imaging experiments and displayed in the order: *GFP signal; mCherry signal; merge*. **a)** Max projections of control CNSs from feeding 3rd instar larvae in the **i)** fed state and **ii)** 3-hours starved state. **b)** Same as **a** but for dATM$^{[JF]}$ larvae. Note that each CNS is in a slightly different plane of orientation due to technical limitations. **c)** Salivary glands from wandering 3rd instars of **i)** control and **ii)** dATM$^{[JF]}$ larvae. **d)** Max projections of control salivary glands from feeding 3rd instar larvae in the **i)** fed state and **ii)** 3-hours starved state. **e)** Same as **d** but for dATM$^{[JF]}$ larvae. Note reduced expression of the reporter in these larvae. **f)** Quantification of **i)** mCherry puncta per salivary gland, and **ii)** the area of mCherry puncta divided by total salivary gland surface area. All larvae reared at 27°C. N numbers indicated below each genotype. Shown are adjusted p-values from Tukey's Honest Significant Differences test. p≤0.05 *, p≤0.01 **, p≤0.001 ***. Full genotypes:
control = *UAS-mCherry-GFP-atg8a;OK371-GAL4/+;+*.
dATM$^{[JF]}$ = *UAS-mCherry-GFP-atg8a;OK371-GAL4/+;dATM$^{[JF01422]}$/+*.
Scale bars: a-c = 60 µm, d-e = 30 µm.

As an alternative, it was noted that an off-target tissue in which OK371 expresses is the salivary glands. The first striking observation was that the green signal from the salivary glands observed through a standard fluorescence dissecting microscope was dependent on the larval stage of the sample, with controls at feeding third instar showing dim expression and then much brighter at late feeding/early wandering third instar. This is presumably due to a strong induction of autophagy which accompanies the wandering stage as the animal prepares for metamorphosis. Secondly, dATM knockdown larvae had significantly reduced basal signal of the GFP component of the construct, which was not due to GAL4 dilution as other RNAi or GFP constructs (e.g., mito-GFP, see later) did not have the same issue. Finally, there was a clear difference in the number of red puncta between salivary glands from fed larvae and those from starved larvae.

Comparing the salivary glands of wandering third instar larvae from controls and dATM knockdown larvae revealed that while the pattern and intensity of diffuse GFP and mCherry fluorescence was similar in both, the control mCherry signal was clearly more punctate (fig 5.9c). After 24-hour starvation of feeding-stage third instars, control larvae showed an extreme increase of red puncta; however, very few dATM knockdown larvae survived the

protocol. Therefore, a starvation period of 3 hours was settled on for the remainder of the experiment. This level of starvation was sufficient to induce mCherry puncta in control salivary glands (fig 5.9d) but not those of dATM[JF] knockdowns (fig 5.9e). These differences were quantified both by automated counting of puncta per salivary gland (fig 5.9f i) and through scaling the surface area of the red puncta to the total salivary gland surface area (from max projections of z-stacks) in case the salivary glands of one genotype were different in size to the other (fig 5.9f ii). There was no significant difference in the number of puncta in the fed state between each genotype; rather, the difference was manifest by a failure to induce autophagic flux upon starvation.

Taken together, and despite being from salivary glands rather than from neurons, the data indicate a defect in autophagy induction following dATM knockdown.

5.2.7 – Evidence of defective mitophagy

The evidence for an autophagy deficit presented above meant that it was possible that the dATM knockdown would show signs of defective mitophagy, as has been seen in other models of A-T (Valentin-Vega *et al.*, 2012). For example, A-T patient-derived iPSCs which have been differentiated into neuronal precursor cells show an increase in markers of senescence, such as phosphorylated p38, and impaired mitophagy as determined by accumulation of parkin and downregulation of mitophagy-inducing genes (Sunderland *et al.*, 2020). Defective mitophagy is also observed in other ATM knockdown cell lines, such as the neuroblastoma SH-SY5Y (Fang *et al.*, 2016). Intriguingly, the mitophagy-promoting role of ATM is hypothesised to be

downstream of its oxidative activation, which offers a further link between oxidative stress and autophagy signalling in neurodevelopment (Cirotti *et al.*, 2021).

Defective mitophagy leads to an accumulation of damaged mitochondria (Ashrafi and Schwarz, 2013), which can be detected using immunohistochemistry. To test whether reduced levels of dATM leads to mitophagy impairment, dATM dsRNA was combined with expression of GFP containing a mitochondrial localisation sequence, mitoGFP (Cox and Spradling, 2003). Dissected wandering third instar showed mitochondrial staining throughout OK371-expressing neurons (fig 5.10). NMJ surface area and bouton number was measured to ensure that expression of mitoGFP did not affect the dATM phenotype – the results show a significant reduction in both metrics in the knockdowns compared to the controls, as expected (fig 5.10b i-ii). Instead of quantifying active zones, the FIJI NMJ morphometrics algorithm was used to count the number of mitochondria per square micron of the NMJ. This showed a clear increase in mitochondrial density in dATM knockdown larvae (fig 5.10b iii) which could be indicative of a failure of mitophagy. Higher magnification images were taken of the NMJs and there appeared to be a qualitative difference between the morphology of the mitochondria across the two conditions (fig 5.10c). An attempt was made to quantify any difference in structure using FIJI – a custom script was written which used the HRP channel to create a mask corresponding to the NMJ, thresholded the mitoGFP channel to distinguish mitochondria from background staining, and then analyse particles gave information on the size and circularity of mitochondria. Although there appeared to be changes in mitochondrial circularity visually, this was not picked up by the FIJI script (fig 5.10d ii) – however, there was a significant reduction in mitochondrial size in the dATM knockdown NMJs (fig 5.10d i). The results

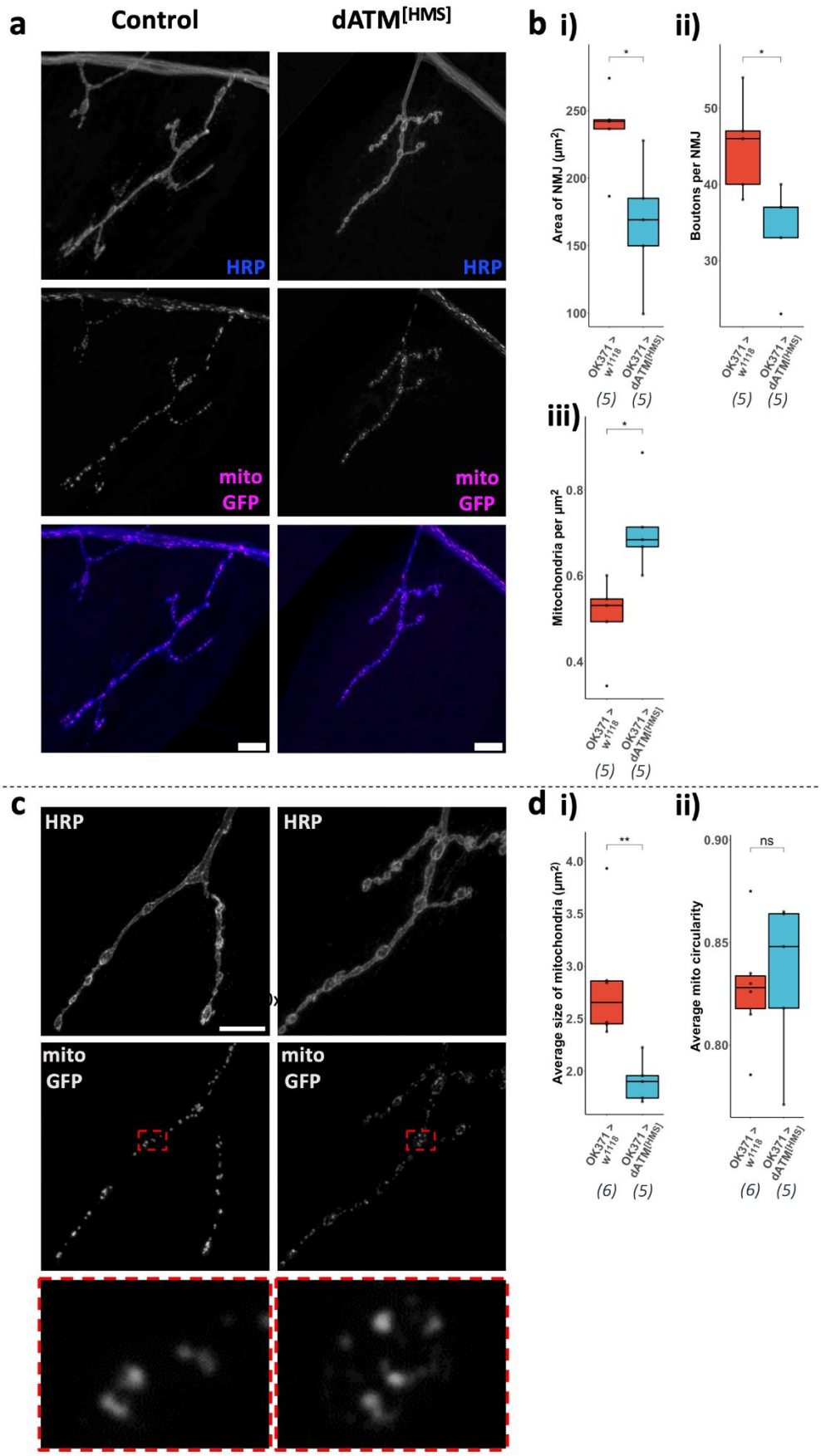
a
Control
dATM[HMS]
HRP
HRP
mito GFP
mito GFP
b i)
ii)
Area of NMJ (µm²)
Boutons per NMJ
OK371 > w1118
OK371 > dATM[HMS]
(5) (5)
(5) (5)
iii)
Mitochondria per µm²
(5) (5)
c
HRP
HRP
mito GFP
mito GFP
d i)
ii)
Average size of mitochondria (µm²)
Average mito circularity
ns
(6) (5)
(6) (5)

Figure 5.10: Knockdown of dATM leads to an increased density of smaller mitochondria. a) Representative control and dATM$^{[HMS]}$ NMJs split into HRP, mitoGFP and merged images. Scale bars = 10 µm. **b)** Quantification of the **i)** NMJ surface area, **ii)** bouton count and **iii)** mitochondrial density per µm^2 of the NMJs of the indicated genotypes. **c)** Representative higher resolution images of the same genotypes as above. **d)** Quantification of more detailed mitochondrial metrics from the higher resolution images: **i)** Average mitochondrial size (surface area of max projections); **ii)** Average mitochondrial circularity, determined from the *analyse particles* function within FIJI. All larvae reared at 27°C. N numbers indicated below each genotype. Shown are p-values from Welch T-tests or Wilcox tests depending on Shapiro-Wilk normality testing of the data. p≤0.05 *, p≤0.01 **. Full genotypes:
control = *OK371-GAL4/+;UAS-mitoGFP/+.*
dATM$^{[HMS]}$ = *OK371-GAL4/dATM$^{[HMS02790]}$;UAS-mitoGFP/+.*

therefore suggest an accumulation of smaller and potentially more fragmented mitochondria, which is consistent with an impairment of mitophagy (Ashrafi and Schwarz, 2013).

5.2.8 – Larval drug rescues

In *5.2.4*, hyper-induction of macroautophagy was achieved genetically through the overexpression of autophagy related proteins. An alternative method for inducing autophagy is pharmacologically through drugs which are bioavailable to *Drosophila* larvae.

Nicotinamide mononucleotide (NMN) is a nicotinamide adenine dinucleotide (NAD+) precursor, which can be synthesised from nicotinamide, nicotinamide riboside (NR) or supplied directly from food intake. The synthesis of NAD+ from NMN is catalysed by the enzyme family NMN adenylyltransferases (NMNATs) of which NMNAT2 shows particularly strong neuronal expression (Yoshino, Baur and Imai, 2018). The link between NAD+ and autophagy has been widely studied (Zhang *et al.*, 2016), while NADases, such as PARPs, SIRTs and cyclic ADP-ribose (cADPR) synthases, can themselves drive autophagy induction (Wilson *et al.*, 2023). Neurons that are autophagy-deficient show excess consumption of NAD, followed by mitochondrial depolarisation and degeneration – this can be overcome through

NMN supplementation (Sun *et al.*, 2023). *In vivo,* it has been found that dietary NMN supplementation of ATM-/- mice improved lifespan and attenuated A-T pathology, while addition of NMN to ATM-deficient rat primary neuronal culture *in vitro* was protective to synapses (Fang *et al.*, 2016). Therefore, to test whether dietary supplementation of NMN was sufficient to alleviate the effects of neuronal dATM knockdown, larvae were reared on food containing 10mM NMN and subject to functional testing of locomotion (fig 5.11a). Dietary NMN supplementation had no significant effect on crawling speed of control larvae, and although there was a trend to increased locomotion, there was no significant difference between dATM knockdown larvae raised on normal food or food supplemented with NMN.

Metformin (IUPAC: N,N-dimethylbiguanide), an anti-hyperglycaemic agent used for the treatment of type II diabetes, is also a potent upregulator of macroautophagy. The mechanism of action of metformin has been something of a mystery for decades; however, it is generally accepted that, in a variety of cell types, the autophagy-promoting effect of metformin centres around the activation of AMPK (Lu *et al.*, 2021). Fig 5.11b shows the effect of rearing larvae on food containing 5mM metformin. Intriguingly, control wandering third instar larvae reared on metformin show a significant decrease in crawling speed than those raised on normal food (fig 5.11b i, light blue vs red), which was not due to any change in percentage time moving (fig 5.11b ii). However, feeding dATM knockdown larvae 5mM metformin significantly increased their locomotion to the level of the controls + drug (fig 5.11b i, dark blue). This offers support to the observation in *5.2.5* that increasing AMPK activity is sufficient to rescue the NMJ structural phenotype of neuronal dATM knockdown.

A strikingly similar effect was observed with 1mM torin, with a decline of the controls and a modest rescue of the dATM knockdowns, although the difference between dATM

knockdown larvae +/- the drug was not statistically significant as determined by Dunn's test (fig 5.11c i). Torin has a more direct influence on autophagy since it is an inhibitor of mTORC1 and mTORC2 (Thoreen *et al.*, 2009). In combination, the results suggest that directly promoting autophagy is deleterious to the locomotor performance of control larvae, but beneficial to that of dATM knockdown larvae. This could imply that autophagy levels are held in a delicate balance and upsetting that balance in either direction (too much or too little) leads to functional decline.

Figure 5.11: A screen of autophagy-enhancing drugs for rescue of larval locomotion. a) Quantification of **i)** mean larval crawling speed and **ii)** percentage time spent moving of control and dATM knockdown larvae reared in normal food +/- 10 mM NMN. **b)** Same as for **a** but +/- 5 mM metformin. **c)** Same as for **a** but +/- 1 mM torin. All larvae reared at 27°C. N numbers indicated below each genotype. Shown are adjusted p-values from Tukey's Honest Significant Differences test or Dunn's test, depending on the outcome of Shapiro-Wilk normality testing. p≤0.05 *, p≤0.01 **, p≤0.001 ***, p≤0.0001 ****. Locomotion experiments performed by D.P Bennett and S.A Ahmed.

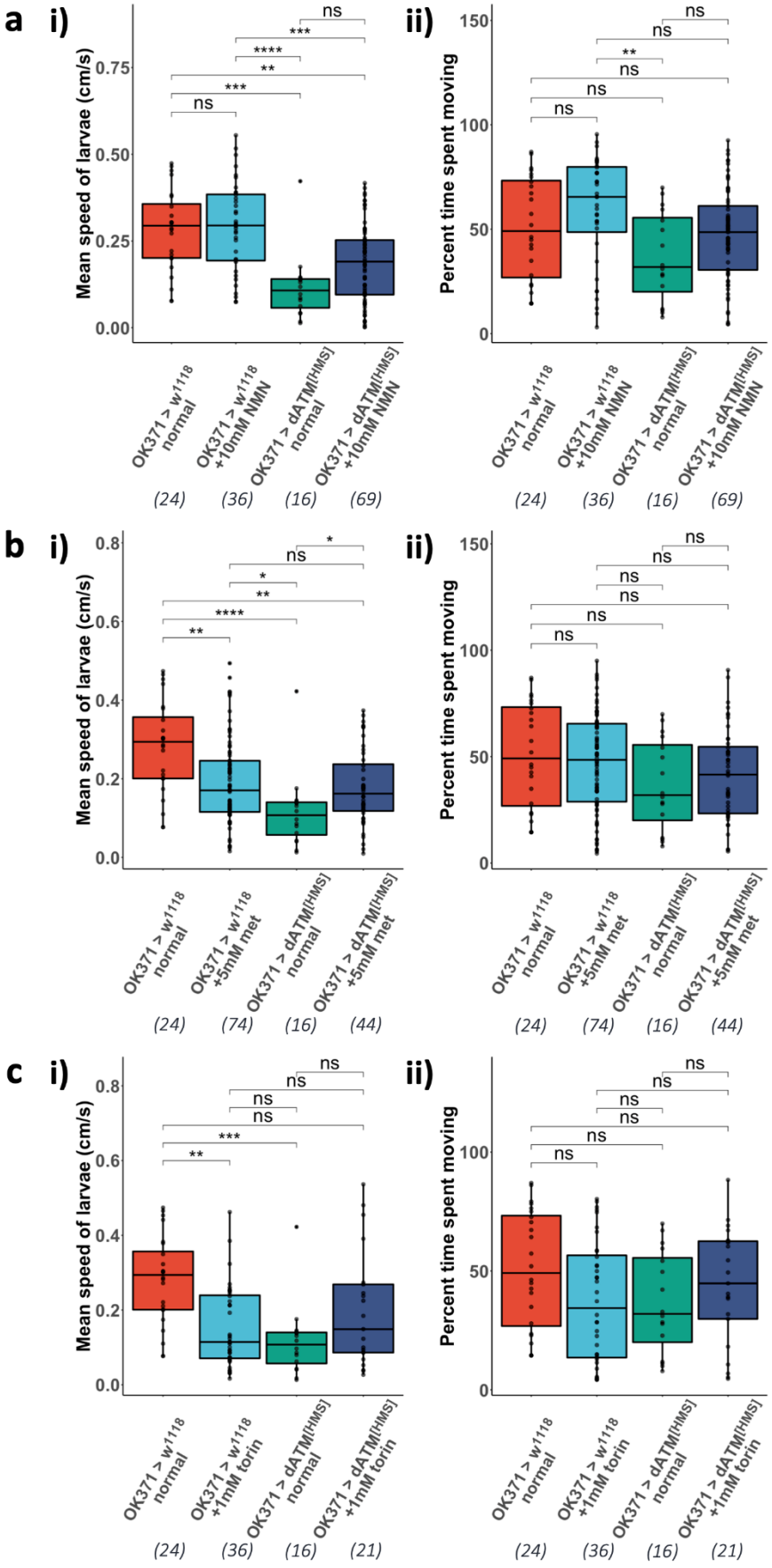
a
i)
ii)
Mean speed of larvae (cm/s)
Percent time spent moving
OK371 > w1118 normal
OK371 > w1118 +10mM NMN
OK371 > dATM[HMS] normal
OK371 > dATM[HMS] +10mM NMN
(24) (36) (16) (69)
b
i)
ii)
Mean speed of larvae (cm/s)
Percent time spent moving
OK371 > w1118 normal
OK371 > w1118 +5mM met
OK371 > dATM[HMS] normal
OK371 > dATM[HMS] +5mM met
(24) (74) (16) (44)
c
i)
ii)
Mean speed of larvae (cm/s)
Percent time spent moving
OK371 > w1118 normal
OK371 > w1118 +1mM torin
OK371 > dATM[HMS] normal
OK371 > dATM[HMS] +1mM torin
(24) (36) (16) (21)

5.3 – Discussion

In this chapter, the function of presynaptic dATM has been evaluated. Neuronal ATM presents something of a conundrum. From early in the study of this kinase, it has been noticed that neurons have a particularly large pool of cytosolic ATM compared to other cell types (Oka and Takashima, 1998; Barlow *et al.*, 2000; Boehrs *et al.*, 2007), although there is controversy around this (Dar *et al.*, 2006; Biton *et al.*, 2007; Gorodetsky *et al.*, 2007). Clearly, a subset of ATM localises to synapses, observed both in mammalian models (Vail *et al.*, 2016) and in the previous chapter of this work. It seems unlikely that this would be coincidental and thus begs the question of what a DNA damage response kinase is doing so far from its more "natural" home in the nucleus. The finding that cytosolic, dimeric ATM can be directly oxidised by reactive oxygen species (Guo *et al.*, 2010) where it then has distinct downstream targets, such as regulation of autophagic flux (Alexander *et al.*, 2010), widened the scope of the putative function of neuronal ATM. In *Drosophila*, both oxidative stress and autophagy are positive regulators of synapse development (Shen and Ganetzky, 2009; Milton *et al.*, 2011). It therefore made sense to target these processes when screening for mediators of presynaptic dATM function.

In *Chapter 3*, it was demonstrated that *dATM* heterozygous mutants had significantly smaller NMJs compared to controls, a phenotype which closely resembles that of *atg* mutants, and that presynaptic dATM knockdown alone was sufficient to replicate this phenotype. ATG1 is downstream of TORC1 signalling (Mizushima, 2010), and its overexpression in *Drosophila* leads to strong induction of autophagy (Scott, Juhász and Neufeld, 2007). In that study, ATG1 was overexpressed using the heat-shock inducible *Hsp70-GAL4* driver and autophagy was quantified in the fat body. Overexpression of ATG1 pan-neuronally using *Elav-GAL4* leads to

significant overgrowth of the NMJ as measured by bouton number (Shen and Ganetzky, 2009). Neuronal overexpression of ATG1 in a background of dATM deficiency has not previously been tested. If dATM is explicitly required for ATG1 activity, then there was the possibility that dATM knockdown would mask the ATG1 overexpression phenotype. Alternatively, the UAS-ATG1 phenotype may be completely independent from dATM signalling, or ATG1 overexpression could compensate for the loss of dATM.

Epistasis is a term applied differently to different fields of study, and the definition can be somewhat flexible. Here, the term is being applied broadly to a study of interactions between the dATM knockdown phenotype with other genetic perturbations of candidate genes in relevant signalling pathways. To unpack this, we can consider the seminal study identifying autophagy as a key regulator of *Drosophila* synapse size – *atg* mutants lead to smaller synapse sizes, while *highwire* (*hiw*) mutants have expanded NMJs (Wan *et al.*, 2000; Shen and Ganetzky, 2009). The hypothesis is that the *atg* mutant phenotype is a synaptic undergrowth caused by failure to upregulate autophagy. Autophagy is required for the degradation of Hiw, which acts by repressing *Wallenda* (Wnd). Since Wallenda generates a positive NMJ growth signal, depleting Hiw therefore drives synaptic growth. In this case, *hiw/atg* double mutants should display the *hiw* phenotype as it is downstream of the *atg* genes, which is indeed the case (Shen and Ganetzky, 2009). This application of epistasis, where one phenotype completely masks the other, makes sense when applied to null mutants where there should be a complete loss of the corresponding protein. However, in this chapter's experiments, one is primarily dealing with ectopic overexpression, or RNAi-mediated knockdowns in which the efficiency is never 100%. Therefore, it is impossible to tell whether

dATM is *obligate* for the activation of these putative enhancers/suppressors since there will always be a residual pool of neuronal dATM remaining.

In the case with UAS-ATG1, the work in this chapter is consistent with previously published work in that pan-neuronal overexpression of ATG1 resulted in an expanded NMJ phenotype, here measured by surface area and active zone number in addition to just bouton count. Few surviving third instar larvae were available from these crosses (and no larvae survived to third instar with the construct on chromosome 2), and they were significantly smaller, which caused the NMJ metrics to be scaled "upwards." This overgrowth is reminiscent of TrpA1-mediated overgrowth, except muscle surface area in the latter was not significantly reduced. Given that further increases of rearing temperature with TrpA1 are deleterious, suggesting that these "overgrown" synapses may be on the cusp of (or at least vulnerable to) neurodegeneration, it begs the question of whether that is also true of ATG1-overexpressing neurons. Is this a "functional" overgrowth as well as a structural one, or are these neurons vulnerable and/or show reduced synaptic output? In addition, *spin* mutants which have significantly increased ROS levels show expanded NMJs and have electrophysiological deficits (Milton *et al.*, 2011), although there is not always a correlation between altered bouton morphology and changes in synaptic transmission (Campbell and Ganetzky, 2012). Therefore, a future direction for this work would be to functionally test these larvae with locomotion and electrophysiology experiments.

The combination of ATG1 overexpression with dATM knockdown resulted in a phenotype which was roughly intermediate of the two conditions alone. One must take care in drawing too strong a conclusion from this, as there are various scenarios in which this phenomenon could occur. One of those scenarios is that the two proteins sit in completely

different pathways that independently regulate NMJ development, and that over-correction in one can compensate for downregulation of the other. A second scenario is that dATM and ATG1 sit within the same pathway (autophagy regulation), and that the reason for an intermediate phenotype is due to the fact that dATM knockdown produces an environment of reduced autophagic flux compared to the control context. Therefore, overexpression of ATG1 in a background of dATM knockdown will not drive autophagy to the same levels as ATG1 overexpression alone, thus the overgrowth is attenuated.

Two observations support the latter possibility. The first is that pan-neuronal overexpression of ATG1 from the UAS construct on chromosome 2 was lethal, which was abrogated by co-expression of dATM dsRNA. In addition, an autophagy deficit was detected in salivary glands of dATM knockdown larvae, as measured by the reporter *UAS-mCherryGFP-Atg8a* (fig 5.9). This adds to the plausibility that ATG1 and dATM both regulate the balance of neuronal autophagy rather than acting via separate signalling pathways.

The role of autophagy in neurodegenerative disorders is widely studied, both in terms of the mechanism of pathology and for treatment (Zatyka, Sarkar and Barrett, 2020). Generally, enhancement of autophagy in neurodegenerative diseases, such as Alzheimer's, Parkinson's and ALS is neuroprotective (Menzies *et al.*, 2017; Djajadikerta *et al.*, 2020). Numerous autophagy-enhancing compounds are at the clinical trial stage for the treatment of these diseases (Nah, Yuan and Jung, 2015). However, some researchers suggest that autophagy levels must be held in a delicate balance (Cherra and Chu, 2008), and excessive autophagy is pathological (Liu and Levine, 2015). As an example, inhibition of autophagy in a mouse model of spinal muscular atrophy rescued motor neuron degeneration, improved righting reflex, and improved survival (Piras *et al.*, 2017). The key differentiating factor here

could be whether the neurodegenerative disorder is associated with an accumulation of aggregative proteins – both a feature of impaired autophagic flux and potentially amenable to autophagy enhancement as a treatment. An additional layer of complexity is that the neonatal nervous system may respond differently to autophagy manipulations than the adult nervous system (Zhu *et al.*, 2005; Corti *et al.*, 2020).

Even simply taking A-T as an example, primary neurons cultured from $ATM^{-/-}$ mice show significantly upregulated autophagic flux and impaired lysosomal trafficking (Cheng *et al.*, 2020), while hiPSC-derived neuronal precursor cells from an A-T patient showed impaired autophagic flux and evidence of defective mitophagy (Sunderland *et al.*, 2020). Other groups have found retention of autophagic flux in ATM-deficient cells, but evidence for a mitophagy deficit – further, removal of one copy of the *beclin-1* gene (an autophagy promoter) rescued mitochondrial function and delayed tumour onset in these cells (Valentin-Vega *et al.*, 2012). These differences may be due to differences in model and cell type, or due to differences between post-mitotic and cycling cells. This inconsistency nevertheless manifests itself in the therapeutic potential of autophagy enhancers/inhibitors for A-T – for example, treatment of ATM-deficient primary mouse neurons with bafilomycin A_1, a potent inhibitor of autophagy (Yamamoto *et al.*, 1998), rescued synapse loss and cell death (Cheng *et al.*, 2020); by contrast, upregulation of autophagy through nicotinamide riboside treatment of $ATM^{-/-}$ mice resulted in reduced cerebellar degeneration and increased lifespan (Fang *et al.*, 2016).

This ambiguity is translated into *Drosophila* models, with further evidence for the balancing act of autophagy levels in benefitting life- and health-span. For example, a study from the Linda Partridge lab assessed the effects of overexpressing ATG1 at different levels in different tissues. Constitutive strong overexpression using *Actin-GAL4* was embryonic lethal,

while strong overexpression at in the adult was also deleterious (Bjedov *et al.*, 2020). Similar to the above noted potential differences between neonates and adults, they also found that if they confined a moderate level of ATG1 overexpression to adult fat body, malphigian tubules and intestine using *temperature-sensitive-GAL80*, developmental deficiencies were avoided and lifespan was significantly extended (Bjedov *et al.*, 2020). For neurons, upregulation of autophagy has been shown to positively regulate NMJ expansion (Shen and Ganetzky, 2009), suppress neuron death in a Huntington's disease model (Wang, Lao and Edgar, 2009), and autophagy in the postsynaptic muscle is crucial for synaptic function and stability (Carnio *et al.*, 2014). However, other *Drosophila* models of neurodegenerative disorders run counter to this – in a Parkinson's disease model, knockdown of ATG7 rescued lifespan, climbing ability and neuronal survival of α-synuclein overexpressing flies (Yan *et al.*, 2019); in an Alzheimer's model, rapamycin-induced autophagy upregulation reduced the lifespan of $A\beta_{1-42}$-expressing flies, while RNAi of ATG5 extended the lifespan of these flies while reducing that of the controls (Ling *et al.*, 2009).

This context adds to the weight of the drug screen evidence in *5.2.8* above. The general pattern with the drugs that have a more direct effect on autophagy levels (metformin and torin) was a degradation of the locomotor performance of controls and an improvement of that of the dATM knockdowns. This is consistent with an autophagy deficit in dATM-deficient neurons and with the hypothesis that autophagy levels are carefully balanced, with both reduced and excessive autophagy being deleterious. Going forward, this hypothesis requires validation by quantifying autophagy levels in each of the conditions using the *GFP-mCherry-Atg8a* reporter alongside NMJ dissections to assess whether the structural phenotype is also rescued. In addition, while it was challenging to detect any differences in basal autophagy in

the CNS, it would be interesting to live-image the NMJs of *GFP-mCherry-Atg8a*-expressing control and dATM knockdown larvae in the presence and absence of H_2O_2 – if dATM is mediating the link between oxidative stress signalling and the upregulation of autophagy (discussed below), then this may be manifest in differences in the dynamic changes of GFP/mCherry colocalisation and puncta formation.

The CNS images from the *GFP-mCherry*-Atg8a experiment suggest that neurons have high levels of basal autophagy in their cell bodies. This perhaps means that the positive correlation between autophagy induction and synapse growth results from local bursts at the synapse level (e.g., through degradation of Hiw) and this is what is defective in dATM knockdown neurons. It would be interesting to test whether *hiw* mutants display the same levels of overgrowth in neurons lacking dATM. If dATM is indeed involved in the autophagic regulation of NMJ expansion, then the prediction would be that dATM knockdown in a *hiw* background would phenocopy the *hiw* mutant alone, since the model is that autophagic degradation of Hiw is what leads to NMJ growth. Hiw is known to localise to synaptic boutons in the larval NMJ (Wan *et al.*, 2000; Wu *et al.*, 2005), so it is an intriguing possibility that dATM could promote the local autophagic degradation of synaptic Hiw, in conjunction with other autophagy regulators, in response to ROS signalling.

If dATM is regulating autophagy in neurodevelopment, then work from mammalian studies suggest that the most likely mediator of this is AMPK (Alexander *et al.*, 2010). In *5.2.5*, neither pan-neuronal knockdown nor overexpression of AMPK alone resulted in any change in NMJ structure, except for a reduction in bouton count when overexpressing. This was a surprise given the known role for AMPK in synaptic plasticity (Marinangeli *et al.*, 2018), although

structural and electrophysiological plasticity are not always correlated. Because dsRNA-mediated RNAi knockdown is never 100% efficient, this suggests that the residual pool of AMPK is sufficient for normal NMJ development. AMPK is expressed at higher levels in the larval nervous system than dATM, which might mean that the larva is more sensitive to perturbations in dATM levels than AMPK (*FlyAtlas2, https://motif.mvls.gla.ac.uk/FlyAtlas2*). By contrast, the combination of AMPK knockdown or overexpression in a dATM knockdown background clearly modified the phenotype. Although the FIJI quantification algorithm was not sensitive enough to detect these differences, there was an obvious qualitative exacerbation of the dATM knockdown phenotype when co-expressing AMPK dsRNA, with a fragmenting of the presynaptic membrane and frequent observation of a "retraction bulb", implying early signs of neurodegeneration.

Overexpressing AMPK in a dATM knockdown restored NMJ structure to that of controls, except for their bouton count. NMJ size, bouton count and active zone number are not always correlated – for example, the nuclear LEM-domain protein MAN1 interacts with BMP signalling during NMJ development, and loss of MAN1 results in a decrease of NMJ size and active zone number, but an increase of smaller, underdeveloped boutons (Laugks, Hieke and Wagner, 2016). The separability of bouton formation from other aspects of NMJ development such as presynaptic homeostasis and overall NMJ enlargement is well established with other signalling pathways that co-regulate these processes (Goold and Davis, 2007; Koles and Budnik, 2012). Therefore, it is plausible that bouton expansion may require other dATM targets than AMPK.

The structural rescue of surface area and active zone count was not simply due to dilution of the knockdown with an extra UAS as there were other UAS constructs (such as UAS-

mitoGFP) which did not rescue the phenotype. What then explains the rescue? One possibility is that increasing the expression of AMPK increases the probability of interactions with dATM, leading to increased signalling of the AMPK-TSC2-mTOR pathway, resulting in autophagy upregulation and NMJ expansion. One criticism of this model is that this would predict that overexpressing AMPK in a wild-type background would lead to an increase in autophagy and thus synapse size because it would likewise increase the probability of AMPK-dATM interactions. Perhaps the difference is that, given the role of ATM in the response to oxidative stress (OS), neurons lacking dATM are constitutively under higher levels of OS and thus there is an increased probability that the remaining dATM molecules are in their ROS-activated state. ATM-AMPK interactions are downstream of ROS-activated ATM (Alexander *et al.*, 2010) – therefore, in this context, increasing these interactions is more likely to lead to activation of the autophagic machinery and increased NMJ growth. It is also known that hyperactivated AMPK is observed in Alzheimer's disease models, and causes excessive autophagy upregulation in cultured primary neurons, leading to synapse destruction (Domise *et al.*, 2019). This again links to the balancing act of autophagy levels in regulating synapse development and homeostasis.

The role of AMPK in neuronal metabolism should also be considered. As a sensor of the AMP:ATP ratio (Xiao *et al.*, 2007), AMPK can induce neuronal mitochondrial respiration upon synaptic stimulation (Marinangeli *et al.*, 2018). It is possible therefore that overexpression of AMPK primes the neuron to show increased sensitivity to changes in activity levels, and this is what rescues the dATM knockdown phenotype. It is worth noting, however, that the construct used here overexpresses the α-subunit of AMPK, while (in mammalian AMPK) it is the ɣ-domain which is responsible for sensing the AMP/ATP ratio (Xiao *et al.*, 2007).

While ATM has been found localised with presynaptic vesicles (Vail *et al.*, 2016), and dATM localised to presynaptic puncta (previous chapter), there is no evidence for a synaptic pool of AMPK. However, it was recently shown that a fraction of AMPK localises to the outer mitochondrial membrane where it maintains cellular energetic homeostasis and promotes mitophagy upon energetic stress (Drake *et al.*, 2021). While that study was focused on AMPK within skeletal muscle, it is possible that the same is true within neurons. In addition, the regulation of mitophagy by ATM is also downstream of its redox activation and not its activation in the DNA damage response (Cirotti *et al.*, 2021). Given the defects in mitophagy resulting from dATM reduction seen above and in other studies, there is thus building evidence for a presynaptic interaction between dATM and AMPK signalling downstream of OS in regulating neuronal homeostasis.

In *model summary 1*, it is hypothesised that ROS-mediated ATM autophagy upregulation is held in a balance with its other downstream pathways, such as upregulation of apoptosis through p53 signalling. However, there is also evidence which suggests a crosstalk between p53 signalling and autophagy regulation (White, 2016; Shi, Norberg and Vakifahmetoglu-Norberg, 2021). For example, following sustained DNA damage signalling, transcription of the autophagy initiation complex proteins ULK1 and ULK2 is upregulated by p53 binding to p53-responsive elements in their respective promoter regions (Gao *et al.*, 2011). This leads to sustained autophagy in response to chronic sublethal DNA damage (Gao *et al.*, 2011). The β1 subunit of AMPK along with TSC2 also contain p53-responsive elements and are upregulated in a p53-dependent fashion following irradiation in HCT116 cells (Feng *et al.*, 2007), although this same paper concedes that this phenomenon is highly dependent on the cell or tissue type

under study. AMPK itself can phosphorylate and activate p53 in response to glucose depravation to induce cell cycle arrest in MEFs (Jones *et al.*, 2005). Another study performed genome-wide ChIP-seq of p53 wild-type and knockout MEFs following acute doxorubicin treatment and found a host of autophagy-related genes under the control of p53, including those noted above such as ULK1 and ULK2, AMPK β subunits and TSC2 (Broz *et al.*, 2013). However, despite the identification of these as p53-bound genes, not all showed p53-dependent upregulation in MEFs or human fibroblasts in response to DNA damage, which highlights the gene and cell-type specificity of autophagy regulation by p53.

The reciprocal interplay of autophagy, DDR signalling and p53 is a complicated picture. Autophagy aids in suppressing DNA damage levels and its deficiency can lead to activation of the DDR, genome instability and consequent tumorigenesis (Mathew *et al.*, 2007); however, in murine breast cancer models, autophagy suppresses p53 activity and itself promotes tumorigenesis through this p53 suppression (Guo, Xia and White, 2013; Huo *et al.*, 2013) – heterozygosity for *Beclin1* deletion was subsequently shown to suppress tumour development through an increase in p53-dependent apoptosis (Huo *et al.*, 2013). This implies a negative feedback mechanism whereby p53 induction of autophagy is balanced by the suppression of p53 activity downstream of autophagy signalling (White, 2016). The picture is further complicated by the fact that, in other cellular contexts, p53 activation can negatively regulate autophagy (Levine and Abrams, 2008; Shi, Norberg and Vakifahmetoglu-Norberg, 2021). Like ATM, the effects of p53 signalling appear to depend on whether it is the nuclear or cytoplasmic pool of the protein which is operating. One study found that the chronic upregulation of autophagy in *p53*$^{-/-}$ HCT116 cells could be abrogated by reintroduction of wild-type or cytosolic p53, but not constitutively nuclear p53 – this inhibition was due to a transcription-

independent interaction of p53 with the AMPK-mTOR signalling axis (Tasdemir *et al.*, 2008). Similarly, nuclear p53 can activate mitophagy through transactivation of the mitophagy effector PRKN (parkin) gene, yet cytoplasmic p53 binds to parkin protein itself and prevents its translocation to damaged mitochondria, which puts a brake on mitophagy (Hoshino *et al.*, 2013).

Taken together, this highlights how p53 and autophagy signalling is intricately interconnected, although the consequences of this on neurons and their synapses have not been elucidated. Further investigation will be required to establish how these signalling pathways downstream of ATM further interact in the development and plasticity of synapses.

As has been found elsewhere (Oswald *et al.*, 2018), overexpression and hyperactivation of the temperature-sensitive cation channel, TrpA1, was sufficient to induce synaptic overgrowth. The key question here was how dATM knockdown would modify this phenotype. In *chapter 3*, it was observed that at low rearing temperatures (19°C) and higher rearing temperatures (≥27°C), presynaptic motor-neuronal dATM knockdown resulted in significant structural deficits in NMJ development and locomotor deficits in the larva. This could be consistent with dATM acting as both a mediator of ROS-induced growth signalling and as a guardian against the excitotoxic effects of ROS. The hypothesis relies on 2 processes being held in balance (see *model summary 1*):

1 – ROS signalling through ATM to drive synapse expansion.

2 – ROS excitotoxicity leading to neurodegeneration or synaptic pruning.

If ATM responds to ROS at the synapse, then it is possible that the different effects of temperature on the dATM knockdown phenotype are the two sides of the same coin: at low

temperatures dATM knockdown synapses fail to respond to normal ROS levels and thus fail to expand appropriately compared to controls; at high temperatures, dATM knockdown synapses show heightened vulnerability to excitotoxicity induced by increased neuronal activity, and thus show signs of degeneration. Somewhere between the two extremes, there is a cross-over where these effects cancel out i.e., ROS levels increase to a point where the reduced sensitivity to their positive "growth" signal is compensated for, without reaching an excitotoxic level.

If this hypothesis is true, one way to validate it would be to increase ROS at low temperatures to see if this rescues the structural phenotype, while at higher temperatures, increasing ROS should exacerbate any potential neurodegeneration. In this chapter, it was found that at higher rearing temperatures, neuronal dATM knockdown sensitised larvae to the excitotoxic effects of TrpA1 and led to increased intracellular ROS sensitivity as demonstrated by the semi-lethality of catalase knockdown. However, these larvae did not show increased sensitivity to hDuOxII expression, and increasing the ROS-scavenging potential through overexpression of catalase did not rescue the phenotype. At lower rearing temperatures, hDuOxII expression was sufficient to rescue NMJ surface area but not bouton count or active zone number.

There are various takeaways from these observations. Because DuOx generates ROS extracellularly (Rada and Leto, 2008), the first is the possibility that dATM knockdowns at higher rearing temperatures are not hypersensitive to increases in extracellular ROS but are sensitive to intracellular ROS, while at lower temperatures, increasing ROS levels may overcome some of the structural deficits that are consistent with a failure in presynaptic ROS sensing during development and maturation of the NMJ. The sensitivity to increased

intracellular ROS production through TrpA1 expression or catalase knockdown may be a secondary effect of reduction of dATM but the fact that the phenotype is not rescued by overexpression of ROS scavengers may suggest the original NMJ structural phenotype is not caused by excessive ROS *per se*. A further validation of this would be to co-express ROS scavengers with TrpA1 expression and dATM knockdown at higher rearing temperatures to test whether this rescues viability. Others have elucidated a role for neuronal redox activated ATM in responding to increased energy demands, and cells lacking ATM are vulnerable to degeneration following prolonged neuronal activity and ATP depletion (Chow *et al.*, 2019). This study does suggest that neuronal activity drives ROS production which is sensed by ATM to regulate synaptic homeostasis. Alternatively, the vulnerability of dATM knockdown larvae to tonic TrpA1 activation may be related to other aspects of neuronal hyperactivity rather than ROS production specifically. While there was no evidence that TrpA1 hyperactivation led to increased DNA damage, absence of evidence is not evidence of absence – it is possible that combining dATM knockdown with TrpA1 hyperactivation leads to toxic levels of unrepaired double-strand breaks, but it is lethal before there is the opportunity to observe it.

Additionally, neuronal hyperactivation leads to chronically elevated calcium levels, which itself can be toxic to neurons. (Randall and Thayer, 1992). Mitochondria can function as a calcium buffer when neuronal intracellular calcium levels reach a certain threshold (Rizzuto *et al.*, 1992), and numerous neurodegenerative disorders are linked to disruption of this capability and the consequential excitotoxic levels of calcium influx (Verma, Lizama and Chu, 2022). Upon neuronal hyperactivation, mitochondria are recruited to presynaptic terminals to buffer calcium levels which results in a homeostatic decrease of neurotransmitter release (Vaccaro *et al.*, 2017). This could account for two phenomena: the increase in mitochondrial

density seen in dATM knockdown motor neurons, suggesting that they are perhaps hypersensitive to increased neuronal signalling, and the reduction in EJP amplitudes observed in *Chapter 3*.

An interesting future experiment would be to express a channelrhodopsin (ChR) in motor neurons to tonically excite them throughout neurodevelopment and test whether this enhances or suppresses the dATM phenotype. This could be done in the presence or absence of overexpressed ROS scavengers to test the ROS-dependence of the neuronal activity and dATM signalling relationship. If ChR expression at lower rearing temperatures was sufficient to rescue the dATM phenotype and this rescue persisted even with increased ROS scavenging, then it would point to a different mechanism for dATM regulation of neurodevelopment and homeostasis based on other aspects of neuronal activity.

Another takeaway from the above experiments is that ROS signalling, neuronal activity and/or rearing temperature influence different aspects of NMJ structure independently. In much of the literature, bouton number is used to quantify NMJ structural phenotypes, and throughout this thesis, that has generally closely correlated with NMJ surface area and active zone number. However, there are some experiments where that has not been the case. At the highest rearing temperature tested (30°C), it was sometimes observed that there would be significant differences in NMJ surface area between control and dATM knockdown, but not bouton or active zone counts. This could imply a disconnect between the signal instructing the entire NMJ to keep growing and the signal coordinating bouton formation and synapse specialisation.

There were some differences between the results here and previously published work. Firstly, motor neuronal expression of hDuOxII did not lead to synaptic overgrowth at either of

the rearing temperatures tested (in a preliminary experiment, pan-neuronal hDuOxII expression at 25°C rearing temperature also failed to induce NMJ overgrowth). This construct was chosen because a previous lab member had success in inducing overgrowth, as measured by manual bouton counting. Other groups have used the *UAS-DuOx* line, an overexpression construct of the *Drosophila* DuOx protein, to successfully induce increased bouton formation (Oswald *et al.*, 2018; Sobrido-Cameán *et al.*, 2023); therefore, expression of the human homologue may explain the differences found here.

In addition, the same authors found that catalase knockdown led to NMJ overgrowth (Oswald *et al.*, 2018) whereas in this chapter, it was deleterious to NMJ development. Nevertheless, this result is consistent with the hypothesis that ROS signalling must be held in a balance – the key difference between the experiments is that in the Oswald et al., study, larvae were reared at 25°C, compared to 30°C here. Within that context the results are more consistent, since a higher rearing temperature will lead to increased baseline neuronal activity and thus higher endogenous ROS levels, where additional increases in ROS are no longer growth signals but result in tipping over the edge into neurodegeneration. It would be interesting to essentially repeat the temperature gradient experiment of *Chapter 3* +/- catalase overexpression and knockdown to see how it influences the phenotype at different basal levels of developmental neuronal activity.

5.4 – Conclusion

This chapter has tackled the question of the specific function of presynaptic dATM and the pathways in which it interacts, with a focus on the known targets of cytosolic ATM signalling from mammalian work. Neuronal activity, ROS signalling and autophagic flux all help shape

the maturing NMJ, yet these processes must be held in balance before their effects become deleterious. ATM is well placed to be this mediator – it localises to presynaptic vesicles, and its redox activation leads to upregulation of autophagy, while prolonged ATM activation results in activation of the pro-apoptotic pathway. This model is supported by the screen of modifiers of the dATM knockdown phenotype performed above. dATM knockdown larvae are sensitive to excitotoxicity and decreased intracellular antioxidant capability and show evidence of an autophagy deficit. Enhancing autophagic flux genetically or pharmacologically tends to be deleterious alone but rescues the dATM knockdown phenotype, again suggesting that dATM mediates this crucial balance. Further, a putative interaction between dATM and AMPK was established as knockdown of AMPK qualitatively worsened, while overexpression of AMPK rescued, dATM knockdown NMJ structure. This provides a framework for ATM as a key coordinator of ROS and autophagy signalling during neuronal development and homeostasis, which will be discussed further in the final chapter.

Chapter 6 – Discussion

6.1 – Summary of findings

Using the *Drosophila* third instar larval neuromuscular junction, this thesis has explored the role of ATM in synapse development, homeostasis, and function. *Chapter 3* provided evidence of a presynaptic requirement for dATM, which was independent of its role in the DNA damage response (DDR). Neurons deficient in dATM had smaller NMJs exhibiting electrophysiological and functional deficits, with some evidence that they were on the cusp of degeneration. While localisation of sfGFP-tagged endogenous dATM provided mixed results, in *Chapter 4* it was shown that overexpressed neuronal dATM[msGFP2] was primarily cytosolic and formed foci in axons and synapses. In *Chapter 5*, the function of this presynaptic pool of dATM and the interacting biological pathways were explored. Given the cytosolic localisation of dATM, the known redox role of mammalian ATM in the AMPK-TORC1 axis, and the influence of ROS signalling and autophagy in synapse development in *Drosophila*, these pathways were targeted in an epistasis screen for modifiers of the dATM knockdown phenotype. Larvae with dATM knockdown were sensitive both to excitotoxicity and to reduction in intracellular antioxidant capacity and showed indications of impaired autophagic flux. Increasing autophagy both pharmacologically and genetically, while deleterious alone, could compensate for dATM deficiency. In addition, there was evidence that the ATM-AMPK axis in the redox regulation of autophagy is conserved in the developing larval nervous system. Together, this suggests a putative model in which presynaptic dATM coordinates ROS and autophagy levels during development and maturation, potentially mediating the balance that

must be held with these pathways in the promotion of synapse growth and prevention of degeneration.

6.2 – The presynaptic requirement for dATM in larval NMJ development – undergrowth or degeneration?

While other studies have focussed on the deleterious effects of *dATM* mutations on the structure of the *Drosophila* adult brain and the effects on adult locomotion and lifespan (Song *et al.*, 2004; Rimkus *et al.*, 2008), this is the first to investigate the consequences on larval neurodevelopment and function, and moreover in a tissue-specific manner. This approach is relevant to the progression of the human disorder, which is an early-onset neurodegenerative disorder (McKinnon, 2004), although there is some indication of a developmental patterning defect also (Vinters, Gatti and Rakic, 1985). The *Drosophila* nervous system offers a unique model, capturing the dynamics of both larval and adult neural development. When assessing the effect of ATM-deficiency in adult flies, there is the risk of being unable to dissociate the role of ATM in neural progenitors, or in coordinating some aspect of neurodevelopment in metamorphosis, which would be distinct from mammalian ATM. There is already inconsistency in the literature as to the effect of specific neuronal knockdown of dATM, with some studies reporting photoreceptor degeneration and temperature-dependent lethality (Rimkus *et al.*, 2008) while others report that it is glia which are vulnerable to ATM-deficiency and not neurons (Petersen, Rimkus and Wassarman, 2012). Previous work in our lab has demonstrated that confining dATM knockdown to adult neurons was neuroprotective and lifespan-extending in different models of neurodegenerative disorders (Taylor *et al.*, 2022). It

is therefore likely that ATM plays different roles in cycling *vs.* non-cycling cells of the nervous system, and in developmental *vs.* mature adult contexts.

The distinction between a neurodevelopmental disorder and an early-onset neurodegenerative disorder is a theme that has emerged repeatedly during this work. The initial *dATM* heterozygous null or neuronal knockdown phenotypes introduced in *Chapter 3*, which are both structural and functional, could indicate either a failure to respond to growth signalling – and thus an undergrown synapse – or a synapse showing signs of degeneration. Evidence was presented that supported both interpretations (and potentially both may be occurring) and in *Chapter 5* an attempt was made to synthesise these observations into one model (*Chapter 5 model summary 1*). The failure of dATM-deficient motor neurons to expand in response to increased rearing temperature was suggestive of a failure to transduce activity-dependent growth signals in the long term. Furthermore, there were indications of a retraction of the presynaptic membrane from the postsynaptic density and an increase in local caspase activity in posterior motor neurons with one of the dsRNA constructs at higher rearing temperatures. This dsRNA was also pharate lethal at rearing temperatures ≥25°C. However, this was not observed with the second dsRNA construct which suggests the phenotype may be dependent on the strength of dATM knockdown. Together, this evidence led to the working model that presynaptic dATM knockdown results in undergrown NMJs through a failure to respond to long-term growth signals. These NMJs are also sensitive to further stressors, such as increased neuronal activity or ROS production.

While an attempt was made to characterise the role for dATM in short-term structural plasticity in *Chapter 3*, the results were inconclusive. It is possible to observe bouton formation

following optogenetic stimulation through confocal live imaging of intact larvae expressing neuronal membrane CD8::GFP (Piccioli and Littleton, 2014; Fernandes *et al.*, 2023). This occurs even when the motor neuron is severed from the cell body indicating the involvement of a local signalling event (Piccioli and Littleton, 2014). It would be interesting to see if local ROS bursts precede bouton formation, which could be achieved through co-expressing a ratiometric ROS sensor such as roGFP2::orp1 (Albrecht *et al.*, 2011). Combining this paradigm with dATM knockdown may give insight as to whether dATM coordinates short term ROS induced plasticity in addition to its role in transducing longer term growth signals.

Further to the regulatory role of neuronal activity in shaping the maturation of the larval nervous system, there is recent evidence of the importance of a "critical period" in larval development in which manipulations have long-lasting results on the later structure and physiological properties of the neurons (Giachello and Baines, 2015). It would be interesting to see whether dATM signalling is required in the critical period establishment of this homeostatic setpoint, or whether a burst of neuronal activity in the critical window (e.g., through optogenetic stimulation) would be sufficient to overcome the reduction in NMJ growth of dATM mutants and knockdowns.

6.3 – The balancing act of ROS and autophagy – mediated by ATM?

A key theme which has emerged multiple times throughout this thesis is the idea of *balance.* The maturing neuron is constantly integrating cues from multiple interlinked pathways to shape its synaptic connectivity, strength, and structure. Because of the previously established role of mammalian ATM in their coordination, the focus here has been on the autophagy machinery and oxidative stress signalling. Both pathways act to positively regulate synapse

expansion in *Drosophila,* yet in excess can be deleterious (Shen and Ganetzky, 2009; Milton *et al.*, 2011; Oswald *et al.*, 2018). The same is true for neuronal activity, which is required for normal synapse development and maintenance while excessive neuronal activity is excitotoxic (Sigrist *et al.*, 2003; Zhong and Wu, 2004), and there are clearly links to oxidative stress signalling since a more active neuron will have increased metabolism leading to increased mitochondrial ROS production.

The evidence presented in this thesis indicates that dATM is involved in transducing ROS-autophagy signalling in neurons and mediating the balance of these interconnected processes. For example, neuronal dATM knockdown sensitised larvae to excitotoxicity and decreased ROS-scavenging but was protective against chronically upregulated autophagy. Pharmacological induction of autophagy in control larvae was detrimental to their locomotion but beneficial to that of dATM knockdowns. This supports other *Drosophila* studies in both neuronal and non-neuronal tissues which suggest a sweet spot for autophagy levels in promoting life and health span (Ling *et al.*, 2009; Bjedov *et al.*, 2020). Furthermore, it fits into the wider context of mammalian research which has highlighted the importance of balancing autophagy levels to maintain neuronal health (Cherra and Chu, 2008), where enhancing autophagy can aid in clearing toxic aggregative proteins in disorders such as Parkinson's (Malagelada *et al.*, 2010) and Alzheimer's (Spilman *et al.*, 2010), while excessive autophagy can result in neurodegeneration (Liu and Levine, 2015).

6.4 – The conservation of the dATM-AMPK-autophagy signalling axis in *Drosophila* neurodevelopment

It was interesting that the role of neuronal dATM appeared to be independent of its role in the DNA damage response. This was supported by the following observations: knockdown of upstream or downstream DDR components had no effect on NMJ morphology or survival; the sensitivity of dATM knockdown larvae to excitotoxicity appeared to be independent of increased DNA damage; and motor neurons expressing dATM[msGFP2] showed predominantly cytosolic localisation of the construct. These, coupled with the epistatic interactions of ATM with the autophagy machinery and AMPK, indicated that the extranuclear, redox-dependent signalling pathways of ATM may underlie its neuronal function. This supports the growing understanding of a specialised pool of cytosolic ATM within neurons that operates independently from the DDR, as other groups have demonstrated in mammalian models. This includes the physical association of ATM with synaptic vesicle proteins VAMP2 and synapsin-I (Li *et al.*, 2009), the regulation of excitatory *vs.* inhibitory neurotransmitter release (Cheng *et al.*, 2018), its role in LTP (Vail *et al.*, 2016), and association with mitochondria and concomitant regulation of mitophagy (Valentin-Vega *et al.*, 2012).

The model for how redox-activated dATM could respond to local ROS signalling to coordinate synapse growth and protection against toxicity is summarised in fig 6.1. Local ROS production, potentially through increased neuronal activity, redox-activates the synaptic pool of dATM, promoting its non-DDR related pathways. The conserved ATM-AMPK-TORC1 axis leads to de-repression of autophagy which stimulates NMJ growth, potentially through the

same pathway as has been previously established (Shen and Ganetzky, 2009). This may then be held in balance with other redox-sensitive ATM pathways, such as p53-mediated pro-apoptotic signalling, upregulation of mitophagy through Parkin, or promotion of the pentose phosphate pathway (PPP) to buffer oxidative stress. This fits with the hypothesis presented in *Chapter 5*: in normal conditions, increased ATM redox signalling results in growth of the NMJ

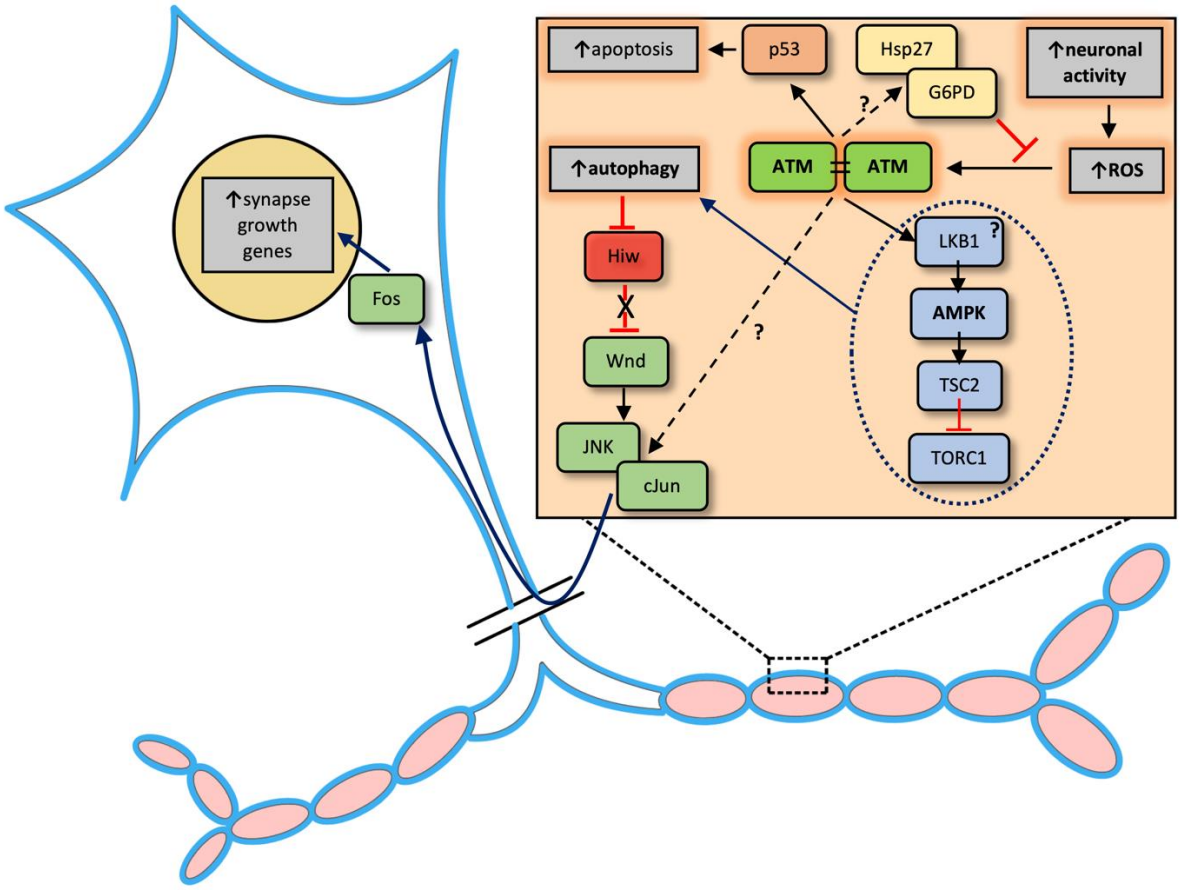

Figure 6.1 – A model of how redox activated synaptic ATM may regulate ROS-autophagy signalling in neuronal development and homeostasis. Dashed lines indicate pathways elucidated in mammals where the conservation with *Drosophila* ATM is not known. In **bold** are proteins and pathways shown to interact with neuronal dATM in this thesis. A question mark is over LKB1 as this intermediate was not tested in this thesis although it is known to be downstream of redox-activated mammalian ATM. An **X** over a red inhibition symbol indicates de-repression. The dotted circle around the LKB1-TORC1 pathway indicates the likely mechanism for dATM redox regulation of autophagy based on Alexander *et al.,* (2010) but the conservation of this pathway in *Drosophila* has not previously been established. *Other ATM redox pathways, such as regulation of the cytoskeleton and promotion of mitophagy, may influence synaptic function but are not depicted here. Also not depicted is the direct pathway of AMPK-mediated autophagy upregulation through ULK1, for clarity.*

and homeostatic feedback to prevent ROS toxicity and degeneration; in ATM-deficiency, neurons both fail to respond to normal ROS signalling during development and are hypersensitive to excitotoxic stressors.

This model predicts that moderately increased ROS production at lower temperatures should compensate for the reduced growth signals in dATM knockdown larvae, and there was some evidence that this did in fact rescue the phenotype. At the other extreme, it predicts that increased ROS production would be toxic in dATM knockdown larvae, while increased ROS scavenging should rescue the NMJ phenotype. Here, there was more ambiguity since catalase overexpression did not rescue the NMJ phenotype, but *dATM*-deficient larvae were sensitive to catalase knockdown. It is still not clear whether dATM knockdown larvae are constitutively oxidatively stressed and therefore hypersensitive to perturbations of ROS, or that the excitotoxicity induced by TrpA1 co-expression is ROS mediated. While tonic TrpA1 activation has been shown elsewhere to lead to increased mitochondrial oxidative stress (Oswald *et al.*, 2018), it is possible the toxicity is caused by other consequences of increased neuronal activity, such as through dysregulated Ca^{++} signalling (Verma, Lizama and Chu, 2022). These alternative hypothesis could be delineated through expanding upon the preliminary *mito-roGFP2::orp1* experiments shown in *Chapter 5* and through the combination of electrophysiology experiments with live calcium imaging.

If the above model is true, further work is necessary to examine how it fits into the bigger picture established by the work of others. Does dATM's role in autophagy induction fit with the known autophagic regulation of Highwire levels, controlling Wallenda degradation, and signalling through the MAPK pathway to induce synapse growth (Shen and Ganetzky, 2009)?

It would be interesting to see if *hiw* mutants or *wnd* overexpression are able to mask the dATM knockdown phenotype which would be predicted if the major consequence of dATM inducing autophagy in the neuron is to cause the degradation of Hiw. Alternatively, redox-activated ATM may bypass the autophagy machinery and activate JNK directly as has been shown elsewhere (Lu *et al.*, 2016), giving both a direct and indirect mechanism for ROS and ATM-mediated JNK signalling upregulation.

The effect of p53 knockdown on NMJ development was not tested in this thesis. Elsewhere, p53 reduction in adult *Drosophila* has been shown to be neuroprotective in adult-onset gain-of-function neurodegeneration models (Taylor and Tuxworth, 2019). Combining p53 and dATM knockdown with increased ROS generation or excitotoxicity (e.g., through TrpA1 activation) and observing whether this rescues survival or NMJ phenotypes may give answers as to whether this is the pathway which mediates neurodegeneration in this context. Further, as redox-activated mammalian ATM is known to signal through the PPP via Hsp70 phosphorylation to increase antioxidant capability (Cosentino, Grieco and Costanzo, 2011; Zhang *et al.*, 2018), this is a potential mechanism for how ATM activation at synapses could act in a local homeostatic feedback mechanism that buffers ROS levels to prevent toxicity. Further epistasis work overexpressing or knocking down *Drosophila* PPP components may help to elucidate the precise nature of this feedback mechanism.

At this stage, it is also not clear whether dATM signalling interacts with other canonical pathways in NMJ development. The model above suggests an intrinsic mechanism for regulating synapse growth in response to neuronal activity, as opposed to a transsynaptic signal. Nevertheless, it would be interesting to test whether manipulations of *Wingless* or BMP signalling are able to compensate for dATM-deficiency, and whether these pathways sit in

parallel, upstream, or downstream of dATM. Furthermore, DJ-1β has been identified as a key ROS sensor required for ROS-mediated overgrowth by regulating PI3K activity through inhibition of PTEN (Oswald *et al.*, 2018). PTEN is a known target of mammalian ATM whereby it regulates its translocation to the plasma membrane (Bassi *et al.*, 2013, 2021), although this it thought to be downstream of DDR-activated rather than redox-activated ATM and it is not known if this pathway is conserved in *Drosophila.* Nevertheless, whether DJ-1β and dATM interact in the ROS-mediated expansion of the NMJ is an avenue for future research.

Thus, while work is still needed to confirm the precise pathway of redox-mediated dATM synaptic signalling, the independence of the phenotype from the DDR, the cytosolic expression of tagged dATM[msGFP2] (*below*) in neurons and the interactions of the phenotype with ROS signalling and autophagy point to this as the likely model.

6.5 – Localisation of dATM[msGFP2]

This research is also the first to demonstrate presynaptic localisation of *Drosophila* ATM, supporting the evidence that showed only presynaptic knockdown – and not post- or peri-synaptic knockdown – was sufficient to phenocopy the *dATM* mutant phenotype. Overexpressed GFP-tagged dATM localises to synaptic puncta, which correlates with mammalian studies showing ATM colocalization with synaptic vesicles (Li *et al.*, 2009; Vail *et al.*, 2016). It is not yet clear what these foci of dATM[msGFP2] were, and further experiments co-staining for presynaptic vesicle markers (such as Csp) or active zones (e.g., BRP) would be necessary. Also, given that these foci were also observed within the axon and given the interaction of dATM with the autophagic machinery, it raises the possibility that these are

autophagosomes which could be confirmed using anti-GABARAP antibodies. This would be consistent with the observation that autophagosomes in neuron are rarely observed in the soma, preferentially form in the distal axon and are transported retrogradely along axons through association with dynein (Maday and Holzbaur, 2014; Cheng *et al.*, 2015). A physical interaction between dATM and autophagosomes could provide further evidence for the local coordination of ROS and autophagy signalling by dATM in synapses, although it would present further questions regarding the trafficking of dATM along axons and how this interaction is mediated.

If the mechanism of dATM's role at the synapse is via redox activation, a further question would be whether these synaptic puncta contain dimeric dATM, as would be predicted from mammalian studies. This could be tested by expressing separate dATM constructs containing fluorescent probes that are fluorescence resonance energy transfer (FRET) compatible, or by extracting proteins from synaptosome preparations and western blotting for the presence of dimeric tagged dATM. In addition, if redox activated ATM is *necessary* for normal neurodevelopment, it would be interesting to test *sufficiency*. In *Structural comparison of hATM and dATM*, a prediction for the dATM nuclear localisation sequence (NLS) was generated. Through expressing a form of dATM with mutations in this sequence, addition of nuclear export sequences (NES), or alternatively containing ectopic constitutive NLSs, would help determine the sufficiency of cytosolic dATM in neurodevelopment and homeostasis, and give insight as to why neurons have a notably large cytosolic pool of ATM compared to other cell types (Barlow *et al.*, 2000).

6.6 – Final thoughts on implications for Ataxia-Telangiectasia

While the aim of this work was not to model A-T in *Drosophila* larvae *per se*, the implications for the pathology and treatment of A-T can still be considered. The autophagy deficit detected in dATM knockdown larvae and the subsequent rescue through either genetic or pharmacological upregulation of autophagy suggests that this may be a viable treatment for A-T. However, care must be taken as clearly there is a threshold at which excessive autophagy becomes deleterious, as shown by the lethality of one of the UAS-Atg1 constructs and by the deleterious effect on locomotor performance of the same small molecule autophagy enhancers on control larvae. As mentioned earlier, the use of autophagy enhancers to treat A-T has produced mixed results (Fang *et al.*, 2016; Cheng *et al.*, 2020). The Fang *et al.,* (2016) study showed that treatment with NAD+ precursors reduced cerebellar degeneration and increased lifespan in a mouse A-T model, which was associated with improved mitophagy. However, there is a more recent study which demonstrates the role of redox activated ATM in neuronal energy homeostasis through phosphorylation of NRF1, which causes its translocation to the nucleus and upregulation of ETC-enhancing mitochondrial genes (Chow *et al.*, 2019). Therefore, supplementation with NAD+ precursors may act to counteract the energy deficit of ATM-deficient neurons, potentially independently of autophagy regulation. This adds another layer of complexity to the function of presynaptic dATM in neurodevelopment which must be considered in the future.

The work in this thesis further supports the idea that ATM may have a unique cytosolic, redox activated role within neurons. However, it is still a mystery why it is the Purkinje cells of the cerebellum that are specifically vulnerable in A-T. There are clearly drawbacks to the use of the *Drosophila* larval NMJ as a model for A-T, despite the structural and functional

phenotype observed in *dATM* heterozygous nulls and with neuronal knockdown. It should be noted that mouse models of A-T do not show progressive ataxia and cerebellar degeneration, with the exception of a recent model which combines disease-relevant *ATM* missense mutations with knockout of *Aptx*, leading to increased genotoxic stress (Perez *et al.*, 2021). Therefore, future work would perhaps be best conducted in cerebellar organoids or iPSCs derived from A-T patients. Here it would be possible to examine whether there is an autophagy deficit and/or a failure to respond to ROS signalling in synapse expansion, whether constitutively dimeric or cytosolic ATM can rescue synaptic function in ATM-deficient networks, and the potential benefits of autophagy enhancers.

As a final point, the answer to why Purkinje neurons are uniquely vulnerable could reside in another key biological pathway not explored in this thesis. Although not unique to Purkinje cells, an important modulator of their function are their dendritic spines and the different morphologies these develop (Lee, Kim and Rhyu, 2005). Spine development and morphology is underpinned by F-actin dynamics and its regulators such as the Arp2/3 complex, profilin, cofilin and formins (Spence and Soderling, 2015). Purkinje cells express regulators of F-actin which are not found in other neurons, including GRID2IP (delphilin) and espin (Miyagi *et al.*, 2002; Sekerková *et al.*, 2003). Upstream of the Arp2/3 complex in the regulation of actin filament nucleation is the WAVE regulatory complex (WRC), which is itself under the regulation of the small GTPase Rac1 (Lebensohn and Kirschner, 2009; Chen *et al.*, 2010). Unique neuron-specific myosins, such as myosin XIV, regulate the formation and structural plasticity of cerebellar dendritic spines, and have an additional role in the formation of

presynaptic vesicles (Roesler *et al.*, 2019). So how could this relate to the role of ATM in neurons?

Firstly, it must be recognised that the formation, stabilisation and morphology of boutons in *Drosophila* is highly dependent on actin cytoskeletal dynamics (Piccioli and Littleton, 2014), and myosin II accumulation precedes activity-induced bouton remodelling (Fernandes *et al.*, 2023). Rac1 is also known in *Drosophila* to be important in regulating synapse growth and bouton formation (Ball *et al.*, 2010; Kim *et al.*, 2019), and there is further evidence in mammals of the direct activation of Rac1 by ROS to promote cellular migration (Tolbert *et al.*, 2019), a process which is mis-regulated in ATM-deficient cells. Secondly, redox activated ATM – independent of DDR signalling – can phosphorylate cortactin on S113 leading to its activation (Lang *et al.*, 2018) and promotion of actin polymerisation through the Arp2/3 complex (Helgeson and Nolen, 2013). Whether dATM regulates cytoskeletal remodelling and structural plasticity in response to ROS signalling is an intriguing question for future study. This is, admittedly, speculative but if true, and if human ATM interacts with the unique actin regulators expressed in Purkinje cells, this could provide major insight into their specific vulnerability in A-T. Some of these potential interactions could be explored using the *Drosophila* NMJ model to uncover the key pathways operating downstream of dATM.

6.7 – Conclusions

In conclusion, this work has uncovered a key role for presynaptic ATM in regulating synapse development and homeostasis in *Drosophila*, with potential implications for the biology of mammalian ATM and therapies for Ataxia-Telangiectasia. This research supports the notion

of a unique cytosolic role for ATM in neurons through its coordination of ROS signalling and autophagy, mediating the delicate balance between synapse growth and degeneration. Further work is required to elucidate the precise downstream pathways of synaptic ATM and evaluate how this knowledge can be applied to the specific vulnerability of cerebellar neurons in A-T. Nevertheless, this thesis lays the groundwork for understanding the multifaceted roles of neuronal ATM and further highlights the utility of the *Drosophila* larval nervous system as a model for neurodevelopmental disorders.

Bibliography

Ababou, M. *et al.* (2000) 'ATM-dependent phosphorylation and accumulation of endogenous BLM protein in response to ionizing radiation', *Oncogene*, 19(52), pp. 5955–5963. Available at: https://doi.org/10.1038/sj.onc.1204003.

Abd Rahim, M.S. *et al.* (2019) 'NMR- and MD simulation-based structural characterization of the membrane-associating FATC domain of ataxia telangiectasia mutated', *The Journal of Biological Chemistry*, 294(17), pp. 7098–7112. Available at: https://doi.org/10.1074/jbc.RA119.007653.

Aberle, H. *et al.* (2002) 'wishful thinking Encodes a BMP Type II Receptor that Regulates Synaptic Growth in Drosophila', *Neuron*, 33(4), pp. 545–558. Available at: https://doi.org/10.1016/S0896-6273(02)00589-5.

Aditi *et al.* (2021) 'Genome instability independent of type I interferon signaling drives neuropathology caused by impaired ribonucleotide excision repair', *Neuron* [Preprint]. Available at: https://doi.org/10.1016/j.neuron.2021.09.040.

Akbergenova, Y. *et al.* (2018) 'Characterization of developmental and molecular factors underlying release heterogeneity at Drosophila synapses', *eLife*. Edited by E. Marder et al., 7, p. e38268. Available at: https://doi.org/10.7554/eLife.38268.

Albrecht, S.C. *et al.* (2011) 'In Vivo Mapping of Hydrogen Peroxide and Oxidized Glutathione Reveals Chemical and Regional Specificity of Redox Homeostasis', *Cell Metabolism*, 14(6), pp. 819–829. Available at: https://doi.org/10.1016/j.cmet.2011.10.010.

Alexander, A. *et al.* (2010) 'ATM signals to TSC2 in the cytoplasm to regulate mTORC1 in response to ROS', *Proceedings of the National Academy of Sciences*, 107(9), pp. 4153–4158. Available at: https://doi.org/10.1073/pnas.0913860107.

Al-Maawali, A., Blaser, S. and Yoon, G. (2012) 'Diagnostic Approach to Childhood-Onset Cerebellar Atrophy: A 10-Year Retrospective Study of 300 Patients', *Journal of Child Neurology*, 27(9), pp. 1121–1132. Available at: https://doi.org/10.1177/0883073812448680.

Amirifar, P. *et al.* (2019) 'Ataxia-telangiectasia: A review of clinical features and molecular pathology', *Pediatric Allergy and Immunology*, 30(3), pp. 277–288. Available at: https://doi.org/10.1111/pai.13020.

Andrade, M.A. and Bork, P. (1995) 'HEAT repeats in the Huntington's disease protein', *Nature Genetics*, 11(2), pp. 115–116. Available at: https://doi.org/10.1038/ng1095-115.

Arnoult, N. *et al.* (2017) 'Regulation of DNA repair pathway choice in S and G2 phases by the NHEJ inhibitor CYREN', *Nature*, 549(7673), pp. 548–552. Available at: https://doi.org/10.1038/nature24023.

Ashley, J. *et al.* (2019) 'Transsynaptic interactions between IgSF proteins DIP-α and Dpr10 are required for motor neuron targeting specificity', *eLife*, 8, p. e42690. Available at: https://doi.org/10.7554/eLife.42690.

Ashrafi, G. and Schwarz, T.L. (2013) 'The pathways of mitophagy for quality control and clearance of mitochondria', *Cell Death & Differentiation*, 20(1), pp. 31–42. Available at: https://doi.org/10.1038/cdd.2012.81.

Ataman, B. *et al.* (2006) 'Nuclear trafficking of Drosophila Frizzled-2 during synapse development requires the PDZ protein dGRIP', *Proceedings of the National Academy of Sciences*, 103(20), pp. 7841–7846. Available at: https://doi.org/10.1073/pnas.0600387103.

Ataman, B. *et al.* (2008) 'Rapid Activity-Dependent Modifications in Synaptic Structure and Function Require Bidirectional Wnt Signaling', *Neuron*, 57(5), pp. 705–718. Available at: https://doi.org/10.1016/j.neuron.2008.01.026.

Ayrapetov, M.K. *et al.* (2014) 'DNA double-strand breaks promote methylation of histone H3 on lysine 9 and transient formation of repressive chromatin', *Proceedings of the National Academy of Sciences of the United States of America*, 111(25), pp. 9169–9174. Available at: https://doi.org/10.1073/pnas.1403565111.

Bakkenist, C.J. and Kastan, M.B. (2003) 'DNA damage activates ATM through intermolecular autophosphorylation and dimer dissociation', *Nature*, 421(6922), pp. 499–506. Available at: https://doi.org/10.1038/nature01368.

Ball, R.W. *et al.* (2010) 'Retrograde BMP Signaling Controls Synaptic Growth at the NMJ by Regulating Trio Expression in Motor Neurons', *Neuron*, 66(4), pp. 536–549. Available at: https://doi.org/10.1016/j.neuron.2010.04.011.

Banin, S. *et al.* (1998) 'Enhanced Phosphorylation of p53 by ATM in Response to DNA Damage', *Science*, 281(5383), pp. 1674–1677. Available at: https://doi.org/10.1126/science.281.5383.1674.

Barbi, G. *et al.* (1991) 'Chromosome instability and X-ray hypersensitivity in a microcephalic and growth-retarded child', *American Journal of Medical Genetics*, 40(1), pp. 44–50. Available at: https://doi.org/10.1002/ajmg.1320400109.

Baretić, D. *et al.* (2017) 'Structures of closed and open conformations of dimeric human ATM', *Science Advances*, 3(5), p. e1700933. Available at: https://doi.org/10.1126/sciadv.1700933.

Barlow, C. *et al.* (1996) 'Atm-Deficient Mice: A Paradigm of Ataxia Telangiectasia', *Cell*, 86(1), pp. 159–171. Available at: https://doi.org/10.1016/S0092-8674(00)80086-0.

Barlow, C. *et al.* (2000) 'ATM is a cytoplasmic protein in mouse brain required to prevent lysosomal accumulation', *Proceedings of the National Academy of Sciences of the United States of America*, 97(2), pp. 871–876.

Bassett, A.R. *et al.* (2013) 'Highly Efficient Targeted Mutagenesis of Drosophila with the CRISPR/Cas9 System', *Cell Reports*, 4(1), pp. 220–228. Available at: https://doi.org/10.1016/j.celrep.2013.06.020.

Bassi, C. *et al.* (2013) 'Nuclear PTEN controls DNA repair and sensitivity to genotoxic stress', *Science (New York, N.Y.)*, 341(6144), pp. 395–399. Available at: https://doi.org/10.1126/science.1236188.

Bassi, C. *et al.* (2021) 'The PTEN and ATM axis controls the G1/S cell cycle checkpoint and tumorigenesis in HER2-positive breast cancer', *Cell Death & Differentiation*, 28(11), pp. 3036–3051. Available at: https://doi.org/10.1038/s41418-021-00799-8.

Batchelor, E. *et al.* (2008) 'Recurrent Initiation: A Mechanism for Triggering p53 Pulses in Response to DNA Damage', *Molecular cell*, 30(3), pp. 277–289. Available at: https://doi.org/10.1016/j.molcel.2008.03.016.

Bate, M. and Rushton, E. (1993) 'Myogenesis and muscle patterning in Drosophila', *Comptes rendus de l'Academie des sciences. Serie III, Sciences de la vie*, 316(9), pp. 1047–1061.

Bayat, V., Jaiswal, M. and Bellen, H.J. (2011) 'The BMP signaling pathway at the Drosophila neuromuscular junction and its links to neurodegenerative diseases', *Current opinion in neurobiology*, 21(1), pp. 182–188. Available at: https://doi.org/10.1016/j.conb.2010.08.014.

Bencokova, Z. *et al.* (2009) 'ATM Activation and Signaling under Hypoxic Conditions', *Molecular and Cellular Biology*, 29(2), pp. 526–537. Available at: https://doi.org/10.1128/MCB.01301-08.

Berger, C. *et al.* (2007) 'The commonly used marker ELAV is transiently expressed in neuroblasts and glial cells in the Drosophila embryonic CNS', *Developmental Dynamics*, 236(12), pp. 3562–3568. Available at: https://doi.org/10.1002/dvdy.21372.

Berghammer, A.J., Klingler, M. and A. Wimmer, E. (1999) 'A universal marker for transgenic insects', *Nature*, 402(6760), pp. 370–371. Available at: https://doi.org/10.1038/46463.

Berke, B. *et al.* (2013) 'Retrograde BMP Signaling at the Synapse: A Permissive Signal for Synapse Maturation and Activity-Dependent Plasticity', *The Journal of Neuroscience*, 33(45), pp. 17937–17950. Available at: https://doi.org/10.1523/JNEUROSCI.6075-11.2013.

Berkovich, E., Monnat, R.J. and Kastan, M.B. (2007) 'Roles of ATM and NBS1 in chromatin structure modulation and DNA double-strand break repair', *Nature Cell Biology*, 9(6), pp. 683–690. Available at: https://doi.org/10.1038/ncb1599.

Bernhofer, M. *et al.* (2021) 'PredictProtein - Predicting Protein Structure and Function for 29 Years', *Nucleic Acids Research*, 49(W1), pp. W535–W540. Available at: https://doi.org/10.1093/nar/gkab354.

Beucher and Lantuejoul, C. (1979) 'Use of Watersheds in Contour Detection', *International Workshop on Image Processing* [Preprint].

Beumer, K.J. *et al.* (2008) 'Efficient gene targeting in Drosophila by direct embryo injection with zinc-finger nucleases', *Proceedings of the National Academy of Sciences*, 105(50), pp. 19821–19826. Available at: https://doi.org/10.1073/pnas.0810475105.

Beumer, K.J. *et al.* (2013) 'Donor DNA Utilization During Gene Targeting with Zinc-Finger Nucleases', *G3: Genes|Genomes|Genetics*, 3(4), pp. 657–664. Available at: https://doi.org/10.1534/g3.112.005439.

Bielorai, B. *et al.* (2013) 'Acute Lymphoblastic Leukemia in Early Childhood as the Presenting Sign of Ataxia-Telangiectasia Variant', *Pediatric Hematology and Oncology*, 30(6), pp. 574–582. Available at: https://doi.org/10.3109/08880018.2013.777949.

Biton, S. *et al.* (2007) 'ATM-mediated response to DNA double strand breaks in human neurons derived from stem cells', *DNA Repair*, 6(1), pp. 128–134. Available at: https://doi.org/10.1016/j.dnarep.2006.10.019.

Bjedov, I. *et al.* (2020) 'Fine-tuning autophagy maximises lifespan and is associated with changes in mitochondrial gene expression in Drosophila', *PLOS Genetics*, 16(11), p. e1009083. Available at: https://doi.org/10.1371/journal.pgen.1009083.

Boder, E. and Sedgwick, R.P. (1958) 'ATAXIA-TELANGIECTASIA: A Familial Syndrome of Progressive Cerebellar Ataxia, Oculocutaneous Telangiectasia and Frequent Pulmonary Infection', *Pediatrics*, 21(4), pp. 526–554.

Boder, E. and Sedgwick, R.P. (1970) 'Ataxia-telangiectasia. (Clinical and immunological aspects)', *Psychiatrie, Neurologie Und Medizinische Psychologie. Beihefte*, 13–14, pp. 8–16.

Bodgi, L. and Foray, N. (2016) 'The nucleo-shuttling of the ATM protein as a basis for a novel theory of radiation response: resolution of the linear-quadratic model*', *International Journal of Radiation Biology*, 92(3), pp. 117–131. Available at: https://doi.org/10.3109/09553002.2016.1135260.

Boehrs, J.K. *et al.* (2007) 'Constitutive expression and cytoplasmic compartmentalization of ATM protein in differentiated human neuron-like SH-SY5Y cells', *Journal of Neurochemistry*, 100(2), pp. 337–345. Available at: https://doi.org/10.1111/j.1471-4159.2006.04254.x.

Bothmer, A. *et al.* (2011) 'Regulation of DNA End Joining, Resection, and Immunoglobulin Class Switch Recombination by 53BP1', *Molecular cell*, 42(3), pp. 319–329. Available at: https://doi.org/10.1016/j.molcel.2011.03.019.

Bott, L. *et al.* (2007) 'Lung disease in ataxia-telangiectasia', *Acta Paediatrica*, 96(7), pp. 1021–1024. Available at: https://doi.org/10.1111/j.1651-2227.2007.00338.x.

Brand, A.H., Manoukian, A.S. and Perrimon, N. (1994) 'Chapter 33 Ectopic Expression in Drosophila', in *Methods in Cell Biology*. Elsevier, pp. 635–654. Available at: https://doi.org/10.1016/S0091-679X(08)60936-X.

Brand, A.H. and Perrimon, N. (1993) 'Targeted gene expression as a means of altering cell fates and generating dominant phenotypes', *Development (Cambridge, England)*, 118(2), pp. 401–415.

Brent, J.R., Werner, K.M. and McCabe, B.D. (2009) 'Drosophila Larval NMJ Dissection', *Journal of Visualized Experiments : JoVE*, (24), p. 1107. Available at: https://doi.org/10.3791/1107.

Britton, S. *et al.* (2020) 'ATM antagonizes NHEJ proteins assembly and DNA-ends synapsis at single-ended DNA double strand breaks', *Nucleic Acids Research*, 48(17), pp. 9710–9723. Available at: https://doi.org/10.1093/nar/gkaa723.

Brodsky, M.H. *et al.* (2004) 'Drosophila melanogaster MNK/Chk2 and p53 Regulate Multiple DNA Repair and Apoptotic Pathways following DNA Damage', *Molecular and Cellular Biology*, 24(3), pp. 1219–1231. Available at: https://doi.org/10.1128/MCB.24.3.1219-1231.2004.

Broz, D.K. *et al.* (2013) 'Global genomic profiling reveals an extensive p53-regulated autophagy program contributing to key p53 responses', *Genes & Development*, 27(9), pp. 1016–1031. Available at: https://doi.org/10.1101/gad.212282.112.

Bruckner, J.J. *et al.* (2016) 'Fife organizes synaptic vesicles and calcium channels for high-probability neurotransmitter release', *Journal of Cell Biology*, 216(1), pp. 231–246. Available at: https://doi.org/10.1083/jcb.201601098.

Burma, S. *et al.* (2001) 'ATM Phosphorylates Histone H2AX in Response to DNA Double-strand Breaks', *Journal of Biological Chemistry*, 276(45), pp. 42462–42467. Available at: https://doi.org/10.1074/jbc.C100466200.

Buscemi, G. *et al.* (2001) 'Chk2 Activation Dependence on Nbs1 after DNA Damage', *Molecular and Cellular Biology*, 21(15), pp. 5214–5222. Available at: https://doi.org/10.1128/MCB.21.15.5214-5222.2001.

Bykhovskaia, M. and Vasin, A. (2017) 'Electrophysiological Analysis of Synaptic Transmission in Drosophila', *Wiley interdisciplinary reviews. Developmental biology*, 6(5). Available at: https://doi.org/10.1002/wdev.277.

Cadet, J. and Wagner, J.R. (2013) 'DNA Base Damage by Reactive Oxygen Species, Oxidizing Agents, and UV Radiation', *Cold Spring Harbor Perspectives in Biology*, 5(2), p. a012559. Available at: https://doi.org/10.1101/cshperspect.a012559.

Campbell, M. and Ganetzky, B. (2012) 'Extensive morphological divergence and rapid evolution of the larval neuromuscular junction in Drosophila', *Proceedings of the National Academy of Sciences*, 109(11), pp. E648–E655. Available at: https://doi.org/10.1073/pnas.1201176109.

Canman, C.E. *et al.* (1998) 'Activation of the ATM Kinase by Ionizing Radiation and Phosphorylation of p53', *Science*, 281(5383), pp. 1677–1679. Available at: https://doi.org/10.1126/science.281.5383.1677.

Cannon, B. *et al.* (2013) 'Visualization of local DNA unwinding by Mre11/Rad50/Nbs1 using single-molecule FRET', *Proceedings of the National Academy of Sciences of the United States of America*, 110(47), pp. 18868–18873. Available at: https://doi.org/10.1073/pnas.1309816110.

Cao, X. *et al.* (2020) 'Inhibition of DNA ligase IV enhances the CRISPR/Cas9-mediated knock-in efficiency in mouse brain neurons', *Biochemical and Biophysical Research Communications*, 533(3), pp. 449–457. Available at: https://doi.org/10.1016/j.bbrc.2020.09.053.

Cara, L. *et al.* (2016) 'The ATM- and ATR-related SCD domain is over-represented in proteins involved in nervous system development', *Scientific Reports*, 6. Available at: https://doi.org/10.1038/srep19050.

Caridi, P.C. *et al.* (2017) 'And yet, it moves: nuclear and chromatin dynamics of a heterochromatic double-strand break', *Philosophical Transactions of the Royal Society B: Biological Sciences*, 372(1731). Available at: https://doi.org/10.1098/rstb.2016.0291.

Carnio, S. *et al.* (2014) 'Autophagy Impairment in Muscle Induces Neuromuscular Junction Degeneration and Precocious Aging', *Cell Reports*, 8(5), pp. 1509–1521. Available at: https://doi.org/10.1016/j.celrep.2014.07.061.

Caron, P. *et al.* (2015) 'Non-redundant Functions of ATM and DNA-PKcs in Response to DNA Double-Strand Breaks', *Cell Reports*, 13(8), pp. 1598–1609. Available at: https://doi.org/10.1016/j.celrep.2015.10.024.

Cassimere, E.K., Mauvais, C. and Denicourt, C. (2016) 'p27Kip1 Is Required to Mediate a G1 Cell Cycle Arrest Downstream of ATM following Genotoxic Stress', *PLoS ONE*, 11(9). Available at: https://doi.org/10.1371/journal.pone.0162806.

Castells-Nobau, A. *et al.* (2017) 'Two Algorithms for High-throughput and Multi-parametric Quantification of Drosophila Neuromuscular Junction Morphology', *Journal of Visualized Experiments : JoVE* [Preprint], (123). Available at: https://doi.org/10.3791/55395.

Chang, H.H.Y. *et al.* (2017) 'Non-homologous DNA end joining and alternative pathways to double-strand break repair', *Nature Reviews Molecular Cell Biology*, 18(8), pp. 495–506. Available at: https://doi.org/10.1038/nrm.2017.48.

Chang, J.-C. and Morton, D.B. (2017) 'Drosophila lines with mutant and wild type human TDP-43 replacing the endogenous gene reveals phosphorylation and ubiquitination in mutant lines in the absence of viability or lifespan defects', *PLOS ONE*. Edited by U. Pandey, 12(7), p. e0180828. Available at: https://doi.org/10.1371/journal.pone.0180828.

Chanut, P. *et al.* (2016) 'Coordinated nuclease activities counteract Ku at single-ended DNA double-strand breaks', *Nature Communications*, 7(1), p. 12889. Available at: https://doi.org/10.1038/ncomms12889.

Chen, Q. *et al.* (2020) 'Structural basis of seamless excision and specific targeting by piggyBac transposase', *Nature Communications*, 11(1), p. 3446. Available at: https://doi.org/10.1038/s41467-020-17128-1.

Chen, Z. *et al.* (2010) 'Structure and Control of the Actin Regulatory WAVE Complex', *Nature*, 468(7323), pp. 533–538. Available at: https://doi.org/10.1038/nature09623.

Cheng, A. *et al.* (2018) 'ATM and ATR play complementary roles in the behavior of excitatory and inhibitory vesicle populations', *Proceedings of the National Academy of Sciences*, 115(2), pp. E292–E301. Available at: https://doi.org/10.1073/pnas.1716892115.

Cheng, A. *et al.* (2020) 'ATM loss disrupts the autophagy-lysosomal pathway', *Autophagy*, 0(0), pp. 1–13. Available at: https://doi.org/10.1080/15548627.2020.1805860.

Cheng, Q. and Chen, J. (2010) 'Mechanism of p53 stabilization by ATM after DNA damage', *Cell cycle (Georgetown, Tex.)*, 9(3), pp. 472–478.

Cheng, X.-T. *et al.* (2015) 'Axonal autophagosomes recruit dynein for retrograde transport through fusion with late endosomes', *The Journal of Cell Biology*, 209(3), pp. 377–386. Available at: https://doi.org/10.1083/jcb.201412046.

Cherra, S.J. and Chu, C.T. (2008) 'Autophagy in neuroprotection and neurodegeneration: A question of balance', *Future neurology*, 3(3), pp. 309–323. Available at: https://doi.org/10.2217/14796708.3.3.309.

Chiesa, N. *et al.* (2000) 'Atm-deficient mice Purkinje cells show age-dependent defects in calcium spike bursts and calcium currents', *Neuroscience*, 96(3), pp. 575–583. Available at: https://doi.org/10.1016/S0306-4522(99)00581-3.

Chiolo, I. *et al.* (2011) 'Double-Strand Breaks in Heterochromatin Move Outside of a Dynamic HP1a Domain to Complete Recombinational Repair', *Cell*, 144(5), pp. 732–744. Available at: https://doi.org/10.1016/j.cell.2011.02.012.

Choi, B.-K. *et al.* (2020) 'WIP1 dephosphorylation of p27/Kip1 Serine 140 destabilizes p27/Kip1 and reverses anti-proliferative effects of ATM phosphorylation', *Cell Cycle*, 19(4), pp. 479–491. Available at: https://doi.org/10.1080/15384101.2020.1717025.

Chothia, C. and Lesk, A.M. (1986) 'The relation between the divergence of sequence and structure in proteins.', *The EMBO Journal*, 5(4), pp. 823–826.

Chow, H.-M. *et al.* (2019) 'ATM is activated by ATP depletion and modulates mitochondrial function through NRF1', *The Journal of Cell Biology*, 218(3), pp. 909–928. Available at: https://doi.org/10.1083/jcb.201806197.

Cirotti, C. *et al.* (2021) 'Redox activation of ATM enhances GSNOR translation to sustain mitophagy and tolerance to oxidative stress', *EMBO reports*, 22(1). Available at: https://doi.org/10.15252/embr.202050500.

Collins, C.A. *et al.* (2006) 'Highwire Restrains Synaptic Growth by Attenuating a MAP Kinase Signal', *Neuron*, 51(1), pp. 57–69. Available at: https://doi.org/10.1016/j.neuron.2006.05.026.

Collins, C.A. and DiAntonio, A. (2007) 'Synaptic development: insights from Drosophila', *Current Opinion in Neurobiology*, 17(1), pp. 35–42. Available at: https://doi.org/10.1016/j.conb.2007.01.001.

Cooke, M.S. *et al.* (2003) 'Oxidative DNA damage: mechanisms, mutation, and disease', *The FASEB Journal*, 17(10), pp. 1195–1214. Available at: https://doi.org/10.1096/fj.02-0752rev.

Cortez, D. *et al.* (1999) 'Requirement of ATM-Dependent Phosphorylation of Brca1 in the DNA Damage Response to Double-Strand Breaks', *Science*, 286(5442), pp. 1162–1166. Available at: https://doi.org/10.1126/science.286.5442.1162.

Corti, O. *et al.* (2020) 'Autophagy in neurodegeneration: New insights underpinning therapy for neurological diseases', *Journal of Neurochemistry*, 154(4), pp. 354–371. Available at: https://doi.org/10.1111/jnc.15002.

Cosentino, C., Grieco, D. and Costanzo, V. (2011) 'ATM activates the pentose phosphate pathway promoting anti-oxidant defence and DNA repair: ATM activates the pentose phosphate pathway', *The EMBO Journal*, 30(3), pp. 546–555. Available at: https://doi.org/10.1038/emboj.2010.330.

Cox, R.T. and Spradling, A.C. (2003) 'A Balbiani body and the fusome mediate mitochondrial inheritance duringDrosophila oogenesis', *Development*, 130(8), pp. 1579–1590. Available at: https://doi.org/10.1242/dev.00365.

Crawford, T.O. (2005) 'Survival probability in ataxia telangiectasia', *Archives of Disease in Childhood*, 91(7), pp. 610–611. Available at: https://doi.org/10.1136/adc.2006.094268.

Cunningham, K.L. and Littleton, J.T. (2019) 'Neurons regulate synaptic strength through homeostatic scaling of active zones', *Journal of Cell Biology*, 218(5), pp. 1434–1435. Available at: https://doi.org/10.1083/jcb.201903065.

Dar, I. *et al.* (2006) 'Analysis of the ataxia telangiectasia mutated-mediated DNA damage response in murine cerebellar neurons', *Journal of Neuroscience*, 26(29), pp. 7767–7774. Available at: https://doi.org/10.1523/JNEUROSCI.2055-06.2006.

Davis, A.J. and Chen, D.J. (2013) 'DNA double strand break repair via non-homologous end-joining', *Translational cancer research*, 2(3), pp. 130–143. Available at: https://doi.org/10.3978/j.issn.2218-676X.2013.04.02.

Davis, G.W. *et al.* (1998) 'Postsynaptic PKA Controls Quantal Size and Reveals a Retrograde Signal that Regulates Presynaptic Transmitter Release in Drosophila', *Neuron*, 20(2), pp. 305–315. Available at: https://doi.org/10.1016/S0896-6273(00)80458-4.

Deisseroth, A. and Dounce, A.L. (1970) 'Catalase: Physical and chemical properties, mechanism of catalysis, and physiological role.', *Physiological Reviews*, 50(3), pp. 319–375. Available at: https://doi.org/10.1152/physrev.1970.50.3.319.

Di Virgilio, M., Ying, C.Y. and Gautier, J. (2009) 'PIKK-dependent phosphorylation of Mre11 induces MRN complex inactivation by disassembly from chromatin', *DNA repair*, 8(11), pp. 1311–1320. Available at: https://doi.org/10.1016/j.dnarep.2009.07.006.

DiAntonio, A. *et al.* (1999) 'Glutamate Receptor Expression Regulates Quantal Size and Quantal Content at the *Drosophila* Neuromuscular Junction', *The Journal of Neuroscience*, 19(8), pp. 3023–3032. Available at: https://doi.org/10.1523/JNEUROSCI.19-08-03023.1999.

Digweed, M., Reis, A. and Sperling, K. (1999) 'Nijmegen breakage syndrome: consequences of defective DNA double strand break repair', *BioEssays*, 21(8), pp. 649–656. Available at: https://doi.org/10.1002/(SICI)1521-1878(199908)21:8<649::AID-BIES4>3.0.CO;2-O.

Djajadikerta, A. *et al.* (2020) 'Autophagy Induction as a Therapeutic Strategy for Neurodegenerative Diseases', *Journal of Molecular Biology*, 432(8), pp. 2799–2821. Available at: https://doi.org/10.1016/j.jmb.2019.12.035.

Domise, M. *et al.* (2019) 'Neuronal AMP-activated protein kinase hyper-activation induces synaptic loss by an autophagy-mediated process', *Cell Death & Disease*, 10(3), pp. 1–15. Available at: https://doi.org/10.1038/s41419-019-1464-x.

Doré, A.S. *et al.* (2004) 'Identification of DNA-PK in the arthropods: Evidence for the ancient ancestry of vertebrate non-homologous end-joining', *DNA Repair*, 3(1), pp. 33–41. Available at: https://doi.org/10.1016/j.dnarep.2003.09.003.

Drake, J.C. *et al.* (2021) 'Mitochondria-localized AMPK responds to local energetics and contributes to exercise and energetic stress-induced mitophagy', *Proceedings of the National Academy of Sciences*, 118(37), p. e2025932118. Available at: https://doi.org/10.1073/pnas.2025932118.

Dyson, A. *et al.* (2022) *Loss of* NF1 *causes tactile hypersensitivity and impaired synaptic transmission in a* Drosophila *model of autism spectrum disorder*. preprint. Neuroscience. Available at: https://doi.org/10.1101/2022.03.04.482984.

Eaton, B.A. and Davis, G.W. (2005) 'LIM Kinase1 Controls Synaptic Stability Downstream of the Type II BMP Receptor', *Neuron*, 47(5), pp. 695–708. Available at: https://doi.org/10.1016/j.neuron.2005.08.010.

Ecovoiu, A.Al. *et al.* (2022) 'Inter-Species Rescue of Mutant Phenotype—The Standard for Genetic Analysis of Human Genetic Disorders in Drosophila melanogaster Model',

International Journal of Molecular Sciences, 23(5), p. 2613. Available at: https://doi.org/10.3390/ijms23052613.

Ehmann, N. *et al.* (2014) 'Quantitative super-resolution imaging of Bruchpilot distinguishes active zone states', *Nature Communications*, 5(1), p. 4650. Available at: https://doi.org/10.1038/ncomms5650.

Falck, J., Coates, J. and Jackson, S.P. (2005) 'Conserved modes of recruitment of ATM, ATR and DNA-PKcs to sites of DNA damage', *Nature*, 434(7033), pp. 605–611. Available at: https://doi.org/10.1038/nature03442.

Fang, E.F. *et al.* (2016) 'NAD+ Replenishment Improves Lifespan and Healthspan in Ataxia Telangiectasia Models via Mitophagy and DNA Repair', *Cell Metabolism*, 24(4), pp. 566–581. Available at: https://doi.org/10.1016/j.cmet.2016.09.004.

Fedak, E.A. *et al.* (2021) 'ATM and ATR Activation Through Crosstalk Between DNA Damage Response Pathways', *Bulletin of Mathematical Biology*, 83(4), p. 38. Available at: https://doi.org/10.1007/s11538-021-00868-6.

Feeney, C.J. *et al.* (1998) 'Motor nerve terminals on abdominal muscles in larval flesh flies,Sarcophaga bullata: Comparisons withDrosophila', *The Journal of Comparative Neurology*, 402(2), pp. 197–209. Available at: https://doi.org/10.1002/(SICI)1096-9861(19981214)402:2<197::AID-CNE5>3.0.CO;2-Q.

Feng, Y., Ueda, A. and Wu, C.-F. (2004) 'A Modified Minimal Hemolymph-Like Solution, Hl3.1, for Physiological Recordings at the Neuromuscular Junctions of Normal and Mutant Drosophila Larvae', *Journal of Neurogenetics*, 18(2), pp. 377–402. Available at: https://doi.org/10.1080/01677060490894522.

Feng, Z. *et al.* (2007) 'The Regulation of AMPK β1, TSC2, and PTEN Expression by p53: Stress, Cell and Tissue Specificity, and the Role of These Gene Products in Modulating the IGF-1-AKT-mTOR Pathways', *Cancer Research*, 67(7), pp. 3043–3053. Available at: https://doi.org/10.1158/0008-5472.CAN-06-4149.

Fernandes, A.R. *et al.* (2023) 'Drosophila motor neuron boutons remodel through membrane blebbing coupled with muscle contraction', *Nature Communications*, 14, p. 3352. Available at: https://doi.org/10.1038/s41467-023-38421-9.

Fiscella, M. *et al.* (1997) 'Wip1, a novel human protein phosphatase that is induced in response to ionizing radiation in a p53-dependent manner', *Proceedings of the National Academy of Sciences of the United States of America*, 94(12), pp. 6048–6053.

Fischer, H. (2009) 'Mechanisms and Function of DUOX in Epithelia of the Lung', *Antioxidants & Redox Signaling*, 11(10), pp. 2453–2465. Available at: https://doi.org/10.1089/ars.2009.2558.

Fischer, J.A. *et al.* (1988) 'GAL4 activates transcription in Drosophila', *Nature*, 332(6167), pp. 853–856. Available at: https://doi.org/10.1038/332853a0.

Fournier, D. *et al.* (2013) 'Functional and Genomic Analyses of Alpha-Solenoid Proteins', *PLoS ONE*, 8(11), p. e79894. Available at: https://doi.org/10.1371/journal.pone.0079894.

Fracassi, A. *et al.* (2021) 'Oxidative Damage and Antioxidant Response in Frontal Cortex of Demented and Nondemented Individuals with Alzheimer's Neuropathology', *Journal of Neuroscience*, 41(3), pp. 538–554. Available at: https://doi.org/10.1523/JNEUROSCI.0295-20.2020.

Frank, C.A. *et al.* (2006) 'Mechanisms Underlying the Rapid Induction and Sustained Expression of Synaptic Homeostasis', *Neuron*, 52(4), pp. 663–677. Available at: https://doi.org/10.1016/j.neuron.2006.09.029.

Frickenhaus, M. *et al.* (2015) 'Highly efficient cell-type-specific gene inactivation reveals a key function for the Drosophila FUS homolog cabeza in neurons', *Scientific Reports*, 5(1), p. 9107. Available at: https://doi.org/10.1038/srep09107.

Fuentes-Medel, Y. *et al.* (2009) 'Glia and Muscle Sculpt Neuromuscular Arbors by Engulfing Destabilized Synaptic Boutons and Shed Presynaptic Debris', *PLoS Biology*, 7(8). Available at: https://doi.org/10.1371/journal.pbio.1000184.

Gao, W. *et al.* (2011) 'Upregulation of human autophagy-initiation kinase ULK1 by tumor suppressor p53 contributes to DNA-damage-induced cell death', *Cell Death & Differentiation*, 18(10), pp. 1598–1607. Available at: https://doi.org/10.1038/cdd.2011.33.

Garson, J.A. *et al.* (1982) 'Monoclonal antibodies against human T lymphocytes label Purkinje neurones of many species', *Nature*, 298(5872), pp. 375–377. Available at: https://doi.org/10.1038/298375a0.

Gatei, M. *et al.* (2011) 'ATM protein-dependent phosphorylation of Rad50 protein regulates DNA repair and cell cycle control', *The Journal of Biological Chemistry*, 286(36), pp. 31542–31556. Available at: https://doi.org/10.1074/jbc.M111.258152.

Gatti, R.A., Berke, I. and Boder, E. (1988) 'Localization of an ataxia-telangiectasia gene to chromosome llq22-23', p. 4.

Giachello, C.N.G. *et al.* (2021) 'Nitric oxide mediates activity-dependent change to synaptic excitation during a critical period in Drosophila', *Scientific Reports*, 11(1), p. 20286. Available at: https://doi.org/10.1038/s41598-021-99868-8.

Giachello, C.N.G. and Baines, R.A. (2015) 'Inappropriate Neural Activity during a Sensitive Period in Embryogenesis Results in Persistent Seizure-like Behavior', *Current Biology*, 25(22), pp. 2964–2968. Available at: https://doi.org/10.1016/j.cub.2015.09.040.

Gilad, S. *et al.* (1998) 'Genotype-phenotype relationships in ataxia-telangiectasia and variants.', *American Journal of Human Genetics*, 62(3), pp. 551–561.

Giniatullin, A.R. *et al.* (2006) 'SNAP25 is a pre-synaptic target for the depressant action of reactive oxygen species on transmitter release', *Journal of Neurochemistry*, 98(6), pp. 1789–1797. Available at: https://doi.org/10.1111/j.1471-4159.2006.03997.x.

Goel, P. *et al.* (2019) 'Homeostatic scaling of active zone scaffolds maintains global synaptic strength', *Journal of Cell Biology*, 218(5), pp. 1706–1724. Available at: https://doi.org/10.1083/jcb.201807165.

Goodarzi, A.A. *et al.* (2008) 'ATM Signaling Facilitates Repair of DNA Double-Strand Breaks Associated with Heterochromatin', *Molecular Cell*, 31(2), pp. 167–177. Available at: https://doi.org/10.1016/j.molcel.2008.05.017.

Goodarzi, A.A., Kurka, T. and Jeggo, P.A. (2011) 'KAP-1 phosphorylation regulates CHD3 nucleosome remodeling during the DNA double-strand break response', *Nature Structural & Molecular Biology*, 18(7), pp. 831–839. Available at: https://doi.org/10.1038/nsmb.2077.

Goold, C.P. and Davis, G.W. (2007) 'The BMP Ligand Gbb Gates the Expression of Synaptic Homeostasis Independent of Synaptic Growth Control', *Neuron*, 56(1), pp. 109–123. Available at: https://doi.org/10.1016/j.neuron.2007.08.006.

Gorodetsky, E. *et al.* (2007) 'ATM, the Mre11/Rad50/Nbs1 complex, and topoisomerase I are concentrated in the nucleus of Purkinje neurons in the juvenile human brain', *DNA Repair*, 6(11), pp. 1698–1707. Available at: https://doi.org/10.1016/j.dnarep.2007.06.011.

Goyal, L. *et al.* (2000) 'Induction of apoptosis by Drosophila reaper, hid and grim through inhibition of IAP function', *The EMBO Journal*, 19(4), pp. 589–597. Available at: https://doi.org/10.1093/emboj/19.4.589.

Graf, E.R. *et al.* (2009) 'Rab3 Dynamically Controls Protein Composition at Active Zones', *Neuron*, 64(5), pp. 663–677. Available at: https://doi.org/10.1016/j.neuron.2009.11.002.

Gratz, S.J. *et al.* (2013) 'Genome Engineering of Drosophila with the CRISPR RNA-Guided Cas9 Nuclease', *Genetics*, 194(4), pp. 1029–1035. Available at: https://doi.org/10.1534/genetics.113.152710.

Gratz, S.J. *et al.* (2014) 'Highly Specific and Efficient CRISPR/Cas9-Catalyzed Homology-Directed Repair in Drosophila', *Genetics*, 196(4), pp. 961–971. Available at: https://doi.org/10.1534/genetics.113.160713.

Gratz, S.J. *et al.* (2015) 'CRISPR-Cas9 genome editing in Drosophila', *Current protocols in molecular biology / edited by Frederick M. Ausubel ... [et al.]*, 111, p. 31.2.1-31.2.20. Available at: https://doi.org/10.1002/0471142727.mb3102s111.

Gratz, S.J. *et al.* (2019) 'Endogenous Tagging Reveals Differential Regulation of Ca2+ Channels at Single Active Zones during Presynaptic Homeostatic Potentiation and Depression', *Journal of Neuroscience*, 39(13), pp. 2416–2429. Available at: https://doi.org/10.1523/JNEUROSCI.3068-18.2019.

Gregory, S.L. *et al.* (2007) 'A Drosophila Overexpression Screen for Modifiers of Rho Signalling in Cytokinesis', *Fly*, 1(1), pp. 13–22. Available at: https://doi.org/10.4161/fly.3806.

Grider, M.H. *et al.* (2009) 'Lipid raft-targeted Akt promotes axonal branching and growth cone expansion via mTOR and Rac1, respectively', *Journal of Neuroscience Research*, 87(14), pp. 3033–3042. Available at: https://doi.org/10.1002/jnr.22140.

Guo, J.Y., Xia, B. and White, E. (2013) 'Autophagy-Mediated Tumor Promotion', *Cell*, 155(6), pp. 1216–1219. Available at: https://doi.org/10.1016/j.cell.2013.11.019.

Guo, Z. *et al.* (2010) 'ATM Activation by Oxidative Stress', *Science*, 330(6003), pp. 517–521. Available at: https://doi.org/10.1126/science.1192912.

Gupta, R. *et al.* (2018) 'DNA Repair Network Analysis Reveals Shieldin as a Key Regulator of NHEJ and PARP Inhibitor Sensitivity', *Cell*, 173(4), pp. 972-988.e23. Available at: https://doi.org/10.1016/j.cell.2018.03.050.

Ha, G.-H. *et al.* (2019) 'Pellino1 regulates reversible ATM activation via NBS1 ubiquitination at DNA double-strand breaks', *Nature Communications*, 10. Available at: https://doi.org/10.1038/s41467-019-09641-9.

Haghighi, A.P. *et al.* (2003) 'Retrograde Control of Synaptic Transmission by Postsynaptic CaMKII at the Drosophila Neuromuscular Junction', *Neuron*, 39(2), pp. 255–267. Available at: https://doi.org/10.1016/S0896-6273(03)00427-6.

Halaby, M.-J. *et al.* (2008) 'ATM protein kinase mediates full activation of Akt and regulates glucose transporter 4 translocation by insulin in muscle cells', *Cellular Signalling*, 20(8), pp. 1555–1563. Available at: https://doi.org/10.1016/j.cellsig.2008.04.011.

Hallermann, S., Heckmann, M. and Kittel, R.J. (2010) 'Mechanisms of short-term plasticity at neuromuscular active zones of *Drosophila*', *HFSP Journal*, 4(2), pp. 72–84. Available at: https://doi.org/10.2976/1.3338710.

Han, T.H. *et al.* (2020) 'Neto-α Controls Synapse Organization and Homeostasis at the Drosophila Neuromuscular Junction', *Cell reports*, 32(1), p. 107866. Available at: https://doi.org/10.1016/j.celrep.2020.107866.

Hara, Y. *et al.* (2018) 'Cell death in neural precursor cells and neurons before neurite formation prevents the emergence of abnormal neural structures in the Drosophila optic lobe', *Developmental Biology*, 436(1), pp. 28–41. Available at: https://doi.org/10.1016/j.ydbio.2018.02.004.

Hardie, D.G., Carling, D. and Carlson, M. (1998) 'THE AMP-ACTIVATED/SNF1 PROTEIN KINASE SUBFAMILY: Metabolic Sensors of the Eukaryotic Cell?', *Annual Review of Biochemistry*, 67(1), pp. 821–855. Available at: https://doi.org/10.1146/annurev.biochem.67.1.821.

Heigwer, F., Kerr, G. and Boutros, M. (2014) 'E-CRISP: fast CRISPR target site identification', *Nature Methods*, 11(2), pp. 122–123. Available at: https://doi.org/10.1038/nmeth.2812.

Helgeson, L.A. and Nolen, B.J. (2013) 'Mechanism of synergistic activation of Arp2/3 complex by cortactin and N-WASP', *eLife*, 2, p. e00884. Available at: https://doi.org/10.7554/eLife.00884.

Hirao, A. *et al.* (2000) 'DNA Damage-Induced Activation of p53 by the Checkpoint Kinase Chk2', *Science*, 287(5459), pp. 1824–1827. Available at: https://doi.org/10.1126/science.287.5459.1824.

Hoang, B. and Chiba, A. (2001) 'Single-Cell Analysis of Drosophila Larval Neuromuscular Synapses', *Developmental Biology*, 229(1), pp. 55–70. Available at: https://doi.org/10.1006/dbio.2000.9983.

Holm, L. and Sander, C. (1996) 'Mapping the Protein Universe', *Science*, 273(5275), pp. 595–602. Available at: https://doi.org/10.1126/science.273.5275.595.

Hong, S.-T. and Choi, K.-W. (2013) 'TCTP directly regulates ATM activity to control genome stability and organ development in Drosophila melanogaster', *Nature Communications*, 4(1), pp. 1–14. Available at: https://doi.org/10.1038/ncomms3986.

Hoover, K.M. *et al.* (2019) 'The calcium channel subunit α2δ-3 organizes synapses via an activity-dependent and autocrine BMP signaling pathway', *Nature Communications*, 10, p. 5575. Available at: https://doi.org/10.1038/s41467-019-13165-7.

Horn, C. *et al.* (2003) 'piggyBac-based insertional mutagenesis and enhancer detection as a tool for functional insect genomics.', *Genetics*, 163(2), pp. 647–661.

Hoshino, A. *et al.* (2013) 'Cytosolic p53 inhibits Parkin-mediated mitophagy and promotes mitochondrial dysfunction in the mouse heart', *Nature Communications*, 4(1), p. 2308. Available at: https://doi.org/10.1038/ncomms3308.

Hunt, C.R. *et al.* (2007) 'Hyperthermia Activates a Subset of Ataxia-Telangiectasia Mutated Effectors Independent of DNA Strand Breaks and Heat Shock Protein 70 Status', *Cancer Research*, 67(7), pp. 3010–3017. Available at: https://doi.org/10.1158/0008-5472.CAN-06-4328.

Huo, Y. *et al.* (2013) 'Autophagy Opposes p53-Mediated Tumor Barrier to Facilitate Tumorigenesis in a Model of PALB2-Associated Hereditary Breast Cancer', *Cancer Discovery*, 3(8), pp. 894–907. Available at: https://doi.org/10.1158/2159-8290.CD-13-0011.

Hwang, M. *et al.* (2023) 'Ataxia-Telangiectasia Mutated Is Involved in Autolysosome Formation', *Biomolecules & Therapeutics* [Preprint]. Available at: https://doi.org/10.4062/biomolther.2023.003.

Illergård, K., Ardell, D.H. and Elofsson, A. (2009) 'Structure is three to ten times more conserved than sequence—A study of structural response in protein cores', *Proteins: Structure, Function, and Bioinformatics*, 77(3), pp. 499–508. Available at: https://doi.org/10.1002/prot.22458.

Ito, K. *et al.* (2007) 'Regulation of Reactive Oxygen Species by Atm Is Essential for Proper Response to DNA Double-Strand Breaks in Lymphocytes', *The Journal of Immunology*, 178(1), pp. 103–110. Available at: https://doi.org/10.4049/jimmunol.178.1.103.

Jaiswal, H. *et al.* (2017) 'ATM/Wip1 activities at chromatin control Plk1 re-activation to determine G2 checkpoint duration', *The EMBO Journal*, 36(14), pp. 2161–2176. Available at: https://doi.org/10.15252/embj.201696082.

James, R.E. *et al.* (2014) 'Crimpy enables discrimination of pre and postsynaptic pools of a BMP at the Drosophila NMJ', *Developmental cell*, 31(5), pp. 586–598. Available at: https://doi.org/10.1016/j.devcel.2014.10.006.

James, R.E. and Broihier, H.T. (2011) 'Crimpy inhibits the BMP homolog Gbb in motoneurons to enable proper growth control at the Drosophila neuromuscular junction', *Development*, 138(15), pp. 3273–3286. Available at: https://doi.org/10.1242/dev.066142.

Jiang, D. *et al.* (2015) 'Alteration in 5-hydroxymethylcytosine-mediated epigenetic regulation leads to Purkinje cell vulnerability in ATM deficiency', *Brain*, 138(12), pp. 3520–3536. Available at: https://doi.org/10.1093/brain/awv284.

Jinek, M. *et al.* (2012) 'A Programmable Dual-RNA–Guided DNA Endonuclease in Adaptive Bacterial Immunity', *Science*, 337(6096), pp. 816–821. Available at: https://doi.org/10.1126/science.1225829.

Jones, R.G. *et al.* (2005) 'AMP-Activated Protein Kinase Induces a p53-Dependent Metabolic Checkpoint', *Molecular Cell*, 18(3), pp. 283–293. Available at: https://doi.org/10.1016/j.molcel.2005.03.027.

Joyce, E.F. *et al.* (2011) 'Drosophila ATM and ATR have distinct activities in the regulation of meiotic DNA damage and repair', *Journal of Cell Biology*, 195(3), pp. 359–367. Available at: https://doi.org/10.1083/jcb.201104121.

Jumper, J. *et al.* (2021) 'Highly accurate protein structure prediction with AlphaFold', *Nature*, 596(7873), pp. 583–589. Available at: https://doi.org/10.1038/s41586-021-03819-2.

Kamsler, A. *et al.* (2001) 'Increased Oxidative Stress in Ataxia Telangiectasia Evidenced by Alterations in Redox State of Brains from Atm-deficient Mice', *Cancer Research*, 61(5), pp. 1849–1854.

Kanca, O. *et al.* (2019) 'An efficient CRISPR-based strategy to insert small and large fragments of DNA using short homology arms', *eLife*. Edited by K. VijayRaghavan and K. VijayRaghavan, 8, p. e51539. Available at: https://doi.org/10.7554/eLife.51539.

Kapur, A. *et al.* (1998) 'L-Type Calcium Channels Are Required for One Form of Hippocampal Mossy Fiber LTP', *Journal of neurophysiology*, 79(4), pp. 2181–2190.

Karunanithi, S. *et al.* (2002) 'Quantal Size and Variation Determined by Vesicle Size in Normal and Mutant *Drosophila* Glutamatergic Synapses', *The Journal of Neuroscience*, 22(23), pp. 10267–10276. Available at: https://doi.org/10.1523/JNEUROSCI.22-23-10267.2002.

Kastenhuber, E. and Lowe, S. (2017) 'Putting p53 in context', *Cell*, 170(6), pp. 1062–1078. Available at: https://doi.org/10.1016/j.cell.2017.08.028.

Keshishian, H. *et al.* (1996) 'The Drosophila Neuromuscular Junction: A Model System for Studying Synaptic Development and Function', *Annual Review of Neuroscience*, 19(1), pp. 545–575. Available at: https://doi.org/10.1146/annurev.ne.19.030196.002553.

Khoronenkova, S.V. and Dianov, G.L. (2015) 'ATM prevents DSB formation by coordinating SSB repair and cell cycle progression', *Proceedings of the National Academy of Sciences of the United States of America*, 112(13), pp. 3997–4002. Available at: https://doi.org/10.1073/pnas.1416031112.

Kim, N. *et al.* (2019) 'BMP-dependent synaptic development requires Abi-Abl-Rac signaling of BMP receptor macropinocytosis', *Nature Communications*, 10(1), p. 684. Available at: https://doi.org/10.1038/s41467-019-08533-2.

Klapoetke, N.C. *et al.* (2014) 'Independent optical excitation of distinct neural populations', *Nature Methods*, 11(3), pp. 338–346. Available at: https://doi.org/10.1038/nmeth.2836.

Klionsky, D.J. *et al.* (2021) 'Guidelines for the use and interpretation of assays for monitoring autophagy (4th edition) [1]', *Autophagy*, 17(1), pp. 1–382. Available at: https://doi.org/10.1080/15548627.2020.1797280.

Koch, I. *et al.* (2008) 'Drosophila Ankyrin 2 Is Required for Synaptic Stability', *Neuron*, 58(2), pp. 210–222. Available at: https://doi.org/10.1016/j.neuron.2008.03.019.

Koles, K. and Budnik, V. (2012) 'Wnt Signaling in Neuromuscular Junction Development', *Cold Spring Harbor Perspectives in Biology*, 4(6), p. a008045. Available at: https://doi.org/10.1101/cshperspect.a008045.

Kozlov, S.V. *et al.* (2006) 'Involvement of novel autophosphorylation sites in ATM activation', *The EMBO journal*, 25(15), pp. 3504–3514. Available at: https://doi.org/10.1038/sj.emboj.7601231.

Kozlov, S.V. *et al.* (2011) 'Autophosphorylation and ATM Activation', *The Journal of Biological Chemistry*, 286(11), pp. 9107–9119. Available at: https://doi.org/10.1074/jbc.M110.204065.

Kracikova, M. *et al.* (2013) 'A threshold mechanism mediates p53 cell fate decision between growth arrest and apoptosis', *Cell Death & Differentiation*, 20(4), pp. 576–588. Available at: https://doi.org/10.1038/cdd.2012.155.

Krejci, L. *et al.* (2012) 'Homologous recombination and its regulation', *Nucleic Acids Research*, 40(13), pp. 5795–5818. Available at: https://doi.org/10.1093/nar/gks270.

Krench, M. and Littleton, J.T. (2013) 'Modeling Huntington disease in *Drosophila*: Insights into axonal transport defects and modifiers of toxicity', *Fly*, 7(4), pp. 229–236. Available at: https://doi.org/10.4161/fly.26279.

Landgraf, M. *et al.* (1997) 'The Origin, Location, and Projections of the Embryonic Abdominal Motorneurons of Drosophila', *Journal of Neuroscience*, 17(24), pp. 9642–9655. Available at: https://doi.org/10.1523/JNEUROSCI.17-24-09642.1997.

Lang, L. *et al.* (2018) 'ATM-Mediated Phosphorylation of Cortactin Involved in Actin Polymerization Promotes Breast Cancer Cells Migration and Invasion', *Cellular Physiology and Biochemistry: International Journal of Experimental Cellular Physiology, Biochemistry, and Pharmacology*, 51(6), pp. 2972–2988. Available at: https://doi.org/10.1159/000496048.

Lau, W.C.Y. *et al.* (2016) 'Structure of the human dimeric ATM kinase', *Cell Cycle*, 15(8), pp. 1117–1124. Available at: https://doi.org/10.1080/15384101.2016.1158362.

Laugks, U., Hieke, M. and Wagner, N. (2016) 'MAN1 Restricts BMP Signaling During Synaptic Growth in Drosophila', *Cellular and Molecular Neurobiology*, pp. 1–17. Available at: https://doi.org/10.1007/s10571-016-0442-4.

Layalle, S. *et al.* (2021) 'Amyotrophic Lateral Sclerosis Genes in Drosophila melanogaster', *International Journal of Molecular Sciences*, 22(2), p. 904. Available at: https://doi.org/10.3390/ijms22020904.

Lebensohn, A.M. and Kirschner, M.W. (2009) 'Activation of the WAVE Complex by Coincident Signals Controls Actin Assembly', *Molecular Cell*, 36(3), pp. 512–524. Available at: https://doi.org/10.1016/j.molcel.2009.10.024.

Lee, J.-H. *et al.* (2010) '53BP1 promotes ATM activity through direct interactions with the MRN complex', *The EMBO Journal*, 29(3), pp. 574–585. Available at: https://doi.org/10.1038/emboj.2009.372.

Lee, J.-H. *et al.* (2013) 'Ataxia telangiectasia-mutated (ATM) kinase activity is regulated by ATP-driven conformational changes in the Mre11/Rad50/Nbs1 (MRN) complex', *The Journal of Biological Chemistry*, 288(18), pp. 12840–12851. Available at: https://doi.org/10.1074/jbc.M113.460378.

Lee, J.-H. *et al.* (2018) 'ATM directs DNA damage responses and proteostasis via genetically separable pathways', *Science Signaling*, 11(512), p. eaan5598. Available at: https://doi.org/10.1126/scisignal.aan5598.

Lee, J.-H. and Paull, T.T. (2005) 'ATM activation by DNA double-strand breaks through the Mre11-Rad50-Nbs1 complex', *Science (New York, N.Y.)*, 308(5721), pp. 551–554. Available at: https://doi.org/10.1126/science.1108297.

Lee, J.-H. and Paull, T.T. (2007) 'Activation and regulation of ATM kinase activity in response to DNA double-strand breaks', *Oncogene*, 26(56), pp. 7741–7748. Available at: https://doi.org/10.1038/sj.onc.1210872.

Lee, K.J., Kim, H. and Rhyu, I.J. (2005) 'The roles of dendritic spine shapes in Purkinje cells', *The Cerebellum*, 4(2), pp. 97–104. Available at: https://doi.org/10.1080/14734220510007842.

Lee, P.-T. *et al.* (2018) 'A gene-specific T2A-GAL4 library for Drosophila', *eLife*. Edited by K. VijayRaghavan, 7, p. e35574. Available at: https://doi.org/10.7554/eLife.35574.

Lee, Y.S. *et al.* (2004) 'Distinct Roles for Drosophila Dicer-1 and Dicer-2 in the siRNA/miRNA Silencing Pathways', *Cell*, 117(1), pp. 69–81. Available at: https://doi.org/10.1016/S0092-8674(04)00261-2.

Levine, B. and Abrams, J. (2008) 'p53: The Janus of autophagy?', *Nature Cell Biology*, 10(6), pp. 637–639. Available at: https://doi.org/10.1038/ncb0608-637.

Li, J. *et al.* (2009) 'Cytoplasmic ATM in neurons modulates synaptic function', *Current biology : CB*, 19(24), pp. 2091–2096. Available at: https://doi.org/10.1016/j.cub.2009.10.039.

Li, R. *et al.* (2012) 'A distinct response to endogenous DNA damage in the development of Nbs1-deficient cortical neurons', *Cell Research*, 22(5), pp. 859–872. Available at: https://doi.org/10.1038/cr.2012.3.

Li, T. and Wang, Z.-Q. (2011) 'Point mutation at the Nbs1 Threonine 278 site does not affect mouse development, but compromises the Chk2 and Smc1 phosphorylation after DNA damage', *Mechanisms of Ageing and Development*, 132(8–9), pp. 382–388. Available at: https://doi.org/10.1016/j.mad.2011.05.001.

Li, X. *et al.* (2013) 'piggyBac transposase tools for genome engineering', *Proceedings of the National Academy of Sciences*, 110(25), pp. E2279–E2287. Available at: https://doi.org/10.1073/pnas.1305987110.

Lin, C.-P. *et al.* (2009) 'Proteasome-dependent Processing of Topoisomerase I-DNA Adducts into DNA Double Strand Breaks at Arrested Replication Forks', *The Journal of Biological Chemistry*, 284(41), pp. 28084–28092. Available at: https://doi.org/10.1074/jbc.M109.030601.

Ling, D. *et al.* (2009) 'Abeta42-Induced Neurodegeneration via an Age-Dependent Autophagic-Lysosomal Injury in Drosophila', *PLoS ONE*. Edited by M.R. Cookson, 4(1), p. e4201. Available at: https://doi.org/10.1371/journal.pone.0004201.

Liu, Y. and Levine, B. (2015) 'Autosis and autophagic cell death: the dark side of autophagy', *Cell Death and Differentiation*, 22(3), pp. 367–376. Available at: https://doi.org/10.1038/cdd.2014.143.

Lou, Z. *et al.* (2006) 'MDC1 Maintains Genomic Stability by Participating in the Amplification of ATM-Dependent DNA Damage Signals', *Molecular Cell*, 21(2), pp. 187–200. Available at: https://doi.org/10.1016/j.molcel.2005.11.025.

Lovejoy, C.A. and Cortez, D. (2009) 'Common mechanisms of PIKK regulation', *DNA repair*, 8(9), pp. 1004–1008. Available at: https://doi.org/10.1016/j.dnarep.2009.04.006.

Lu, G. *et al.* (2021) 'The effects of metformin on autophagy', *Biomedicine & Pharmacotherapy*, 137, p. 111286. Available at: https://doi.org/10.1016/j.biopha.2021.111286.

Lu, Y.-C. *et al.* (2016) 'ER-Dependent Ca++-mediated Cytosolic ROS as an Effector for Induction of Mitochondrial Apoptotic and ATM-JNK Signal Pathways in Gallic Acid-treated Human Oral Cancer Cells', *Anticancer Research*, 36(2), pp. 697–705.

Lukas, C. *et al.* (2003) 'Distinct spatiotemporal dynamics of mammalian checkpoint regulators induced by DNA damage', *Nature Cell Biology*, 5(3), pp. 255–260. Available at: https://doi.org/10.1038/ncb945.

Ma, X. *et al.* (2016) 'DNA damage-induced Lok/CHK2 activation compromises germline stem cell self-renewal and lineage differentiation', *Development*, 143(23), pp. 4312–4323. Available at: https://doi.org/10.1242/dev.141069.

Maday, S. and Holzbaur, E.L.F. (2014) 'Autophagosome biogenesis in primary neurons follows an ordered and spatially regulated pathway', *Developmental cell*, 30(1), pp. 71–85. Available at: https://doi.org/10.1016/j.devcel.2014.06.001.

Malagelada, C. *et al.* (2010) 'Rapamycin Protects against Neuron Death in In Vitro andIn Vivo Models of Parkinson's Disease', *The Journal of Neuroscience*, 30(3), pp. 1166–1175. Available at: https://doi.org/10.1523/JNEUROSCI.3944-09.2010.

Maldonado-Díaz, C., Vazquez, M. and Marie, B. (2021) 'A comparison of three different methods of eliciting rapid activity-dependent synaptic plasticity at the Drosophila NMJ', *PLOS ONE*, 16(11), p. e0260553. Available at: https://doi.org/10.1371/journal.pone.0260553.

Mao, Z. *et al.* (2008) 'Comparison of nonhomologous end joining and homologous recombination in human cells', *DNA repair*, 7(10), pp. 1765–1771. Available at: https://doi.org/10.1016/j.dnarep.2008.06.018.

Mari, P.-O. *et al.* (2006) 'Dynamic assembly of end-joining complexes requires interaction between Ku70/80 and XRCC4', *Proceedings of the National Academy of Sciences of the United States of America*, 103(49), pp. 18597–18602. Available at: https://doi.org/10.1073/pnas.0609061103.

Marinangeli, C. *et al.* (2018) 'AMP-Activated Protein Kinase Is Essential for the Maintenance of Energy Levels during Synaptic Activation', *iScience*, 9, pp. 1–13. Available at: https://doi.org/10.1016/j.isci.2018.10.006.

Marqués, G. (2005) 'Morphogens and synaptogenesis in Drosophila', *Journal of Neurobiology*, 64(4), pp. 417–434. Available at: https://doi.org/10.1002/neu.20165.

Mathew, D. *et al.* (2005) 'Wingless Signaling at Synapses Is Through Cleavage and Nuclear Import of Receptor DFrizzled2', *Science (New York, N.Y.)*, 310(5752), pp. 1344–1347. Available at: https://doi.org/10.1126/science.1117051.

Mathew, R. *et al.* (2007) 'Autophagy suppresses tumor progression by limiting chromosomal instability', *Genes & Development*, 21(11), pp. 1367–1381. Available at: https://doi.org/10.1101/gad.1545107.

Matsumoto, Y. *et al.* (2011) 'Two unrelated patients with MRE11A mutations and Nijmegen breakage syndrome-like severe microcephaly', *DNA Repair*, 10(3), pp. 314–321. Available at: https://doi.org/10.1016/j.dnarep.2010.12.002.

Matsuoka, S., Huang, M. and Elledge, S.J. (1998) 'Linkage of ATM to Cell Cycle Regulation by the Chk2 Protein Kinase', *Science*, 282(5395), pp. 1893–1897. Available at: https://doi.org/10.1126/science.282.5395.1893.

McCabe, B.D. *et al.* (2003) 'The BMP Homolog Gbb Provides a Retrograde Signal that Regulates Synaptic Growth at the Drosophila Neuromuscular Junction', *Neuron*, 39(2), pp. 241–254. Available at: https://doi.org/10.1016/S0896-6273(03)00426-4.

McCabe, B.D. *et al.* (2004) 'Highwire Regulates Presynaptic BMP Signaling Essential for Synaptic Growth', *Neuron*, 41(6), pp. 891–905. Available at: https://doi.org/10.1016/S0896-6273(04)00073-X.

McKinnon, P.J. (2004) 'ATM and ataxia telangiectasia', *EMBO Reports*, 5(8), pp. 772–776. Available at: https://doi.org/10.1038/sj.embor.7400210.

McLachlan, E.M. and Martin, A.R. (1981) 'Non-linear summation of end-plate potentials in the frog and mouse.', *The Journal of Physiology*, 311(1), pp. 307–324. Available at: https://doi.org/10.1113/jphysiol.1981.sp013586.

Menon, K.P., Carrillo, R.A. and Zinn, K. (2013) 'Development and plasticity of the *Drosophila* larval neuromuscular junction: Development and plasticity of the neuromuscular junction', *Wiley Interdisciplinary Reviews: Developmental Biology*, 2(5), pp. 647–670. Available at: https://doi.org/10.1002/wdev.108.

Menzies, F.M. *et al.* (2017) 'Autophagy and Neurodegeneration: Pathogenic Mechanisms and Therapeutic Opportunities', *Neuron*, 93(5), pp. 1015–1034. Available at: https://doi.org/10.1016/j.neuron.2017.01.022.

Metcalfe, J.A. *et al.* (1996) 'Accelerated telomere shortening in ataxia telangiectasia', *Nature Genetics*, 13(3), pp. 350–353. Available at: https://doi.org/10.1038/ng0796-350.

Miech, C. *et al.* (2008) 'Presynaptic Local Signaling by a Canonical Wingless Pathway Regulates Development of the Drosophila Neuromuscular Junction', *Journal of Neuroscience*, 28(43), pp. 10875–10884. Available at: https://doi.org/10.1523/JNEUROSCI.0164-08.2008.

Milton, V.J. *et al.* (2011) 'Oxidative stress induces overgrowth of the Drosophila neuromuscular junction', *Proceedings of the National Academy of Sciences of the United States of America*, 108(42), pp. 17521–17526. Available at: https://doi.org/10.1073/pnas.1014511108.

Milton, V.J. and Sweeney, S.T. (2012) 'Oxidative stress in synapse development and function', *Developmental Neurobiology*, 72(1), pp. 100–110. Available at: https://doi.org/10.1002/dneu.20957.

Mirdita, M. *et al.* (2022) 'ColabFold: making protein folding accessible to all', *Nature Methods*, 19(6), pp. 679–682. Available at: https://doi.org/10.1038/s41592-022-01488-1.

Miyagi, Y. *et al.* (2002) 'Delphilin: a Novel PDZ and Formin Homology Domain-Containing Protein that Synaptically Colocalizes and Interacts with Glutamate Receptor δ2 Subunit', *The Journal of Neuroscience*, 22(3), pp. 803–814. Available at: https://doi.org/10.1523/JNEUROSCI.22-03-00803.2002.

Mizushima, N. (2010) 'The role of the Atg1/ULK1 complex in autophagy regulation', *Current Opinion in Cell Biology*, 22(2), pp. 132–139. Available at: https://doi.org/10.1016/j.ceb.2009.12.004.

Mockett, R.J. *et al.* (2003) 'Phenotypic effects of familial amyotrophic lateral sclerosis mutant *Sod* alleles in transgenic *Drosophila*', *Proceedings of the National Academy of Sciences*, 100(1), pp. 301–306. Available at: https://doi.org/10.1073/pnas.0136976100.

Moon, N.-S. *et al.* (2008) 'E2F and p53 Induce Apoptosis Independently during Drosophila Development but Intersect in the Context of DNA Damage', *PLOS Genetics*, 4(8), p. e1000153. Available at: https://doi.org/10.1371/journal.pgen.1000153.

Morgan, S.E. and Kastan, M.B. (1997) 'Foundations in Cancer Research p53 and ATM: Cell Cycle, Cell Death, and Cancer', in G.F. Vande Woude and G. Klein (eds) *Advances in Cancer Research*. Academic Press, pp. 1–25. Available at: https://doi.org/10.1016/S0065-230X(08)60095-0.

Moriwaki, T., Yamasaki, A. and Zhang-Akiyama, Q.-M. (2018) 'ATM Induces Cell Death with Autophagy in Response to H2O2 Specifically in Caenorhabditis elegans Nondividing Cells', *Oxidative Medicine and Cellular Longevity*, 2018. Available at: https://doi.org/10.1155/2018/3862070.

Mosca, T.J. *et al.* (2005) 'Dissection of synaptic excitability phenotypes by using a dominant-negative Shaker K+ channel subunit', *Proceedings of the National Academy of Sciences of the United States of America*, 102(9), pp. 3477–3482. Available at: https://doi.org/10.1073/pnas.0406164102.

Nah, J., Yuan, J. and Jung, Y.-K. (2015) 'Autophagy in Neurodegenerative Diseases: From Mechanism to Therapeutic Approach', *Molecules and Cells*, 38(5), pp. 381–389. Available at: https://doi.org/10.14348/molcells.2015.0034.

Nanou, E. and Catterall, W.A. (2018) 'Calcium Channels, Synaptic Plasticity, and Neuropsychiatric Disease', *Neuron*, 98(3), pp. 466–481. Available at: https://doi.org/10.1016/j.neuron.2018.03.017.

Nanou, E., Scheuer, T. and Catterall, W.A. (2016) 'Calcium sensor regulation of the CaV2.1 Ca2+ channel contributes to long-term potentiation and spatial learning', *Proceedings of the National Academy of Sciences*, 113(46), pp. 13209–13214. Available at: https://doi.org/10.1073/pnas.1616206113.

Nezis, I.P. *et al.* (2010) 'Autophagic degradation of dBruce controls DNA fragmentation in nurse cells during late Drosophila melanogaster oogenesis', *The Journal of Cell Biology*, 190(4), pp. 523–531. Available at: https://doi.org/10.1083/jcb.201002035.

Nguyen Ba, A.N. *et al.* (2009) 'NLStradamus: a simple Hidden Markov Model for nuclear localization signal prediction', *BMC Bioinformatics*, 10(1), p. 202. Available at: https://doi.org/10.1186/1471-2105-10-202.

Nguyen, T.T.N., Shim, J. and Song, Y.-H. (2021) 'Chk2-p53 and JNK in irradiation-induced cell death of hematopoietic progenitors and differentiated cells in Drosophila larval lymph gland', *Biology Open*, 10(8), p. bio058809. Available at: https://doi.org/10.1242/bio.058809.

Nijhof, B. *et al.* (2016) 'A New Fiji-Based Algorithm That Systematically Quantifies Nine Synaptic Parameters Provides Insights into Drosophila NMJ Morphometry', *PLOS Computational Biology*, 12(3), p. e1004823. Available at: https://doi.org/10.1371/journal.pcbi.1004823.

Nissenkorn, A. *et al.* (2011) 'Neurologic Presentation in Children with Ataxia-Telangiectasia: Is Small Head Circumference a Hallmark of the Disease?', *The Journal of Pediatrics*, 159(3), pp. 466-471.e1. Available at: https://doi.org/10.1016/j.jpeds.2011.02.005.

Nissenkorn, A. and Ben-Zeev, B. (2015) 'Chapter 14 - Ataxia telangiectasia', in M.P. Islam and E.S. Roach (eds) *Handbook of Clinical Neurology*. Elsevier (Neurocutaneous Syndromes), pp. 199–214. Available at: https://doi.org/10.1016/B978-0-444-62702-5.00014-7.

O'Driscoll, M. *et al.* (2003) 'A splicing mutation affecting expression of ataxia–telangiectasia and Rad3–related protein (ATR) results in Seckel syndrome', *Nature Genetics*, 33(4), pp. 497–501. Available at: https://doi.org/10.1038/ng1129.

Oikemus, S.R. *et al.* (2004) 'Drosophila atm/telomere fusion is required for telomeric localization of HP1 and telomere position effect', *Genes & Development*, 18(15), pp. 1850–1861. Available at: https://doi.org/10.1101/gad.1202504.

Oka, A. and Takashima, S. (1998) 'Expression of the ataxia-telangiectasia gene (ATM) product in human cerebellar neurons during development', *Neuroscience Letters*, 252(3), pp. 195–198. Available at: https://doi.org/10.1016/S0304-3940(98)00576-X.

Oswald, M.C. *et al.* (2018) 'Reactive oxygen species regulate activity-dependent neuronal plasticity in Drosophila', *eLife*. Edited by G.W. Davis and E. Marder, 7, p. e39393. Available at: https://doi.org/10.7554/eLife.39393.

Packard, M. *et al.* (2002) 'The Drosophila Wnt, Wingless, Provides an Essential Signal for Pre- and Postsynaptic Differentiation', *Cell*, 111(3), pp. 319–330. Available at: https://doi.org/10.1016/S0092-8674(02)01047-4.

Palmer, E. and Freeman, T. (2004) 'Investigation Into the use of C- and N-terminal GFP Fusion Proteins for Subcellular Localization Studies Using Reverse Transfection Microarrays', *Comparative and Functional Genomics*, 5(4), pp. 342–353. Available at: https://doi.org/10.1002/cfg.405.

Park, S. *et al.* (2015) 'Smad7 enhances ATM activity by facilitating the interaction between ATM and Mre11-Rad50-Nbs1 complex in DNA double-strand break repair', *Cellular and Molecular Life Sciences*, 72(3), pp. 583–596. Available at: https://doi.org/10.1007/s00018-014-1687-z.

Parkes, T.L. *et al.* (1998) 'Extension of Drosophila lifespan by overexpression of human SOD1 in motorneurons', *Nature Genetics*, 19(2), pp. 171–174. Available at: https://doi.org/10.1038/534.

Paull, T.T. (2015) 'Mechanisms of ATM Activation', *Annual Review of Biochemistry*, 84(1), pp. 711–738. Available at: https://doi.org/10.1146/annurev-biochem-060614-034335.

Pédelacq, J.-D. *et al.* (2006) 'Engineering and characterization of a superfolder green fluorescent protein', *Nature Biotechnology*, 24(1), pp. 79–88. Available at: https://doi.org/10.1038/nbt1172.

Pedersen, M., Tiong, S. and Campbell, S.D. (2010) 'Molecular genetic characterization of Drosophila ATM conserved functional domains', *Genome*, 53(10), pp. 778–786. Available at: https://doi.org/10.1139/G10-067.

Perez, H. *et al.* (2021) 'A novel, ataxic mouse model of ataxia telangiectasia caused by a clinically relevant nonsense mutation', *eLife*. Edited by R.V. Sillitoe et al., 10, p. e64695. Available at: https://doi.org/10.7554/eLife.64695.

Perry, J. and Kleckner, N. (2003) 'The ATRs, ATMs, and TORs Are Giant HEAT Repeat Proteins', *Cell*, 112(2), pp. 151–155. Available at: https://doi.org/10.1016/S0092-8674(03)00033-3.

Peters, M. *et al.* (2002) 'Chk2 regulates irradiation-induced, p53-mediated apoptosis in Drosophila', *Proceedings of the National Academy of Sciences of the United States of America*, 99(17), pp. 11305–11310. Available at: https://doi.org/10.1073/pnas.172382899.

Petersen, A.J., Rimkus, S.A. and Wassarman, D.A. (2012) 'ATM kinase inhibition in glial cells activates the innate immune response and causes neurodegeneration in Drosophila', *Proceedings of the National Academy of Sciences*, 109(11), pp. E656–E664. Available at: https://doi.org/10.1073/pnas.1110470109.

Piazza, I. *et al.* (2014) 'Association of condensin with chromosomes depends on DNA binding by its HEAT-repeat subunits', *Nature Structural & Molecular Biology*, 21(6), pp. 560–568. Available at: https://doi.org/10.1038/nsmb.2831.

Piccioli, Z.D. and Littleton, J.T. (2014) 'Retrograde BMP Signaling Modulates Rapid Activity-Dependent Synaptic Growth via Presynaptic LIM Kinase Regulation of Cofilin', *The Journal of Neuroscience*, 34(12), pp. 4371–4381. Available at: https://doi.org/10.1523/JNEUROSCI.4943-13.2014.

Piras, A. *et al.* (2017) 'Inhibition of autophagy delays motoneuron degeneration and extends lifespan in a mouse model of spinal muscular atrophy', *Cell Death & Disease*, 8(12), p. 3223. Available at: https://doi.org/10.1038/s41419-017-0086-4.

Pizzamiglio, L. *et al.* (2016) 'New Role of ATM in Controlling GABAergic Tone During Development', *Cerebral Cortex*, 26(10), pp. 3879–3888. Available at: https://doi.org/10.1093/cercor/bhw125.

Politano, S.F. *et al.* (2019) '*Tao* Negatively Regulates BMP Signaling During Neuromuscular Junction Development in *Drosophila*', *Developmental Neurobiology*, 79(4), pp. 335–349. Available at: https://doi.org/10.1002/dneu.22681.

Pulver, S.R. *et al.* (2009) 'Temporal Dynamics of Neuronal Activation by Channelrhodopsin-2 and TRPA1 Determine Behavioral Output in *Drosophila* Larvae', *Journal of Neurophysiology*, 101(6), pp. 3075–3088. Available at: https://doi.org/10.1152/jn.00071.2009.

Qi, Y. *et al.* (2016) 'ATM mediates spermidine-induced mitophagy via PINK1 and Parkin regulation in human fibroblasts', *Scientific Reports*, 6. Available at: https://doi.org/10.1038/srep24700.

Queiroz-Machado, J. *et al.* (2001) 'tef: a mutation that causes telomere fusion and severe genome rearrangements in Drosophila melanogaster', *Chromosoma*, 110(1), pp. 10–23. Available at: https://doi.org/10.1007/s004120000116.

Quick, K.L. and Dugan, L.L. (2001) 'Superoxide stress identifies neurons at risk in a model of ataxia-telangiectasia', *Annals of Neurology*, 49(5), pp. 627–635. Available at: https://doi.org/10.1002/ana.1005.

Rada, B. and Leto, T.L. (2008) 'Oxidative innate immune defenses by Nox/Duox family NADPH Oxidases', *Contributions to microbiology*, 15, pp. 164–187. Available at: https://doi.org/10.1159/000136357.

Ramesh, N. and Tasdizen, T. (2021) 'Detection and segmentation in microscopy images', in. Available at: https://doi.org/10.1016/B978-0-12-814972-0.00003-5.

Ramos, C.I. *et al.* (2015) 'Neto-Mediated Intracellular Interactions Shape Postsynaptic Composition at the Drosophila Neuromuscular Junction', *PLOS Genetics*, 11(4), p. e1005191. Available at: https://doi.org/10.1371/journal.pgen.1005191.

Randall, R. and Thayer, S. (1992) 'Glutamate-induced calcium transient triggers delayed calcium overload and neurotoxicity in rat hippocampal neurons', *The Journal of Neuroscience*, 12(5), pp. 1882–1895. Available at: https://doi.org/10.1523/JNEUROSCI.12-05-01882.1992.

Rawson, J.M. *et al.* (2003) 'Drosophila neuromuscular synapse assembly and function require the TGF-β type I receptor saxophone and the transcription factor Mad', *Journal of Neurobiology*, 55(2), pp. 134–150. Available at: https://doi.org/10.1002/neu.10189.

Rego, A.C. and Oliveira, C.R. (2003) 'Mitochondrial Dysfunction and Reactive Oxygen Species in Excitotoxicity and Apoptosis: Implications for the Pathogenesis of Neurodegenerative Diseases', *Neurochemical Research*, 28(10), pp. 1563–1574. Available at: https://doi.org/10.1023/A:1025682611389.

Reif, A.E. and Allen, J.M.V. (1964) 'THE AKR THYMIC ANTIGEN AND ITS DISTRIBUTION IN LEUKEMIAS AND NERVOUS TISSUES', *The Journal of Experimental Medicine*, 120(3), pp. 413–433.

Restrepo, L.J. *et al.* (2022) 'γ-secretase promotes Drosophila postsynaptic development through the cleavage of a Wnt receptor', *Developmental Cell*, 57(13), pp. 1643-1660.e7. Available at: https://doi.org/10.1016/j.devcel.2022.05.006.

Revaitis, N.T. *et al.* (2020) 'Quantitative analyses of EGFR localization and trafficking dynamics in the follicular epithelium', *Development*, 147(15), p. dev183210. Available at: https://doi.org/10.1242/dev.183210.

Rezaeian, A.-H. *et al.* (2017) 'A hypoxia-responsive TRAF6-ATM-H2A.X signalling axis promotes HIF1α activation, tumorigenesis and metastasis', *Nature cell biology*, 19(1), pp. 38–51. Available at: https://doi.org/10.1038/ncb3445.

Rezával, C., Werbajh, S. and Ceriani, M.F. (2007) 'Neuronal death in Drosophila triggered by GAL4 accumulation', *European Journal of Neuroscience*, 25(3), pp. 683–694. Available at: https://doi.org/10.1111/j.1460-9568.2007.05317.x.

Rieckhof, G.E. *et al.* (2003) 'Presynaptic N-type Calcium Channels Regulate Synaptic Growth*', *Journal of Biological Chemistry*, 278(42), pp. 41099–41108. Available at: https://doi.org/10.1074/jbc.M306417200.

Riley, D.A. (1977) 'Spontaneous elimination of nerve terminals from the endplates of developing skeletal myofibers', *Brain Research*, 134(2), pp. 279–285. Available at: https://doi.org/10.1016/0006-8993(77)91073-3.

Rimkus, S.A. *et al.* (2008) 'Mutations in String/CDC25 inhibit cell cycle re-entry and neurodegeneration in a Drosophila model of Ataxia telangiectasia', *Genes & Development*, 22(9), pp. 1205–1220. Available at: https://doi.org/10.1101/gad.1639608.

Rimkus, S.A. and Wassarman, D.A. (2018) 'A pharmacological screen for compounds that rescue the developmental lethality of a Drosophila ATM mutant', *PLoS ONE*, 13(1). Available at: https://doi.org/10.1371/journal.pone.0190821.

Rizzuto, R. *et al.* (1992) 'Rapid changes of mitochondrial Ca2+ revealed by specifically targeted recombinant aequorin', *Nature*, 358(6384), pp. 325–327. Available at: https://doi.org/10.1038/358325a0.

Roesler, M.K. *et al.* (2019) 'Myosin XVI Regulates Actin Cytoskeleton Dynamics in Dendritic Spines of Purkinje Cells and Affects Presynaptic Organization', *Frontiers in Cellular Neuroscience*, 13. Available at: https://doi.org/10.3389/fncel.2019.00330.

Rotman, G. and Shiloh, Y. (1997) 'Hypothesis: Ataxia-telangiectasia: Is ATM a sensor of oxidative damage and stress?', *BioEssays*, 19(10), pp. 911–917. Available at: https://doi.org/10.1002/bies.950191011.

Rowe, L.A., Degtyareva, N. and Doetsch, P.W. (2008) 'DNA Damage-induced Reactive Oxygen Species (ROS) Stress Response in Saccharomyces cerevisiae', *Free radical biology & medicine*, 45(8), pp. 1167–1177. Available at: https://doi.org/10.1016/j.freeradbiomed.2008.07.018.

Rui, Y.-N. *et al.* (2015) 'Huntingtin functions as a scaffold for selective macroautophagy', *Nature Cell Biology*, 17(3), pp. 262–275. Available at: https://doi.org/10.1038/ncb3101.

Ruiz-Cañada, C. and Budnik, V. (2006) 'Introduction on The Use of The Drosophila Embryonic/Larval Neuromuscular Junction as A Model System to Study Synapse Development and Function, and A Brief Summary of Pathfinding and Target Recognition', in *International Review of Neurobiology*. Academic Press (The Fly Neuromuscular Junction: Structure and Function Second Edition), pp. 1–31. Available at: https://doi.org/10.1016/S0074-7742(06)75001-2.

Sahama, I. *et al.* (2014) 'Radiological Imaging in Ataxia Telangiectasia: a Review', *The Cerebellum*, 13(4), pp. 521–530. Available at: https://doi.org/10.1007/s12311-014-0557-4.

Sauvola, C.W. *et al.* (2021) 'The decoy SNARE Tomosyn sets tonic versus phasic release properties and is required for homeostatic synaptic plasticity', *eLife*. Edited by H.J. Bellen, C. Desplan, and H. Broihier, 10, p. e72841. Available at: https://doi.org/10.7554/eLife.72841.

Savitsky, K. *et al.* (1995) 'A single ataxia telangiectasia gene with a product similar to PI-3 kinase', *Science*, 268(5218), pp. 1749–1753. Available at: https://doi.org/10.1126/science.7792600.

Schaefer, J.E., Worrell, J.W. and Levine, R.B. (2010) 'Role of Intrinsic Properties in Drosophila Motoneuron Recruitment During Fictive Crawling', *Journal of Neurophysiology*, 104(3), pp. 1257–1266. Available at: https://doi.org/10.1152/jn.00298.2010.

Schott, S. *et al.* (2017) 'A fluorescent toolkit for spatiotemporal tracking of apoptotic cells in living *Drosophila* tissues', *Development*, p. dev.149807. Available at: https://doi.org/10.1242/dev.149807.

Schuster, C.M. *et al.* (1996a) 'Genetic Dissection of Structural and Functional Components of Synaptic Plasticity. I. Fasciclin II Controls Synaptic Stabilization and Growth', *Neuron*, 17(4), pp. 641–654. Available at: https://doi.org/10.1016/S0896-6273(00)80197-X.

Schuster, C.M. *et al.* (1996b) 'Genetic Dissection of Structural and Functional Components of Synaptic Plasticity. II. Fasciclin II Controls Presynaptic Structural Plasticity', *Neuron*, 17(4), pp. 655–667. Available at: https://doi.org/10.1016/S0896-6273(00)80198-1.

Scott, R.C., Juhász, G. and Neufeld, T.P. (2007) 'Direct Induction of Autophagy by Atg1 Inhibits Cell Growth and Induces Apoptotic Cell Death', *Current Biology*, 17(1), pp. 1–11. Available at: https://doi.org/10.1016/j.cub.2006.10.053.

Seidel, J.J., Anderson, C.M. and Blackburn, E.H. (2008) 'A Novel Tel1/ATM N-Terminal Motif, TAN, Is Essential for Telomere Length Maintenance and a DNA Damage Response', *Molecular and Cellular Biology*, 28(18), pp. 5736–5746. Available at: https://doi.org/10.1128/MCB.00326-08.

Sekerková, G. *et al.* (2003) 'Novel Espin Actin-Bundling Proteins Are Localized to Purkinje Cell Dendritic Spines and Bind the Src Homology 3 Adapter Protein Insulin Receptor Substrate p53', *The Journal of Neuroscience*, 23(4), pp. 1310–1319. Available at: https://doi.org/10.1523/JNEUROSCI.23-04-01310.2003.

Shackelford, R.E. *et al.* (2001) 'The Ataxia telangiectasia Gene Product Is Required for Oxidative Stress-induced G1 and G2Checkpoint Function in Human Fibroblasts', *Journal of Biological Chemistry*, 276(24), pp. 21951–21959. Available at: https://doi.org/10.1074/jbc.M011303200.

Shaikh, A.G. *et al.* (2011) 'Ataxia telangiectasia: a "disease model" to understand the cerebellar control of vestibular reflexes', *Journal of Neurophysiology*, 105(6), pp. 3034–3041. Available at: https://doi.org/10.1152/jn.00721.2010.

Shaikh, A.G. *et al.* (2013) 'Disorders of Upper Limb Movements in Ataxia-Telangiectasia', *PLOS ONE*, 8(6), p. e67042. Available at: https://doi.org/10.1371/journal.pone.0067042.

Shen, W. and Ganetzky, B. (2009) 'Autophagy promotes synapse development in Drosophila', *The Journal of Cell Biology*, 187(1), pp. 71–79. Available at: https://doi.org/10.1083/jcb.200907109.

Sheng, Y. *et al.* (2014) 'Superoxide Dismutases and Superoxide Reductases', *Chemical Reviews*, 114(7), pp. 3854–3918. Available at: https://doi.org/10.1021/cr4005296.

Shi, Y., Norberg, E. and Vakifahmetoglu-Norberg, H. (2021) 'Mutant p53 as a Regulator and Target of Autophagy', *Frontiers in Oncology*, 10. Available at: https://www.frontiersin.org/articles/10.3389/fonc.2020.607149 (Accessed: 24 January 2024).

Shieh, S.-Y. *et al.* (2000) 'The human homologs of checkpoint kinases Chk1 and Cds1 (Chk2) phosphorylate p53 at multiple DNA damage-inducible sites', *Genes & Development*, 14(3), pp. 289–300.

Shimura, T. *et al.* (2016) 'Severe mitochondrial damage associated with low-dose radiation sensitivity in ATM- and NBS1-deficient cells', *Cell Cycle*, 15(8), pp. 1099–1107. Available at: https://doi.org/10.1080/15384101.2016.1156276.

Shreeram, S. *et al.* (2006) 'Wip1 Phosphatase Modulates ATM-Dependent Signaling Pathways', *Molecular Cell*, 23(5), pp. 757–764. Available at: https://doi.org/10.1016/j.molcel.2006.07.010.

Sigrist, S.J. *et al.* (2003) 'Experience-Dependent Strengthening of *Drosophila* Neuromuscular Junctions', *The Journal of Neuroscience*, 23(16), pp. 6546–6556. Available at: https://doi.org/10.1523/JNEUROSCI.23-16-06546.2003.

Silva, E. *et al.* (2004) 'ATM Is Required for Telomere Maintenance and Chromosome Stability during Drosophila Development', *Current Biology*, 14(15), pp. 1341–1347. Available at: https://doi.org/10.1016/j.cub.2004.06.056.

Sobrido-Cameán, D. *et al.* (2023) 'Activity-regulated growth of motoneurons at the neuromuscular junction is mediated by NADPH oxidases', *Frontiers in Cellular Neuroscience*, 16, p. 1106593. Available at: https://doi.org/10.3389/fncel.2022.1106593.

Song, Y.-H. *et al.* (2004) 'The Drosophila ATM Ortholog, dATM, Mediates the Response to Ionizing Radiation and to Spontaneous DNA Damage during Development', *Current Biology*, 14(15), pp. 1354–1359. Available at: https://doi.org/10.1016/j.cub.2004.06.064.

Song, Y.-H. (2005) 'Drosophila melanogaster: a Model for the Study of DNA Damage Checkpoint Response', *Molecules and Cells*, 19(2), pp. 167–179.

Sopko, R. *et al.* (2014) 'Combining Genetic Perturbations and Proteomics to Examine Kinase-Phosphatase Networks in Drosophila Embryos', *Developmental Cell*, 31(1), pp. 114–127. Available at: https://doi.org/10.1016/j.devcel.2014.07.027.

Sordet, O. *et al.* (2009) 'Ataxia telangiectasia mutated activation by transcription- and topoisomerase I-induced DNA double-strand breaks', *EMBO Reports*, 10(8), pp. 887–893. Available at: https://doi.org/10.1038/embor.2009.97.

Spence, E.F. and Soderling, S.H. (2015) 'Actin Out: Regulation of the Synaptic Cytoskeleton', *The Journal of Biological Chemistry*, 290(48), pp. 28613–28622. Available at: https://doi.org/10.1074/jbc.R115.655118.

Spilman, P. *et al.* (2010) 'Inhibition of mTOR by Rapamycin Abolishes Cognitive Deficits and Reduces Amyloid-β Levels in a Mouse Model of Alzheimer's Disease', *PLoS ONE*, 5(4), p. e9979. Available at: https://doi.org/10.1371/journal.pone.0009979.

Steinegger, M. and Söding, J. (2017) 'MMseqs2 enables sensitive protein sequence searching for the analysis of massive data sets', *Nature Biotechnology*, 35(11), pp. 1026–1028. Available at: https://doi.org/10.1038/nbt.3988.

Stevens, C.F. (1976) 'A comment on Martin's relation', *Biophysical Journal*, 16(8), pp. 891–895. Available at: https://doi.org/10.1016/S0006-3495(76)85739-6.

Stewart (1999) 'The DNA Double-Strand Break Repair Gene hMRE11 Is Mutated in Individuals with an Ataxia-Telangiectasia-like Disorder', *Cell* [Preprint]. Available at: https://doi.org/10.1016/S0092-8674(00)81547-0.

Stewart, G.S. *et al.* (2001) 'Residual Ataxia Telangiectasia Mutated Protein Function in Cells from Ataxia Telangiectasia Patients, with 5762ins137 and 7271T→G Mutations, Showing a Less Severe Phenotype*', *Journal of Biological Chemistry*, 276(32), pp. 30133–30141. Available at: https://doi.org/10.1074/jbc.M103160200.

Stolarova, L. *et al.* (2020) 'CHEK2 Germline Variants in Cancer Predisposition: Stalemate Rather than Checkmate', *Cells*, 9(12), p. 2675. Available at: https://doi.org/10.3390/cells9122675.

Stucki, M. *et al.* (2005) 'MDC1 Directly Binds Phosphorylated Histone H2AX to Regulate Cellular Responses to DNA Double-Strand Breaks', *Cell*, 123(7), pp. 1213–1226. Available at: https://doi.org/10.1016/j.cell.2005.09.038.

Sulkowski, M.J. *et al.* (2016) 'A Novel, Noncanonical BMP Pathway Modulates Synapse Maturation at the Drosophila Neuromuscular Junction', *PLOS Genetics*. Edited by H.J. Bellen, 12(1), p. e1005810. Available at: https://doi.org/10.1371/journal.pgen.1005810.

Sun, C. *et al.* (2023) 'NAD depletion mediates cytotoxicity in human neurons with autophagy deficiency', *Cell Reports*, 42(5), p. 112372. Available at: https://doi.org/10.1016/j.celrep.2023.112372.

Sun, Y. *et al.* (2007) 'DNA damage-induced acetylation of lysine 3016 of ATM activates ATM kinase activity', *Molecular and Cellular Biology*, 27(24), pp. 8502–8509. Available at: https://doi.org/10.1128/MCB.01382-07.

Sunderland, P. *et al.* (2020) 'ATM-deficient neural precursors develop senescence phenotype with disturbances in autophagy', *Mechanisms of Ageing and Development*, 190, p. 111296. Available at: https://doi.org/10.1016/j.mad.2020.111296.

Sweeney, S.T. and Davis, G.W. (2002) 'Unrestricted Synaptic Growth in spinster—a Late Endosomal Protein Implicated in TGF-β-Mediated Synaptic Growth Regulation', *Neuron*, 36(3), pp. 403–416. Available at: https://doi.org/10.1016/S0896-6273(02)01014-0.

Swift, M. *et al.* (1986) 'The incidence and gene frequency of ataxia-telangiectasia in the United States.', *American Journal of Human Genetics*, 39(5), pp. 573–583.

Tait, S.W.G. *et al.* (2004) 'Mechanism of action of Drosophila Reaper in mammalian cells: Reaper globally inhibits protein synthesis and induces apoptosis independent of mitochondrial permeability', *Cell Death & Differentiation*, 11(8), pp. 800–811. Available at: https://doi.org/10.1038/sj.cdd.4401410.

Tang, M. *et al.* (2019) 'SIRT7-mediated ATM deacetylation is essential for its deactivation and DNA damage repair', *Science Advances*, 5(3). Available at: https://doi.org/10.1126/sciadv.aav1118.

Tasdemir, E. *et al.* (2008) 'Regulation of autophagy by cytoplasmic p53', *Nature Cell Biology*, 10(6), pp. 676–687. Available at: https://doi.org/10.1038/ncb1730.

Tavani, F. *et al.* (2003) 'Ataxia-telangiectasia: the pattern of cerebellar atrophy on MRI', *Neuroradiology*, 45(5), pp. 315–319. Available at: https://doi.org/10.1007/s00234-003-0945-9.

Taylor, A.M.R. *et al.* (2015) 'Ataxia telangiectasia: more variation at clinical and cellular levels', *Clinical Genetics*, 87(3), pp. 199–208. Available at: https://doi.org/10.1111/cge.12453.

Taylor, M.J. *et al.* (2022) 'Inhibition of Chk2 promotes neuroprotection, axon regeneration, and functional recovery after CNS injury', *Science Advances*, 8(37), p. eabq2611. Available at: https://doi.org/10.1126/sciadv.abq2611.

Taylor, M.J. and Tuxworth, R.I. (2019) 'Continuous tracking of startled *Drosophila* as an alternative to the negative geotaxis climbing assay', *Journal of Neurogenetics*, 33(3), pp. 190–198. Available at: https://doi.org/10.1080/01677063.2019.1634065.

Thoreen, C.C. *et al.* (2009) 'An ATP-competitive Mammalian Target of Rapamycin Inhibitor Reveals Rapamycin-resistant Functions of mTORC1', *The Journal of Biological Chemistry*, 284(12), pp. 8023–8032. Available at: https://doi.org/10.1074/jbc.M900301200.

Tolbert, C.E. *et al.* (2019) 'Loss of ATM positively regulates Rac1 activity and cellular migration through oxidative stress', *Biochemical and Biophysical Research Communications*, 508(4), pp. 1155–1161. Available at: https://doi.org/10.1016/j.bbrc.2018.12.033.

Toyoshima, M. *et al.* (1998) 'Ataxia-telangiectasia without immunodeficiency: Novel point mutations within and adjacent to the phosphatidylinositol 3-kinase-like domain', *American Journal of Medical Genetics*, 75(2), pp. 141–144. Available at: https://doi.org/10.1002/(SICI)1096-8628(19980113)75:2<141::AID-AJMG4>3.0.CO;2-W.

Traven, A. and Heierhorst, J. (2005) 'SQ/TQ cluster domains: concentrated ATM/ATR kinase phosphorylation site regions in DNA-damage-response proteins', *BioEssays: News and Reviews in Molecular, Cellular and Developmental Biology*, 27(4), pp. 397–407. Available at: https://doi.org/10.1002/bies.20204.

Tripathi, V. *et al.* (2018) 'MRN complex-dependent recruitment of ubiquitylated BLM helicase to DSBs negatively regulates DNA repair pathways', *Nature Communications*, 9. Available at: https://doi.org/10.1038/s41467-018-03393-8.

Tuxworth, R.I. *et al.* (2019) 'Attenuating the DNA damage response to double-strand breaks restores function in models of CNS neurodegeneration', *Brain Communications*, 1(1), p. fcz005. Available at: https://doi.org/10.1093/braincomms/fcz005.

Uziel, T. *et al.* (2003) 'Requirement of the MRN complex for ATM activation by DNA damage', *The EMBO journal*, 22(20), pp. 5612–5621. Available at: https://doi.org/10.1093/emboj/cdg541.

Vaccaro, V. *et al.* (2017) 'Miro1-dependent mitochondrial positioning drives the rescaling of presynaptic Ca2+ signals during homeostatic plasticity', *EMBO Reports*, 18(2), pp. 231–240. Available at: https://doi.org/10.15252/embr.201642710.

Vail, G. *et al.* (2016) 'ATM protein is located on presynaptic vesicles and its deficit leads to failures in synaptic plasticity', *Journal of Neurophysiology*, 116(1), pp. 201–209. Available at: https://doi.org/10.1152/jn.00006.2016.

Valbuena, F.M. *et al.* (2020) 'A photostable monomeric superfolder green fluorescent protein', *Traffic*, 21(8), pp. 534–544. Available at: https://doi.org/10.1111/tra.12737.

Valentin-Vega, Y.A. *et al.* (2012) 'Mitochondrial dysfunction in ataxia-telangiectasia', *Blood*, 119(6), pp. 1490–1500. Available at: https://doi.org/10.1182/blood-2011-08-373639.

Vasin, A. *et al.* (2019) 'Two Pathways for the Activity-Dependent Growth and Differentiation of Synaptic Boutons in Drosophila', *eNeuro*, 6(4). Available at: https://doi.org/10.1523/ENEURO.0060-19.2019.

Verhagen, M.M.M. *et al.* (2012) 'Presence of ATM protein and residual kinase activity correlates with the phenotype in ataxia-telangiectasia: A genotype–phenotype study', *Human Mutation*, 33(3), pp. 561–571. Available at: https://doi.org/10.1002/humu.22016.

Verma, M., Lizama, B.N. and Chu, C.T. (2022) 'Excitotoxicity, calcium and mitochondria: a triad in synaptic neurodegeneration', *Translational Neurodegeneration*, 11(1), p. 3. Available at: https://doi.org/10.1186/s40035-021-00278-7.

Vermezovic, J. *et al.* (2015) 'Notch is a direct negative regulator of the DNA-damage response', *Nature Structural & Molecular Biology*, 22(5), pp. 417–424. Available at: https://doi.org/10.1038/nsmb.3013.

Vicars, H. *et al.* (2021) 'Kinetochore-independent mechanisms of sister chromosome separation', *PLOS Genetics*, 17(1), p. e1009304. Available at: https://doi.org/10.1371/journal.pgen.1009304.

Vinters, H.V., Gatti, R.A. and Rakic, P. (1985) 'Sequence of cellular events in cerebellar ontogeny relevant to expression of neuronal abnormalities in ataxia-telangiectasia', *Kroc Foundation Series*, 19, pp. 233–255.

Waltes, R. *et al.* (2009) 'Human RAD50 Deficiency in a Nijmegen Breakage Syndrome-like Disorder', *The American Journal of Human Genetics*, 84(5), pp. 605–616. Available at: https://doi.org/10.1016/j.ajhg.2009.04.010.

Wan, H.I. *et al.* (2000) 'Highwire Regulates Synaptic Growth in Drosophila', *Neuron*, 26(2), pp. 313–329. Available at: https://doi.org/10.1016/S0896-6273(00)81166-6.

Wang, H. *et al.* (2013) 'The Interaction of CtIP and Nbs1 Connects CDK and ATM to Regulate HR–Mediated Double-Strand Break Repair', *PLoS Genetics*, 9(2), p. e1003277. Available at: https://doi.org/10.1371/journal.pgen.1003277.

Wang, M. *et al.* (2013) 'Novel Smad proteins localize to IR-induced double-strand breaks: interplay between TGFβ and ATM pathways', *Nucleic Acids Research*, 41(2), pp. 933–942. Available at: https://doi.org/10.1093/nar/gks1038.

Wang, T., Lao, U. and Edgar, B.A. (2009) 'TOR-mediated autophagy regulates cell death in *Drosophila* neurodegenerative disease', *Journal of Cell Biology*, 186(5), pp. 703–711. Available at: https://doi.org/10.1083/jcb.200904090.

Wang, Y. *et al.* (2021) 'Structural and Functional Synaptic Plasticity Induced by Convergent Synapse Loss in the Drosophila Neuromuscular Circuit', *The Journal of Neuroscience*, 41(7), pp. 1401–1417. Available at: https://doi.org/10.1523/JNEUROSCI.1492-20.2020.

Wang, Z. *et al.* (2019) 'MRE11 UFMylation promotes ATM activation', *Nucleic Acids Research*, 47(8), pp. 4124–4135. Available at: https://doi.org/10.1093/nar/gkz110.

Watters, D. *et al.* (1997) 'Cellular localisation of the ataxia-telangiectasia (ATM) gene product and discrimination between mutated and normal forms', *Oncogene*, 14(16), pp. 1911–1921. Available at: https://doi.org/10.1038/sj.onc.1201037.

Watters, D. *et al.* (1999) 'Localization of a Portion of Extranuclear ATM to Peroxisomes', *Journal of Biological Chemistry*, 274(48), pp. 34277–34282. Available at: https://doi.org/10.1074/jbc.274.48.34277.

White, E. (2016) 'Autophagy and p53', *Cold Spring Harbor Perspectives in Medicine*, 6(4), p. a026120. Available at: https://doi.org/10.1101/cshperspect.a026120.

Williams, A.B. and Schumacher, B. (2016) 'p53 in the DNA-Damage-Repair Process', *Cold Spring Harbor Perspectives in Medicine*, 6(5), p. a026070. Available at: https://doi.org/10.1101/cshperspect.a026070.

Williams, R.M., Yates, L.A. and Zhang, X. (2020) 'Structures and regulations of ATM and ATR, master kinases in genome integrity', *Current Opinion in Structural Biology*, 61, pp. 98–105. Available at: https://doi.org/10.1016/j.sbi.2019.12.010.

Wilson, M.H. and Deschenes, M.R. (2005) 'The neuromuscular junction: Anatomical features and adaptations to various forms of increased, or decreased neuromuscular activity', *International Journal of Neuroscience*, 115(6), pp. 803–828. Available at: https://doi.org/10.1080/00207450590882172.

Wilson, N. *et al.* (2023) 'The autophagy–NAD axis in longevity and disease', *Trends in Cell Biology*, p. S0962892423000235. Available at: https://doi.org/10.1016/j.tcb.2023.02.004.

Woodbine, L. *et al.* (2011) 'Endogenously induced DNA double strand breaks arise in heterochromatic DNA regions and require ataxia telangiectasia mutated and Artemis for their repair', *Nucleic Acids Research*, 39(16), pp. 6986–6997. Available at: https://doi.org/10.1093/nar/gkr331.

Wu, C. *et al.* (2005) 'Highwire Function at the Drosophila Neuromuscular Junction: Spatial, Structural, and Temporal Requirements', *The Journal of Neuroscience*, 25(42), pp. 9557–9566. Available at: https://doi.org/10.1523/JNEUROSCI.2532-05.2005.

Xiao, B. *et al.* (2007) 'Structural basis for AMP binding to mammalian AMP-activated protein kinase', *Nature*, 449(7161), pp. 496–500. Available at: https://doi.org/10.1038/nature06161.

Xiao, J. *et al.* (2019) 'Structural insights into the activation of ATM kinase', *Cell Research*, 29(8), pp. 683–685. Available at: https://doi.org/10.1038/s41422-019-0205-0.

Xu, B. *et al.* (2002) 'Phosphorylation of Serine 1387 in Brca1 Is Specifically Required for the Atm-mediated S-Phase Checkpoint after Ionizing Irradiation1', *Cancer Research*, 62(16), pp. 4588–4591.

Xu, D. *et al.* (2009) 'Genetic control of programmed cell death (apoptosis) in Drosophila', *Fly*, 3(1), pp. 78–90.

Yamamoto, A. *et al.* (1998) 'Bafilomycin A1 Prevents Maturation of Autophagic Vacuoles by Inhibiting Fusion between Autophagosomes and Lysosomes in Rat Hepatoma Cell Line, H-4-

II-E Cells.', *Cell Structure and Function*, 23(1), pp. 33–42. Available at: https://doi.org/10.1247/csf.23.33.

Yan, C. *et al.* (2019) 'IRE1 promotes neurodegeneration through autophagy-dependent neuron death in the Drosophila model of Parkinson's disease', *Cell Death & Disease*, 10(11), pp. 1–15. Available at: https://doi.org/10.1038/s41419-019-2039-6.

Yang, H. *et al.* (2017) 'Mechanisms of mTORC1 activation by RHEB and inhibition by PRAS40', *Nature*, 552(7685), pp. 368–373. Available at: https://doi.org/10.1038/nature25023.

Yoshimura, S.H. and Hirano, T. (2016) 'HEAT repeats – versatile arrays of amphiphilic helices working in crowded environments?', *Journal of Cell Science*, 129(21), pp. 3963–3970. Available at: https://doi.org/10.1242/jcs.185710.

Yoshino, J., Baur, J.A. and Imai, S. (2018) 'NAD+ Intermediates: The Biology and Therapeutic Potential of NMN and NR', *Cell Metabolism*, 27(3), pp. 513–528. Available at: https://doi.org/10.1016/j.cmet.2017.11.002.

You, Z. *et al.* (2005) 'ATM Activation and Its Recruitment to Damaged DNA Require Binding to the C Terminus of Nbs1', *Molecular and Cellular Biology*, 25(13), pp. 5363–5379. Available at: https://doi.org/10.1128/MCB.25.13.5363-5379.2005.

You, Z. *et al.* (2007) 'Rapid activation of ATM on DNA flanking double-strand breaks', *Nature Cell Biology*, 9(11), pp. 1311–1318. Available at: https://doi.org/10.1038/ncb1651.

You, Z. *et al.* (2009) 'CtIP Links DNA Double-strand Break Sensing to Resection', *Molecular cell*, 36(6), pp. 954–969. Available at: https://doi.org/10.1016/j.molcel.2009.12.002.

Young, D.B. *et al.* (2005) 'Identification of Domains of Ataxia-telangiectasia Mutated Required for Nuclear Localization and Chromatin Association', *Journal of Biological Chemistry*, 280(30), pp. 27587–27594. Available at: https://doi.org/10.1074/jbc.M411689200.

Zatyka, M., Sarkar, S. and Barrett, T. (2020) 'Autophagy in Rare (NonLysosomal) Neurodegenerative Diseases', *Journal of Molecular Biology*, 432(8), pp. 2735–2753. Available at: https://doi.org/10.1016/j.jmb.2020.02.012.

Zhang, B. and Stewart, B. (2010a) 'Electrophysiological Recording from Drosophila Larval Body-Wall Muscles', *Cold Spring Harbor Protocols*, 2010(9), p. pdb.prot5487. Available at: https://doi.org/10.1101/pdb.prot5487.

Zhang, B. and Stewart, B. (2010b) 'Equipment Setup for Drosophila Electrophysiology', *Cold Spring Harbor Protocols*, 2010(9), p. pdb.ip80. Available at: https://doi.org/10.1101/pdb.ip80.

Zhang, C. *et al.* (2022) 'US-align: universal structure alignments of proteins, nucleic acids, and macromolecular complexes', *Nature Methods*, 19(9), pp. 1109–1115. Available at: https://doi.org/10.1038/s41592-022-01585-1.

Zhang, D.-X. *et al.* (2016) 'The potential regulatory roles of NAD+ and its metabolism in autophagy', *Metabolism*, 65(4), pp. 454–462. Available at: https://doi.org/10.1016/j.metabol.2015.11.010.

Zhang, J. *et al.* (2013) 'Visualization of caspase-3-like activity in cells using a genetically encoded fluorescent biosensor activated by protein cleavage', *Nature Communications*, 4(1), p. 2157. Available at: https://doi.org/10.1038/ncomms3157.

Zhang, J. *et al.* (2015) 'ATM Functions at the Peroxisome to Induce Pexophagy in Response to ROS', *Nature cell biology*, 17(10), pp. 1259–1269. Available at: https://doi.org/10.1038/ncb3230.

Zhang, Y. *et al.* (2018) 'Mitochondrial redox sensing by the kinase ATM maintains cellular antioxidant capacity', *Science signaling*, 11(538), p. eaaq0702. Available at: https://doi.org/10.1126/scisignal.aaq0702.

Zhao, X. *et al.* (2017) 'Cell cycle-dependent control of homologous recombination', *Acta Biochimica et Biophysica Sinica*, 49(8), pp. 655–668. Available at: https://doi.org/10.1093/abbs/gmx055.

Zhong, Y., Budnik, V. and Wu, C. (1992) 'Synaptic plasticity in Drosophila memory and hyperexcitable mutants: role of cAMP cascade', *The Journal of Neuroscience*, 12(2), pp. 644–651. Available at: https://doi.org/10.1523/JNEUROSCI.12-02-00644.1992.

Zhong, Y. and Wu, C.-F. (2004) 'Neuronal Activity and Adenylyl Cyclase in Environment-Dependent Plasticity of Axonal Outgrowth in *Drosophila*', *The Journal of Neuroscience*, 24(6), pp. 1439–1445. Available at: https://doi.org/10.1523/JNEUROSCI.0740-02.2004.

Zhou, Y. *et al.* (2017) 'Regulation of the DNA damage response by DNA-PKcs inhibitory phosphorylation of ATM', *Molecular cell*, 65(1), pp. 91–104. Available at: https://doi.org/10.1016/j.molcel.2016.11.004.

Zhu, C. *et al.* (2005) 'The influence of age on apoptotic and other mechanisms of cell death after cerebral hypoxia–ischemia', *Cell Death & Differentiation*, 12(2), pp. 162–176. Available at: https://doi.org/10.1038/sj.cdd.4401545.

Zito, K. *et al.* (1999) 'Watching a Synapse Grow: Noninvasive Confocal Imaging of Synaptic Growth in Drosophila', *Neuron*, 22(4), pp. 719–729. Available at: https://doi.org/10.1016/S0896-6273(00)80731-X.

Ziv, Y. *et al.* (2006) 'Chromatin relaxation in response to DNA double-strand breaks is modulated by a novel ATM- and KAP-1 dependent pathway', *Nature Cell Biology*, 8(8), pp. 870–876. Available at: https://doi.org/10.1038/ncb1446.